ORIGIN AND GROWTH OF FRACTURES ON LOW-GRAVITY BODIES: INSIGHTS FROM 4 VESTA, 1 CERES, AND EARTH

by

Hiu Ching Jupiter Cheng

(Under the Direction of Christian Klimczak)

ABSTRACT

Fracturing on small planetary bodies is controlled by low gravity, which differs from what is observed on Earth and other large planets. Studying the tectonics of small bodies is crucial for understanding the planetary evolution of recent and past lithospheres, from large to small, rocky to non-rocky bodies in the Solar System. Asteroid 4 Vesta displays a remarkably large set of troughs, Divalia Fossae, encircling the asteroid around the equator, while planetary-scale impact basins occupy most of the southern hemisphere. These structures provide vital clues for understanding the growth and origin of large fractures on small bodies. Moreover, the fractures hidden beneath the regolith layer or invisible in spacecraft imagery can be revealed using the planform shape of impact craters and provide insight into the planetary evolution that has not been studied before. Furthermore, studying the evolution of fractures in extensional tectonic regimes on Earth allows us to compare to the structures on low-gravity planetary bodies, which is crucial to understand the geologic processes on extraterrestrial worlds.

This research investigates several topics related to the growth and origin of fractures on low-gravity planetary bodies, drawing a comprehensive understanding of the deformation of planetary lithospheres. The study of the structure and tectonics of the Divalia Fossae on Vesta involved structural mapping, rock mechanical calculations, crater counting, and geomorphologic characterizations. A series of geologic constraints are inconsistent with the leading hypothesis that the Divalia Fossae were directly formed by the large impact in the southern hemisphere via normal faulting, but rather had a spinning-related origin as a long-term consequence of large impacts, accommodating opening-mode displacements. The planform shape of impact craters on Vesta and the dwarf planet Ceres reveals regional and global tectonic patterns. Modeling predictions specifically tied to the low gravity and associated rock properties of these bodies are needed to evaluation of the origins of these patterns. A field investigation of the Koa'e Fault System, Hawaii studied an analog process to that of the Divalia Fossae. The conceptual model and fracture scaling capture the transition from jointing to faulting, which is comparable to the proposed fracturing process on low-gravity bodies.

INDEX WORDS: Rock fractures, structural geology, planetary tectonics, impact cratering, 4 Vesta, 1 Ceres, Terrestrial analog, Koa'e Fault Zone, Hawaii, rift zone

ORIGIN AND GROWTH OF FRACTURES ON LOW-GRAVITY BODIES: INSIGHTS FROM 4 VESTA, 1 CERES, AND EARTH

by

HIU CHING JUPITER CHENG

BS, University of Hong Kong, Hong Kong, 2017

MPhil, University of Hong Kong, Hong Kong, 2019

A Dissertation Submitted to the Graduate Faculty of The University of Georgia in Partial Fulfillment of the Requirements for the Degree

DOCTOR OF PHILOSOPHY

ATHENS, GEORGIA

2023

ORIGIN AND GROWTH OF FRACTURES ON LOW-GRAVITY BODIES:

INSIGHTS FROM 4 VESTA, 1 CERES, AND EARTH

by

HIU CHING JUPITER CHENG

Major Professor:	Christian Klimczak
Committee:	Steven Holland
	Robert B. Hawman
	Caleb Fassett

Electronic Version Approved:

Ron Walcott
Vice Provost for Graduate Education and Dean of the Graduate School
The University of Georgia
May 2023

DEDICATION

For Peter, who makes all things possible

ACKNOWLEDGEMENTS

I would like to begin by expressing my sincere gratitude to my advisor, Dr. Christian Klimczak, for his invaluable guidance, encouragement, and support throughout my academic journey. Dr. Klimczak is a brilliant scientist who not only allowed me to pursue my research interests but also challenged me to improve my work with his insightful feedback. He remained a compassionate mentor who understood the challenges faced by an international student like me. Although I may have given him some hard times with my quirks and idiosyncrasies, working with him has been both productive and enjoyable, and I am grateful for his mentorship.

I would also like to thank my committee members for their contributions to my research. Dr. Caleb Fassett provided important insights and assistance in the area of crater counting research, and also provided guidance in pursuing a career in planetary science. Dr. Steven Holland provided helpful advice on academic writing and statistical analysis, which greatly improved my research papers. Lastly, I would like to thank Dr. Rob Hawman for his geophysical input and continuous support. He has also helped me in my teaching project and demonstrated the kind of teacher I aspire to be. I am grateful for the opportunity to have worked with such a distinguished group of scholars. Without their guidance and support, this dissertation would not have been possible.

Additionally, I would like to express my gratitude to Jay Mrazek, who provided invaluable support during the fieldwork at the Hawaii Volcanoes National Park as a field assistant. Jay was an exceptional partner who worked tirelessly with me in the field, and his assistance was integral to the successful completion of my research. Furthermore, the two weeks we spent in a cabin under the stars next to an erupting volcano was an unforgettable experience, and I am grateful for the memories we shared.

Next, I would like to express my sincere gratitude to the various organizations that provided funding for my research and travel. I am especially grateful to the Eugene M. Shoemaker Impact Cratering Award from the GSA Planetary Geology Division, which helped me continue my research on impact craters during the challenging times of the COVID-19 pandemic. The Frank E. Kottlowski Memorial Grant from AAPG Foundation Grants-in-Aid Award and Watts Wheeler Research Award from UGA Department of Geology allowed me to conduct fieldwork in Hawaii during the summer of 2022. Furthermore, I am grateful to NASA Small Bodies Assessment Group, AGU 2022 Fall Meeting Student Travel Grant, GSA Meeting Division Travel Grant from the Planetary Geology Division, UGA Graduate School, and Watts Wheeler Award from the Department of Geology for providing travel grants that enabled me to attend conferences and present my research as an early-career scientist.

I would like to extend my thanks to my lab mates Isik, Melanie, Sierra, Stevie, and Sydney, who have been an integral part of my life in the US for the past four years. Not only have they been great friends, but they have also made working in the lab more enjoyable. Additionally, my best friend Charlotte, who is also from Hong Kong and

studying for her Ph.D. in the US, has been a tremendous source of support and companionship while being 1000 miles away in Corpus Christi TX.

Last but definitely not least, I want to take this opportunity to express my deep appreciation to Peter, my husband, who has been my rock by the end of this journey. He is truly the best thing that has happened to me since I arrived in the US. He has been my constant support system, always believing in me even when I didn't believe in myself. He has given me a place to call home, despite being from the other side of the world, and has been willing to follow me wherever my dreams take us.

TABLE OF CONTENTS

Page

LIST OF TABLES

Page

LIST OF FIGURES

Page

CHAPTER 1

INTRODUCTION AND LITERATURE REVIEW

Fractures formed in extensional tectonic regimes, including opening-mode fractures (i.e., joints) and normal faults, are important structures in the lithosphere of Earth and other planetary bodies. Within the uppermost parts of a lithosphere that is under extension, subvertical joints form near the surface and propagate downwards until they reach a critical depth, where the overburden pressure is large enough to shift any tensile stresses to a fully compressive stress regime. At that depth, joints transition to normal faults (Figure 1.1a). Normal faulting is therefore expected to dominate the fracturing behavior as faults penetrate deeper into the lithosphere. Normal faults can also form as blind/subsurface faults that trigger jointing at the surface. In either case, such fractures possess opening-mode and sliding-mode displacement, i.e., they are mixed-mode fractures, and joints and normal faults form as part of the same fracture population (Figure 1.1a). As these mixed-mode fractures grow, they develop even more complex systems with segmented and interacting fault systems and other geologic phenomena arising from the interaction of volcanic resurfacing and previous deformation. This type of mixed-mode structure is commonly found associated with large rift systems on Earth, forming fissures such as the Almannagjá normal fault at the Reykjaneshryggur-Langjökull rift system of southwest Iceland (e.g., Gudmundsson, 1992, 2011), Koa'e fault system associated with the Kīlauea volcano rift zone in Hawaii (Figure 1.1b;

Denlinger and Okubo, 1995; Holland et al., 2006; Martel and Langley, 2006; Ge et al., 2019), and the Wonji Fault Belt associated with the Ethiopian Rift in East Africa (e.g., Acocella et al., 2003), as well as related structures on other planetary bodies, such as pit crater chains associated with normal faults on Mars (Ferrill et al., 2004) and the troughs on asteroid 4 Vesta that are subject of this dissertation (Cheng and Klimczak, 2022).

The surface gravitational acceleration, g, of a planetary body (referred to as 'gravity' hereon) plays a key role in the development of fractures formed in extensional tectonic regimes. In particular, the depth of the joining-faulting transition (Figure 1.1 a) depends on the gravity of the body in combination with the physical properties of the rock in which the fracturing occurs. On large terrestrial bodies like the Earth, the transition is estimated to occur between 260 to 800 m in depth (Gudmundsson, 1992; Acocella et al., 2003; Grant and Kattenhorn, 2004; Hardy, 2013), depending on the tensile strength and density of basalt. Therefore, while opening-mode fracturing such as jointing is a ubiquitous fracturing behavior in the upper portion of the Earth's lithosphere, large-scale normal faulting also occurs near the surface. For lithospheres with the same strength and density properties on small, low-gravity bodies, such as moons and asteroids, the jointing-faulting transition is expected to lie deeper since the overburden pressure gradient is not steep enough to reach a stress state in which joints transition to normal faults at a shallow depth. Therefore, opening-mode fracturing should be the dominant fracturing mode on small bodies, and joint openings and lengths are expected to be much larger compared to what we see on Earth. However, this type of fracturing behavior has not been widely considered in the tectonics of small planetary bodies, especially for

bodies with a series of large-scale surface troughs that are proposed to form under extension, such as those on Asteroid 4 Vesta and Mars' moon Phobos.

Studying the origin and growth of these extensional fractures and comparing them across planetary bodies of various sizes will highlight the differences in the rheology and brittle strength of the lithospheres of small bodies and shed light on their tectonic structures and processes. This dissertation describes the formation and development of fracturing in extensional tectonic regimes on Asteroid 4 Vesta (Figure 1.1 c; from now on referred to as "Vesta"), 1 Ceres (an icy dwarf planet located in Vesta's planetary neighborhood in the Main Asteroid Belt; from now on referred to as "Ceres"), and an analog site on Earth (Figure 1.1 b). This dissertation also examines what these fracture patterns and their relationships with other structures reveal about the tectonics of the planetary bodies. A literature review and research gaps are discussed in the following sections.

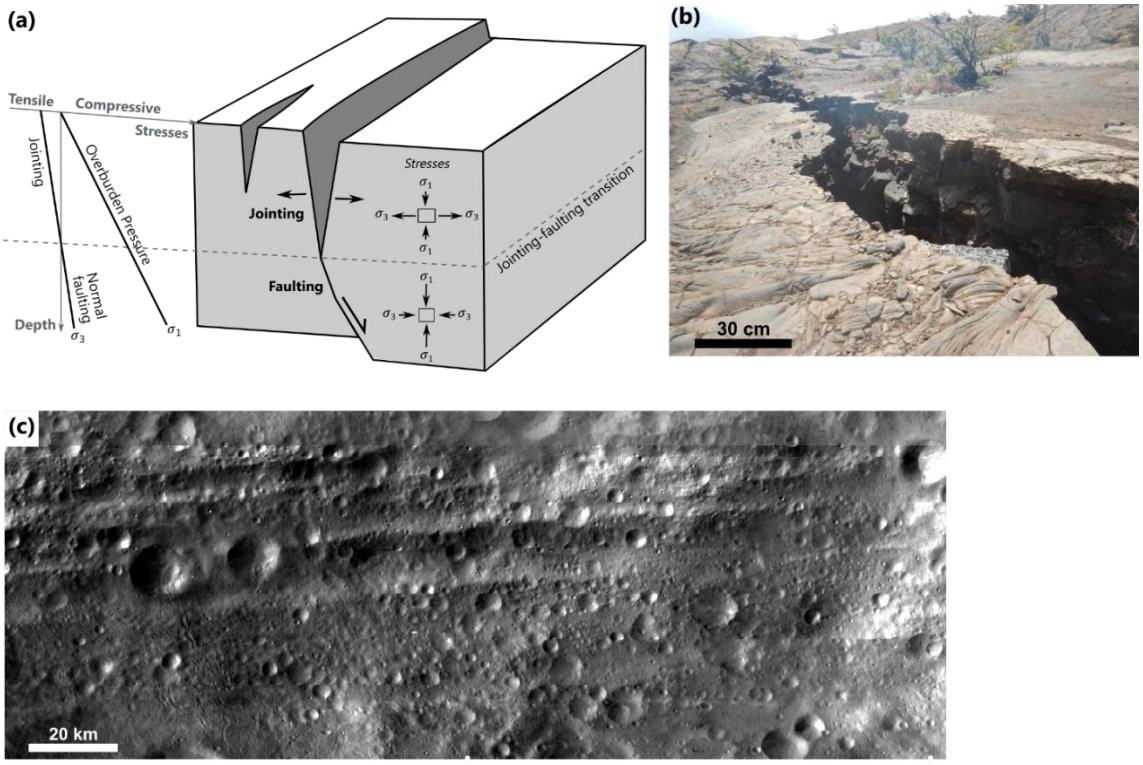

Figure 1.1 *Diagram of fracturing under extensional tectonic regimes and examples on Earth and Vesta. (a) Block diagram conceptually showing the geometry of jointing and faulting along the mixed-mode fracture (on the right) and the stress profile in the lithospheric strength envelope format (brittle only; on the left). The maximum principal stress, σ_1, is always the vertical overburden pressure in an extensional tectonic regime whereas the minimum principal stress, σ_3, will be along the horizontal parallel to the surface. (b) Photographs of the Koa'e Fault Zone, Hawaii. (c) An image of the surface Vesta taken by the Dawn spacecraft showing a portion of the Divalia Fossae.*

Large-scale Fractures on Vesta

Vesta is one of the largest asteroids in the Main Asteroid Belt with a mean diameter of 525 km (Russell et al., 2012). The Howardite-eucrite-diogenite (HED) meteorites that have fallen to Earth are thought to have originated from the crust and possibly the upper mantle of Vesta (McSween et al., 2013). These are differentiated meteorites formed by igneous processes, which makes Vesta the only known differentiated small body, i.e., a planetesimal or protoplanet, and is therefore thought to be a remnant of the building blocks that accreted to form the terrestrial planets. These radioisotope ratios of HED meteorites give crystallization ages between 4.43 and 4.55 Ga (McSween et al., 2013). The Dawn mission (Russell and Raymond, 2011) entered orbit around Vesta on July 16, 2011, and mapped the surface of Vesta with its Framing Camera instrument (FC; Ruesch et al., 2014) and Visible and Infrared Spectrometer (VIR; De-Sanctis et al., 2010) with resolutions of ~260 m/pixel for the FC and ~700 m/pixel for the VIR. Its igneous crust is consistent with differentiated terrestrial planets (Zuber et al., 2011). The shape of Vesta is an oblate spheroid with concavity and

protrusion at the south pole, and its surface has a complex topography (Jaumann et al., 2012).

Two large impact basins are present at the southern pole with the Rheasilvia basin, which has an approximate diameter of 500 ± 20 km, a relatively low crater density, a smoother surface compared with its surrounding terrain, and is bounded by steep terracing scarps (e.g., Russell et al., 2012; Marchi et al., 2012). An older impact basin called Veneneia is around 400 ± 20 km wide and mostly overlaid by the Rheasilvia basin (Jaumann et al., 2012). The Dawn mission also documented two sets of large-scale linear structures, one located around the equator and the other located in the northern hemisphere. The equatorial troughs, called Divalia Fossae (Figure 1.1 c), vary in width from several 100s of meters to about 20.5 km, are bounded by steep scarps, and encircle about two-thirds of the asteroid. The northern troughs, called Saturnalia Fossae, extend to the northwest oriented approximately 30° from the equatorial troughs and are exposed only in the northern hemisphere due to the superposition at their southern extensions by the Divalia Fossae. The leading hypothesis is that Divalia Fossae are grabens (fault-related landforms) that were directly formed by the impact that led to the emplacement of the Rheasilvia impact basin at the south pole. Previous work established that the poles of vertical planes along the two sets of troughs cluster near the center of Veneneia and Rheasilvia impact basins are at the south pole, therefore implying a genetic link between the two impacts and the two sets of troughs (Jaumann et al., 2012). Divalia Fossae were described as flat-floored and interpreted as a graben, formed by normal faulting, with vertical displacements in excess of 5 km (Buczkowski et al. (2012). Since then, this leading hypothesis has been the basis of other studies such as global stratigraphy (Schäfer

et al., 2014; Williams et al., 2014; Yingst et al., 2014) and numerical modeling (Jutzi et al., 2013; (Bowling et al., 2014; Stickle et al., 2015).

One major issue is that the rheology and brittle strength of Vesta's lithosphere have not been evaluated, and other fracture types have not been considered in the tectonics of the asteroid. Since Vesta is a low-gravity body, it is questionable if the overburden pressure is large enough for normal faulting to occur at the scale of the Divalia Fossae near the surface. Although previous study evaluated the shapes of the largest troughs of the Divalia and Saturnalia Fossae and interpreted them to be analogous to grabens on the terrestrial planets (Buczkowski et al., 2012), other smaller troughs occur among these structures, but their characteristics have not been analyzed for their structure and origin. Moreover, the temporal relationship between the troughs and the two impact basins has not been studied. Crater counting works have been conducted to determine the age of the Veneneia and Rheasilvia impact event (e.g., Schenk et al., 2012; Schmedemann et al., 2014). However, the formation age of the troughs has never been determined by crater size-frequency analysis prior to this work. Therefore, the relative age of the basins and the troughs has not been determined by crater counting. If the leading hypothesis of impact-induced large-scale is true, the basin and the troughs should be formed at a similar time. Furthermore, the structures found within the Rheasilvia basin and especially their relationships with the Divalia Fossae have not been explored, leaving the geographic relationship (Jaumann et al., 2012) as the sole evidence for the leading hypothesis.

Hidden Fracture Patterns on Small Bodies

While some fractures (e.g., Divalia and Saturnalia Fossae) are visible in spacecraft imagery, some if not most fractures are not directly visible on the planetary surface. Where in the target rock has pre-existing fractures, impact craters may have straight rim segments that create polygonal geometries (e.g., Fielder, 1961; Öhman et al., 2005; Shoemaker, 1962, 1987; Weihs et al., 2015), revealing invisible tectonic patterns. A prominent example is the nearly square-shaped Meteor Crater in Arizona with its straight rim segments that are parallel to two regional joint sets on the Colorado Plateau (e.g., Schoemaker, 1960; Kumar and Kring, 2008). Planform impact craters abound on various planetary bodies, including the Moon, Mercury, Venus, Mars, icy moons, and asteroids (e.g., Beddingfield et al., 2016; Neidhart, 2018; Öhman et al., 2005; Shoemaker, 1962; Watters et al., 2011; Weihs et al., 2015). Several studies have characterized the planform shapes of impact craters on the terrestrial planets with implications for their tectonics, but very few studies have been conducted on low-gravity bodies and asteroids, including Vesta and Ceres (see Neidart, 2017; Zeilnhofer and Barlow, 2021).

Vesta and Ceres are heavily cratered, and they have also experienced tectonics. NASA's Dawn mission (Russell and Raymond, 2011) revealed a remarkable variety of tectonic landforms on Ceres and Vesta, including pit crater chains, troughs, impact craters, and ridges. Most of these landforms have been recorded and analyzed during the construction of global geological maps (e.g., Williams et al., 2018; Yingst et al., 2014) but they were not systematically compared to the planform impact crater shapes. As these planform shapes may reveal the presence of these hidden planetary structures, it is intriguing to ask: *Can the planform shape of impact craters be used to identify fracture*

sets and thus reveal local, regional, or even global tectonic patterns on Vesta and Ceres? Moreover, since the first descriptions of polygonal impact craters on Ceres and Vesta (Platz et al., 2015; Ruesch et al., 2014), several studies have examined these features. The majority of craters on Ceres and Vesta are polygonal (Neidhart, 2018; Otto et al., 2016). However, all previous literature mapped the straight rims of these impact craters based mainly on the visual selection and investigated only the crater sizes, spatial distributions, and numbers of straight rim segments. No systematic approach has been applied to identify the straight rims of impact craters on Vesta and Ceres, and the hidden tectonics that may have controlled the crater geometry has never been explored. Developing a *quantitative method* that can be applied to other bodies is vital for any planform impact crater shape characterization and aims for proper comparison of the data between Vesta and Ceres, as well as other different planetary objects in future studies.

If global tectonic patterns are present on Ceres and/or Vesta, *what are the origins of these patterns on Vesta and Ceres?* Although these bodies are likely too small to have driven internal tectonic processes at present, large impacts and stresses from rotational bulging are hypothesized to generate regional and global tectonic structures on small bodies (Thomas and Prockter, 2010). Impacts play an essential role by creating new fractures and reactivating existing structures, which in turn produce local and global fracture patterns depending on the impact energy. Stresses from rotational bulging may form global tectonic patterns such as the prominent grooves on Phobos (Hurford et al., 2016). In particular, Vesta and Ceres both have an extremely fast rotation period of ~9 and 5 hours, respectively, which may induce equatorial bulging. However, an impact as large as the one that formed the Rheasilvia basin may potentially cause the tectonic

patterns on Vesta. No such large impact basin is present on Ceres, and thus an associated tectonic pattern may be missing there (Marchi et al., 2016). By comparing the tectonic/fracture patterns of Vesta and Ceres, we can deduce the origin of these patterns and reveal the hidden geological history of the two small bodies.

Koa'e Fault Zone as a Planetary Analog on Earth

Studying how rocks fracture on Earth is the key to understanding the rock mechanics on other planetary bodies of various sizes, especially as an end-member of large terrestrial bodies. In this dissertation, I focus on mixed-mode fracturing that involves the opening displacements from jointing and sliding mode displacements from normal faulting (Figure 1.1a). The Koa'e Fault Zone is an active ~12-km long and ~2.5-km wide normal fault system (Denlinger and Okubo, 1995; Holland et al., 2006; Ge et al., 2019). It lies between the Southwestern Rift Zone and East Rift Zone that join at the Kīlauea edifice. The main faults all have a dilational component of up to several meters wide (Figure 1.1b; Holland et al., 2006; Martel and Langley, 2006), and they are associated with numerous subparallel prominent joints (Le Gall et al., 2000). Koa'e Fault Zone develops at the southern flank of the Kilauea volcano, which is facing the Pacific Ocean at the southern part of the Hawaii Big Island. Since the volcano structure is unsupported on this side, the confining pressure is lower along this flank, causing an overall southward displacement of the fault, breaking off from the volcanic structure. Together with the gravity difference between Earth and Vesta, the tectonic setting of the Koa'e Fault Zone makes it an ideal site for investigating the transition from opening to sliding-mode fracturing.

Numerous studies have demonstrated that the maximum displacement along faults and joints scale with their lengths (e.g., Muraoka and Kamata, 1983; Cowie and Scholz; 1992; Schultz et al., 2006; 2008; 2013). Displacement-length (D_{max}/L) scaling is an important technique for characterizing fracture populations on Earth (e.g., Scholtz et al., 1993; Poulimenos, 2000; Wilkins and Gross, 2002) and other terrestrial bodies (e.g., Schultz, 1997; Schultz et al., 2006; Polit et al., 2009). D_{max}/L scaling has far reaching implications for rock mechanics, structural geology, and tectonics, such as tectonic strains (e.g., Nahm and Schultz, 2011), fault growth and segmentation (e.g., Cowie et al., 1993; Hughes and Shaw, 2014), rock properties (e.g., Dawers et al., 1993; Soliva et al., 2005), and fluid flow through fractures (Klimczak et al., 2010). This technique has been used in many applications from petroleum exploration (e.g., Torabi et al., 2019) to planetary studies (e.g., Schultz et al., 2006; Nahm and Schultz, 2011). While D/L scaling of normal faulting and jointing has been extensively studied with sufficient field data of faults and joints, the length scaling of the displacements of mixed-mode fracturing, which includes the opening, sliding, and any associated dilation, has had far less study.

To investigate the transition from jointing to faulting, a conceptual model of Koa'e Fault Zone evolution is needed, with extensive and detailed field observations along a representative number of structures. Moreover, fracture measurements of various lengths from a few meters to kilometers along the Koa'e Fault Zone can be used to establish a D_{max}/L scaling relationship of mixed-mode fracturing. Such measurements would allow the characterization of a mixed-mode fracture population within an extensional tectonic regime on Earth, allowing the comparison to the fracture behavior to small bodies, including the Divalia Fossae on Vesta (Figure 1.1c).

Overview of the Chapters of the Dissertation and their Significance

Fracturing via jointing and normal faulting of various scales under an extensional tectonic regime is controlled by the gravity of the planetary body. However, the fracture pattern, behavior, and origins have not been widely explored among small bodies, and hence the role of gravity in tectonics is not fully understood. This dissertation aims to investigate this research gap and showcase several approaches for investigating the origin and growth of fractures from regional-scale fracturing on Earth to the tectonic structures and global patterns on small planetary bodies. Each chapter in this dissertation addresses aspects of fracturing under extension on small, low-gravity planetary bodies:

Chapters 2 to 4 focus on the structure and origin of the Divalia Fossae on Vesta. *Chapter* 2 investigates the map pattern, geomorphologic characteristics, and cross-sectional geometry. It provides rock mechanical calculations that account for the low gravity to distinguish the fracturing behavior of jointing vs. faulting of Divalia Fossae. *Chapter* 3 explores the relative age relationship between the Divalia Fossae and Rheasilvia basin by crater counting, thereby testing the proposed synchronous development of troughs and basin formation. To explore the structural relationship between the troughs and the basin, *Chapter* 4 examines the structures in the Rheasilvia basin and compares that to the Divalia Fossae described in *Chapter* 2. Together, these three chapters provide new geologic constraints on the fracturing behavior and tectonic evolution of Vesta. *Chapter* 5 reveals the hidden fracture patterns on Vesta and Ceres revealed by planform impact crater shapes and investigates the origin by comparative planetology. *Chapter* 6 presents a field study at the Koa'e Fault Zone, Hawaii, showing how mixed-mode fractures grow and develop on Earth as a comparative analog site to the

Divalia Fossae on Vesta and other large-scale fractures on planetary bodies with various sizes and gravities. This dissertation provides an in-depth understanding of how the fractures of different scales originate and grow over time in extensional tectonic regimes on small bodies, how gravity controls the fracturing behavior, and how these fractures differ from what we observe on Earth.

CHAPTER 2

LARGE-SCALE TROUGHS ON ASTEROID 4 VESTA ACCOMMODATE OPENING-MODE DISPLACEMENT[1]

[1] Cheng, H. C. J. and Klimczak, C. 2022. *Journal of Geophysical Research: Planets, 127*(6), e2021JE007130.

Abstract

Asteroid 4 Vesta hosts two sets of enormous troughs, Divalia Fossae that encircle two-thirds of the equator and Saturnalia Fossae located in the northern hemisphere. These troughs were interpreted as grabens, thus invoking faulting. The trough sizes, their linear arrangement, and overall morphology leave no doubt that their origin is tectonic, but structures other than faults have not been considered. To test if they are fault-related or formed by accommodating opening-mode displacement (i.e., jointing) without subsequent shear, I investigate the map patterns, cross-sectional geometries, and variations of relief and width along the trough lengths. Relief and width could relate to the vertical displacement of faults and aperture of joints, respectively, and they therefore reveal differences in fracturing behavior. I analyzed six major troughs on Vesta, four belonging to Divalia Fossae, and two to Saturnalia Fossae. No map patterns are diagnostic of faulting or jointing. For each pair of trough-bounding scarps, the maximum relief does not lie at the trough center, and the two maxima occur at different positions along the trough. In contrast, troughs are widest near the centers of the troughs. These characteristics are inconsistent with graben formation but are consistent with jointing. Furthermore, rock-mechanical calculations that account for Vesta's low gravitational acceleration and degree of fracturing reveal that faulting is not favored to be initiated at depths above at least ~3 but as much as 55 km within Vesta's lithosphere. Therefore, jointing or mixed-mode fracturing, both involving opening-mode displacements, are more plausible fracturing mechanisms for the Divalia Fossae.

Introduction

Vesta's tectonics

The Dawn mission (Russell and Raymond, 2011) explored Asteroid 4 Vesta and revealed the presence of two sets of large-scale linear structures (Figure 2.1). The Divalia Fossae vary in width from several hundreds of meters to up to ~20.5 km, are bounded by steep scarps, and encircle approximately two-thirds of the asteroid. The Saturnalia Fossae are oriented northwest–southeast and differ in orientation from the Divalia Fossae by ~30°. Saturnalia Fossae are exposed only in the northern hemisphere, and their southern extent is truncated by the Divalia Fossae. Photomosaics and the digital terrain model derived from Dawn Framing Camera (FC) images (Sierks et al., 2011) allow for detailed mapping and structural analysis of these troughs.

Previous work found that the Divalia and Saturnalia Fossae are concentric around the Rheasilvia and Veneneia basin centers, respectively (Figure 2.1), which was interpreted as evidence that trough formation was directly triggered by impacts (Jaumann et al., 2012). The impactor-origin has been the leading hypothesis for the formation of the Davila Fossae and thus it serves as a geologic constraint for establishing global stratigraphy (e.g., Schäfer et al., 2014; Williams et al., 2014; Yingst et al., 2014) and numerical studies (e.g., Bowling et al., 2014; Stickle et al., 2015) of Vesta. However, recent work identified the Divalia Fossae to clearly crosscut the Rheasilvia basin, and the Divalia Fossae to have no spatial relationship with the center of the Rheasilvia basin (Cheng and Klimczak., 2022). Although the established crater statistics in Cheng et al. (2021) neither confirm nor refute the simultaneous formation of the Divalia Fossae and Rheasilvia Basin, their large uncertainties allow for the Divalia Fossae to have formed

long before or after the Rheasilvia impact (Cheng et al., 2021). Taking together the established age relationships and the crosscutting relationships between troughs and basin, it is plausible for the Divalia Fossae to have formed as a long-term consequence of the Rheasilvia impact (Cheng and Klimczak., 2022), perhaps tied to changes in orientation or rotation of the asteroid (Mao and McKinnon., 2020; Karimi and Dombard, 2016). This newly proposed formation hypothesis contradicts with the leading hypothesis of the impact directly triggering the troughs, and is yet to be tested and serve as a geologic constraint by other research.

Divalia Fossae are observed to be flat-floored and interpreted as grabens formed by normal faulting, with vertical displacements in excess of 5 km (Buczkowski et al. 2012). Subsequently, multiple studies have interpreted Divalia Fossa and similar troughs on Vesta as grabens, half-grabens, and horst-graben structures (Ruesch et al., 2014; Schäfer et al., 2014; Scully et al., 2014; Yingst et al., 2014). Several modeling studies have considered the specific tectonic causes for the faulting. They have used numerical modeling to simulate the amount of deformation associated with the formation of the Rheasilvia basin (Bowling et al., 2013). They have also combined laboratory and numerical experiments to model subsurface failure as a consequence of oblique impacts into a spherical target (Stickle et al., 2015).

No alternative types of tectonic landforms and corresponding structures, such as different fracture types (e.g., opening-mode or mixed-mode fractures) or other origins (e.g., the collapse caused by perhaps some compositional layering or dike intrusion), have been proposed for the troughs on Vesta, so far. Since each set of troughs formed along a structural trend (i.e., an east–west orientation for all troughs as part of Divalia Fossae)

with their origin linked to the large impact basins (i.e., Rheasilvia and Veneneia; Jaumann et al., (2012)) or spinning of the asteroid (Karimi and Dombard, 2016; Mao and McKinnon, 2020; Cheng and Klimczak., 2022), it is plausible that the troughs have a tectonic origin. In particular, opening-mode fracturing through jointing and diking is an ubiquitous fracturing process in the upper portion of the Earth's lithosphere, but it is unknown to what extent these processes played a role in the formation of Vesta's troughs. Furthermore, the rheologic structure and depth of the brittle portion of Vesta's lithosphere and its influence on the formation of tectonic structures have not been evaluated. In this study, I specifically test if the troughs could have been formed by opening-mode fracturing in the form of jointing. To achieve that, I collect geologic observations that distinguish between faulting and jointing, and I assess the potential for faulting and jointing from a rock mechanical standpoint. Because faulting and jointing are each forms of brittle deformation, rock-mechanical assessments require characterizing the rheologic structure and the depth of the brittle lithosphere on the asteroid.

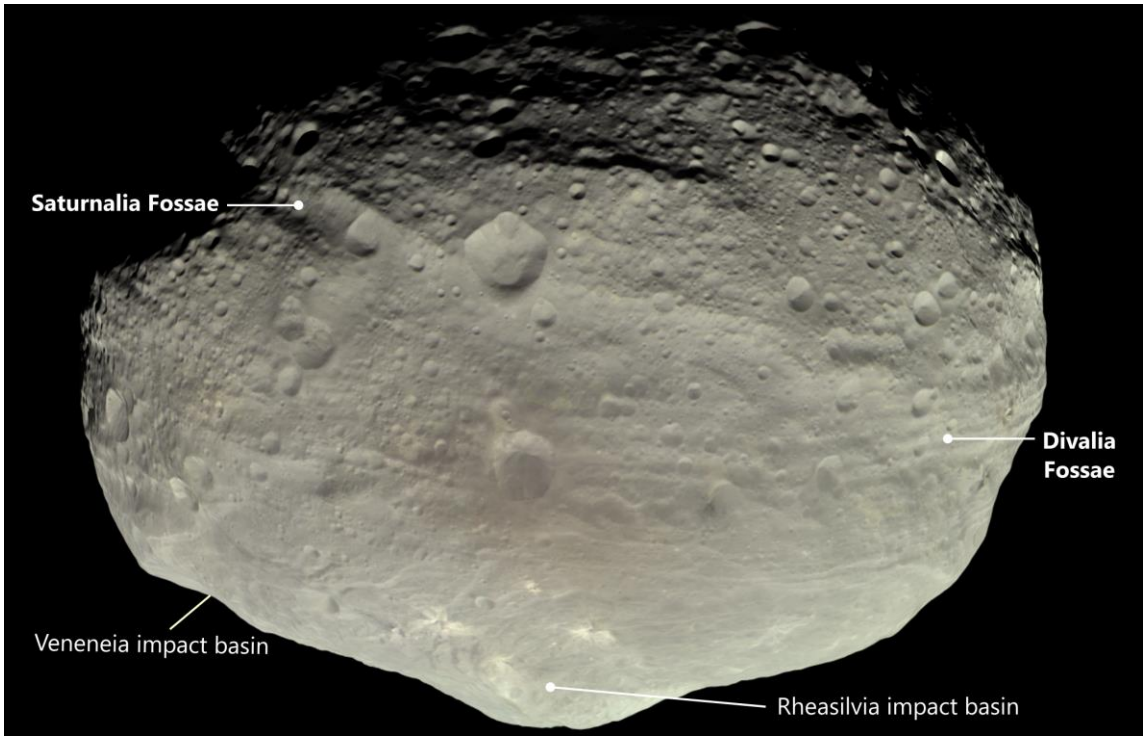

Figure 2.1. *Image of Asteroid 4 Vesta, showing the locations of the Divalia and Saturnalia Fossae, and the Veneneia and Rheasilvia impact basins. The image was captured by the NASA Dawn mission on 24 July 2011 with image processing by Björn Jónsson.*

Normal faulting vs. Jointing

Brittle failure in an extensional tectonic regime, where the overburden pressure represents the maximum principal stress, occurs by opening along joints or slip on normal faults. Joints are planar discontinuities in rock, where fracture walls move perpendicularly apart from one another due to opening displacement (Pollard and Aydin, 1988), and thus they are considered opening-mode fractures along with veins and dikes. In contrast, faulting shows movement parallel to the fault plane and is called sliding-mode or tearing-mode fracturing.

Joints form if tensile stresses reach the tensile strength of the rock in a direction largely perpendicular to the fracture plane. Normal faults form in an entirely compressive stress state via frictional sliding if the hanging wall, the rock mass above the fault plane, slips downward relative to the footwall, the rock mass beneath the fault plane.

In a lithosphere undergoing extension, joints propagate from the surface until they reach a critical depth, where they reactivate as normal faults if the overburden is large enough to shift tensile stresses into the compressive regime (pp. 235–236 in Gudmundsson, 2011). Such fractures possess opening-mode and sliding-mode displacements, and they are known as hybrid or mixed-mode fractures. Mixed-mode fractures are commonly associated with large rift zones on Earth, such as the Almannagjá normal fault at the Reykjaneshryggur–Langjökull rift system of southwest Iceland (Gudmundsson, 1992, 2011), Koa'e fault system associated with the Kīlauea volcano rift zone in Hawaii (Holland et al, 2006), and the Wonji Fault Belt associated with the Ethiopian Rift in East Africa (Acocella et al., 2003). For Earth's gravitational acceleration and its strong basaltic crust, the jointing–faulting transition may be as deep as ~800 meters (Gudmundsson, 2011). With lower gravitational accelerations but given similar rock-mechanical properties, this transition is expected to occur much deeper, and fracture sizes are expected to be much larger in the lithospheres of small bodies, such as moons and asteroids. Hence, opening-mode displacement should be important for structures formed in extensional tectonic regimes on small bodies. Despite this, opening-mode or mixed-mode fractures have not attracted much attention in the planetary community. Establishing the fracturing mode of brittle structures on planetary bodies is

important because it dictates interpretations of the stress regime, as well as the kinematics and mechanics of the tectonics responsible for forming the structures.

Structures formed by jointing versus normal faulting can be distinguished by their map patterns, cross-sectional geometries, and displacement profiles, and all have been widely studied in numerous fracturing systems on Earth and other planetary bodies. Normal faults commonly appear as grabens, which are narrow, negative relief structures bounded by oppositely dipping normal faults that create a central down-dropped block (Melosh and Williams Jr, 1989; Schultz et al., 2007; Fossen, 2016). Grabens display a wide range of map patterns, some of which are diagnostic of normal faulting and are found on many different planetary bodies. Grabens commonly have bounding scarps that are straight to arcuate as well as segmented. They may form en echelon patterns and transfer zones between overstepping segments called relay ramps (Peacock and Sanderson, 1994; Crider and Pollard, 1998). Grabens may also involve multiple faulted borders and floors, such as those in complex terrestrial rift systems (Hauber and Kronberg, 2005). In some cases, pit crater chains, which are connected circular depressions that form by the collapse of material into subsurface voids, are aligned with or superimposed on a graben, such as in those in Hawaii (Okubo and Martel., 1998) and on Mars (Wyrick et al., 2004). Normal faults of any kind typically have their point of maximum displacement near the center of the fault, with displacement tapering to zero at the fault tips. This symmetry is well-documented on Earth (e.g., Muraoka and Kamata, 1983; Dawers et al., 1993; Cartwright et al., 1996), Mars (e.g, Schultz and Lin, 2001; Polit et al., 2009), and the Moon (e.g., Callihan and Klimczak, 2019). Maximum displacements increase linearly with fault length as they grow (Schultz et al., 2006). In

cross-section, grabens are typically flat-floored depressions, bounded by two (or more) scarps that face each another.

In contrast, joints can appear in map view as the straight trace of a continuous single crack, or as segmented and discontinuous en echelon traces of small subparallel segments. Although joints can occur as isolated structures, they commonly occur as sets of parallel joints. Closely spaced joints may interact to form hook-shaped linkages (Pollard and Aydin, 1988). Joint displacement, commonly referred to as aperture, reaches its maximum in the center of the structure, tapering out symmetrically toward the tips (Vermilye and Scholz, 1995). In map view, joints may therefore appear as wide troughs that narrow toward the tips. The maximum aperture increases sublinearly with length as joints grow (Olson, 2003). In contrast to a graben, the surface expression of a vertical joint is expected to be shaped as a narrow V in cross-section, but this shape is likely degraded by slope instability, where infilling of collapsed material causes it to become shaped like a wide bowl. Open void spaces within the joint may not be visible at the surface due to collapse of and filling by surficial material.

In this chapter, I investigate the map patterns, cross-sectional geometries, and morphological variations of the large-scale troughs in detail to assess whether they display characteristics of opening-mode or sliding-mode fractures. Based on previously published interior constitution and thermal evolution models of the asteroid, and considerations of strengths of fractured basaltic rock masses, I assess the physical conditions for frictional sliding to be triggered within Vesta's lithosphere for a wide range of rock mechanical properties.

Trough map patterns

For structural mapping, I use the HAMO-based Dawn FC clear filter image mosaic with an average pixel scale of 60 m/pixel (Roatsch et al., 2015) and the ~93 m/pixel digital terrain model (DTM; Gaskell, 2012). The DTM is based on the shape model of Vesta derived from FC images, and it has a vertical accuracy of ~6 m (Preusker et al., 2014). These datasets were projected using a sphere with a diameter of 255 km and the Claudia Double-Prime system (Li et al., 2012; WGCCRE., 2014). The two large sets of troughs and their related landforms are included in the mapping, as are the bounding scarps and pit crater chains. For structural mapping, I use ESRI's ArcGIS software to create hillshade images with different illumination conditions and draw topographic cross-sections at ~5 km intervals across the troughs. Trough-bounding scarps are defined by a sharp surface break on the topographic profiles, which were traced on the hillshade images. Structures identified as *certain troughs* are mapped where negative linear relief is bounded by two facing scarps. Long depressions with a single bounding scarp are mapped as *inferred troughs*. Troughs of any category were grouped into one structure where multiple troughs were aligned and separated by only one or several impact craters. Pit craters and chains of pit craters are included in my mapping, as they are aligned with the Divalia Fossae (Buczkowski et al., 2012; Jaumann et al., 2012) and because they are commonly associated with grabens on other planetary bodies (Wyrick et al., 2004). They are mapped where there is a series of at least three aligned circular to elliptical, steep-sided depressions that lack diagnostic features for impact craters or volcanic pits, including elevated rims, ejecta deposits, or lava flows.

Previous work mapped 86 trough lineaments of Divalia Fossae and 7 trough lineaments of Saturnalia Fossae (Jaumann et al., 2012; Yingst et al., 2014), but those analyses did not consider that some troughs are parts of the same structure. Based on the mapping criteria, I identified 55 individual trough lineaments comprising 155 bounding scarps as well as 30 pit crater chains (Figure 2.2). The structural map is included as shapefiles in the supporting information. Of the 55 troughs, 36 are classified as certain and 19 as inferred. Among those, 30 certain and 9 inferred troughs form six main structures, and the other 16 troughs are smaller structures associated with Divalia Fossae. To each trough, I assigned an id number that increases from south to north. The Divalia Fossae consist of closely spaced E−W striking troughs 1 to 4, with lengths of 335−815 km and widths up to 20.5 km. Trough 1 consists of at least three segments that are widely separated by long inferred trough lineaments, whereas troughs 2 to 4 consist of certain trough lineaments superposed by a few impact craters. Troughs 5 and 6 are part of the Saturnalia Fossae with trough 6 being the widest and longest one. The southern ends of the Saturnalia Fossae are truncated by the Divalia Fossae, therefore their full original lengths are not preserved. All troughs are categorized as being isolated, continuous, and subparallel within their own sets (Figure 2.2).

None of the Vesta structures have map patterns diagnostic of faulting, such as en echelon segmentation, relay ramps, or multiple faulted borders and floors (nested graben). Instead, trough-bounding scarps are consistently scalloped (Figure 2.3a). The rims are too scalloped or too degraded to be interpreted as normal faults. In contrast, Matronalia Rupes and other scarps that form the rim of the Rheasilvia impact basin, which is thought to have been emplaced at a similar time as Divalia Fossae, appear

remarkably fresh. Map patterns diagnostic for jointing, such as hook-shaped linkages and en echelon traces of subparallel openings, are not readily apparent. Degradation and slope instability are therefore inferred to have influenced the surface expression of the troughs.

Consistent with previous studies (Buczkowski et al., 2012; Jaumann et al., 2012), pit crater chains are aligned with the Divalia Fossae (Figure 2.2 and 2.3). Generally, pit crater chains are located on the floors of planetary grabens (Wyrick et al., 2004), but none on Vesta occur within a trough, that is, between two bounding scarps. Pit crater chains on Vesta vary widely in their map patterns, and their full number and extent are unclear due to the superposition of impact craters. Only trough 1 shows a direct transition from the trough into a pit crater chain (Figure 2.3a). This trough narrows and terminates in a pit crater chain, and smaller pits align with the trough farther away from the termination of the trough. One completely preserved pit crater chain has larger pits in the middle and smaller pits at the two ends of the chain (Figure 2.3b). Following these map observations, the structures possibly represent multiple stages of trough formation where the scalloped edges of the troughs may be coalesced pits forming from collapsed openings and unstable slopes.

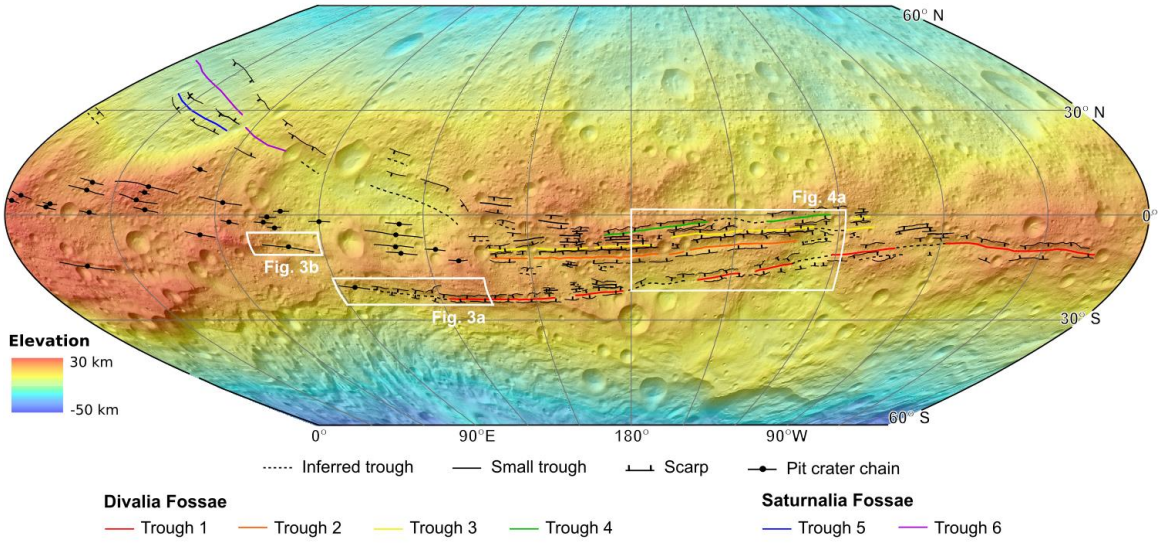

Figure 2.2. *Digital terrain model of Vesta overlain on hillshade showing a structural map of large-scale troughs and pit crater chains. The map is displayed in sinusoidal projection extending between latitudes 60ºN to 60ºS and longitudes 0º to 30ºW. Refer to text for the definition of structural map units. Locations and geographic extents of subsequent maps are indicated by white boxes. The reference elevation is defined to be the mean planetary radius of 262 km.*

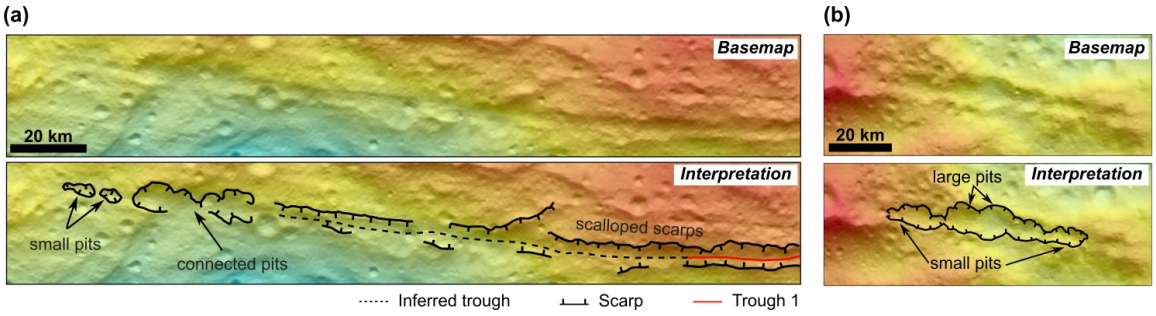

Figure 2.3. *Base map (top) and structural interpretations (bottom) of scalloped scarps and pits and pit crater chains. (a) Trough 1 terminates into coalesced pits, with smaller pits aligned with and beyond the termination of the trough. (b) A pit-crater chain with*

larger pits in the middle and smaller pits at the ends. Refer to Figure 2.2 for the location on Vesta.

Trough geomorphology

Previous work showed that troughs display a classic flat-floored shape with both walls having a similar slope, which led to their interpretation as grabens (Buczkowski et al., 2012). Based on that interpretation, Buczkowski et al. (2012) measured the topographic differences between the rim and floor of the Divalia and Saturnalia Fossae at several locations and related them to the vertical displacement component of graben-bounding normal faults. Here, I extract and analyze 233 topographic profiles at spacings of 5 km across six large troughs, to examine the cross-sectional geometries, relief, and width variations along the troughs (see supporting information).

Cross-sectional trough geometries

Cross-sectional shapes for the six troughs were assessed along the 233 extracted profiles. Most profiles contain more than one trough, and 392 individual trough geometries were analyzed. All profiles were examined for topographic changes between the trough rims to identify whether the troughs are flat-floored (no major topographic changes in the center of the trough), or have a different geometry. Trough geometries lacking distinctive rims or superposed by impact craters are classified as inconclusive. One representative profile of the Divalia Fossae has four troughs, with troughs 1, 2, and 3 being bowl-shaped, and trough 4 having a V shape (Figure 2.4a). Among all assessed topographic profiles, 207 out of 260 conclusive troughs are not flat-floored: 176 are bowl-shaped, and 31 are V-shaped. Only 53 out of 260 conclusive troughs (~20%) are flat-floored; thus, most troughs do not show the cross-sectional geomorphology that is

typical for graben. In comparison, Rima Ariadaeus on the Moon (Figure 2.4b) and grabens and horsts on the northeast flank of Alba Patera on Mars (Figure 2.4c) have the characteristic flat-floor cross section of landforms caused by normal faulting.

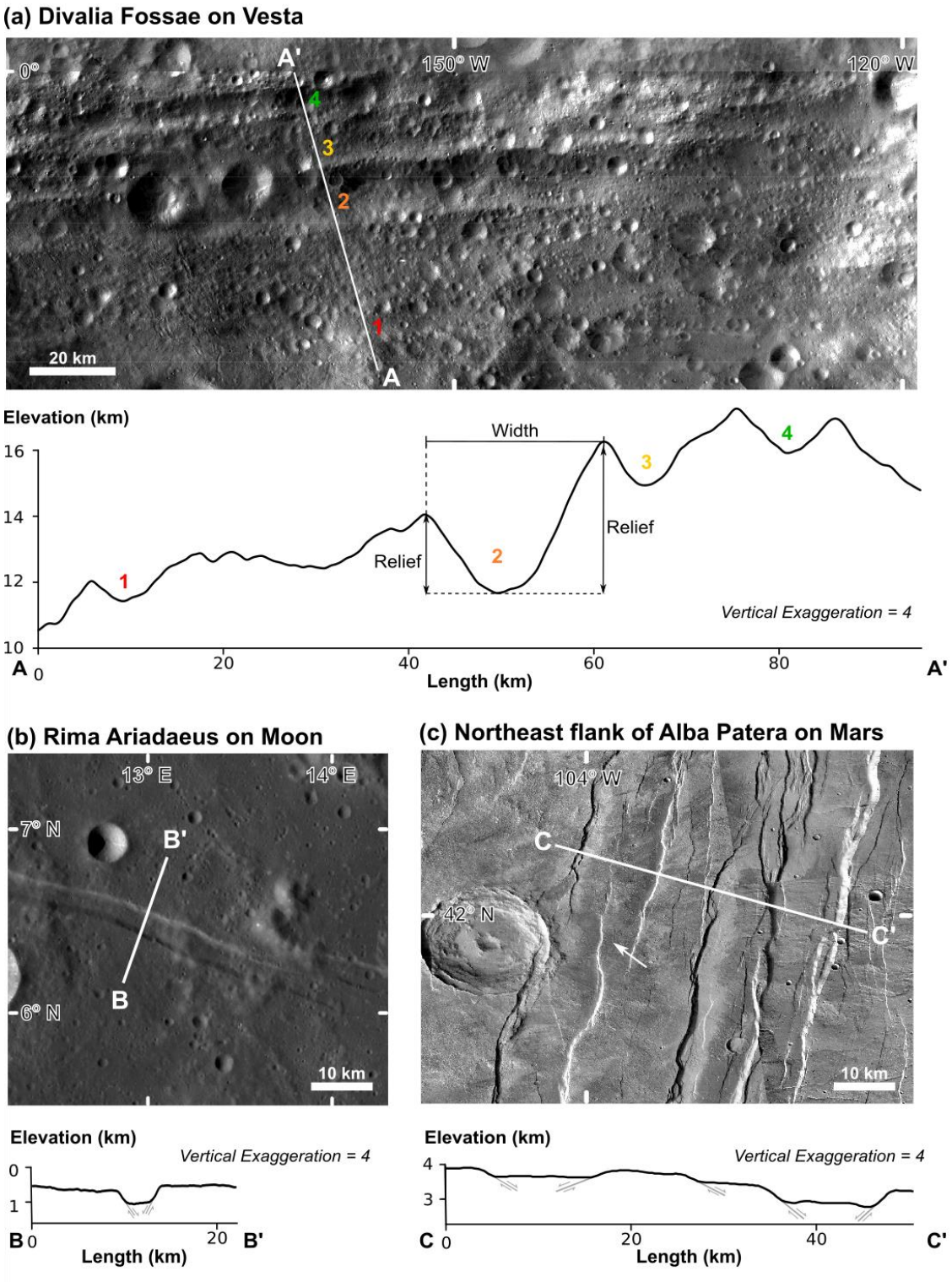

Figure 2.4. *Typical topographic expressions of troughs on Vesta compared to grabens on the Moon and Mars. The horizontal and vertical scales, and vertical exaggeration are the*

same for the three topographic profiles. (a) Dawn FC images and topographic profile A–A' of the Divalia Fossae. Refer to Figure 2.2 for the location on Vesta. The profile shows the geometries of four major troughs part of Divalia Fossae. The trough width and relief of two rims are labeled for trough 2. (b) Lunar Reconnaissance Orbiter Camera image (Robinson et al., 2010) with a pixel scale of 73.24 m/pixel and topographic profile B–B' of Rima Ariadaeus on the Moon. The elevation data is based on High-resolution Lunar Topography (SLDEM2015; Barker et al., 2016) with a vertical resolution of ~10 cm and horizontal pixel scale of ~60 m/pixel. An en-echelon stepover is present at the eastern end of the graben. (c) Mars Reconnaissance Orbiter Context Camera (CTX; Malin et al., 2007) image with a pixel scale of ~5 m/pixel and topographic profile C–C' of the northeast flank of Alba Patera on Mars. The elevation data is based on the High-Resolution Stereo Camera of Mars Express (image h0068_0009; Gwinner et al., 2009) with a grid spacing of 125 m, and a vertical accuracy of ~20 m. Normal fault structures are present, including fault segments forming a relay ramp on the western graben (white arrow) and multiple faulted borders at the western rim of the eastern graben.

Shape variations along troughs

Trough reliefs

Buczkowski et al. (2012) analyzed the topographic differences between the trough floor and rim of Divalia and Saturnalia Fossae and related them to the vertical displacements of faults that form grabens. For comparison, I use the same methodology and expand upon this analysis by assessing six troughs also including Divalia and Saturnalia Fossae but with a denser sampling of the topographic data (supporting information). Structural reliefs for the trough-bounding scarps for each major trough are

assessed at 5 km intervals. The shortest trough, trough 5, is 115 km long and includes 24 measurements of relief, whereas the longest trough, trough 1, with a length of 835 km, has 168 measurements of relief. The reliefs of scarps are determined by the maximum elevation differences between the trough floor and rims (Figure 2.4a). Relief is plotted against the length of map trace, scaled to the total length of the trace, to allow comparison of the two scarps that bound each trough and to test whether maximum relief is at the center of each scarp (Figure 2.5). If a trough formed as a graben, the maximum vertical displacement of each bounding fault, measured by scarp relief, should lie at the midpoint of the scarp, and maximum vertical displacement should decrease to zero towards each end of the scarp. The shapes of the two profiles per trough, one for each of the trough-bounding scarps, are expected to mimic each other, considering that they lack fault segmentation and linkages. As the southern portion of the Saturnalia Fossae is no longer preserved, the observed maximum relief and its position along the scarp may not reflect the original values, owing to truncation by the Divalia Fossae; nonetheless, I analyze them to investigate if part of the relief profile shows the typical characteristics of faults.

Each pair of relief profiles for the six troughs show that their points of maximum relief are at different positions along trough (Figure 2.5). Trough 1 is separated into three segments by long muted troughs far from each other, which makes it difficult to determine if they belong to a single structure or multiple structures; the maximum reliefs are marked for each of its segments. Trough 1 is 835 km long with maximum reliefs of the northern and southern rims of 4.74 km and 2.78 km. Trough 2, Divalia Fossa, is 400 km long with corresponding maximum reliefs of 5.73 km and 2.96 km. The northern rim of Trough 2 has the largest relief among the Divalia Fossae, consistent with Buczkowski

et al. (2012). Trough 3 is 495 km long with maximum reliefs of 2.92 km and 2.82 km. Trough 4 is 345 km long with maximum reliefs of 3.22 km and 2.68 km. Among the 8 relief profiles of the Divalia Fossae, only the northern rim of trough 2 and the southern rim of trough 3 have maximum relief near the midpoint of the trough with relief decreasing toward the tips (Figure 2.5a), whereas the point of maximum relief on the other 6 profiles is not near the midpoint, or the scarps have multiple peaks of relief. The results for Divalia Fossae are also consistent with Buczkowski et al. (2012). The opposing scarps of the four troughs in Divalia Fossae have differing relief distributions (Figure 2.5a).

For the Saturnalia Fossae, the traceable length of trough 5 is 115 km with the maxima of 1.29 km and 3.99 km on the two scarps, whereas the traceable length of trough 6 is 275 km and its maxima of structural relief are 4.20 km and 6.89 km. Since these troughs are truncated by the Divalia Fossae, the measured changes in relief (Figure 2.5b) reflect an unknown portion of the original structure. Therefore, the location of maximum relief with respect to the full length of the scarps cannot be known. Nevertheless, the preserved portions of the Saturnalia Fossae show a similar asymmetric pattern to that on the Divalia Fossae, where the point of maximum relief occurs at a different location on the opposing scarps (Figure 2.5b).

In summary, the point of maximum relief lies in the center of only two of twelve scarps. In addition, none of the opposing scarps for any trough have similar relief profiles, making the variations in trough geomorphology highly non-systematic. These findings are inconsistent with normal faulting and suggest that troughs are not grabens.

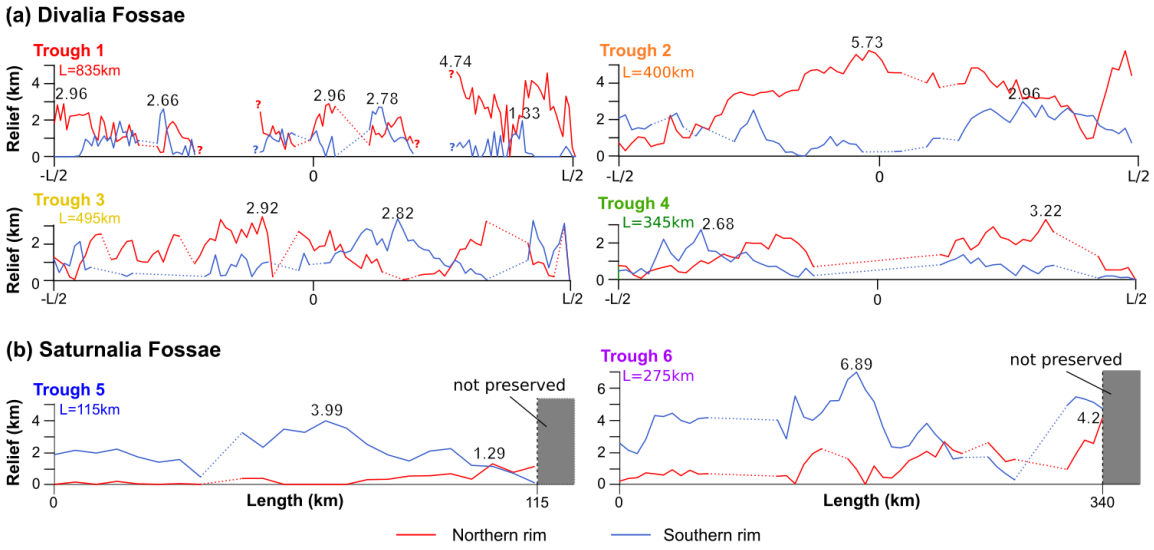

Figure 2.5. *Relief profiles of all analyzed troughs. The reliefs of (a) Divalia Fossae are plotted against distance along the scaled length (L) of the trough. The numerical values of maxima (in km) are labeled at their locations long the trace. Scarps bounding troughs on the north are plotted in red, and southern scarps are plotted in blue. Note that the southern extent of the Saturnalia Fossae (b) is truncated by the Divalia Fossae, and thus their total length and maximum relief are unknown. Their reliefs are plotted against the traceable length in km.*

Trough widths

As with faults, opening-mode fractures typically have displacement profiles with centrally located maxima that taper to zero at the fracture tips. As the mode of displacement differs, the aperture is formed perpendicular to the fracture surface and is related to the trough widths. Trough width is defined by the horizontal distance between the elevated portions of the two trough-bounding scarps, and it is measured perpendicular to the trough (Figure 2.4a). I extract width measurements from the previously extracted topographic sections (supporting information) across each of the previously analyzed

troughs and plot them along the length of the trough set from west to east (Figure 2.6). The relief profiles are analyzed for the location of maxima. These individual profiles are summed to identify the cumulative widths for each of the two trough sets to explore their potential total opening-mode displacement. The cumulative width of one set of joints should display a central maximum that tapers towards both ends of the fracture set. Although this pattern is not present, I note that the centers of the troughs could also be the widest if grabens are bounded by dipping normal faults and maximum displacement is centrally located.

The width profiles for each of the four troughs within the Divalia Fossae and the cumulative width profile show their maxima near the center of the troughs (Figure 2.6a, b). As in the relief analysis, trough 1 (Figure 2.6a) has three segments, and it is difficult to determine if it is a single structure or multiple structures. Trough 1 generally widens eastward and is widest (20.4 km) near the eastern tip. Troughs 2, 3, and 4 have maximum widths of 20.5 km, 15.8 km, and 17.3 km. Maximum width of troughs 2 to 4 occur at a similar longitudinal position on Vesta, centrally located along the length extent of the trough set (Figure 2.6a). These maxima are all tend to be to the east of the midpoint of troughs. Cumulative width summed across the strike of the Divalia Fossae shows a ~800 km long profile with a maximum of 60.8 km at the center of the overall length trace, tapering toward the tips (Figure 2.6b).

For the Saturnalia Fossae, the preserved portions of troughs 5 and 6 have maximum widths of 18.9 and 42.0 km (Figure 2.6c). The cumulative width profile of the Saturnalia Fossae shows a ~280 km long profile with a maximum of 56.2 km near 110 km, tapering towards the western end while the eastern end is not preserved (Figure

2.6d). The systematic changes and shapes of the individual and cumulative profiles for both trough sets are consistent with the mechanics of opening-mode fractures, suggesting that troughs formed through opening-mode displacement. Although the width distribution along the troughs is also expected for graben formed by dipping normal faults, the relief distributions (Figure 2.5) are inconsistent with the vertical displacements of graben-bounding faults. Taken together, the shape variation along the troughs is inconsistent with the displacement profiles of normal faults.

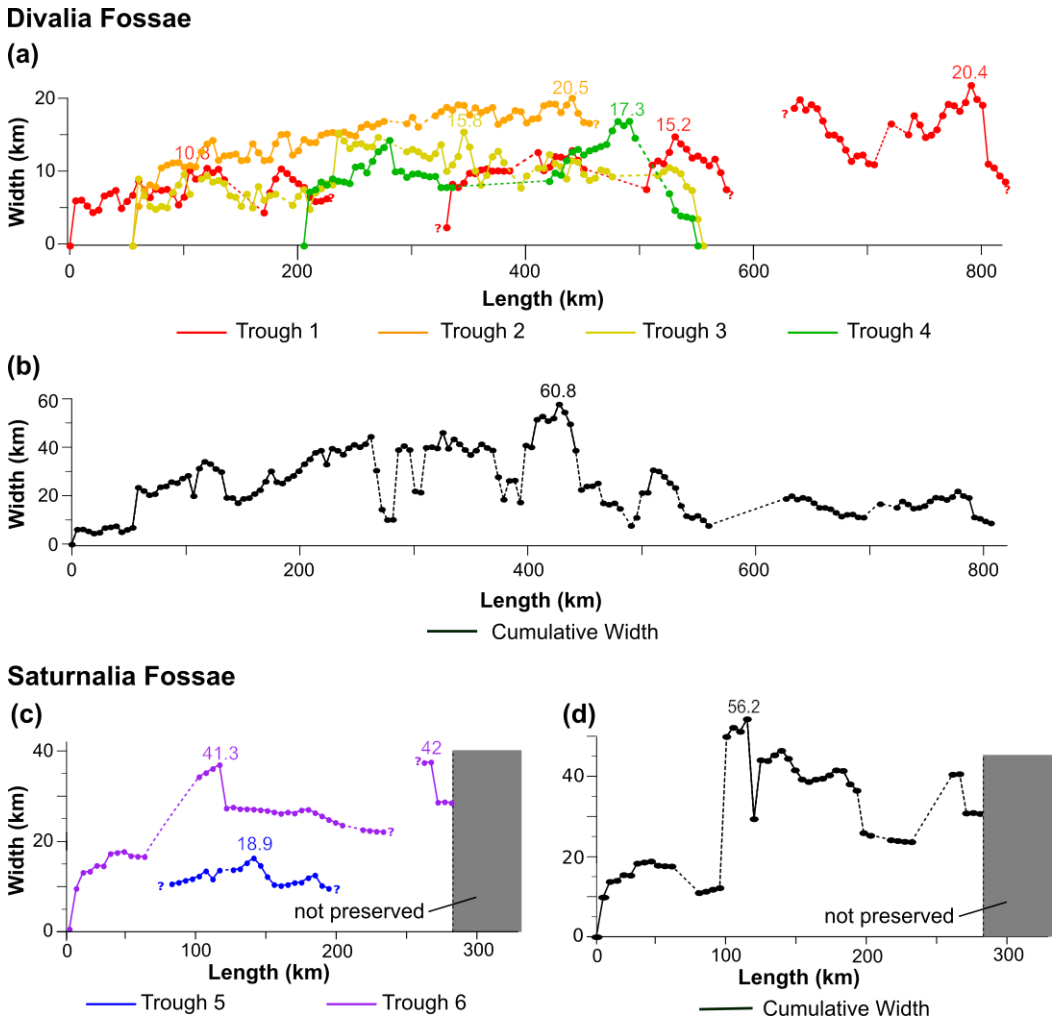

Figure 2.6. *Width profiles of all analyzed troughs. (a) Individual and (b) cumulative width profiles of the Divalia Fossae of troughs 1 to 4. (c) Individual and (d) cumulative*

width profiles of the Saturnalia Fossae of trough 5 and 6. The numeric values of width maxima are labeled (in km) at their locations long the trace. Note that the true extent of the Saturnalia Fossae (b) is not preserved and thus the true length and maximum width are unknown.

Lithospheric structure of Vesta

As both faulting and jointing are brittle deformation behaviors, it is important to characterize the strength and depth extent of the brittle portion of the lithosphere, which establishes to what depth brittle failure criteria are appropriate for assessing fracturing behaviors. Since lithospheric strength is influenced by the overburden pressure, which in turn is governed by gravitational acceleration, these parameters must be derived first. Gravitational acceleration is generally assumed to be linear in the upper parts of a planetary body, but for low-gravity objects like Vesta, gravitational acceleration is markedly nonlinear and thus the variation in gravitational acceleration must be considered.

Furthermore, Vesta is a monolithic asteroid that is likely heavily fractured. Such fractured lithospheres are governed by friction between blocks of rock, creating a degree of cohesive strength at the surface of the asteroid. This strength must therefore be considered in assessments of fracture behaviors. For these reasons, I (1) derive the gravitational acceleration and overburden pressure profiles for Vesta, which I use to (2) determine lithospheric strength envelopes. The strength envelopes provide insight to the extent of the brittle portion of the lithosphere, which allows us to specify to what depth brittle failure would have been possible on Vesta. Additional rock-mechanical considerations (3) help us determine at what depths faulting via frictional sliding is the

predicted fracturing mode, while accounting for both the nonlinear gravitational acceleration profile and strength of the rock volume.

Gravitational acceleration and pressure profiles of Vesta

The first step is to derive the gravitational acceleration profile for Vesta can be established from published interior models. Vesta is a differentiated asteroid, and thicknesses, compositions, and densities of core, mantle, and crust have been estimated from geophysical and spectral data collected by the Dawn mission as well as howardite–eucrite–diogenite (HED) meteorites, for which Vesta is widely thought to be the parent body. Vesta has an iron core with a radius of ~108 km and density of ~7850 kg m^{-3} (Ruzicka et al., 1997; Russell et al., 2012; Ermakov et al., 2014), a ~118 km thick (Ermakov et al., 2014) olivine-rich mantle with a density of ~3400 kg m^{-3} (Ruzicka et al., 1997; Zuber et al., 2011; Russell et al., 2012), and a ~36 km thick basaltic crust with a density of 2900 kg m^{-3} (Ruzicka et al., 1997; Zuber et al., 2011; Russell et al., 2012). Using this three-layer model of the interior structure and approximating the shape of the asteroid as a sphere (Figure 2.6a), the gravity acceleration profile of Vesta can be calculated as:

$$\frac{\delta g}{\delta r} = 4\pi G \rho_r r - 2\frac{g}{r}, \quad (1)$$

where g is gravitational acceleration, r is the radius of the body, G is the gravitational constant, and ρ_r is local material density. The calculated surface gravitational acceleration is 0.26 m/s^2 (Figure 2.7b), bracketed by the values measured by the Dawn spacecraft, which range from 0.23 to 0.27 m/s^2 (Ermakov et al., 2014). The acceleration due to gravity gradually decreases with depth to the lower mantle at ~120 km, where it then increases until it reaches the core–mantle boundary. From that point, gravitational

acceleration drops linearly to zero at the center of the core (Figure 2.7b), consistent with Stickle et al. (2015).

Next, I utilize the calculated gravitational acceleration profile to assess how overburden pressure, P, changes with depth, z , as given by:

$$P(z) = -\rho_z z g_z. \quad (2)$$

Overburden pressure increases with depth roughly linearly from 0 MPa at the surface to ~120 MPa at the core–mantle boundary, and it increases nonlinearly from there to the core (Figure 2.7c). This pressure profile is taken as the reference state of stress for the rock-mechanical considerations below.

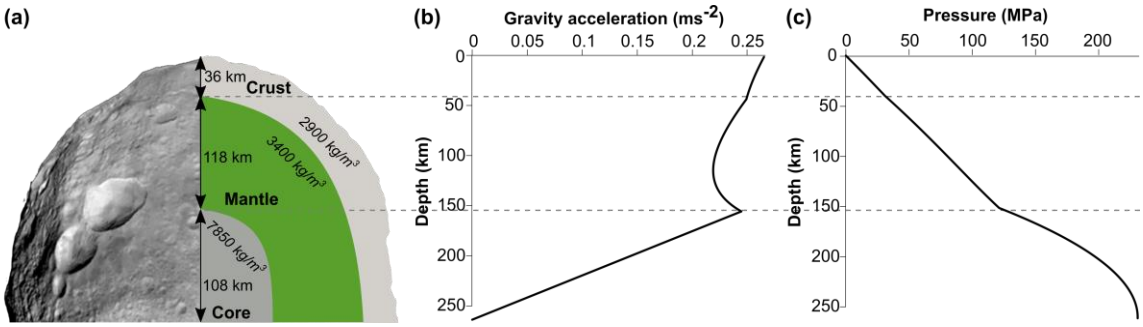

Figure 2.7. *Gravitational acceleration and pressure profiles calculated using physical parameters of Vesta's interior structure. (a) A three-layer model of Vesta's interior was used to compute depth profiles of gravitational acceleration and pressure. (b) Depth profile of gravitational acceleration. (c) Depth profile of pressure. Dashed lines across the three diagrams indicate crust–mantle and mantle–core boundaries.*

Vesta's lithospheric strength

To explore the type of fracturing involved in the formation of Vesta's large troughs, the extent of the brittle portion of the lithosphere at the time of fracture formation must be established. Overburden pressure plays an important role in defining

the lithospheric strength. The thickness of the lithosphere is controlled by the brittle and ductile strength of rock, and rock strength is determined by the weakest rheology at a given depth for a given stress. The upper portion of a solid-surface body with low temperature and confining pressure is controlled by brittle behavior (Byerlee, 1978) with the strength increasing linearly with depth, independent of the rock type and surface condition (Byerlee, 1978). For all stress calculations, I follow the geologic sign convention where compression is positive. Critical values of the principal stresses for frictional sliding in a dry lithosphere, regardless of its composition, are typically obtained from Byerlee's intermediate- and high-pressure laws (Brace and Kohlstedt, 1980; Kohlstedt and Mackwell, 2010) as:

$$\sigma_1 \cong 5\sigma_3 \qquad \text{for } P < 110\ MPa \tag{3}$$

$$\sigma_1 \cong 3.1\sigma_3 + 210\ MPa \qquad \text{for } P > 110\ MPa, \tag{4}$$

where σ_1 and σ_3 are the maximum and minimum principal stress components with zero pore fluid pressure, respectively. Rock strength in a lithosphere under extension is obtained where the overburden pressure, P, given in Equation (2), is the maximum principal stress (i.e., $P = \sigma_1$). Failure is predicted to occur if the calculated values of σ_3 in Equations (3) or (4) are reached. Rock strength in a lithosphere undergoing shortening is obtained where the overburden pressure is the minimum principal stress (i.e., $P = \sigma_3$), and brittle failure is predicted to occur if the calculated values of σ_1 in Equations (3) or (4) are reached.

In the lower hotter portions of the lithosphere, ductile behavior dominates by several microstructural deformation mechanisms, which are combined under the term *creep*. Here, the strength sharply decreases with increasing temperature and is described

by a thermally activated power law (Ranalli and Murphy, 1987; Mackwell et al., 1990; Burov and Diament, 1992):

$$(\sigma_1 - \sigma_3)_d = \sqrt[n]{\frac{\dot{\varepsilon}}{A}} \exp\left(\frac{Q}{nRT}\right), \quad (5)$$

where $\dot{\varepsilon}$ is the strain rate, A and n are material constants, Q is the activation energy of creep, R is the gas constant (8.31447 J mol^{-1} K^{-1}), and T is temperature. Strain rates are bracketed by 10^{-14} and 10^{-20} s^{-1} for all calculations. The faster strain rate of 10^{-14} s^{-1} represents active deformation, such as at orogenic belts (Pfiffner and Ramsay, 1982). The slower strain rate of 10^{-20} s^{-1} represents deformation on one-plate, stagnant-lid bodies, such as Mercury (Crane and Klimczak, 2017), which is one to two orders of magnitude slower than the strain rate at intraplate continental tectonic settings (Gordon, 1998). For creep parameters, I take the widely used properties of Maryland diabase (n = 3, A = 6.3x10^{-2} MPa^{-n}s^{-1}, Q = 276 kJ mol^{-1}) for the crust (Caristan, 1982), and dry olivine (n = 3, A = 1x10^{4} MPa^{-n}s^{-1}, Q = 510 kJ mol^{-1}) for the mantle (Goetze and Evans, 1979). I apply the simulated thermal evolution from Fu et al. (2014), which considered three time steps for each of their two end-member models: one with no megaregolith and one with a megaregolith layer that is 5-km thick.

I calculated the possible lithospheric structures of Vesta (Figure 2.8) for the end-member cases of no megaregolith (top row) and with megaregolith layer (bottom row) at different times in Vesta's thermal evolution (Fu et al., 2014). The ages refer to the time after the cessation of convection, which has been estimated to be shortly (<10 Ma) after asteroid accretion (Sterenborg and Crowley, 2013). All strength envelopes are plotted for the crust and mantle with a total thickness of 154 km. Strength in the core is not calculated because thermal structure and other necessary material properties are

unknown. Any brittle behavior in the core, if present, especially with present thermal conditions, should mimic the shape of the curve of the reference state of stress (Figure 2.6c). All envelopes depict the strength for a lithosphere undergoing extension and shortening, showing the difference between tectonic and reference state of stress.

These results indicate that Vesta's crust and its upper mantle to ~100 km depth are entirely brittle for every combination of the parameter space. In contrast, Vesta's lower mantle is in the ductile regime only early in its history and only in the lower range of considered strain rates. For the case without megaregolith, the brittle–ductile transition (BDT) occurs at a depth of ~85 km at 20−100 Ma (Figure 2.8a). At 500 Ma, the BDT migrated deeper to depths of ~110 km for the lower strain rate and ~140 km for the higher strain rate. (Figure 2.8b). At present, crust and mantle are completely brittle for the considered strain rates (Figure 2.8c). For the case with megaregolith, this 5-km layer slows the cooling process of the asteroid. In Vesta's early history, the strength envelopes with insulating megaregolith layer (Figure 2.8d) are nearly indistinguishable from the one without regolith (Figure 2.8a), but the lower mantle remains in the ductile regime for much longer, potentially until 1500 Ma after accretion for the slow strain rates, while the crust and mantle would have been entirely brittle for fast strain rates at that point in time (Figure 2.8e). Crust and mantle are brittle for both strain rates at present (Figure 2.8f). In addition, the brittle upper portion of the lithosphere will be even thicker than depicted in Figure 2.8 for even higher strain rates, such as would be expected during an impact.

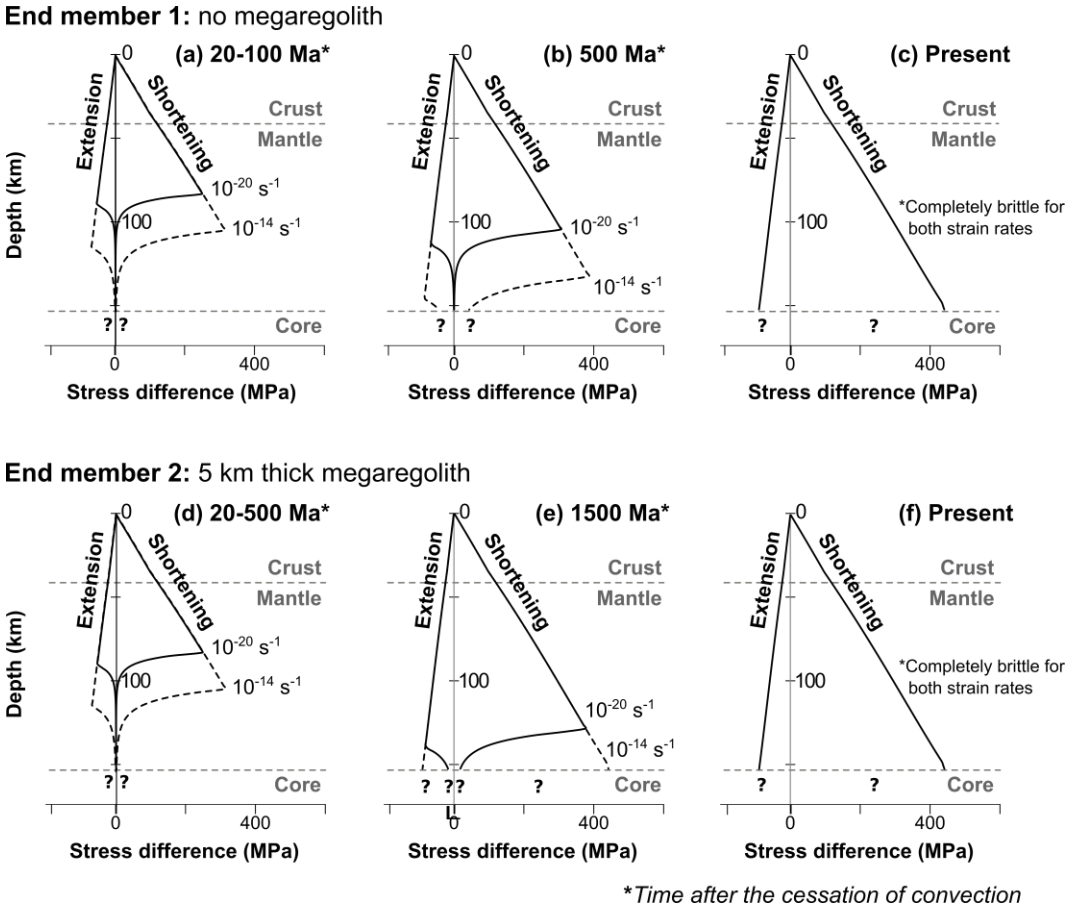

Figure 2.8. *Strength envelopes and evolution for lithospheres under extension and shortening calculated for scenarios where Vesta has no megaregolith (top row) or with 5 km thick megaregolith (bottom row). Lithospheric structures with no megaregolith at (a) 20−100 Ma after the cessation of accretion, estimated to be <10 Ma after asteroid accretion, (b) 500 Ma., and (c) present. Lithospheric structures with insulating megaregolith at (d) 20−500 Ma, (e) 1500 Ma, and (f) present. The time steps and end-members are based on the thermal evolution simulated by Fu et al. (2014).*

Depth extent of frictional sliding

These results establish that Vesta's lithosphere is thick and that the crust and much of the mantle were in the brittle regime throughout Vesta's history for every

combination of plausible parameters. The deformation behavior in the upper ~100 km of the lithosphere can thus be assessed with more complex brittle failure criteria. Specifically, I employ the Coulomb criterion (Handin, 1969; Schofield, 2005) to assess the depth at which frictional sliding is predicted in Vesta's lithosphere. The Coulomb criterion is better suited than Byerlee's law for the tectonics of Vesta, because it relates loading conditions to frictional and cohesive properties of the rock volume, whereas Byerlee's law assumes no cohesive strength (e.g., rubble pile conditions) at the surface of the lithosphere (Schultz, 1992). Vesta is likely a monolithic, albeit highly fractured asteroid, as a prominent slumping block at Matronalia Rupes indicates that Vesta's lithosphere has some cohesive strength (Krohn et al., 2014). Furthermore, mass wasting structures on Vesta maintain most of their original shape along the surface of rupture, indicating that cohesion within the sliding mass prevents extensive spreading (Otto et al., 2013). No observation of Vesta suggests it is a cohesionless rubble pile asteroid. Hence, I consider Vesta to have a lithosphere consisting of a fractured basaltic rock mass possessing some strength at the surface that is best characterized with the Coulomb criterion.

Principal stresses in a dry lithosphere for the Coulomb criterion for frictional slip (Jaeger et al., 2007, p. 92) are given as:

$$\sigma_1 = \sigma_c + \sigma_3(\sqrt{\mu^2 + 1} + \mu)^2, \tag{6}$$

where σ_c represents the unconfined compressive strength of intact rock and μ the coefficient of friction. By this relationship, unconfined compressive strength is a measure of the cohesive properties of the rock, and it closely relates to the cohesion term in the form of the Coulomb criterion in Mohr space. As Vesta's lithosphere has likely never

been intact, the unconfined compressive strength must be adjusted for rock mass conditions (see below). For the coefficient of friction, values of $\mu = 0.85$ and $\mu = 0.6$ are used for the pressures below and above 110 MPa, consistent with Byerlee's intermediate and high friction laws (Byerlee, 1978). Vesta's crust and most of its mantle fall under intermediate pressure friction law as 110 MPa is not reached until the lowermost mantle at ~146 km (Figure 2.7c).

Values of unconfined compressive strengths from rock testing of a series of intact basalt samples fall between 168 MPa and 364 MPa (Schultz, 1993, 1995). As no rock sample from Vesta has been tested for its unconfined compressive strength, I assume that intact basaltic rocks on Vesta display a similar range of compressive strengths at unconfined conditions (i.e., at the surface). Because Vesta's lithosphere is not expected to be intact, these values of unconfined compressive strength for intact rock must be adjusted for rock-mass conditions.

A rock mass consists of small and large blocky, interlocked rock fragments, held together by the frictional properties of fractures forming the fragments, with rock-mass strength properties depending on the degree and nature of fracturing. Rock Mass Rating system (RMR) is commonly used to assess the degree and nature of fracturing of a rock mass (Bieniawski, 1989; Aksoy, 2008) and has previously been applied to a variety of topics in planetary rock mechanics (e.g., Schultz, 1993; Schultz et al., 2006; Nahm and Schultz, 2007; Klimczak, 2015). The rating ranges from 0 to 100, with 100 representing intact rock and values less than 25 corresponding to rubble-pile conditions. For reference, RMR = 75 refers to a relatively fresh, unweathered volume of strong basaltic rock with ~3 sets of widely spaced, clean, and rough joints (Schultz, 1995), leading to tightly

interlocking angular blocks of rock. In contrast, RMR = 25 refers to disintegrated rock masses consisting of poorly interlocked, heavily broken rock pieces, which serves as a useful lower limit of a cohesive rock mass (pp. 119 in Schultz, 2019). Nearly all imaged asteroids have impact craters with diameters comparable to the body itself (Bottke et al., 2002). The size and age of Vesta's craters imply that its interior must have been highly fractured since its early geologic history (Davison et al., 2013). Since Vesta is neither a cohesionless rubble pile nor an intact asteroid, I take a range of $25 \leq \text{RMR} \leq 60$ to be representative of Vesta's lithosphere.

The unconfined compressive strength of a rock mass, σ_c^*, can be determined by (Hoek and Brown, 1980):

$$\sigma_c^* = \sigma_c \sqrt{s}, \tag{7}$$

where s relates to RMR (pp. 178 in Bieniawski, 1989; Hoek, 2007) by:

$$s = e^{\frac{RMR-100}{9}} \qquad \text{for RMR} > 25 \tag{8a}$$

and

$$s = 0 \qquad \text{for RMR} < 25. \tag{8b}$$

Although I use the framework of the Hoek–Brown criterion (e.g., Hoek and Brown, 1980; Hoek et al., 2002; Langford and Diederichs., 2015) to assess the unconfined compressive strength of a rock mass, I select the Coulomb failure criterion for frictional slip (Equation 6) for its simplicity to calculate the initiation of normal faulting. The Hoek–Brown criterion is equally applicable to address this problem, but it depends on more empirical parameters that would introduce more assumptions.

I solve for the valid solutions to the Coulomb criterion for Vesta's lithosphere under extension, where normal faults are expected to form, by calculating the minimum

principal stresses (σ_3) needed such that the frictional resistance to sliding is overcome, and normal faulting is triggered. I present these solutions for the lower and upper strength limits of intact basalts adjusted for the full range of degrees of fracturing from rubble pile conditions to intact rock (i.e., $0 \leq RMR \leq 100$) over the entire depth of the brittle lithosphere as 3-dimensional curves (Figure 2.9).

The curves present the conditions at which frictional sliding is possible for the full range of degrees of fracturing from rubble pile conditions to intact rock with the minimum principal stresses at zero marking the transition to a fully compressive state of stress. This transition therefore represents the minimum condition to be met in extensional tectonic regimes where normal faults are formed, with the part of the curve at $0 \leq RMR \leq 25$ being analogous to Byerlee's law (as in Equation 3) and the part of the curve at RMR = 100 analogous to the Coulomb criterion of intact rock (as given in Equation 6). The graphs indicate that rock masses with a higher degree of fracturing corresponding to lower RMR values can experience frictional sliding at a shallower depth. For cohesionless rubble piles (RMR < 25), frictional sliding and thus normal faulting can be triggered anywhere in the brittle lithosphere, including at or near the surface (Figure 2.9). In contrast, for an intact lithosphere (RMR = 100), conditions for frictional sliding are not met anywhere in Vesta's lithospheric crust and mantle (Figure 2.9).

But since Vesta's lithosphere is neither a rubble pile nor intact, I focus on the range of a highly fractured rock mass at $25 \leq RMR \leq 60$ (Figure 2.9). For basalts with the lower bound of strength parameters (i.e., $\sigma_c = 168$ MPa), the minimum depth at which the frictional resistance to sliding could be overcome in Vesta's lithosphere is at 3 km,

but it may be as deep as 25 km, depending on the degree of lithospheric fracturing (Figure 2.9a). For basalts with the upper bounds of strength parameters (i.e., $\sigma_c = 364$ MPa), the minimum depth at which frictional resistance to sliding is overcome is at 5 km, but it may be as deep as 55 km for moderate degrees of fracturing (Figure 2.9b). These results establish that stress magnitudes needed to overcome the frictional resistance to sliding to trigger shear displacement, and thus normal faulting, are not met in Vesta's lithosphere until substantial depths of at least 3 km but as much as 55 km. Normal fault growth is therefore not predicted by the Coulomb criterion to be triggered in the uppermost 3 to 55 km of Vesta's lithosphere.

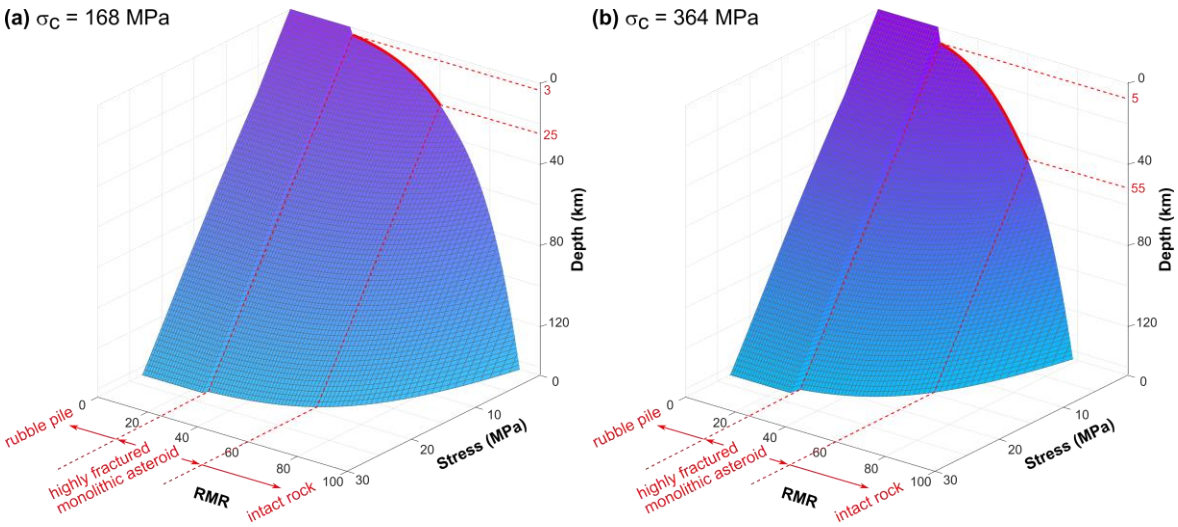

Figure 2.9. *Valid solutions to the Coulomb criterion for lithospheric conditions of Vesta in the extensional tectonic regime calculated for basalts with unconfined compressive strengths of* σ_c *= 168 MPa (a) and* σ_c *= 364 MPa (b) that are adjusted for the full range of degrees of lithospheric fracturing from rubble pile conditions to intact rock (i.e.,* $0 \leq RMR \leq 100$*).*

Discussion

I investigated map patterns and the geomorphology of the large-scale troughs on Vesta, as well as the lithospheric strength to assess what type of fracture could have formed these troughs. Map patterns, geomorphology, and rock mechanical assessments individually and collectively have important implications for the tectonics on Vesta.

Geological interpretations from observations

All large-scale troughs are isolated, continuous, and subparallel among their own sets, and these lack the diagnostic map patterns of faulting or jointing. Rims of troughs are scalloped (Figure 2.3a), and most troughs have bowl-shaped cross-sectional geometries (Figure 2.4, supporting information). In contrast to previous studies (Buczkowski et al., 2012; Schäfer et al., 2014; Scully et al., 2014; Yingst et al., 2014), a distinct flat floor is not the most common trough geomorphology . A flat-floor geometry is preserved over billions of years on some terrestrial bodies, such as on the Moon (Figure 2.4b; Lucchitta and Watkins, 1978), Mars (Figure 2.4c; Kneissl et al., 2015; Ruj et al., 2019), or Mercury (Klimczak et al., 2013; Cunje and Ghent, 2016). Considering the trough geometry of a graben- or joint-origin could be degraded into a bowl shape by impact shaking and mass wasting, these findings show only that the troughs are heavily degraded, and there is no diagnostic evidence for fault traces of graben or joint walls.

Although mapping does not reveal patterns diagnostic of faulting or jointing, pit-crater chains associated with the troughs may have more definitive patterns that can be related to the origin of troughs. For example, one trough shows a direct transition to a pit-crater chain. The trough narrows toward its tips and directly transitions into a pit-crater chain, which aligns with smaller pits beyond the end of the trough (Figure 2.3a). Another

well-preserved pit chain has larger pits in the center and smaller pits at the ends of the chain (Figure 2.3b). These patterns are also associated with dilational normal faults that bound grabens on Mars (e.g., Tanaka and Golombek, 1989; Montési, 2001; Wyrick et al., 2004). Some pit crater chains have larger pits in the center of the chain and smaller pits at the ends, representing different stages of fault-related landform formation (Wyrick et al., 2004). However, Martian pits are commonly located on the floors of grabens (Wyrick et al., 2004), which does not occur on Vesta. An opening-mode fracture origin may explain the absence of fault-bordered pits. Additionally, the pit craters are circular depressions that form by the collapse of material into subsurface voids, which may represent subsurface fractures that did not propagate to the surface. In this case, the preserved pit crater chain with larger pits in the center of the chain and smaller pits at the end (Figure 2.3b) is consistent with joints, in that the maximum aperture commonly lies at the center of the joint with smaller apertures near the tips (e.g., Vermilye and Scholz, 1995). As pit crater chains are commonly associated with grabens or joints, their presence on Vesta does not distinguish between the two structure types.

Relief and width measurements of the troughs have implications for the graben and opening-mode fracture interpretations by relating them to the corresponding structural components. Vesta is a small body that is not in hydrostatic equilibrium, its lithosphere is thick relative to the size of the body, and its troughs are long enough to encircle two-thirds of its equator. Planetary curvature in elastic interactions may make interpretations of displacements and their distributions difficult. However, this effect is difficult to quantify, given the irregular shape of the asteroid.

Nevertheless, trough reliefs were previously measured as permanent deformation in the form of vertical displacements of graben components (Buczkowski et al., 2012). I followed these authors' methods and collected measurements of elevation differences between the trough floor and rims along the trough length. Relief profiles do not reach a maximum near the midpoint of a trough and taper toward the trough tips. Moreover, the point of maximum relief is located at different locations along the bounding scarps of every structure investigated (Figure 2.5). Following observations of the mechanics of fault growth (e.g., Dawers et al., 1993; Cartwright et al., 1996), these observations imply that the proposed faults originated at different positions but grew toward one another to interact and form grabens. However, none of the patterns indicating fault interaction, such as segmentation and linkage, are present on Vesta. Such fault growth and mismatch in locations of maximum displacements are atypical for graben.

Since the troughs are heavily degraded, the measured relief at each location may not reflect the original displacement on a fault. However, visual inspection of the troughs shows that the degree of degradation of the scarps is similar along the length of the troughs, suggesting that present-day relief corresponds to original relief, allowing at least qualitative insight into whether relief is related to fault displacement. Nonetheless, variations of relief along the troughs are inconsistent with normal fault displacement, and thus they cannot be used as evidence to support a graben origin. Hence, relief should not be regarded as a measure of vertical displacements of normal faults, nor should relief be used for fault analysis.

Trough widths may serve as a measure for apertures of opening-mode fractures. For three out of four mapped troughs at Divalia Fossae, maximum width occurs at a

similar position along the trough set (Figure 2.6), and the cumulative width distribution is roughly symmetrical with one maximum at the center of the overall length trace, tapering toward the tips. These characteristics are consistent with opening-mode fracture mechanics, where the displacement profiles have centrally located displacement maxima that taper to zero at the fracture tips for individual joints (e.g., Vermilye and Scholz, 1995). The cumulative profiles also suggest that troughs in each set belong to a single group that formed during the same opening event, and thus troughs may be part of a large set of parallel joints. As troughs are heavily degraded, the present-day widths do not represent the widths of the original structure, and these width measurements therefore likely do not represent the actual aperture of joints. However, the degree of degradation is similar along the length of the troughs, so variations in present-day trough width may still correlate with original joint aperture.

Lithospheric fracturing behavior of Vesta

The calculated lithospheric strength shows that Vesta's crust and upper mantle are completely brittle for every combination of plausible parameters applicable to the asteroid. The Coulomb criterion predicts that in an extensional tectonic regime on Vesta, shear displacement to form normal faults by overcoming the frictional resistance to sliding is initiated only at substantial depth. Only at these depths does the prevalent pressure gradient (Figure 2.7c) shift all principal stress components to be compressive, such that it is possible to initiate normal faulting. For the weakest, most heavily fractured cohesive basaltic rock mass applicable to the lithosphere of Vesta, sliding-mode fracturing is predicted to be triggered no shallower than 3 km. For stronger, moderately fractured rock masses, frictional sliding and thus normal faulting is not possible to be

triggered above a depth of 55 km (Figure 2.9). These depths are explained by the combined effect of the low gravitational acceleration and the unconfined compressive strength of a basaltic rock mass. This result is consistent with the expectation of Stickle et al. (2015) that materials within Vesta are fractured by tensile stresses, considering the added strengthening effect of the overburden pressure. Although, one might argue that there is a thick cohesionless regolith layer on the surface of Vesta and that frictional sliding could occur within the cohesionless layer (Figure 2.9, for RMR $\leq$ 25), Vesta troughs occur where regolith is thinner than 1 km (Denevi et al., 2016). Given the large size of the troughs, with maximum reliefs that generally exceed 2 km and locally 5 km, these structures must extend deeper into the lithosphere and be contained in fractured but cohesive basalt.

Although small graben have formed in low-cohesion regolith on the Moon, a cohesionless regolith layer need not be present for normal faulting to develop on the surface of the Moon or Mars as the effects of the 6x and 15x greater gravitational acceleration on these bodies allow frictional sliding to occur at much shallower depths. For the same basaltic strength properties, frictional sliding is predicted to occur at depths as shallow as ~0.62 km on the Moon and ~0.27 km on Mars. In contrast, large-scale fracturing on other monolithic, low-gravity bodies, such as 2 Pallas, 10 Hygiea, and 16 Psyche or perhaps even Phobos, may also be driven mainly by jointing. Because Phobos is not a rubble pile but a very small, cohesive body, faulting is not expected, and its grooves probably formed through opening-mode displacements.

Owing to the strength of basaltic rock masses and the low gravity of Vesta, normal faulting is not required to explain the troughs. Even if normal faulting occurred at

depth, it must have been preceded or accompanied by large opening-mode fractures above depths where normal faulting is possible. At shallower depths, the prevalent pressure gradient on Vesta is not steep enough to have placed the lithosphere experiencing extension into a fully compressive stress state, instead of requiring tensile stresses there. Opening-mode fracturing, such as jointing, is the preferred fracturing mode if at least one principal stress is tensile. These strength calculations do not include the effect of centrifugal acceleration that results from Vesta's fast rotation. Because centrifugal acceleration counters the overburden pressure, incorporating centrifugal acceleration would increase the depth of the jointing–faulting transition in the equatorial region where the Divalia Fossae are located.

Large fracture openings in extensional tectonic regimes also occur on Earth. One analogue on Earth is the Almannagjá normal fault, which forms the western boundary of the Þingvellir Graben in the Reykjaneshryggur–Langjökull rift system of southwest Iceland. The fault is accompanied by joints, or fissures, which opened by as much as 60 m before the fractures were large and deep enough for them to be reactivated as normal faults, which generated a vertical displacement of 40 m (Gudmundsson, 1992, 2011). The troughs on Vesta may seem to be too large for joints as we know them on Earth. However, the scale of jointing depends not only on the strength properties of basaltic rock masses but also on gravitational acceleration that, in turn, affects the pressure gradient. Because this pressure gradient is much lower on Vesta, it is possible that joints on Vesta could be much larger than joints on Earth.

An opening-mode fracture origin of troughs

These observations of Vesta's troughs are inconsistent with normal faulting, or they are inconclusive. In contrast, none of the geology is inconsistent with jointing, and some observations support it. In particular, relief and overall shape of troughs are inconsistent with a graben interpretation, but their variations in width are consistent with a joint interpretation. Furthermore, rock-mechanical calculations suggest that initiation of faulting via frictional sliding is possible only at depths below at least 3 km, and it may not occur down to as much as 55 km, with jointing being the favorable fracturing behavior above those depths.

I propose that Vesta's large-scale troughs are the topographic expression of opening-mode displacement caused by jointing or mixed-mode fracturing that was subject to subsequent landform degradation (Figure 2.10). Given an extensional tectonic regime, joints on Vesta may have formed at the surface or in the subsurface (Figure 2.10a), regardless of their underlying cause of extension. It is beyond the scope of this manuscript to identify the actual cause of this extension. If joints propagated deep enough, exceeding the jointing-faulting transition, they may have been reactivated as normal faults at that depth, forming mixed-mode fractures. In this case, the width of the trough would consist of the joint aperture coupled with a dilational component from normal faulting. Alternatively, fractures could have formed initially beneath the jointing–faulting transition as normal faults deeper than 3 km and potentially as deep as 55 km, but it remains to be tested if the width and spacing of troughs is compatible with geologically plausible fault geometries at those depths.

During degradation of the troughs, the slope material on the wall of the scarps collapsed into the trough, widening the initially sharp and narrow V shape of the troughs and also forming the scalloped rims (Figure 2.10b). Collapse above subsurface openings formed pit crater chains (Figure 2.10b). Over time, slumping and degradation caused by slope failure and impact shaking likely further widened the troughs and caused pit crater chains to coalesce into linear troughs (Figure 2.10c). This process produced a variety of trough geometries, including ones that are bowl-shaped (n=176), flat-floored (n=53), or V-shaped (n=31), irrespective of whether the joint or mixed-mode fracture was initially formed at the surface or subsurface (Figure 2.10a). While normal faulting may have played a role in the formation of these troughs, I propose that trough geomorphology is governed primarily by opening-mode displacement from large-scale jointing (Figure 2.10a).

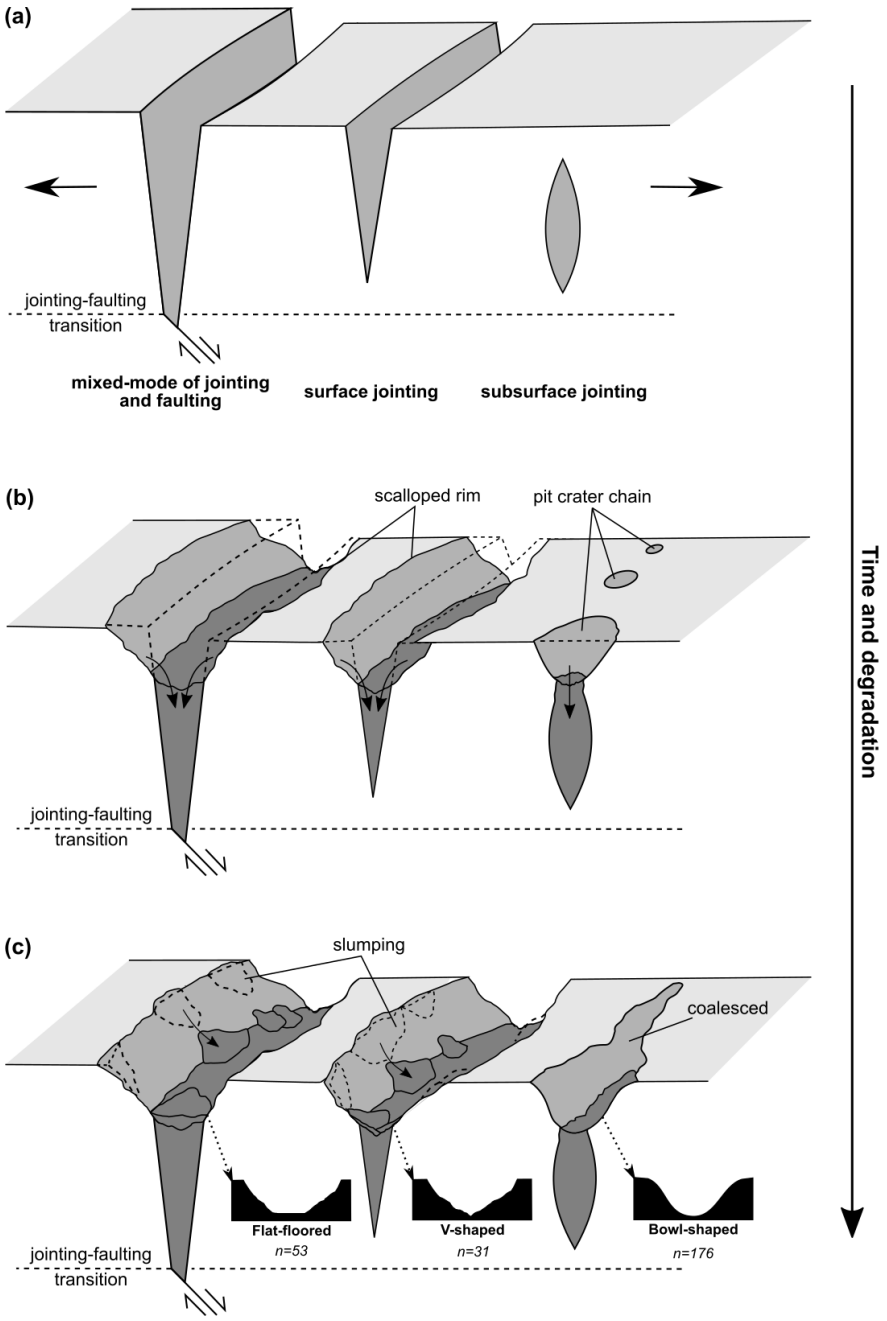

Figure 2.10. *Diagram showing the geomorphologic evolution for opening-mode fractures on Vesta. (a) Large-scale jointing occurs on the surface and in the subsurface. If a joint propagates deep enough, it develops into normal faulting at that depth. (b) Steep joint walls collapse into the void for the surface joints, whereas the collapse of subsurface openings forms pit crater chains. (c) Slumping and degradation widen*

troughs to form and coalesce the pit crater chains to form continuous troughs. Degradation shapes the troughs into various geometries in cross section, regardless of their origin shown in (a). The jointing–faulting transition is at least 3 km below the surface, but it may be as deep as 55 km, depending on the degree of fracturing of the lithosphere.

Conclusions

I investigated the fracture origin for the large-scale troughs on Vesta by analyzing their map patterns, cross-sectional geometries, and shape variations along the lengths of the structures. Vesta's troughs have scalloped rims, mainly bowl-shaped and V-shaped cross-sections and points of maximum relief that are not at the midpoint of troughs. Collectively, these provide no conclusive evidence for, or are inconsistent with a graben origin. The individual and cumulative widths of troughs are instead consistent with an origin through opening-mode fracturing.

The jointing origin is corroborated by calculations of Vesta's lithospheric strength and fracturing behavior. Based on the end-member thermal models (Fu et al. 2014), strength envelopes suggest that Vesta's lithospheric crust and mantle followed brittle behavior throughout much of its geologic history, considering strain rates of 10^{-20} s^{-1} and higher, applicable to an impact event with very high strain rates or to long-term planetary processes (e.g., deformation on one-plate, stagnant-lid bodies) with low strain rates. Using the Coulomb criterion for the brittle lithosphere under extension predicts that even for highly fractured basaltic rock masses, frictional sliding and thus normal faulting could be triggered only below depths of 3 km, possibly only below depths of up to 55 km, whereas jointing was consistently possible above that depth. While normal faulting could

take part in the formation of these troughs at depth, the topographic expressions of the troughs are controlled primarily by opening-mode displacement from jointing. I therefore conclude that the relief of troughs was not primarily produced by faulting and should not be considered as vertical displacement on the fault. Taken together with the trough origin may not be a direct consequence of a large impact (Cheng and Klimczak, 2022), future modeling studies need to consider that the Divalia Fossae are joints or mixed-mode fractures that are resulted from a long-term tectonic consequence of the Rheasilvia impact.

While this study provides an explanation for the type of structure involved in the formation of the troughs by comparing the two plausible options of normal faulting and opening-mode fracturing, some details remain uncertain. For example, future studies should investigate the extent to which other opening-mode processes such as dike intrusions or perhaps even non-tectonic processes that served to degrade the troughs played a role in the formation and evolution of troughs. These findings and the proposed evolution of large-scale joints are important for understanding the tectonic history of Vesta. They may even help identify the type and mode of formation of large fractures on other low-gravity monolithic planetary bodies.

Acknowledgments

I thank Michael Sori, Bill McKinnon, Laurent Montesi, Nancye Dawers, Chris Okubo, Laura Fattaruso, and two anonymous reviewers, who provided feedback on several earlier versions of this manuscript. I also thank Steven Holland for his language input and proofreading of the paper. The supporting information and data of this manuscript can be accessed at Cheng (2021).

I acknowledge and thank the NASA Dawn Mission, instrument teams at the Max Planck Institute, and stereo analysis team at German Aerospace Center (DLR) for the acquisition and processing of Dawn data used in this work. Dawn data are archived in the NASA Planetary Data System. The original data used in this study are available from https://pds-smallbodies.astro.umd.edu/data_sb/missions/dawn/index.shtml.

CHAPTER 3

AGE RELATIONSHIPS OF LARGE-SCALE TROUGHS AND IMPACT BASINS ON VESTA[2]

[2] Cheng, H. C. J. Klimczak, C. and Fassett, C. I. 2021. *Icarus*, *366*, 114512.
Reprinted here with permission of the publisher.

Abstract

The Dawn mission at Asteroid 4 Vesta revealed two sets of enormous troughs with Divalia Fossae spanning around two-thirds of the equator and Saturnalia Fossae located in the northern hemisphere. Previous studies showed that the Divalia and Saturnalia Fossae are concentric around the Rheasilvia and Veneneia impact basins, respectively, and hence the troughs are widely considered to be genetically linked to the impact events forming the basins. In the existing literature, the Fossae are assumed to be formed directly by, and simultaneously with the basin-forming impacts; however, the temporal relationships of the troughs and how they compare to the impact basins have never been documented. I count crater populations superposed on the Divalia and Saturnalia Fossae to establish their crater frequency distributions and compare that with the previously published data of the Rheasilvia and Veneneia basins, respectively. The comparisons allow us to determine the relative temporal relationships of the troughs and impact basins. The results show that the Divalia Fossae and the Rheasilvia basin overlap in their crater frequencies, indicating they can be considered coeval within the bounds of the errors. A restrictive age relationship of the Saturnalia Fossae and Veneneia basin emplacement cannot be determined from the crater counts on Vesta since the preserved surface geology of the eastern Veneneia basin may not provide any meaningful information on the emplacement age of the impact structure. However, the Rheasilvia basin superposes the Veneneia basin, and thus the Veneneia basin-forming impact must predate that of Rheasilvia. The crater frequencies of Saturnalia Fossae and the Rheasilvia basin indicate that Saturnalia Fossae are older than or coeval with the Rheasilvia basin emplacement. Taken together, the derived relative age relationships do not contradict but

also do not yield tight constraints on the hypothesis that the basin-forming impacts on Vesta directly triggered the formation of troughs.

Introduction

Large-scale troughs and impact basins on Vesta

The Dawn mission (Russell and Raymond, 2011) explored the ~525-km-diameter Asteroid 4 Vesta and revealed the presence of two sets of large-scale troughs named Divalia and Saturnalia Fossae (Figure 3.1). Divalia Fossae parallel the equator. They range in width from several 100s of meters up to about 20.5 km and encircle about two-thirds of the asteroid. Saturnalia Fossae are found in the northern hemisphere and they are oriented northwest-southeast, showing an orientation difference from Divalia Fossae of approximately 30°. The southernmost extent of Saturnalia Fossae is rendered undetectable as they are clearly truncated by Divalia Fossae. Suggested mechanisms of trough formation include normal faulting (Buczkowski et al., 2012; Scully et al. 2014) and opening-mode fracturing (Cheng and Klimczak., 2021). Poles of vertical planes defined along the Divalia Fossae cluster near the center of the 450-km-diameter Rheasilvia impact basin at the south pole (Figure 3.1), which was interpreted as evidence for an impact-induced origin of these troughs (Jaumann et al., 2012; Scully et al., 2014; Schäfer et al., 2014). Similarly, the Saturnalia Fossae are also concentric around the Veneneia impact basin, implying they are genetically linked (Jaumann et al., 2012; Scully et al., 2014; Schäfer et al., 2014; Figure 3.1). The Veneneia basin has an inferred diameter of ~421 km and is partially superposed by the Rheasilvia basin (Jaumann et al., 2012; Marchi et al., 2012; Schenk et al., 2012). The superposition and truncation

relationships present clear evidence for the Veneneia basin being older relative to the Rheasilvia basin, and that the Saturnalia Fossae are older than the Divalia Fossae.

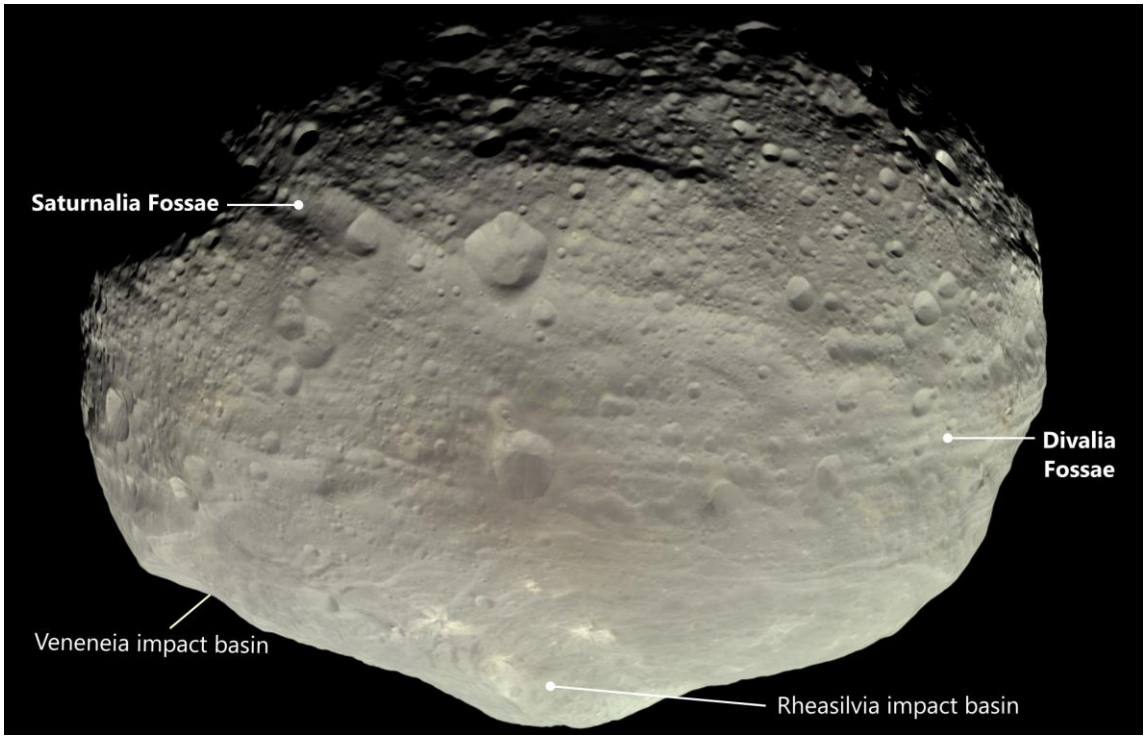

Figure 3.1. Image of Asteroid 4 Vesta, showing the locations of the Divalia Fossae and Saturnalia Fossae, and the Veneneia and Rheasilvia impact basins. The image was captured by the NASA Dawn mission on 24 July 2011 with image processing by Björn Jónsson. (same as Figure 2.1)

Numerical modeling has been conducted to investigate the tectonic processes triggered by the impacts to form the troughs and simulate the amount of deformation produced by the Rheasilvia impact (Bowling et al., 2014). A combination of laboratory and numerical experiments were performed to model subsurface failure as a consequence of oblique impacts into a spherical target (Stickle et al., 2015). Both studies find that the concentric troughs could have been formed directly by, and immediately following the collision. Under the assumption that propagation rates on Vesta compared to typical earthquake ruptures on Earth of 3 km/s and that continued loading will cause the deep fractures to propagate to the surface, fractures forming deep within the asteroid during

impact will grow toward the surface within approximately 100 to 150 s after the collision (Stickle et al., 2015). Although these modeling studies support the hypothesis that the large impacts directly and simultaneously triggered the formation of the troughs, they are constrained only by a single geologic observation based on the configuration of poles of the troughs with respect to the impact basin centers (Jaumann et al., 2012; Scully et al., 2014; Schäfer et al., 2014). No additional evidence has been documented to further support the hypothesis and corroborate the results of the modeling. For example, the temporal relationships between the two sets of troughs and the two impact basins have never been established. Crater-counting techniques are commonly used to determine the ages of planetary surfaces and are well suited to investigate the temporal relationship of the troughs and impact basins on Vesta.

Timing of Rheasilvia and Veneneia impacts

The ages of the Rheasilvia and Veneneia impacts have been under investigation since the availability of the Dawn image data and critical to our understanding of the geological history of Vesta. In particular, the Rheasilvia impact is thought to be the youngest global-scale impact on Vesta (Schenk et al., 2012) and the primary source of the Vesta family (Marzari et al., 1996; Asphaug, 1997). Hence, the age of the Rheasilvia impact is an essential constraint on the understanding of the dynamical evolution of the Vesta family and collisional asteroid families in general. Multiple studies have been conducted to investigate the timing of the Rheasilvia and Veneneia impacts with various crater-counting approaches (e.g., Marchi et al., 2012; Schenk et al., 2012; Schmedemann et al., 2014). One major debate remains as to the choice of count areas that can represent

the emplacement ages of the basins. I summarized the estimated ages and their count areas of the two impact basins from previous studies below.

Multiple investigators have estimated the Rheasilvia formation age with different count areas. Marchi et al. (2012) and Schenk et al. (2012) conducted crater measurements on the entire Rheasilvia basin floor and estimated the age to be around 1 Ga based on the Main Belt crater production function (O'Brien et al., 2007). Similarly, the floor of the Rheasilvia basin is estimated to have a crater retention age of ~1.8 Ga by Schmedemann et al. (2014) applying a lunar-derived crater production function. The underlying measured size-frequency distribution for the floor compared closely to Marchi et al. (2012) and Schenk et al. (2012), so the difference in the derived ages between these earlier papers and Schmedemann et al. (2014) was mainly due to the use of the different crater chronology model and production function. The advantage of using the entire basin floor is that it follows observable unit boundaries and provides a substantial area for well-founded crater statistics. However, Schmedemann et al. (2014) suggested that these crater statistics may severely underestimate the Rheasilvia basin emplacement age as it shows substantial geologic heterogeneity that could have affected the retention of post-Rheasilvia craters, such as mass wasting (Kneissl et al., 2014; Krohn et al., 2014; Williams et al., 2014; Otto et al., 2013; 2016) and burial by crater ejecta from later impacts.

To account for those heterogeneities, Schmedemann et al. (2014) limited the crater counting area to the top of Rheasilvia's central peak, which stands out as a positive topographic structure and shows no obvious evidence for mass wasting. Based on this assessment, the basin was estimated to have a lunar-derived absolute age of around ~3.5

Ga ago. Schmedemann et al. (2014) argued this central peak-derived age estimate was a better indication of the formation age for Rheasilvia compared to the crater statistics of the entire basin floor. However, this count area does not follow an observable unit boundary but loosely follows the elevation. The size of the count area is also limited, yielding poor crater statistics. Moreover, resurfacing may affect only the basin interior on a local scale and thus erase only smaller craters below a few km in size. Large craters are likely not completely erased by local mass wasting and thus should be preserved since the Rheasilvia basin was emplaced (Marchi et al., 2012; Schenk et al., 2012).

Almost half of the Veneneia basin, including its central peak, is superposed by the Rheasilvia basin. The preserved parts of the Veneneia basin floor are heavily resurfaced by the Rheasilvia impact (Schenk et al., 2012). Thus, the derived surface ages can serve only as a lower limit for the age of the impact. Marchi et al. (2012) and Schenk et al. (2012) counted the exposed part of the Veneneia basin floor. The estimated age is about 2 Ga, using the Main Belt crater production function (Marchi et al., 2012; Schenk et al., 2012). Schmedemann et al. (2014) counted only the eastern exposed part of the Veneneia basin, as the western part shows a different morphology with topographically muted craters, indicating potential resurfacing. This count area does not follow an observable geological boundary. Based on that count area, the crater retention age of the eastern Veneneia basin was determined to be about 3.1 Ga by fitting the lunar-derived production function for a diameter range of 7 to 35 km (Schmedemann et al., 2014).

All the above count areas of the Rheasilvia and Veneneia basins give great differences in crater frequencies and estimated ages exceeding 1 Ga for each basin. These ages need to be put into stratigraphic context to one another. Among all the ages for the

Veneneia basin, the age of ~3.1 Ga estimated by Schmedemann et al. (2014) provides the oldest age by measuring the eastern basin floor. However, given that the Veneneia basin is superposed by the Rheasilvia basin, it must be older than the Rheasilvia impact. Therefore, if the top of the Rheasilvia basin central peak with an age of ~3.5 Ga truly represents the basin emplacement age, the inferred age from the eastern Veneneia basin floor does not indicate the emplacement age of the Veneneia basin, but rather resurfacing of the earlier basin by Rheasilvia and other processes that erase craters. In this case, the emplacement of the Veneneia basin must predate that of the Rheasilvia basin at ~3.5 Ga ago, which could be used as the youngest age bound of the Veneneia basin emplacement.

Schmedemann et al. (2014) also proposed that an absolute model age of the Veneneia basin could theoretically be derived from crater counts of the Saturnalia Fossae, assuming a large impact indeed triggered the simultaneous formation of the troughs and Veneneia basin. However, the Saturnalia Fossae may be affected by secondary projectiles ejected from the Veneneia and Rheasilvia impact events, which would introduce an inaccuracy for the derived age of the Saturnalia Fossae and the inferred age of the Veneneia basin. Irrespective of that, the age of the Saturnalia Fossae has not been assessed using crater statistics.

Goals of this study

Based on the spatial relationship between the Divalia and Saturnalia Fossae sets with the Rheasilvia and Veneneia impact basins, respectively (Jaumann et al., 2012; Scully et al., 2014; Schäfer et al., 2014), the troughs are widely accepted to be formed by these large impacts and, consequently must have formed nearly coevally. Even so, these structures have yet to be dated by crater counting using Dawn image datasets. Analyses

of crater populations superposed on these fossae are essential to (1) assess whether the widely accepted coeval formation of trough sets with their associated basin is actually consistent with the geologic record, (2) determine their absolute model ages, and (3) evaluate their relative temporal relationship with other units on Vesta. In addition to a coeval formation time, two additional, previously not considered temporal relationships of the troughs and impact basins are possible. The troughs could be younger than their associated impact basin, which would require a reconsideration of the common origin. On the other hand, the troughs could be older than the impact basin they are associated with, in which case the origin of the troughs would have to be reinterpreted as being unrelated to the impact and the spatial relationships of troughs and basins would be a coincidence.

Crater statistics can help to determine the temporal relationship of the Fossae and the impact basins, therefore enhancing the understanding of Vesta's geological history. To establish the relative age relationships of the troughs and impact basins, I performed crater counting on the Divalia and Saturnalia Fossae. After that, I compared the crater statistics of Divalia and Saturnalia Fossae with previously published crater counts of various count areas on the Rheasilvia and Veneneia basins, respectively, to deduce age relationships between the structures.

Methodology

Datasets and crater counting

I conducted crater counting in *ESRI's ArcGIS software* using the *CraterTools plug-in* (Kneissl et al., 2011), which has a built-in projection correction and buffered crater-counting functions (Kneissl et al., 2015). The mapping of count areas and the superposed craters was performed on the HAMO-based Dawn FC clear filter image

mosaic with an average resolution of 60 m/pixel (Roatsch et al., 2015), assisted by the use of ~93 m/pixel digital terrain model (DTM; Gaskell, 2012) and hillshade maps with different illumination conditions derived from the DTM. These datasets were projected using a 255-km-diameter sphere and the Claudia Double-Prime system (Li et al., 2012; WGCCRE., 2014) for the mapping. The *CraterTools software* automatically determined the correct crater diameters independent of the applied projection, even though some craters may appear elliptical on the map view (Kneissl et al., 2011). I also applied the "*topographic correction*" function that is built into the *CraterTools plug-in* to calculate the count areas according to the shape of Vesta. Polygons and values of mapped areas and craters used in this study are stored in the shapefiles databases which are provided as supporting information.

To conduct crater counting on the Divalia and Saturnalia Fossae, I first defined the count areas of these large-scale troughs. The count areas of the Divalia and Saturnalia Fossae were defined by a linear depression bounded by two scarps where sharp surface breaks are observed on the topographic profiles facing each other (Figure 3.2a). I did not define a count area where there is only a single scarp present. Detailed mapping criteria and a structural map of these troughs were presented in Cheng and Klimczak (2021).

Only craters that directly superpose troughs within the count areas were counted (Figure 3.2b). The minimum crater diameters measured in this study was chosen to be 0.6 km, which corresponds to ~10 pixels of the average resolution of FC images acquired by the FC during the HAMO phase (Roatsch et al., 2015), a value recommended by Robbins et al (2014) for studying complex terrains. An impact crater was identified by a sub-circular shadow from the crater rim facing away from the illuminator with a fresh to

degraded rim on the FC image and a sub-circular depression on the hillshade map constructed from the DTM. However, some craters may hardly preserve their distinctive landform, especially on the trough scarps. Therefore, I marked craters with an irregular shape or barely recognizable depression during crater counting as uncertain. These uncertain craters could be impact craters, but could also be other landforms, such as mass wasting or slumping on the trough scarps, part of the coalesced pit-crater chain during trough formation (see Cheng and Klimczak., 2021), artifacts by other impact crater rims or structures, and possible pre-existing craters deformed by seismic shaking considering a graben-origin of the troughs (see below).

I emphasize that craters pre-dating trough formation should not be counted for accurate assessment of the trough formation age. In principle, if the troughs are grabens (Buczkowski et al., 2012), the down-dropped graben floor could contain preserved craters. If the troughs are opening-mode fractures (Cheng and Klimczak., 2021), the trough floor should entirely be resurfaced by the slope materials filling from the fracture walls, and thus should not contain any pre-existing craters. Cheng and Klimczak (2021) presented multiple lines of evidence for the troughs to be opening-mode fractures, and thus I do not expect any pre-existing craters to be preserved on the troughs. Even if the troughs are grabens and considering the displacements in excess of 5 km (Buczkowski et al., 2012), floors may have experienced substantial seismic shaking when they formed that helped to erase pre-existing craters there.

After I mapped the superposing craters in the count area (Figure 3.2), I exported the crater statistics by using all craters with centers in the count area with the *CraterTools plug-in*. Typically, crater statistics of linear structures on the planetary surface have

limited areas and thus a buffered crater-counting technique is used (e.g., Fassett and Head., 2008; Kneissl et al., 2015; Kreslavsky et al., 2015; Tanaka., 1982; Wichman and Schultz., 1989). However, the Divalia and Saturnalia Fossae do show large surface areas. Therefore, I derived their crater statistics using a non-buffered approach that directly computes the crater frequencies by normalizing the number of craters with the topographically corrected count area.

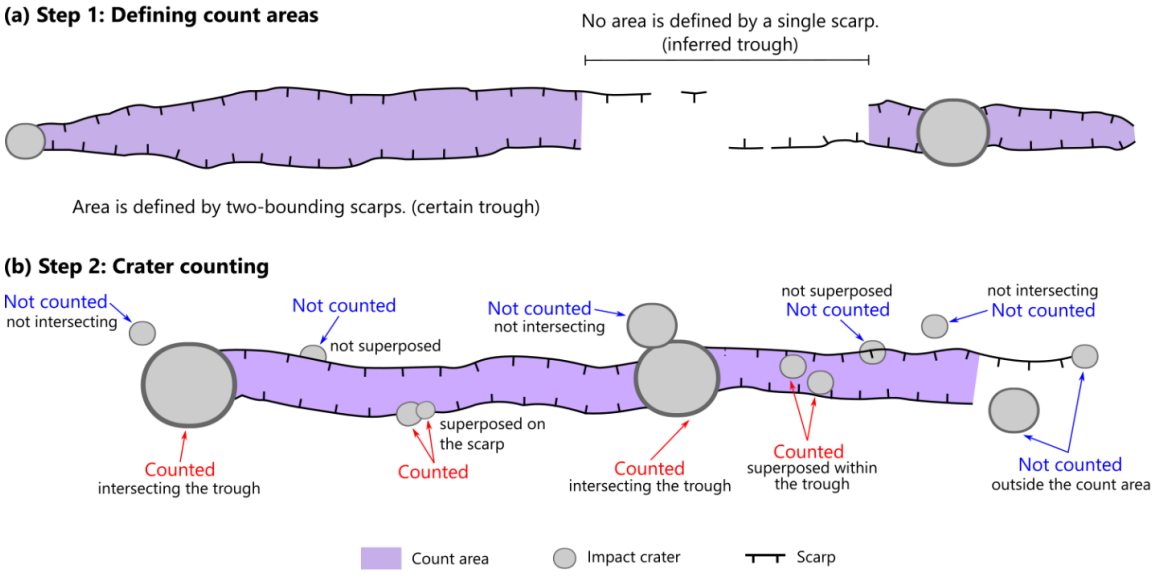

Figure 3.2. *Schematic diagram illustrating the crater counting procedure for Divalia and Saturnalia Fossae on Vesta. (a) Step 1 is to map the count areas, which are defined by the two trough-bounding scarps. (b) Step 2 involves counting only those craters that directly superpose the troughs. Craters are not included if they are not superposed on the trough, that is, if they are crosscut by the scarp or if they are outside the count areas. I mapped all superposing craters on the troughs. However, only the craters with their centers in the count area were exported for the crater statistics.*

Determination of relative and absolute ages

Two crater size-frequency plotting techniques were used to analyze the crater counting results. I generated the data as *differential frequencies* and as *relative frequencies* in a standard root-2 binning, which are common techniques for displaying crater data (see Crater Techniques Working Group, 1979; Michael, 2013). The main differences between them are the crater frequency calculation and the way data are aggregated for plotting. The *differential frequency plot* displays the crater frequency, $n\,[D_a, D_b]$ per unit area, into a series of chosen crater sizes, in which n is the number of craters within the diameter size range from D_a to D_b. The differential frequency at the diameter D_c is $F(D_c) = n\,[D_a, D_b]/(D_b - D_a)$ with D_c is the geometric mean of the crater bin size. An advantage of differential plots of data is that each point in the size-frequency distribution is independent. However, the binning effect can lead to biases (e.g., Michael, 2013). The *relative frequency plot*, commonly referred to as R-plot, is constructed by dividing the differential size-frequency by D_c^{-3}, which removes the steep power-law trend from the data. Variations in the structure of the crater population can be rapidly assessed with the vertical axis representing the spatial density of craters of different sizes. Uncertainties of the two types of frequencies were calculated based on Poisson counting statistics (Haight, 1967) with a 90% confidence level in gamma cumulative distribution. I also applied the Mean 2nd Closest Neighbor Distance (M2CND) randomness analyses (Michael et al., 2012) using the *CraterStats II software*[3] (Michael and Neukum, 2010) for statistical identification and exclusion of the affected crater diameters by secondary crater clusters.

[3] https://www.geo.fu-berlin.de/en/-eol/fachrichtungen/planet/software/_content/software/craterstats.html

I computed the differential and relative frequencies of the Divalia and Saturnalia Fossae using *only certain* and *all craters*. The computation using *only certain* craters may underestimate the crater frequencies without taking into account heavily deformed or degraded craters that are superposing the troughs, and thus provide a younger bound of the surface age. In contrast, the crater frequencies may be overestimated when computing with *all craters*, as they may include false detections of other landforms or pre-existing craters. Therefore, these frequencies serve as an older surface age bound of the troughs. Hence, this approach provides rigorous crater frequencies of the troughs for the determination of relative and absolute ages.

The main purpose of this study is to determine the relative age relationship of the troughs and impact basins on Vesta. The relative ages of planetary surfaces can be determined by comparing the crater frequency on the two plots. As crater density and age increase, the plotted differential and relative size-frequency distribution shift up on the vertical axes. Therefore, I compared my newly-derived crater counts of the Divalia and Saturnalia Fossae with previously published data of the Rheasilvia and Veneneia impact basins. I used the crater counts of the entire Rheasilvia basin floor, the top of the Rheasilvia basin central peak, and the eastern Veneneia basin floor from Schmedemann et al. (2014) since their count areas and crater maps are published, which allowed us to replicate and compute their crater statistics for the comparison (Supporting Information S1 to S4).

I also derived the *absolute model ages* for Divalia and Saturnalia Fossae by applying the lunar-derived crater production and chronology function for Vesta based on the physical parameters from the Dawn mission (see Schmedemann et al., 2014 for

justification and details). These functions are publicly available and implemented in the *CraterStats II software*. I used the least-squares multiple linear regression approach for isochron fitting and Poisson timing analysis (Michael et al., 2016) in the *CraterStats II software* (Michael and Neukum, 2010). The least-square approach is a commonly used method for absolute age determination. The derived chronology allows direct comparison with the published absolute ages derived from the same approach, such as Schmedemann et al. (2014). However, this method is sensitive to crater size binning. The Poisson timing analysis utilizes the incremental crater size-frequency distribution during the age derivation process and therefore represents a binning-independent method to derive absolute ages (Michael et al., 2016).

This work emphasizes the relative age relationship of the troughs and impact basins. All absolute model ages are referenced to the specific system derived by Schmedemann et al. (2014) and contain a systematic uncertainty. The uncertainties consist of the intrinsic uncertainties within the lunar model (Neukum., 1984; Neukum et al., 2001) and those pertaining to the scaling laws and parameters used to translate the impactor size-frequency distribution to a Vesta crater production size-frequency distribution. Any reassessment of the production function with new information would change the absolute model ages, but the relative chronology would be unaffected.

Results

In this section, I present the derived crater size-frequencies for the Divalia and Saturnalia Fossae, and assess their meaning for the temporal relationships with the Rheasilvia and Veneneia basins. Their crater frequencies are plotted with those from impact basins from Schmedemann et al. (2014) in differential and relative crater size-

frequency plots to examine their relative chronology. Results of the M2CND randomness analysis that fall within ± 3σ above or below the Monte-Carlo-derived means are interpreted as an indicator for a spatially random distribution with some suspicion at trends towards ± 2 or 3σ (Michael et al., 2012). All model ages and isochrons presented are based on the lunar-derived crater production function for Vesta with the physical parameters of Vesta derived by Dawn data (Schmedemann et al., 2014).

Divalia Fossae and the Rheasilvia basin

The Divalia Fossae comprise 13 individual count areas following the criteria stated in methodology (Figures 3.2a), yielding a total count area of 22016 km^2 with topographic correction (Figure 3.3a). I mapped 3378 craters centered in the count area ranging from 0.6 km up to ~19 km in diameter with 887 of them are marked as uncertain (Figure 3.3b). I computed the crater frequencies by including and excluding these marked craters with results being shown in Figures 4a and b (and the data reported in Appendix Tables 3.1 and 3.2). The differential size-frequency distributions of the Divalia Fossae with only certain and all craters exhibit a relatively constant slope with the production functions for craters with $D \geq 2$ km (Figures 3.4a). Craters larger than 2 km were considered to be randomly distributed (Figure 3.4c), regardless of the inclusion and exclusion of craters marked as uncertain, and therefore the frequencies were used for the relative age and absolute age determinations. The derived frequencies are deficient in craters below ~2 km diameter (Figures 3.4a, b), especially compared to the production function in both plots. These smaller craters were considered to be clustered (Figure 3.4c); therefore, I did not consider them in the age determinations. I determined the best-fit lunar-derived absolute model ages for the Divalia Fossae for craters of $D \geq 2$ km

counting only certain craters to be $3.41^{+0.04}_{-0.05}$ Ga by the least-squares multiple linear regression approach and $3.37^{+0.03}_{-0.04}$ Ga by the Poisson timing analysis. Older absolute ages of $3.62^{+0.01}_{-0.02}$ Ga and $3.60^{+0.01}_{-0.01}$ Ga are resulted when counting all craters using the least-squares multiple linear regression approach and the Poisson timing analysis, respectively.

I also plotted the crater frequencies from Schmedemann et al. (2014) of the Rheasilvia basin for the entire basin floor and the top of the central peak in Figures 4a and b (Supporting Information S2 and S3). The crater frequencies of the entire Rheasilvia basin are indistinguishable from those for the Divalia Fossae for $D \geq 5.65$ km and appear to be lower than the Divalia Fossae for smaller craters. However, the derived frequencies of the entire Rheasilvia basin are deficient in crater size $D < 5.65$ km (Figure 3.4a, b), and the counting does not include craters smaller than ~1.4 km in diameter by Schmedemann et al. (2014) (Supporting Information S1). Therefore, a valid comparison with the Divalia Fossae crater counts cannot be made for the smaller craters.

In contrast, the top of the basin central peak has comparable crater frequencies with the Divalia Fossae for $D < 8$ km (Figure 3.4a, b). The crater frequencies of Divalia Fossae without craters marked as uncertain are generally lower than the frequencies of the top of the basin central peak. Divalia Fossae with craters marked as uncertain have higher crater frequencies than the top of the basin central peak in most of the bins, except for the largest comparable crater size bin of $D \geq 16$ km. However, it is not possible to statistically distinguish the crater frequencies of the two landforms, as the frequencies of the Divalia Fossae lie entirely within the large frequency uncertainties of the top of the Rheasilvia basin central peak.

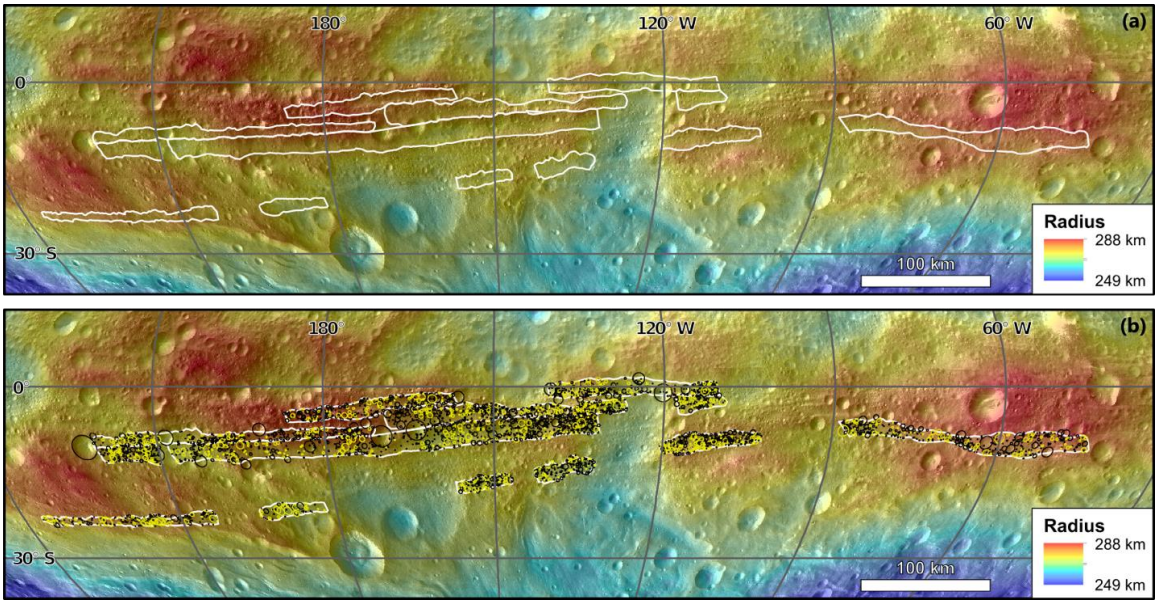

Figure 3.3. *Maps of crater count areas and craters of the Divalia Fossae displayed in Dawn FC images color-coded by elevation. (a) Map showing count areas outlined by white solid lines with a total area of 22016 km^2 (topographically corrected). (b) Crater count map with the certain craters outlined in black (n = 2491) and marked (uncertain) craters outlined in yellow (n = 887). I projected the Divalia Fossae, extended from 24°S to 4°N and 123°E to 42°W, using sinusoidal projections.*

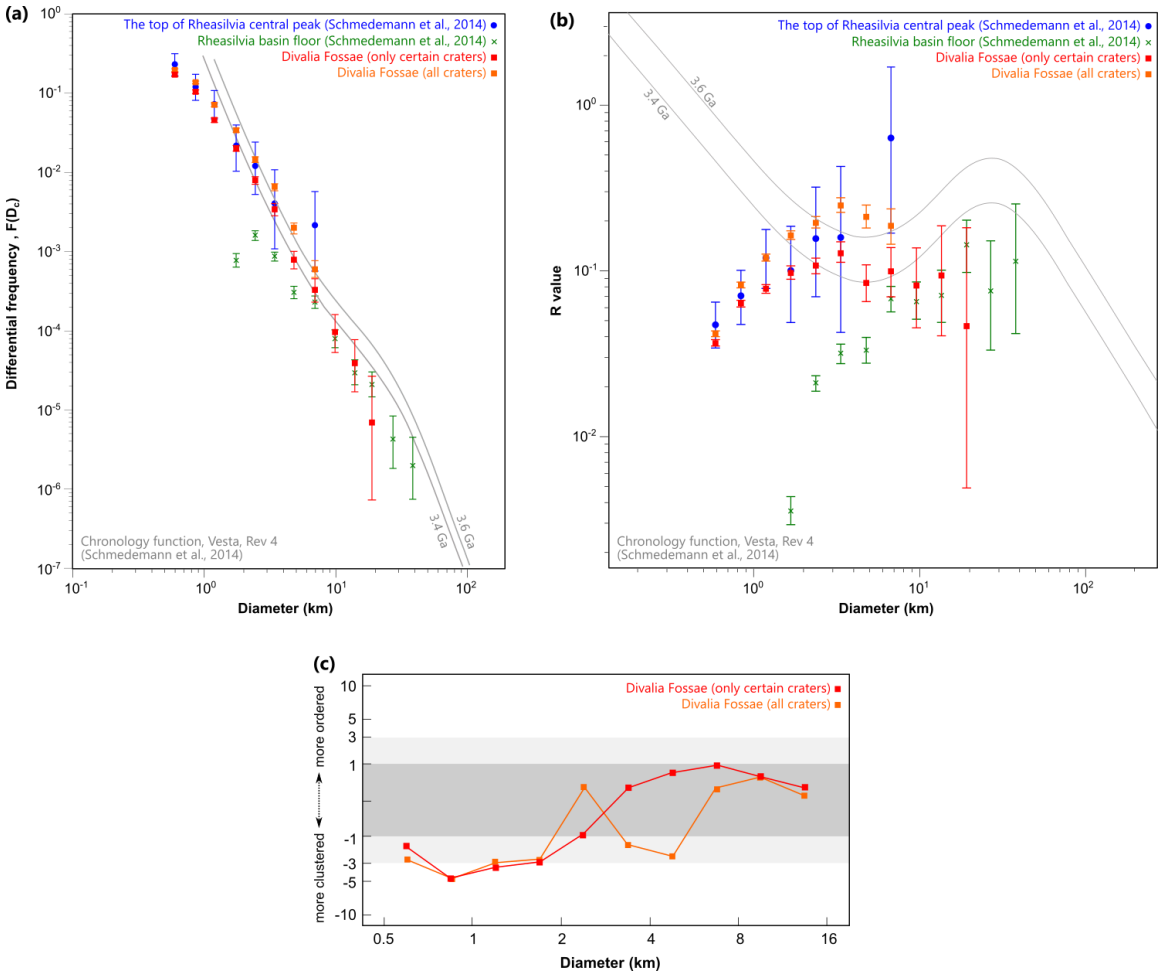

Figure 3.4. Crater size-frequency distributions of Divalia Fossae with spatial randomness analyses (this study), the entire Rheasilvia basin floor (Schmedemann et al., 2014), and the top of the Rheasilvia basin peak (Schmedemann et al., 2014). (a) Differential crater size-frequencies of the Divalia Fossae with certain craters only (red squares) and all craters including those marked as uncertain (orange squares), the top of the Rheasilvia basin peak (blue circle), and the entire basin floor (green cross) are plotted against the mean crater diameter of each bin. (b) The relative crater size-frequency distribution for the Divalia Fossae with the same symbology as in (a). The lunar-derived production functions for 3.4 Ga and 3.6 Ga (Schmedemann et al., 2014) are also plotted as grey lines in both of the plots. Error bars are of 90% confidence in Poisson counting statistics. (c)

The Mean 2nd Closest Neighbor Distance (M2CND) spatial randomness analysis results are plotted for Divalia Fossae with the same symbology as in (a) shown in standard deviations above or below the Monte-Carlo-derived means (Michael et al., 2012).

Saturnalia Fossae and the Veneneia basin

The Saturnalia Fossae have one count area outlining two adjoining large-scale troughs, yielding 10673 km^2 with topographic correction (Figure 3.5a). A total of 2179 craters ranging from 0.6 km up to ~20 km in diameter were mapped and center in the count area with 242 of them marked as uncertain (Figure 3.5b). I computed the crater frequencies by including and excluding these marked craters and the results are shown in Figures 3.6a and 3.b (with data found in Appendix , Tables 3.3 and 3.4). The differential size-frequency distributions of the Saturnalia Fossae with and without craters marked as uncertain exhibit a reasonably constant slope with the production function for craters of $D \geq 2$ km (Figure 3.6a). Relative frequencies display a similar pattern, showing a reasonably flat slope for craters with $D \geq 2$ km (Figure 3.6b). Craters larger than 2 km were considered to be randomly distributed for all craters and those counts excluding uncertain craters (Figure 3.6c). There is a deficiency of craters with $D \leq 2$ km from the expected production population observed in differential and relative size-frequency plots (Figure 3.6a, b). These smaller craters were considered to be clustered (Figure 3.4c). Therefore, I only consider craters of the Saturnalia Fossae with $D \geq 2$ km for the relative age and absolute age determinations. I determined the best-fit lunar-derived absolute model ages for the Saturnalia Fossae for craters of $D \geq 2$ km counting only certain craters to be $3.68^{+0.02}_{-0.02}$ Ga by the least-squares multiple linear regression approach and $3.65^{+0.01}_{-0.01}$ Ga by the Poisson timing analysis. Older absolute ages of $3.72^{+0.01}_{-0.02}$ Ga and $3.69^{+0.01}_{-0.01}$ Ga

are resulted when counting all craters using the least-squares multiple linear regression approach and the Poisson timing analysis, respectively.

I also plotted the crater frequencies from Schmedemann et al. (2014) of the eastern Veneneia basin floor in Figure 6a and b. The counts of only certain and all craters reveal that the Saturnalia Fossae show distinctively higher differential and relative crater size-frequencies than the eastern Veneneia basin for craters with $D < 11.31$ km (Figure 3.6a, b). The crater size-frequencies of the two landforms are overlapping for the larger craters of $D \geq 11.31$ km. I note that the apparent deficiency of craters in the eastern Veneneia basin floor with $D \leq 1$ km since the count by Schmedemann et al. (2014) is not inclusive of these small craters (Supporting Information S1), and no comparison can be made with the frequencies of this size range.

These crater counts have to be placed into context with stratigraphic relationships to assess their relevance for the geologic history of Vesta. The crater counts from Schmedemann et al. (2014) suggested that the derived age from the Rheasilvia central peak is older than the eastern Veneneia basin, which contradicts the stratigraphic relationship of two basins (see introduction). Therefore, the inferred age from the eastern Veneneia basin floor may not indicate the emplacement age of the Veneneia basin, if the cratered surface of Rheasilvia's central peak is taken to represent the emplacement age of Rheasilvia. Hence, I also plotted the crater frequencies of the top of the Rheasilvia basin central peak from Schmedemann et al. (2014) in Figure 3.6a and b for comparison with the Saturnalia Fossae.

The top of the Rheasilvia basin central peak exhibits crater frequencies of the comparable crater sizes with the Saturnalia Fossae for $D < 8$ km (Figure 3.6a, b). The

crater frequencies of Saturnalia Fossae with only certain and all craters are generally higher than that of the top of the Rheasilvia basin central peak in most of the bins, except for the largest comparable crater size bin of D ≥ 16 km. However, it is not possible to statistically distinguish the crater frequencies of the two landforms, as the frequencies of the Saturnalia Fossae overlap with the frequencies of the top of the Rheasilvia basin central peak.

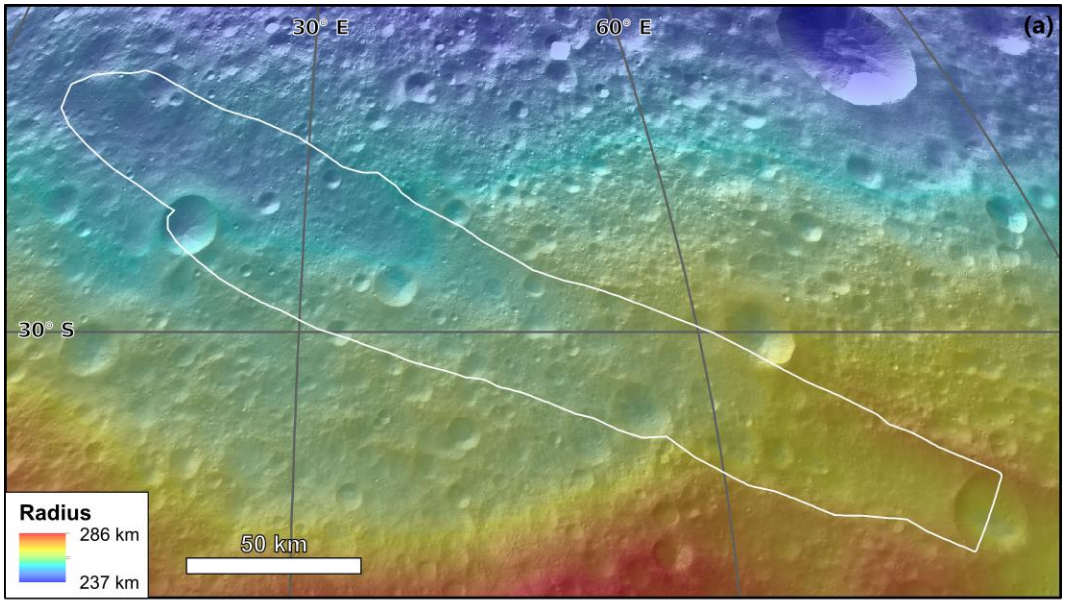

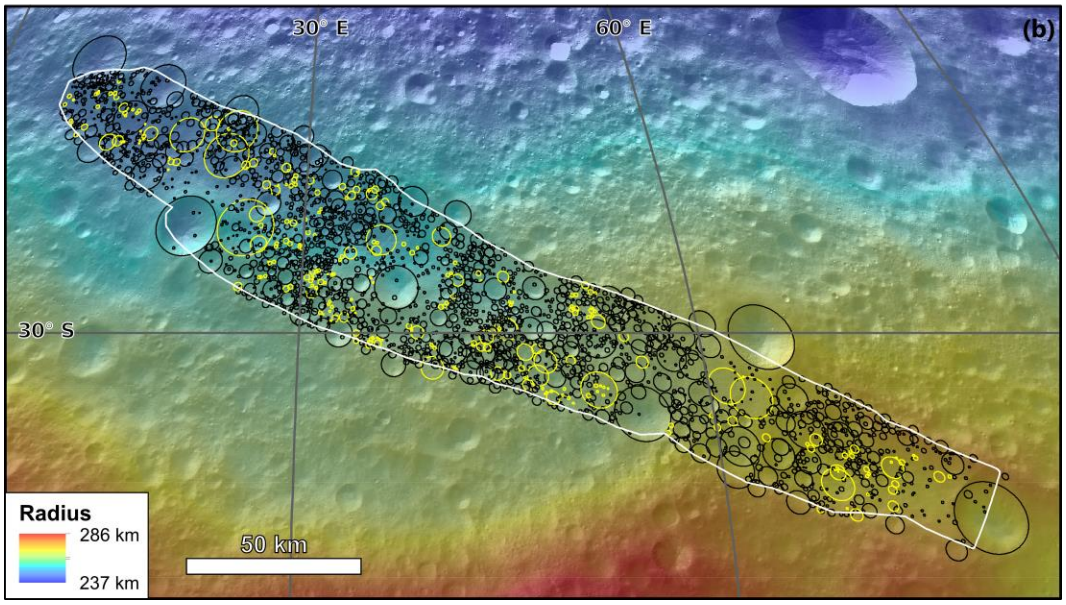

Figure 3.5. *Maps of crater count areas of the Saturnalia Fossae display with the Dawn FC images color-coded by elevation. (a) Map showing a count area outlined by white solid lines with a total area of 10673 km^2 (topographically corrected). (b) Crater count map with the certain craters outlined in black (n = 1937) and marked (uncertain) craters outlined in yellow (n = 242). I projected the Saturnalia Fossae, centered at 32°S and 42°E, using sinusoidal projections.*

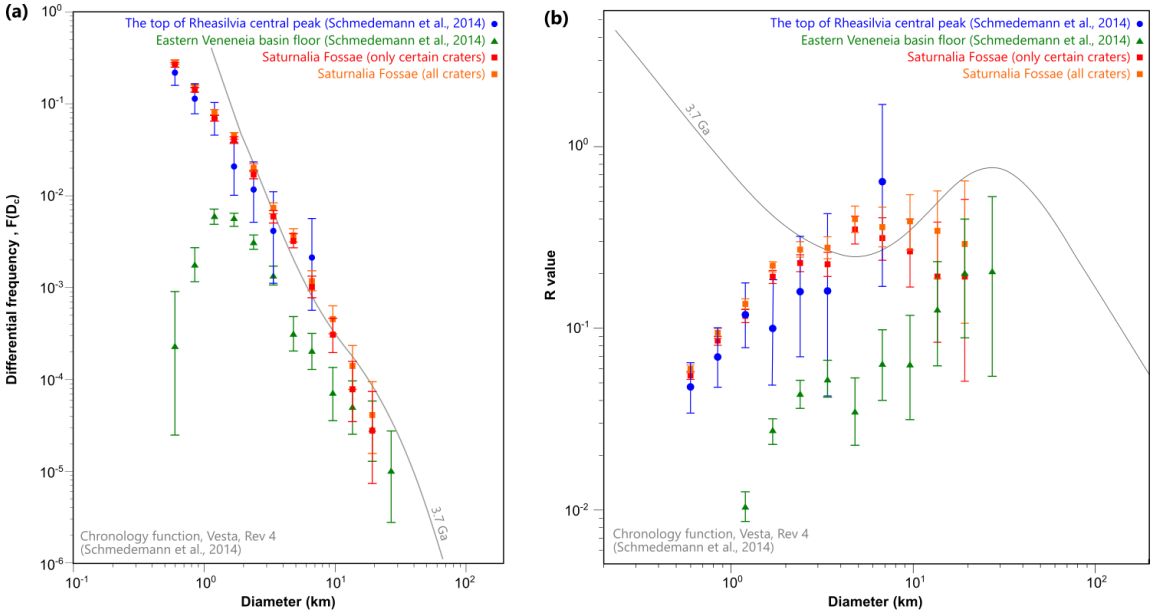

Figure 3.6. *Crater size-frequency distributions of Saturnalia Fossae with spatial randomness analyses (this study), the entire Rheasilvia basin floor (Schmedemann et al., 2014), and the top of the Rheasilvia basin peak (Schmedemann et al., 2014). (a) Differential crater size-frequencies of the Saturnalia Fossae with certain craters only*

(red squares) and all craters including those marked as uncertain (orange squares), the top of the Rheasilvia basin peak (blue circle), and the entire basin floor (green cross) are plotted against the mean crater diameter of each bin. (b) The relative crater size-frequency distribution for the Saturnalia Fossae with the same symbology as in (a). The lunar-derived production functions for 3.7 Ga (Schmedemann et al., 2014) are also plotted as grey lines in both of the plots. Error bars are of 90% confidence in Poisson counting statistics. (c) The Mean 2nd Closest Neighbor Distance (M2CND) spatial randomness analyses results are plotted for Saturnalia Fossae with the same symbology as in (a) shown in standard deviations above or below the Monte-Carlo-derived means (Michael et al., 2012).

Discussion and implications

Relative age relationships of troughs and impact basins

To evaluate the relative age relationship of the troughs and impact basins on Vesta, I derived crater statistics for the Divalia Fossae and Saturnalia Fossae and compared them with previously published crater statistics of the Rheasilvia and Veneneia basins from Schmedemann et al. (2014). To date, there are no cross-cutting relationships of the Divalia Fossae and the Rheasilvia basin recognized and reported in the literature, thus leaving the only comparison of crater statistics between the two landform types to analyze their temporal relationship at this point.

The crater frequencies of the entire Rheasilvia basin (Schmedemann et al., 2014) overlap with those from Divalia Fossae for $D \geq 5.65$ km, indicating that they share a similar surface age. However, the crater counts by Schmedemann et al. (2014) are not inclusive for smaller craters on the Rheasilvia basin floor limiting a direct comparison

with the Divalia Fossae to only the largest preserved crater diameters. Although large craters give reliable crater statistics as they are hardly erased by geological processes, their smaller quantity gives crater statistics with large uncertainties. The uncertainties in this comparison allow for hundreds of millions of years to have passed between the formation of the basin and the troughs. Moreover, the crater frequencies of the Divalia Fossae also overlap with those of the top of Rheasilvia central peak for crater sizes of $D <$ 8 km; thus indicating that they share a similar surface age, too. However, there are large uncertainties in the frequencies derived for the Rheasilvia central peak, which leaves this temporal overlap loosely constrained.

Based on the comparison of crater counts, the hypothesis that the Rheasilvia impact directly and simultaneously triggered the formation of the Divalia Fossae remains valid, irrespective of the count areas used for the Rheasilvia basin. However, the large uncertainties associated with the crater frequencies of the Rheasilvia basin allow for the troughs to have formed well after the emplacement of the basin, perhaps as a long-term consequence of basin tectonics or other physical processes on the asteroid. Tectonic processes operating over an extended period of time, exceeding those related to the basin emplacement, may have contributed to the formation or continued growth of the troughs. Future relative age comparisons and interpretations would be much improved for crater counts involving smaller impact craters and distinguishing craters in uncertain and certain on the Rheasilvia basin floor.

The Saturnalia Fossae have crater frequencies distinctively higher than the eastern Veneneia basin for craters with diameters of ~1 km up to 11.31 km but the data overlap for craters with diameters larger than 11.31 km within the bound of large uncertainties.

This indicates that the Saturnalia Fossae could be coeval or somewhat older than the Veneneia basin, if the eastern Veneneia basin count area truly represents the basin emplacement age. But the crater counts from Schmedemann et al. (2014) suggested that the Rheasilvia central peak is older than the eastern Veneneia basin in the determined surface ages, contradicting with the observed stratigraphic relationship where the Rheasilvia basin superposes the Veneneia basin. If the top of the Rheasilvia basin central peak truly represents the Rheasilvia basin emplacement age, the count area of the Veneneia basin may not be meaningful for exploring its emplacement age. Although Schmedemann et al. (2014) attempted to locate other count areas, such as an ancient crater centered at 250°E and 30°N, the age of the Rheasilvia emplacement age is the only direct and restrictive younger bound for the formation of the Veneneia basin.

Given that the crater frequencies of Saturnalia Fossae mostly overlap with the upper bound of the frequency uncertainties of the Rheasilvia basin central peak, I deduce that the Saturnalia Fossae are coeval with, or formed somewhat before the Rheasilvia central peak. The uncertainties in the crater counts leave the temporal relationships between the Saturnalia Fossae and both impact basins loosely constrained, and thus they do not disproof nor directly confirm the hypothesis that the Veneneia impact directly and simultaneously triggered the formation of the Saturnalia Fossae. Therefore, this hypothesis remains to be tested with other methods.

The Divalia and Saturnalia Fossae crater counts also need to be placed into context with their observed stratigraphic relationship to validate how meaningful they are for the interpretation of Vesta's geologic history. Since the southernmost extent of Saturnalia Fossae is clearly truncated by Divalia Fossae (Cheng and Klimczak, 2021), the

Divalia Fossae must be younger than the Saturnalia Fossae. The crater frequencies of the Divalia Fossae are lower than those of the Saturnalia Fossae (Appendix, Tables 3.1 to 3.4), irrespective of the uncertain craters. This indicates that the Divalia Fossae are likely to have formed after the Saturnalia Fossae, consistent with the geological observation. Therefore, the crater frequencies for the Divalia and Saturnalia Fossae are meaningful for the interpretation of their relative chronology and their geological context. Since the hypothesis that the Venenea impact triggered the formation of the Saturnalia Fossae remains valid, the surface age of the Saturnalia Fossae may better represent the emplacement age of the Venenea basin than its partially preserved basin floor.

Effect of secondary cratering from Rheasilvia impact

Secondary cratering on Vesta is considered insignificant because of the low escape velocity (Bierhaus et al., 2018). However, this finding may not be applicable to a basin-forming event in the scales of Rheasilvia. Based on Melosh (1989), secondary craters are found to reach up to 5% of the size of their primary crater. Secondary cratering from the Rheasilvia impact might therefore involve craters up to ~22.5 km in diameter. This overlaps with the diameter range of mapped primary craters used in this study for the relative age assessment of the Divalia and Saturnalia Fossae. I thus evaluate the possible effects of secondary cratering from the Rheasilvia impact on the relative chronology of the troughs and basins determined in section 3.4.1.

The effect of secondary cratering by the Rheasilvia impact depends on its relative age with the surfaces of interest. Secondary cratering could cause the surfaces pre-dating the Rheasilvia impact to show higher crater frequencies and thus appear to be even older. The same effect will affect surfaces that are coeval with the Rheasilvia impact. Under the

assumption that the secondary impactors form craters shortly after the Rheasilvia impact, they will not have any effect on younger surfaces. Among those scenarios, the only problematic case for the relative age determination and geologic interpretation is the one in which surfaces appear older than the Rheasilvia impact when in fact they share similar ages. Therefore, if secondary craters from the Rheasilvia impact are superposed on a surface, interpretation of ages of such surfaces must account for the fact that they either truly are older or only appear to be older than the Rheasilvia basin.

Crater frequencies between the Rheasilvia impact and the Divalia Fossae overlap, thus allowing for a contemporaneous formation. While secondary craters from the Rheasilvia impact may contaminate the crater counts within the Divalia Fossae, their inclusion into the crater counts would not affect the deduced relative chronology as the Divalia Fossae do not show resolvable higher crater frequencies and thus are not likely older than Rheasilvia.

I also determined that crater frequencies between the Rheasilvia impact and the Saturnalia Fossae overlap but that that the Saturnalia Fossae show a somewhat higher density. This indicated that the formation of these troughs could have taken place along with or somewhat prior to the Rheasilvia impact. As the crater densities are somewhat higher, the crater counts within the Saturnalia Fossae may include secondaries from the Rheasilvia impact, and therefore overestimate the crater counts. Therefore, the crater densities at the Saturnalia Fossae may either truly be or only appear somewhat older than those of the Rheasilvia basin.

The Veneneia impact may also have produced sizeable secondary craters that could affect the crater counting results. However, it is not possible to deduce a direct and

restrictive age relationship between the Saturnalia Fossae and Veneneia basin emplacement and secondary craters from the Veneneia impact do not influence the relative age determination for any of the stratigraphically younger structures. Even if secondaries from the Veneneia impact are superposed on Saturnalia Fossae, they would not affect their age relationship with the younger Rheasilvia basin, especially after accounting for secondaries from the Rheasilvia impact.

Limitations in absolute age relationships

I determined the absolute ages of the Divalia and Saturnalia Fossae from their differential crater frequencies. Accounting for uncertainties in crater identification and using different statistical approaches, the best fit absolute model ages for the Divalia Fossae and Saturnalia Fossae are ~3.4–3.6 Ga and ~3.6–3.7 Ga, respectively. However, various limitations of these absolute ages exist. In contrast to the relative chronology, these absolute ages are directly derived from the crater frequencies of the troughs by fitting isochrons with the least-square regression or Poisson timing analysis. Therefore, potential secondaries from Rheasilvia and Veneneia impacts will directly affect the accuracies of these absolute ages. Moreover, the uncertainties of the absolute age consider only the Poisson counting errors but not the uncertainties of the specified production and chronology functions, or the misfits of the isochrons and crater size-frequency data.

Consequently, any derived absolute ages of the troughs and basins will be subject to these limitations. Therefore, I did not compare and discuss the absolute ages of the Divalia and Saturnalia Fossae with and the basins. All absolute model ages are referenced to the specific system derived by Schmedemann et al. (2014) and contain a systematic

uncertainty due to the lack of knowledge. Any reassessment of the production function with new information would change the absolute model ages, but the relative chronology discussed here will remain unaffected.

Potential crater saturation equilibrium

In all the data, a systematic divergence of the crater size-frequencies from isochrons occurs at around crater diameters of 2 km and smaller for the two Fossae in this study (Figures 3.4a, 3.4b, 3.6a, and 3.6b). These smaller craters are somewhat clustered from the spatial randomness analyses (Figure 3.4c, 6c). The observed sub-production slope could be the result of false-negative crater detection but also due to a possible equilibrium of the crater population with regards to the crater degradation, which is referred to as "saturation equilibrium" or "degradation equilibrium" (e.g., Gault, 1970; Hartmann, 1984; Minton et al., 2019). Such a divergence at ~2 km was also previously observed in multiple crater frequency plots for surface units on Vesta (e.g., Marchi et al., 2012; Schmedemann et al., 2014). There is limited research about how crater degradation controls the observed equilibrium size-frequency distribution on Vesta. The transition point between production and equilibrium of craters occurs at diameters of 100 to 200 m on the lunar maria (Gault, 1970), up to a few kilometers on the lunar highlands (Povilaitis et al., 2018), and at crater diameters of ~1 km on Borealis Planitia on Mercury (Chapman et al., 2011; Fassett et al., 2018). However, the impact conditions (i.e., impact velocity, impactor size-frequency distribution, and physical parameters) vary between different planetary bodies, which makes a comparison of the inflection due to equilibrium incomparable. Future studies of how degradation controls equilibrium behavior in the

observed crater population on Vesta may lead to further progress on this topic and provide additional insight into the cratering history for Vesta and other asteroids.

Conclusions

Crater counting of the Divalia and Saturnalia Fossae was performed to establish their crater frequency distributions, and the results were compared with previously published data of the Rheasilvia and Veneneia basins by Schmedemann et al. (2014) to determine their relative ages on Vesta. Differential crater size-frequencies of the Divalia Fossae and the Rheasilvia basin overlap with one another, indicating that these two landforms are coeval. The hypothesis that the impact that formed the Rheasilvia basin triggered the formation of the Divalia Fossae remains valid. However, the large frequency uncertainties of the Rheasilvia counts allow for the troughs to have formed well after the emplacement of the Rheasilvia basin. This relative age relationship will need to be reassessed if any updated crater counts of the Rheasilvia basin floor or other age constraints of the Rheasilvia impact become available.

A restrictive age relationship of the Saturnalia Fossae and Veneneia basin emplacement cannot be determined from crater counts as the surface geology of the eastern Veneneia basin may not provide any meaningful information on the emplacement age of the impact structure. But since the Rheasilvia basin superposes the Veneneia basin, the emplacement age of the Rheasilvia basin serves as a younger marker for the emplacement of the Veneneia basin. While the crater frequencies of Saturnalia Fossae are generally higher than those derived for the central peak of the Rheasilvia basin, their uncertainties overlap. This indicates that the Saturnalia Fossae are at least coeval with but likely somewhat older than the Rheasilvia basin emplacement. Since the Veneneia basin

is superposed by, and thus is also older than the Rheasilvia basin, the results leave valid the hypothesis that the impact that formed the Veneneia basin directly and simultaneously triggered the formation of the Saturnalia Fossae.

I demonstrated that any secondary cratering should it have occurred from the Rheasilvia impact would not affect the relative chronology of the troughs and impacts. However, the secondary cratering will affect the accuracies of the lunar-derived model formation ages of Divalia and Saturnalia Fossae of ~3.4–3.6 Ga and ~3.6–3.7 Ga, respectively. These absolute ages are also affected by the uncertainties of the specified production and chronology functions as well as by the misfits of the isochrons and crater size-frequency data. Therefore, I emphasized only the relative age relationship of the troughs and impact basins in this study.

These results are important for the understanding of the geological evolution of Vesta because they provide new crater statistics for the Divalia and Saturnalia Fossae that served to investigate a previously hypothesized temporal correlation between the troughs and impact basins (e.g., Buczkowski et al., 2012; Jaumann et al., 2012; Scully et al., 2014; Schäfer et al. 2014). These relative age relationships of landforms are useful constraints for numerical models of lithospheric deformation produced by the Rheasilvia impact and its relation to the formation of troughs (Bowling et al., 2014; Stickle et al., 2015).

Acknowledgments

I thank Alicia Neesemann and Gregory Michael, who provided valuable feedback on this manuscript.

Appendix

Crater statistics for the Divalia and Saturnalia Fossae

Table 3.1. Divalia Fossae crater size-frequency data with uncertain craters excluded. (Area = 22016 km^2)

D_a [a]	D_c [b]	n[c]	10.00% [d]	90.00% [d]	Differential			Relative		
					$F(D_c)$	-[e]	+[e]	R	-[e]	+[e]
0.5	0.5946	809	774.14	843.86	1.77E-01	7.64E-03	7.64E-03	3.73E-02	1.61E-03	1.61E-03
0.70711	0.8409	696	663.67	728.33	1.08E-01	5.01E-03	5.01E-03	6.42E-02	2.98E-03	2.98E-03
1	1.189	427	401.68	452.32	4.68E-02	2.78E-03	2.78E-03	7.87E-02	4.67E-03	4.67E-03
1.4142	1.682	265	244.36	287.10	2.05E-02	1.60E-03	1.71E-03	9.78E-02	7.61E-03	8.16E-03
2	2.378	147	131.69	163.79	8.06E-03	8.39E-04	9.21E-04	1.08E-01	1.13E-02	1.24E-02
2.8284	3.364	89	77.14	102.35	3.45E-03	4.60E-04	5.18E-04	1.31E-01	1.75E-02	1.97E-02
4	4.757	29	22.35	37.20	7.95E-04	1.82E-04	2.25E-04	8.56E-02	1.96E-02	2.42E-02
5.6569	6.727	17	11.98	23.61	3.30E-04	9.74E-05	1.28E-04	1.00E-01	2.96E-02	3.90E-02
8	9.514	7	3.89	11.77	9.59E-05	4.26E-05	6.54E-05	8.26E-02	3.67E-02	5.63E-02
11.314	13.45	4	1.74	7.99	3.88E-05	2.19E-05	3.87E-05	9.43E-02	5.32E-02	9.42E-02
16	19.03	1	0.11	3.89	6.85E-06	6.13E-06	1.98E-05	4.72E-02	4.23E-02	1.36E-01

[a] Minimum crater diameters in km for the crater size bins

[b] Mean crater diameters in km for the crater size bins

[c] Number of craters per diameter bin

[d] Lower and upper limits of counts at 90% confidence level in Poisson distribution

[e] Uncertainty given by the lower and upper limits of counts at 90% confidence level in Poisson distribution

Table 3.2. Divalia Fossae crater size-frequency data that includes uncertain craters. (Area = 22016 km^2)

D_a [a]	D_c [b]	n[c]	10.00% [d]	90.00% [d]	Differential			Relative		
					$F(D_c)$	-[e]	+[e]	R	-[e]	+[e]
0.5	0.5946	882	845.60	918.40	1.93E-01	7.98E-03	7.98E-03	3.73E-02	1.61E-03	1.61E-03
0.70711	0.8409	875	838.75	911.25	1.36E-01	5.62E-03	5.62E-03	6.42E-02	2.98E-03	2.98E-03
1	1.189	641	609.97	672.03	7.03E-02	3.40E-03	3.40E-03	7.87E-02	4.67E-03	4.67E-03
1.4142	1.682	438	412.35	463.65	3.40E-02	1.99E-03	1.99E-03	9.78E-02	7.61E-03	8.16E-03
2	2.378	262	241.48	283.99	1.44E-02	1.13E-03	1.21E-03	1.08E-01	1.13E-02	1.24E-02
2.8284	3.364	166	149.72	183.76	6.44E-03	6.31E-04	6.89E-04	1.31E-01	1.75E-02	1.97E-02
4	4.757	71	60.44	83.07	1.95E-03	2.90E-04	3.31E-04	8.56E-02	1.96E-02	2.42E-02
5.6569	6.727	31	24.11	39.43	6.01E-04	1.34E-04	1.63E-04	1.00E-01	2.96E-02	3.90E-02
8	9.514	7	3.89	11.77	9.59E-05	4.26E-05	6.54E-05	8.26E-02	3.67E-02	5.63E-02
11.314	13.45	4	1.74	7.99	3.88E-05	2.19E-05	3.87E-05	9.43E-02	5.32E-02	9.42E-02
16	19.03	1	0.11	3.89	6.85E-06	6.13E-06	1.98E-05	4.72E-02	4.23E-02	1.36E-01

[a] Minimum crater diameters in km for the crater size bins

[b] Mean crater diameters in km for the crater size bins

[c] Number of craters per diameter bin

[d] Lower and upper limits of counts at 90% confidence level in Poisson distribution

[e] Uncertainty given by the lower and upper limits of counts at 90% confidence level in Poisson distribution

Table 3.3. Saturnalia Fossae crater size-frequency data with uncertain craters excluded. (Area = 10673 km^2)

D_a [a]	D_c [b]	n[c]	10.00% [d]	90.00% [d]	Differential			Relative		
					$F(D_c)$	-[e]	+[e]	R	-[e]	+[e]
0.5	0.5946	587	557.31	616.69	2.66E-01	1.34E-02	1.34E-02	5.58E-02	2.82E-03	2.82E-03
0.70711	0.8409	455	428.86	481.14	1.46E-01	8.36E-03	8.36E-03	8.65E-02	4.97E-03	4.97E-03
1	1.189	312	290.35	333.65	7.06E-02	4.90E-03	4.90E-03	1.19E-01	8.23E-03	8.23E-03
1.4142	1.682	255	234.76	276.71	4.08E-02	3.24E-03	3.47E-03	1.94E-01	1.54E-02	1.65E-02
2	2.378	152	136.43	169.05	1.72E-02	1.76E-03	1.93E-03	2.31E-01	2.37E-02	2.59E-02
2.8284	3.364	75	64.14	87.36	6.00E-03	8.69E-04	9.89E-04	2.28E-01	3.31E-02	3.76E-02
4	4.757	58	48.48	69.03	3.28E-03	5.38E-04	6.24E-04	3.53E-01	5.80E-02	6.72E-02
5.6569	6.727	26	19.72	33.84	1.04E-03	2.51E-04	3.13E-04	3.16E-01	7.65E-02	9.54E-02
8	9.514	11	7.02	16.60	3.11E-04	1.13E-04	1.58E-04	2.68E-01	9.69E-02	1.36E-01
11.314	13.45	4	1.74	7.99	8.00E-05	4.51E-05	7.98E-05	1.95E-01	1.10E-01	1.94E-01
16	19.03	2	0.53	5.32	2.83E-05	2.08E-05	4.70E-05	1.95E-01	1.43E-01	3.24E-01

[a] Minimum crater diameters in km for the crater size bins

[b] Mean crater diameters in km for the crater size bins

[c] Number of craters per diameter bin

[d] Lower and upper limits of counts at 90% confidence level in Poisson distribution

[e] Uncertainty given by the lower and upper limits of counts at 90% confidence level in Poisson distribution

Table 3.4. Saturnalia Fossae crater size-frequency data that includes uncertain craters. (Area = 10673 km^2)

D_a [a]	D_c [b]	n[c]	10.00% [d]	90.00% [d]	Differential			Relative		
					$F(D_c)$	-[e]	+[e]	R	-[e]	+[e]
0.5	0.5946	635	604.12	665.88	2.87E-01	1.40E-02	1.40E-02	6.04E-02	2.94E-03	2.94E-03
0.70711	0.8409	503	475.51	530.49	1.61E-01	8.79E-03	8.79E-03	9.57E-02	5.23E-03	5.23E-03
1	1.189	362	338.68	385.32	8.19E-02	5.27E-03	5.27E-03	1.38E-01	8.87E-03	8.87E-03
1.4142	1.682	285	263.59	307.88	4.56E-02	3.42E-03	3.66E-03	2.17E-01	1.63E-02	1.74E-02
2	2.378	180	163.03	198.44	2.04E-02	1.92E-03	2.09E-03	2.74E-01	2.58E-02	2.80E-02
2.8284	3.364	92	79.94	105.55	7.36E-03	9.64E-04	1.08E-03	2.80E-01	3.67E-02	4.13E-02
4	4.757	66	55.83	77.68	3.73E-03	5.75E-04	6.61E-04	4.02E-01	6.19E-02	7.11E-02

5.6569	6.727	30	23.23	38.32	1.20E-03	2.71E-04	3.32E-04	3.65E-01	8.24E-02	1.01E-01
8	9.514	16	11.14	22.45	4.52E-04	1.38E-04	1.82E-04	3.90E-01	1.18E-01	1.57E-01
11.314	13.45	7	3.89	11.77	1.40E-04	6.21E-05	9.54E-05	3.41E-01	1.51E-01	2.32E-01
16	19.03	3	1.10	6.68	4.24E-05	2.68E-05	5.20E-05	2.92E-01	1.85E-01	3.59E-01

[a] Minimum crater diameters in km for the crater size bins

[b] Mean crater diameters in km for the crater size bins

[c] Number of craters per diameter bin

[d] Lower and upper limits of counts at 90% confidence level in Poisson distribution

[e] Uncertainty given by the lower and upper limits of counts at 90% confidence level in Poisson distribution

Supporting Information

The supporting information and shapefile data of this paper are available at https://osf.io/79j26/.

CHAPTER 4

STRUCTURAL RELATIONSHIPS IN AND AROUND THE RHEASILVIA BASIN ON VESTA[4]

[4] Cheng, H. C. J. and Klimczak, C. 2022. *Journal of Structural Geology, 161,* 104677. Reprinted here with permission of the publisher.

Abstract

The Rheasilvia basin is an impact structure occupying most of Vesta's southern hemisphere. Divalia Fossae, a set of circum-equatorial troughs, were previously proposed to be concentric around the basin, which is widely regarded as evidence that the Rheasilvia impact directly caused the formation of the troughs. Here, I produce a structural map of Rheasilvia that allows for geologic interpretations and quantitative analyses of structure orientations and densities. I mapped basin-bounding scarps, scarps within the basin, ridges, and undefined lineaments. Scarps abound near the basin rim, with ridges being densely located on the basin floor near the central mound, forming a spiral pattern. This pattern is well-preserved on the basin floor except in the area superposing the older Veneneia basin, indicating that pre-existing Veneneia structures substantially influenced those of Rheasilvia. This implies that the lithosphere must have remained highly shattered after the Veneneia impact until Rheasilvia was emplaced. The Divalia Fossae cross-cut the Rheasilvia basin, and reanalysis of the geometric relationship between both landforms reveals that the troughs are not concentric around the basin center. These results are inconsistent with the previous hypothesis of trough formation and require a reconsideration of Vesta's tectonic history.

Introduction

Geology of the Rheasilvia Basin

The existence of a major impact basin on Asteroid 4 Vesta, hereon referred to as Vesta, was first hypothesized when Hubble Space Telescope observations revealed a large depression in the south polar region of the asteroid (Thomas et al., 1997). The Dawn mission to Vesta (Russell and Raymond, 2011) revealed that the basin is 450 km in diameter, which is ~85% of the mean diameter of the asteroid, and that it occupies a large portion of the southern hemisphere. The impact that formed the basin is thought to be the youngest global-scale impact on Vesta (Schenk et al., 2012), and it likely excavated sufficient crustal material to have created the Vestoid asteroid family (Marzari et al., 1996; Asphaug, 1997) and the howardite–eucrite–diogenite (HED) meteorites (McCord et al., 1970; Drake and Consolmagno, 1977).

The Framing Camera (FC; Sierks et al., 2011) aboard the Dawn spacecraft captured high-resolution images of the Rheasilvia basin (Roatsch et al., 2015), allowing the construction of a detailed digital terrain model (DTM; Figure 4.1; Preusker et al., 2016). The Rheasilvia basin is roughly hexagonal and outlined by discontinuous scarps (Figure 4.1; Schenk et al., 2012), with the most prominent one named Matronalia Rupes (Figure 4.1). No large melt sheet associated with the impact is observed, and its absence is interpreted to indicate a slow impactor (O'Brian and Sykers, 2011). Spacecraft observations also revealed a second large basin, Veneneia, that is partly superposed by the Rheasilvia basin. Veneneia is inferred to have a diameter of ~421 km (Figure 4.1; Jaumann et al., 2012; Marchi et al., 2012; Schenk et al., 2012). The basin rim of

Rheasilvia that superposes the Veneneia depression has a lower elevation when compared with those portions of the rim that fall outside this depression (Figure 4.1). This asymmetry was previously interpreted to be caused either by the pre-existing Veneneia topography (Collins et al., 2008) or by an oblique impact (Poelchau and Kenkmann, 2008).

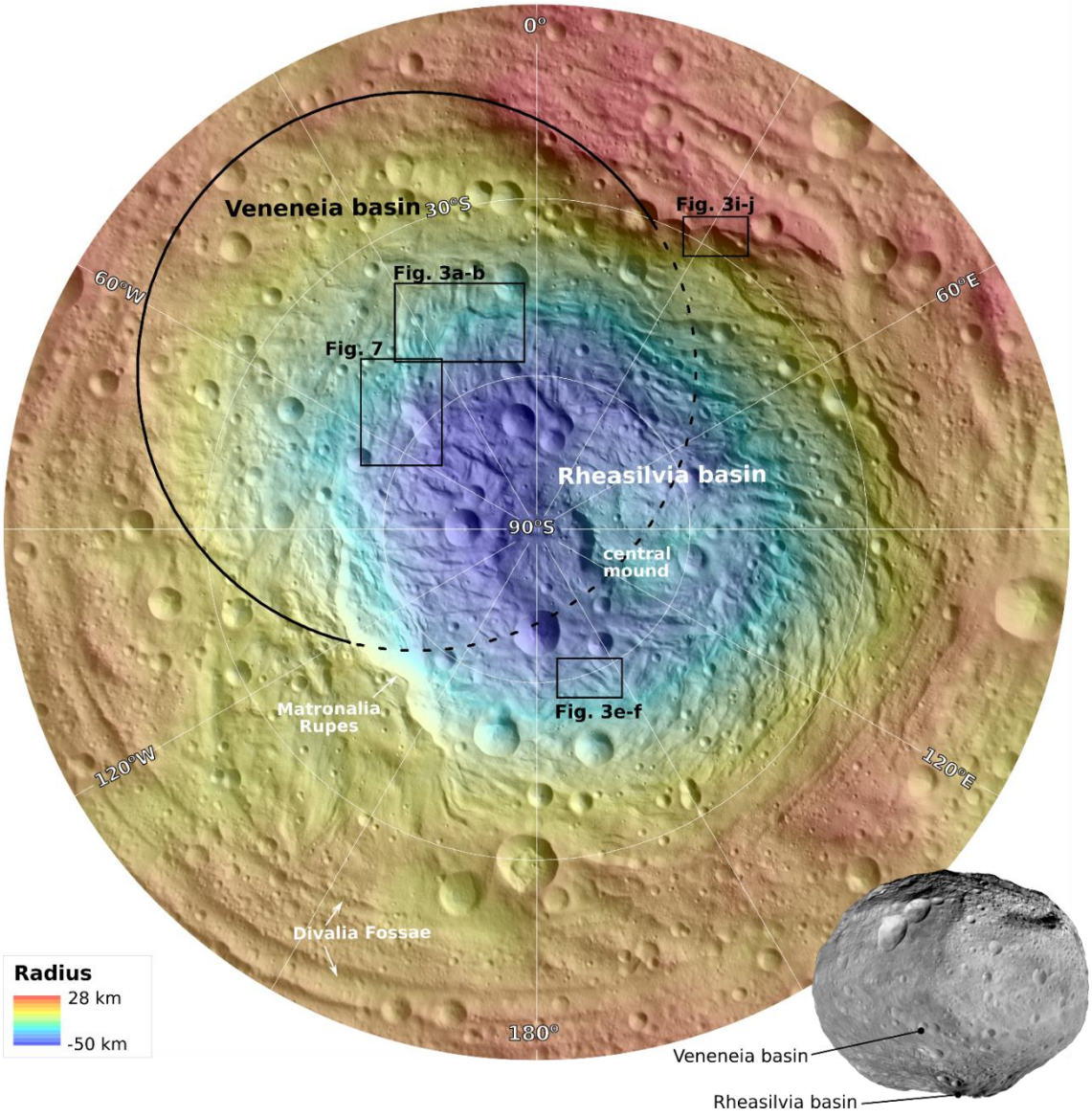

Figure 4.1. *Overview map of the Rheasilvia and Veneneia basins displayed as hillshade generated from the Dawn Digital Terrain Model (DTM; Preusker et al., 2016) with the*

solar azimuth of 56°E and incidence angle of 45°, color-coded by elevation in south polar stereographic projection. The reference elevation is defined to be the mean planetary radius of 262 km. The estimated circular basin rim of Veneneia basin is outlined with the preserved part as a black solid line and the part superposed by the Rheasilvia basin as a black dotted line. The location of the Divalia Fossae, the Rheasilvia central mound, and Matronalia Rupes are also indicated. For global reference, a Framing Camera image of Vesta is displayed at the lower right with the Veneneia and Rheasilvia basins labelled at the southern hemisphere.

Yingst et al. (2014) mapped terrains and structures of the Rheasilvia basin as part of the geological mapping effort of Vesta. The basin has a large central mound, a broad sloping basin floor with ridge-and-groove terrain, and mass-wasting materials. The irregular central mound (Figure 4.1) is bisected by structures aligned with the larger structural trend of the basin floor. The basin floor has curvilinear ridges, grooves, and inward-facing scarps of kilometers to tens of kilometers long and a few kilometers high. These structures form two pronounced trends with one sub-radial from the mound and another parallel to basin-bounding scarps, generating a pervasive spiral pattern within the basin floor (Figure 4.1; Schenk et al., 2012; Yingst et al., 2014). The spiral pattern was previously described as clockwise when measured from the basin center towards the rims (e.g., Schenk, et al., 2012; 2022).

Numerical modeling (Jutzi et al., 2013) and the prediction of mass motion related to the Rheasilvia impact on a fast-spinning asteroid (Otto et al., 2016) support the hypothesis that these structures are remnants of mass wasting that occurred during the original modification with their orientations influenced by the Coriolis effect (Schenk et

al., 2012; Otto et al., 2013; Jutzi et al., 2013). The observed spiral pattern is consistent with the prediction that deflections of materials moving from the basin rim towards the south pole during the modification stage, in which the horizontal component of the Coriolis effect should be to the left in the southern hemisphere under the rotational direction of Vesta (i.e., rotating counterclockwise as viewed from above the north pole). Mass-wasting materials were deposited along the bases of steep slopes and basin-bounding scarps, indicating the mobility of the regolith (Jaumann et al., 2012; Pieters et al., 2012). Several types of mass-wasting structures are identified within the Rheasilvia basin, including flow-like patterns, creep-like mounds (which are elongated positive-relief landforms with a straight or slightly curved shape), rotational slumping, landslides, and curved ridges (Otto et al., 2013).

Despite its large size, the geomorphology of the Rheasilvia basin is unlike those of large multi-ring impact structures on other terrestrial bodies, such as the Moon or Mercury (Melosh, 1989), but it is like large (complex) craters on low-gravity bodies with deep depressions and broad central mounds (Schenk et al., 2012). The spiral deformation pattern within the Rheasilvia basin is unique among large impact structures throughout the solar system in its size and preservation. Although these structures have been mapped at a large scale or locally in multiple works (e.g., Otto et al, 2013; Krohn et al., 2014; Yingst et al., 2014), a detailed structural map has not been constructed for the entire basin using a set of clearly defined and consistently applied mapping criteria. The basin is outlined by stratigraphic units in the geologic map from Yingst et al. (2014), but the rim and its center have yet to be defined by structural mapping and geometric analysis.

Basin relationship with Divalia Fossae

Dawn images also revealed the presence of two sets of large-scale troughs named Divalia and Saturnalia Fossae. The Divalia Fossae encircle about two-thirds of the asteroid at the equator, and their width ranges from several 100s of meters to 20.5 km. The Saturnalia Fossae are oriented northwest–southeast, and differ in orientation from the Divalia Fossae by approximately 30°. They are exposed only in the northern hemisphere, and their southern extent is truncated by the Divalia Fossae. The poles of planes defined along the Divalia and Saturnalia Fossae cluster near the centers of Rheasilvia and Veneneia impact basins, respectively, which is widely regarded as a genetic link between the troughs and basins (Jaumann et al., 2012; Scully et al., 2014; Schäfer et al., 2014). In particular, the impact that led to the emplacement of the Rheasilvia basin is proposed to have occurred at the south pole with no later reorientation of the asteroid (Karimi and Dombard, 2016) directly triggering the formation of the Divalia Fossae at the equator (Bowling et al., 2014; Stickle et al., 2015). Numerical experiments show that stresses from the impact shock wave were localized in the equatorial region and caused fracturing (Bowling et al., 2014; Stickle et al., 2015). The underlying fracturing mode that is responsible for the formation of the troughs was assumed to be normal faulting (Buczkowski et al., 2012), but the recent research points to an opening-mode or mixed-mode fracture origin of the troughs (Cheng and Klimczak, 2022). The scenario described here for the formation of the Divalia Fossae by the impact that formed the Rheasilvia basin is also invoked for the Saturnalia Fossa and Veneneia impact.

The geographic relationship of the poles of planes through the troughs clustering near the center of the basin is the only observation that suggests the formation of the

Divalia and Saturnalia Fossae were caused by the impacts that led to the emplacements of the Rheasilvia and Veneneia basins. The implication that arises from this scenario is that the troughs and basins must have formed simultaneously, specifically that the Divalia Fossae must have formed coevally with the Rheasilvia impact and the Saturnalia Fossae with the Veneneia impact. No cross-cutting relationships between the Divalia Fossae and Rheasilvia basin (and Saturnalia Fossae and Veneneia basin) that could provide relative ages have been documented, such that age relationships rely only on comparisons of crater frequencies on the two landform types (Cheng et al., 2021). Although the reported crater frequencies permit their simultaneous formation, large uncertainties allow for the Divalia Fossae to have formed well before or after the emplacement of the Rheasilvia basin (Cheng et al., 2021).

Moreover, stratigraphic relationships of the Rheasilvia basin with the geological units and structures in Vesta's northern hemisphere are mostly inferred from the assumed simultaneous basin formation with the Divalia Fossae. For example, the Divalia Fossae crosscut the Saturnalia Fossae and cratered highland units, which led to the inference that the Rheasilvia basin postdates these units in the global stratigraphy (Schäfer et al., 2014; Williams et al., 2014; Yingst et al., 2014). Any additional findings on the relative timing of troughs and basins, especially the Rheasilvia basin and Divalia Fossae will help better constrain the geologic history of Vesta.

The relationship between the Rheasilvia basin and Divalia Fossae plays an important role in determining the tectonic and, more broadly, the geological evolution of Vesta, as well as large impact structures on small bodies in general. That large impacts cause geologic activity far from the site of impact is not surprising, as antipodal focusing

of seismic waves and ejecta is widely hypothesized to trigger volcanism or tectonics (e.g., Schultz and Gault, 1975; Williams and Greely, 1994; Schultz and Crawford, 2011; Meschede et al., 2011). On Vesta, ancient cratered highlands and small-scale linear depressions are present near the north pole at the antipode of the Rheasilvia impact (Blewett et al., 2014), but large-scale troughs or other tectonic or volcanic phenomena are absent at the antipode (Bowling et al., 2013). "Hilly and lineated terrains" that are found at the antipodes of large basins on the Moon and Mercury (e.g., Schultz and Gault, 1975; Murray et al., 1974; Melosh and McKinnon, 1988) are also absent at the Rheasilvia or Veneneia antipodes.

Numerical studies reveal that troughs, grooves, or other lineaments could be formed by a large impact on small bodies (Asphaug et al., 1996; Benz and Asphaug, 1994), with observations on asteroid Ida corroborating this finding. However, grooves and lineaments on Ida occur in the antipodal region of a large impact structure. Prominent grooves not at the antipode of impact structures, such as those on Mars' moon Phobos, are unlikely to have an impact origin (Wilson and Head, 2015). That the Divalia Fossae are tied to an impact structure but are not localized at the antipodal region but instead at 90° from the impact distinguishes them from the Moon, Mercury, and other small bodies, and leaves open the question of why they are localized in the equatorial region of Vesta.

Goals of the study

Basin-bounding and intra-basin structures of the Rheasilvia basin have yet to be systematically and consistently mapped and described in detail using Dawn-derived photogeological datasets. A detailed structural map that documents the distribution of different structure types is the basis for analyses that assess cross-cutting relationships

among intra-basin structures as well as structural orientations and patterns. Cross-cutting relationships, orientations, and patterns of structures may reveal the deformation that took place during or after the basin was emplaced. Determining the structural outline of the Rheasilvia basin allows us to recalculate the basin center and reassess its location with respect to the Divalia Fossae. This work aims to (1) produce a detailed structural map of the Rheasilvia basin using consistent and rigorous mapping criteria, (2) quantify the orientations and pattern of basin structures with length-weighted rose diagrams in regional bins, (3) analyze the density of each type of structures and their relationships within the basin, (4) assess the cross-cutting relationships among the intra-crater structures and other structures, including impact craters and the Divalia Fossae, and (5) determine the geographic relationship of the Rheasilvia basin and the Divalia Fossae. These results will contribute towards understanding the post-emplacement Rheasilvia basin and global tectonics on Vesta.

Methodology

Structural map production and quantitative analyses

I conducted structural mapping on the HAMO-based Dawn FC clear filter image mosaic that has an average resolution of 60 m/pixel (Roatsch et al., 2015). I complemented the image mosaic by calculating several hillshade maps with the shade function in the open-access USGS software ISIS3 from the ~70 m/pixel DTM (Figure 4.1; Preusker et al., 2016). The mapping was assisted with topographic profiles in *ESRI's ArcGIS software*. The topographic expression of a structure is distinctly shown when the structure is perpendicular to the source of illumination on the hillshade. To capture all

basin structures, I computed four hillshades for different solar azimuths (Figure 4.2), including 56°E, 146°E, 124°W, and 34°W, with a fixed zenith of 45° for all hillshades.

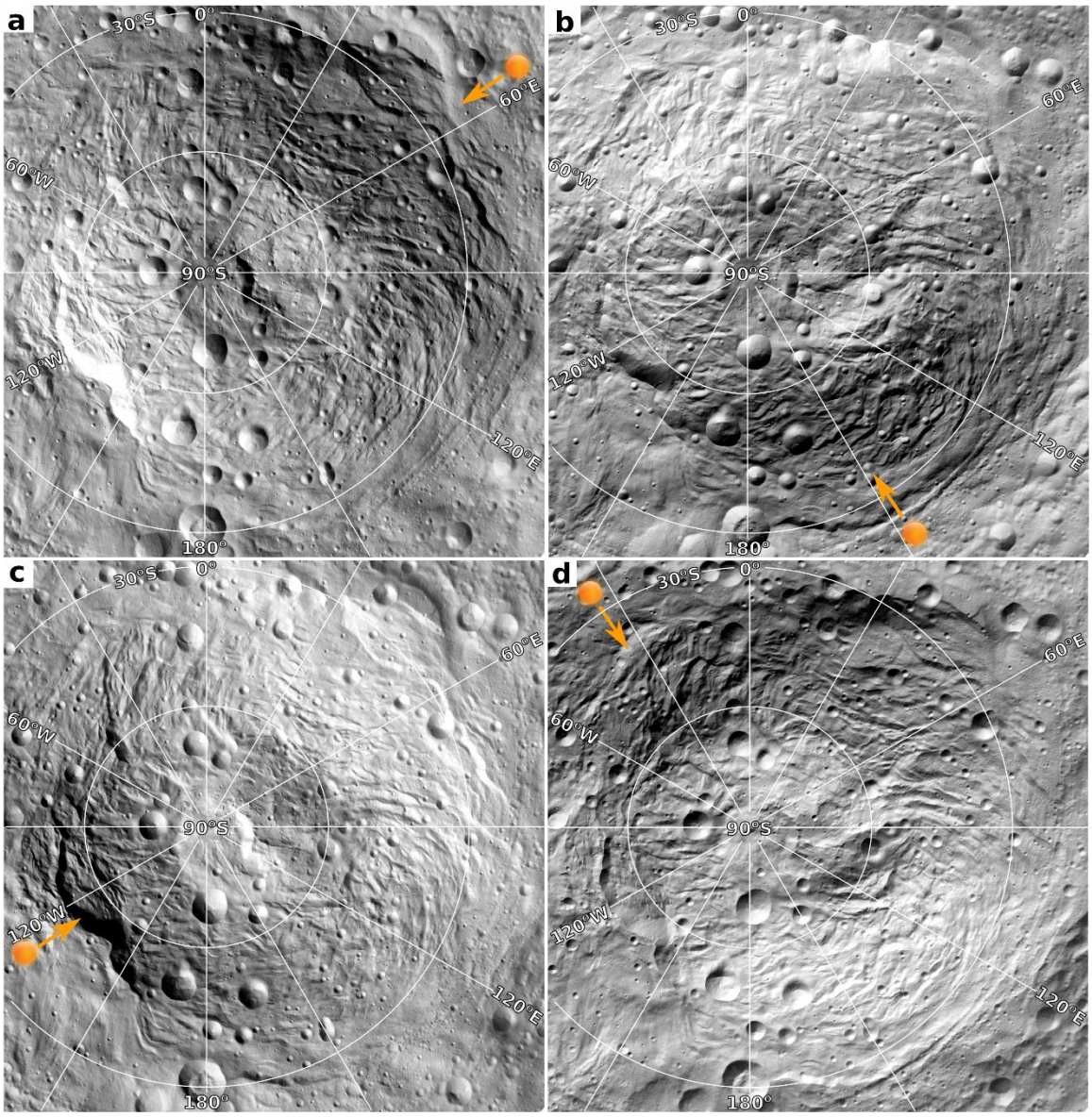

Figure 4.2. *Hillshade maps of Rheasilvia Basin generated from the Dawn Digital Terrain Model (DTM) with four azimuths (the angular directions of the sun) and a fixed solar incidence angle of 45°. The four azimuths I used include (a) 56°E, (b) 146°E, (c) 124°W, and (d) 34°W, which correspond to 0°, 90°E, 180°, and 90°W, respectively, in the original Claudia coordinate system for Vesta. The illumination direction is shown with*

an orange circle on each of the hillshades. The hillshades are in south polar stereographic projection.

These datasets were projected to a south-pole stereographic projection using a 255-km-diameter sphere model. I used the Claudia Double-Prime system (Li et al., 2012; WGCCRE., 2014), a coordinate system for Vesta adopted by the International Astronomical Union (IAU) Working Group on Cartographic Coordinates and Rotational Elements (WGCCRE) since 2014[5], which assigns a positive longitude of 146° to the Claudia crater. Literature prior to that (e.g., Roatsch et al., 2012; Russell et al., 2012) use the ‘‘Claudia’ system (the original coordinate system for Vesta), in which the longitude of Claudia crater is assigned as 0°.

Three types of basin structures were mapped based on their topographic expressions (Figure 4.3), specifically *scarps*, *ridges*, and *undefined lineaments*, which I define below. Basin structures were previously described as ridges, grooves, and scarps (see section 4.1.1. of this manuscript), with grooves being defined by the depressions between two ridges or two oppositely down-dipping scarps; thus, they are not included as a separate type of structure in this study. Apart from ridges and scarps, the surface texture of the basin is also defined by densely intersecting lineaments visible on the FC imagery, which have not been mapped before and are therefore included in the mapping.

Scarps are here defined as long and narrow linear structures that display a sharp topographic break. The scarp surface appears to be distinctively bright when facing the sun and is in the shade when facing away from the sun (Figures 4.3a, b). All scarps were mapped by placing a polyline along the top of the continuous sharp topographic break as shown in the topographic profile (Figure 4.3c) and presented using map symbols with the

[5] https://www.iau.org/news/announcements/detail/ann14003/

tick marks indicating the downslope direction (Figure 4.3d). I designated the most prominent scarps that define the edge of the Rheasilvia basin as *basin-bounding scarps*. These scarps are meaningful for outlining the basin perimeter, and they help define the basin center.

Ridges are defined as long, narrow, positive-relief structures. The slope facing the illumination appears as a bright surface that gradually darkens as the slope becomes less steep near the crest with the opposite slope being in the shade or less illuminated (Figures 4.3e, f). Continuous ridge crests are identified (Figure 4.3g) and traced in the mapping (Figure 4.3h) using map symbols with a pair of arrows pointing away from one another indicating the downslope of the two sides of the ridge. *Undefined lineaments* are linear structures on the FC images (Figure 4.3i), but they are too fine to display any characteristic topographic properties in the hillshades or topographic profiles (Figures 4.3j, k). These structures were mapped entirely based on the FC imagery (Figure 4.3l).

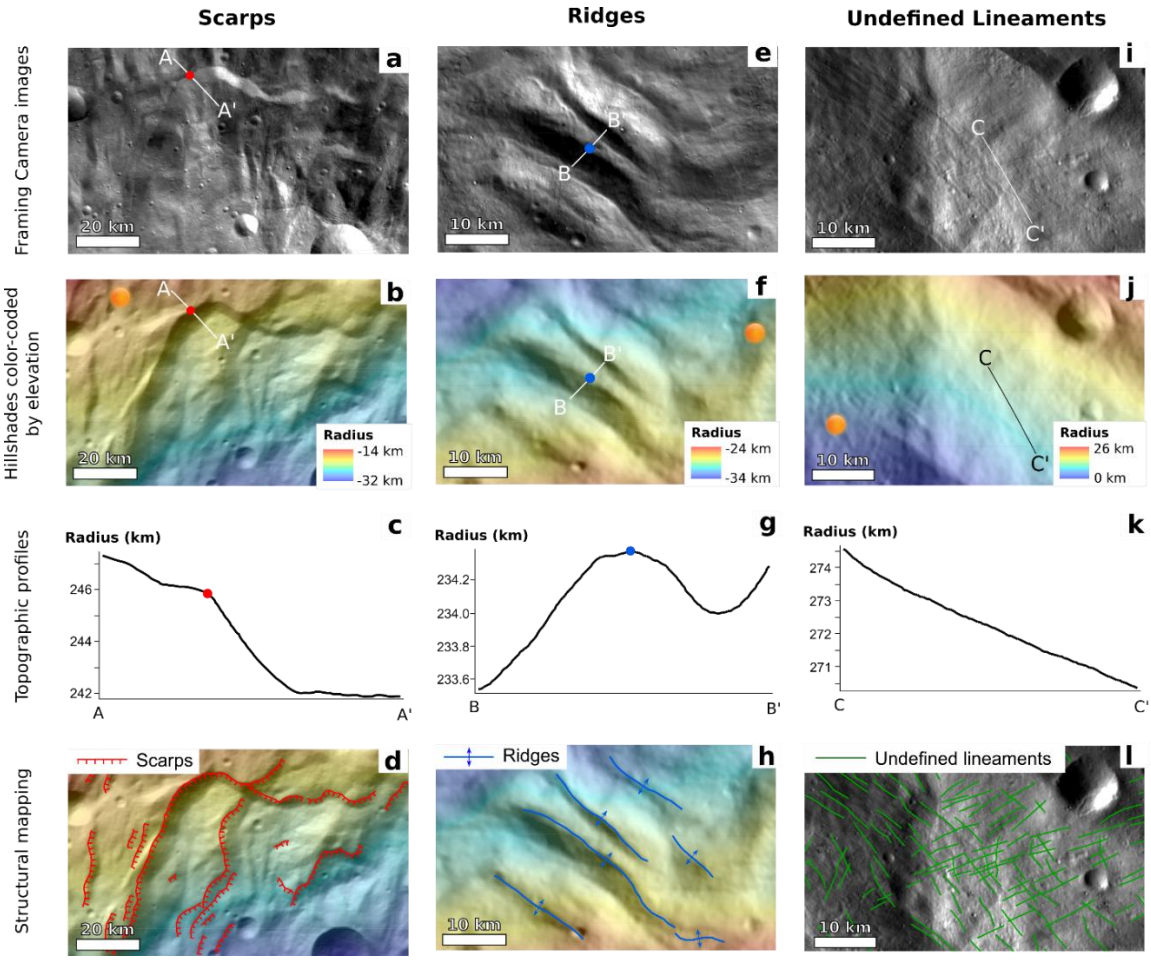

Figure 4.3. *Identification and classification of basin structures based on FC image, hillshades, and topographic profiles with examples of mapping. An example of scarps as seen in (a) FC images and (b) hillshades (with the azimuth of 34°W from Figure 4.2d) color-coded by elevation. (c) Topographic profile A-A' across a scarp displays a sharp topographic break, marked by a red dot. The location of the profile is labeled in (a) and (b) and the point of the topographic break is also indicated as red dot in the profile. (d) Map of scarps. An example of ridges in (e) FC images and (f) hillshades (with the azimuth of 56°E from Figure 4.2a) color-coded by elevation. (g) Topographic profile B-B' across a ridge displays positive relief with its crest marked by a blue dot. The location of the profile is labeled in (e) and (f) with the ridge crest also marked with blue dots. (h)*

Ridges are mapped on the hillshade by tracing their crests. Examples of undefined lineaments in (i) FC images and (j) hillshades (with the azimuth of 124°W from Figure 4.2c) color-coded by elevation. These lineaments are visible on the FC image in (i) but are barely recognizable or invisible on the hillshade in (j). (k) Topographic profile C-C' displays no distinctive topographic properties of these lineaments. The location of the profile is labeled in (i) and (j). (l) Undefined lineaments are mapped on the FC image. All images are in south pole stereographic projection. The reference elevation is defined to be the mean planetary radius of 262 km. Refer to Figure 4.1 for the locations of the examples.

All structures are mapped at a fixed map scale of 1:200,000 as polylines with regularly spaced vertices set to 1 km by using the streaming function of the ArcMap Editor to ensure equal and consistent sampling for orientation and spatial density analyses in this work. The structural map is provided as supplementary shapefiles that can be viewed and edited in an ArcGIS environment. I analyzed the orientations and densities of each type of structure within the basin. The detailed methods of these analyses will be elaborated on in the respective sections of this paper (see sections 4.3.2 and 4.3.3).

Determination of the basin and troughs configurations

To determine the geographic relationship of the Divalia Fossae and the Rheasilvia basin, I need to determine the planes defined by the troughs and compare their poles with the previously calculated basin center. I used the dataset from Cheng and Klimczak (2022), which includes maps of all 19 trough segments of Divalia Fossae. The planes of these troughs and their poles were calculated using *Stereonet 11* (Allmendinger et al., 2013; Cardozo and Allmendinger, 2013). I subsequently computed the ellipses of two

standard deviations (2σ) and three standard deviations (3σ) of the location of the poles, which are corresponding to 95% and 99.7% confidence intervals (CIs), respectively, using the built-in Kamb contouring function in *Stereonet 11*. These ellipses were compared with the location of the central mound and two center points for the Rheasilvia basin, including the calculated center in this study and the original one defined by Jaumann et al. (2012), who determined the center of the basin by fitting a perfect circle to the basin. An in-depth explanation of these methods is provided in section 4 of this paper.

Rheasilvia basin structures

Structural map

I mapped 30 prominent basin-bounding scarps equaling a total length of 1311 km, 563 scarps within the basin with a total length of 8586 km, 494 ridges with a total length of 5814 km, and 4393 undefined lineaments with a total length of 29340 km (Figure 4.4). I have also outlined the location of the central mound of the basin following outward-facing scarps that bound the local topographic high. In this mapping, I included the floors and rims of those impact craters with diameters greater than 20 km that were listed in the crater catalogue in Liu et al. (2018) to provide a full picture of the structures of the basin floor and to investigate cross-cutting relationships between the craters and structures. I also included the troughs and their bounding scarps of the Divalia Fossae from Cheng and Klimczak (2022) in the structural map of this research to explore their potential cross-cutting relationships with basin.

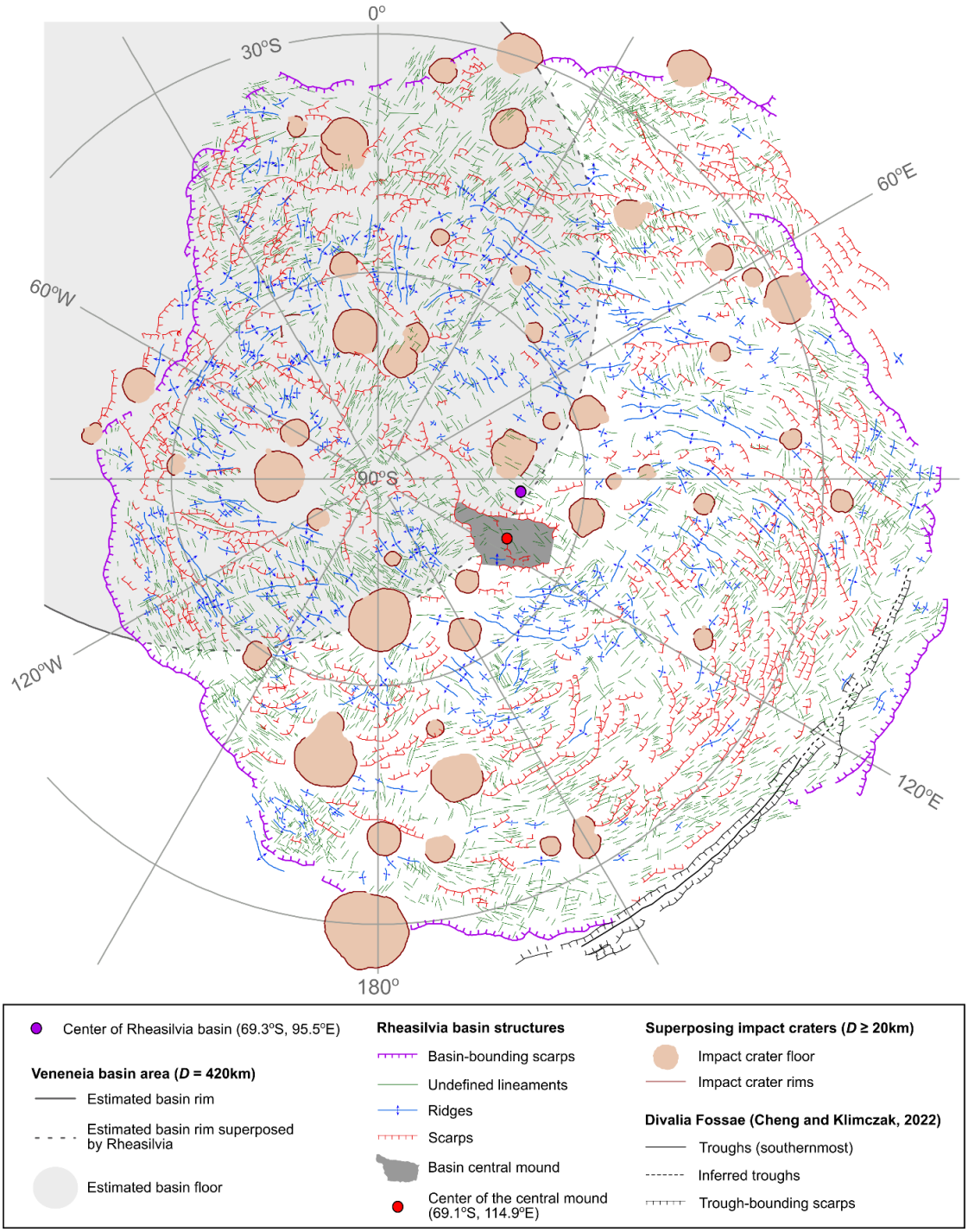

Figure 4.4. *Structural map of the Rheasilvia basin. The geometric mean center of the basin is calculated from the basin-bounding scarps and plotted as a purple dot. The geometric mean center of the central mound is calculated from the area outlined by*

scarps bordering the local topographic high in the basin center, it is displayed with a red dot. Refer to the text for the definition of structural map units. The map is in south polar stereographic projection.

The basin is asymmetrically hexagonal and outlined by basin bounding-scarps, consistent with previous study (Schenk et al., 2012). I calculated the geometric mean center of the basin based on the basin-bounding scarps and estimate it at 69.3°S and 95.5°E (Figure 4.4). The calculated center somewhat differs from the basin center of 75°S and 87°E of Jaumann et al. (2012), who defined the center by fitting a perfect circle to the basin structure and did not account for the true basin shape. Both centers are located near the central mound of the Rheasilvia basin. From the mapped outline of the central mound, I also calculated its geometric mean center to be located at 69.1^{o}S and 114.9^{o}E (Figure 4.4), which is very close but not coincident with the basin centers. I estimated the extent of the Veneneia basin that is superposed by the Rheasilvia basin as a circle using the three-point method in the *CraterTools plug-in* (Kneissl et al., 2011) by identifying three points along the preserved basin scarps. The resulting circular area has a ~420 km-diameter (Figures 4.1 and 4.4), consistent with the widely accepted estimated size of Veneneia basin (e.g., Jaumann et al., 2012; Marchi et al., 2012; Schenk et al., 2012).

Visual inspection of the mapped structures reveals a partly preserved clockwise spiral pattern of basin structures extending from the central mound to the rim (Figure 4.4). The pattern is most distinctly expressed by scarps and ridges, but some lineaments also follow the same structural trend on the Rheasilvia basin floor outside of the estimated area of the Veneneia basin floor. Scarps mostly face the basin center along and near the basin-bounding scarps. There, they show a pattern concentric to the basin center,

but they systematically deviate from this concentric pattern closer to the center of the basin. This pattern is the most distinct and systematic in the eastern part of the basin between 60°E to 150°E. The occurrence of ridges is sparse near the basin-bounding scarps at 0° to 60°E and 120°E to 180°, but they are densely distributed at the low-lying basin floor between the central mound and basin slope. Some ridges follow the spiral pattern of the scarps, such as the curved ridges observed at 60°E to 120°E. The pattern of scarps and ridges is less systematic at the western part of the basin at 30°W to 120°W, which I attribute to pre-existing structure in the Veneneia basin (Figure 4.4). Although some undefined lineaments follow the orientations of scarps and ridges locally, they generally do not follow the spiral pattern.

Orientation of each type of structure

To assess the orientation of each type of structure, the basin was subdivided into bins using three concentric circles with radii of 100 km, 200 km, and 300 km from the calculated basin center. Those concentric bins were subdivided into 12 radial bins, resulting in 36 regional bins around the basin center. Length-weighted rose diagrams were plotted for the three types of structures in each bin to visualize their orientations across the basin to aid the assessment of the structural patterns (Figure 4.5).

The basin-bounding scarps are large concentric structures around the basin center as seen on both the structural map and rose diagrams (Figure 4.5a, b). Deviations from the concentric pattern are most pronounced in those parts of the Rheasilvia basin that superpose the Veneneia basin. The intra-basin scarps form a pervasive spiral pattern within the basin, especially near the basin-bounding scarps (Figure 4.5a). The rose diagrams quantitatively capture the spiral pattern with the scarps furthest from the basin

center showing distinctively concentric orientations, but their orientation increasingly and systematically deviates from this concentric orientation closer to the basin center (Figure 4.5b).

Ridges are less prominent than scarps, as they have shorter individual lengths and their pattern relative to the basin center is not as well defined as the scarps (Figure 4.5c). Overall, the ridges show concentric and, in a few places, radial orientations to the basin center with concentric orientations mostly near the basin-bounding scarps (Figure 4.5d). There are regional bins that show ridge orientations like those of the scarps (Figure 4.5b), but they do not form an obvious spiral pattern throughout the basin. The ridges between latitudes of 30^{o}S to 60^{o}S and longitudes of 0^{o} to 90^{o}E show a regional fabric trending roughly from east and west (Figure 4.5c). This pattern is also captured by the rose diagrams with a high density of ridge segments (Figure 4.5d).

Undefined lineaments are widely and densely distributed across the basin floor (Figure 5e). Most are relatively short compared to ridges and scarps, and they form no distinctive map patterns. Rose diagrams show that the undefined lineaments display preferred orientations in all regional bins (Figure 4.5f). There are regional bins that show radial and concentric patterns with respect to the basin center, but they do not form a consistent pattern across all bins, such that no systematic pattern is present throughout the basin. Some undefined lineaments between the latitudes of 30^{o}S to 60^{o}S and longitudes of 0^{o} to 90^{o}E mimic the regional fabric of ridges (Figure 4.5c) trending roughly from east and west (Figure 4.5e).

Lighting may potentially impose a bias on the detectability of structures. Where solar illumination is parallel to the structure, the contrast in illumination of the structure

is so low as to render the structure nearly invisible, whereas a structure approximately perpendicular to this direction is prominently visible on the FC images. The mapping of scarps and ridges was verified with hillshades created from multiple azimuths (Figures 4.2 and 4.3a-h), but the undefined lineaments could not be verified (Figure 4.3i-l). Thus, the preferred orientations of ridges and scarps have no or minimal lighting bias and can be accounted for by the tectonics of the basin. However, preferred orientations of undefined lineaments may be biased by the lighting of FC images, and they may not fully characterize the tectonics of the basin.

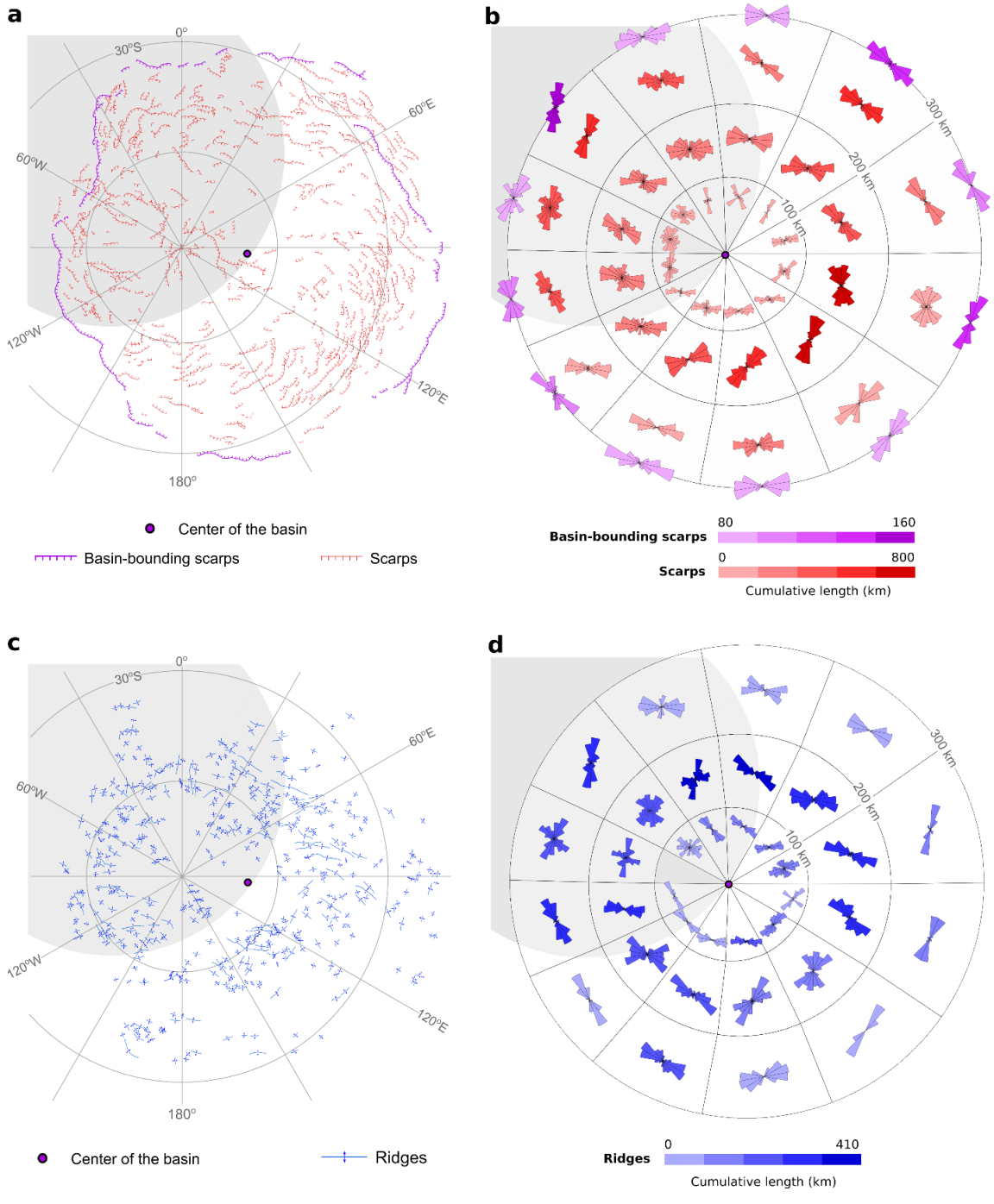
a
0°
30°S
60°E
60°W
120°W
120°E
180°
Center of the basin
Basin-bounding scarps
Scarps
b
300 km
200 km
100 km
80
160
Basin-bounding scarps
0
800
Scarps
Cumulative length (km)
c
0°
30°S
60°E
60°W
120°W
120°E
180°
Center of the basin
Ridges
d
300 km
200 km
100 km
0
410
Ridges
Cumulative length (km)

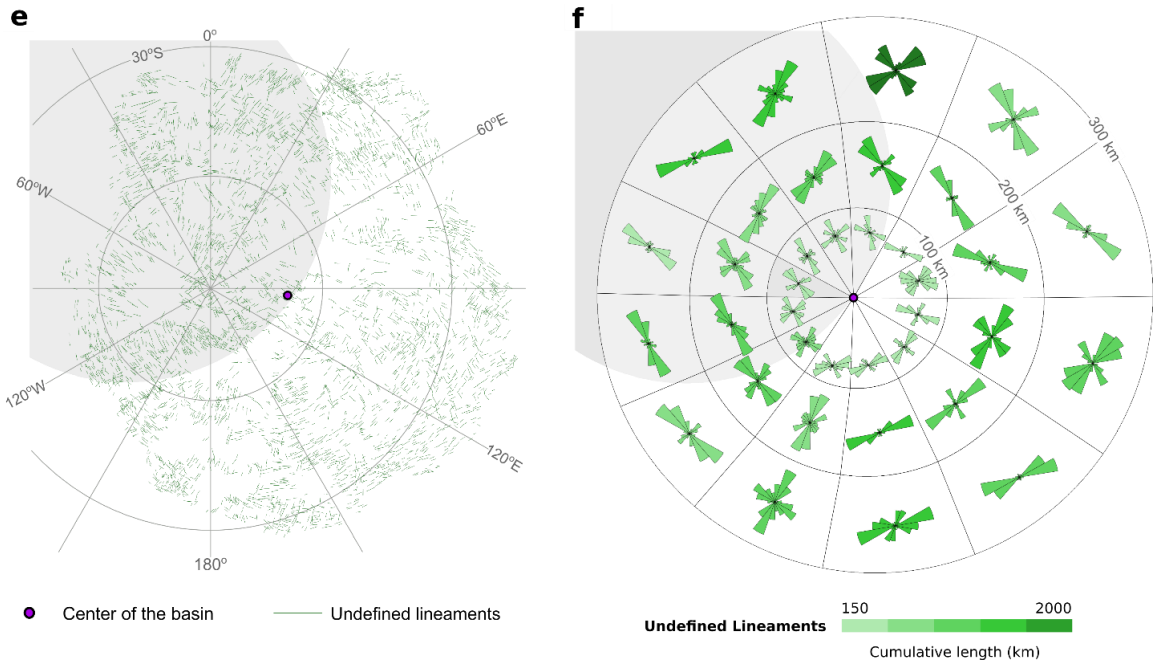

Figure 4.5. *Structural units shown on separate maps on the left with their orientations presented as rose diagrams on the right. The basin was binned by three concentric circles with radii of 100 km, 200 km, and 300 km from the geometric mean center of the basin (purple dot) and further divided by 12 lines radiating from the center with an equal angle of 30°, resulting in 36 bins (outlined in black). As with previous maps (Figure 4.1 and 4.6), the estimated Veneneia basin floor is shaded in grey. (a) Basin-bounding scarps (purple) and scarps as they occur in the basin (red). (b) Length-weighted rose diagrams are plotted for each bin, with color variation showing their cumulative lengths for the basin-bounding scarps in purple and scarps within the basins in red. (c) Ridges (blue) as they occur on the map. (d) Length-weighted rose diagrams of ridges are plotted for each bin, with variations of intensity of the blue indicating their cumulative lengths. (e) Undefined lineaments (green) as they occur on the map. (f) Length-weighted rose diagrams of the undefined lineaments are plotted for each bin, with the intensity of the*

green color indicating the cumulative lengths. All maps are in south polar stereographic projection.

Density of structures

I analyzed the density of each type of structure within the Rheasilvia basin. Each structure was split at its vertices into ~1 km long segments. The splitting ensures that longer structures are more prominently represented in the density calculation because longer structures will return more segments. The coordinate of the centroid of each segment was calculated, and the number of centroids per square kilometer was computed for each type of structure using the *Kernel Density Calculates function* in ArcMap, which calculates the density of point features around each output raster cell in an equal area stereographic projection. Basin-bounding scarps were not considered for this calculation, as they would weigh scarps more heavily along the basin boundary.

Basin structures are densely distributed across almost the entire basin floor. Some areas near post-Rheasilvia impact craters or at the downslope of scarps (e.g., Matronalia Rupes and the central mound-bounding scarps) show only undefined lineaments or no structures (Figures 4.4 and 4.6). These smoother areas are possibly covered with resurfaced materials produce by impacts or by landslides. The density of the scarps is highest between 80°E to 150°E along the latitude of 30°S. The scarps have a high density (dark red in Figure 4.6a) on the basin floor that slopes toward the basin center, where they are associated with the basin-bounding scarps, and they show a low density on the flat basin floor near the central mound (light red in Figure 4.6a).

Ridges show a low density near the central mound and near the basin-bounding scarps (light blue in Figure 4.6b) but they cluster between these two regions on the flat

basin floor (dark blue in Figure 4.6b), encircling the central mound. Hence, scarps and ridges show an opposite spatial distribution, with scarps densely located near the basin perimeter surrounding a group of ridges at the basin floor around the central mound (Figure 4.6a, b). Undefined lineaments show a less distinct pattern in their spatial density with some of them densely located near the basin-bounding scarps (Figure 4.6c). Regions of low structural density occur where superposed impact craters are recorded, and thus resurfacing has occurred and erased the expressions of this structure type.

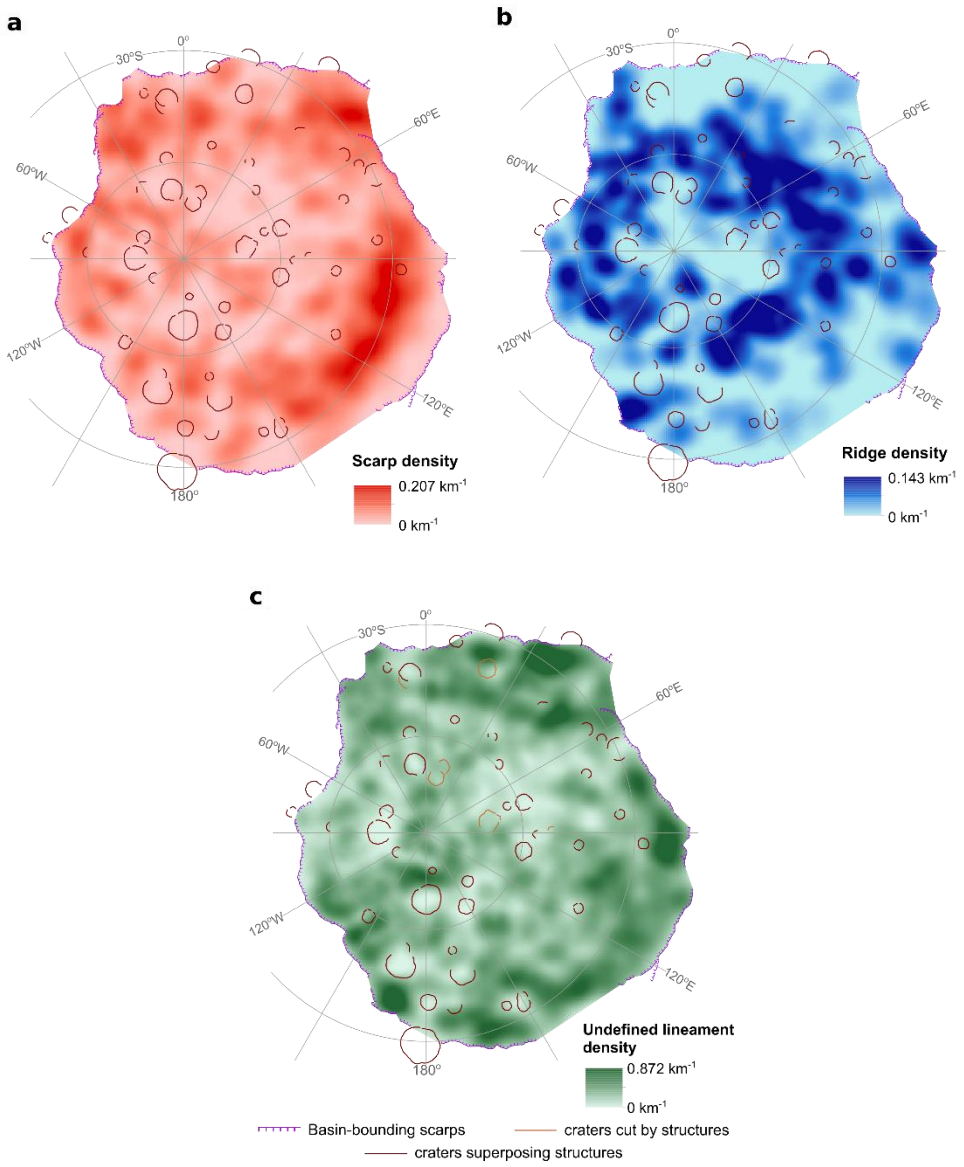

Figure 4.6. *Structure density maps shown for (a) scarps in red, (b) ridges in blue, and (c) undefined lineaments in green across the Rheasilvia basin outlined by the basin-bounding scarps. Structural density is expressed in kilometers of structure length per square kilometers (km^{-1}) with darker colors representing a higher density across the basin. Rheasilvia basin-bounding scarps are shown in purple. The rims of post-Rheasilvia craters that superpose the structure type are outlined in dark brown, and those that are cut by the structure type are outlined in light brown. All impact craters superpose scarps and ridge in (a) and (b). Some impact craters are cut by undefined lineaments, whereas some impact craters superpose the undefined lineaments in (c).*

Cross-cutting relationships

The three types of structures in the Rheasilvia basin lack a systematic pattern of cross-cutting relationships. An example of an area displaying wide variation in cross-cutting relationships is shown in Figure 4.7. These relationships (all labeled in Figure 4.7c) include one basin-bounding scarp truncating a large scarp within the basin (1), that large scarp cutting smaller scarps (2) and ridges (3), and a ridge abutting that large scarp (4). Such mutually cross-cutting relationships are present across the entire basin floor (Figure 4.6), indicating that all these structure types formed simultaneously and not sequentially.

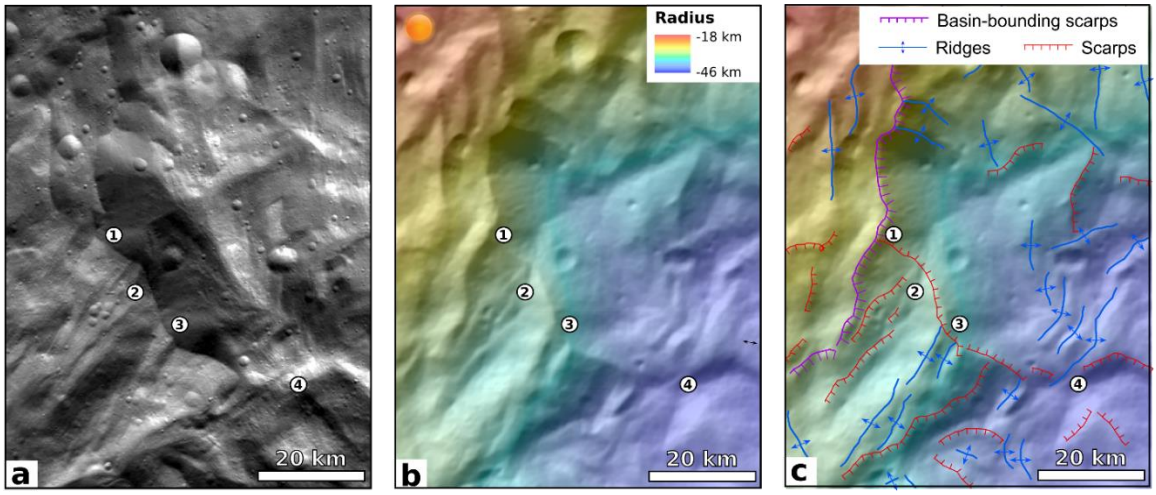

Figure 4.7. *A representative area showing multiple examples of cross-cutting relationships between basin-bounding scarps, scarps within the basin, and ridges labeled by numbers. (a) FC image and (b) hillshade color-coded by elevation of an area displaying complex cross-cutting relationships of structures, including (1) a basin-bounding scarps cutting scarps within the basin, a large scarp cutting (2) smaller scarps and (3) ridges, and (4) a ridge cutting a scarp. No systematic cross-cutting relationships among the different structural units are observed across the basin. The images are in south pole stereographic projection. The reference elevation is defined to be the mean planetary radius of 262 km. Refer to Figure 4.1 for the image location.*

Scarps and ridges are in all cases superposed by impact craters (Figure 4.4), indicating that the structures were formed before any of the craters were emplaced. Most undefined lineaments are also superposed by impact craters, and only 34 out of 4393 of the lineaments (0.77%) cross-cut crater floors (Figure 4.4). This shows that most lineaments were formed before the emplacement of the craters, but also that their formation continued locally for some time.

The southernmost trough belonging to the Divalia Fossae cuts the Rheasilvia basin-bounding scarps and lies partly within the basin. The relationship is most obvious in the hillshade images (Figure 4.2b, d) that differ the most in illumination conditions as compared to the natural lighting in the FC images. The trough is not cut by any of the scarps and ridges, but it is cut by undefined lineaments (Figure 4.4). That the trough cuts the basin-bounding scarp and basin floor but is not cut itself by scarps and ridges indicates that the trough formed after the emplacement of the Rheasilvia basin and after the formation of all major basin interior structures. This heretofore unrecognized cross-cutting relationship adds crucial information to the interpretation of the origin of the troughs. I will explore the basin and trough relationship in the next section.

Spatial Relationship of Rheasilvia basin and Divalia Fossae

With no cross-cutting relationships previously described, the Rheasilvia basin and Divalia Fossae were widely considered to be genetically linked because of the spatial correlation of the basin center with the poles to vertical planes projected through the troughs. I have plotted the Divalia Fossae and their associated pit-crater chains from Cheng and Klimczak (2022) with the Rheasilvia basin-bounding scarps and basin center of this study (Figure 4.4). This map highlights the spatial relationship of the basin and throughs that include the southernmost trough of the Divalia Fossae cutting into the Rheasilvia basin. This newly recognized cross-cutting relationship suggests that this trough was formed after the emplacement and modification of Rheasilvia basin.

The series of parallel troughs of the Divalia Fossae were recognized as parts of a single structure with a common origin (e.g., Buczkowski et al., 2012; Jaumann et al., 2012; Scully et al., 2014; Schäfer et al., 2014). Furthermore, all of the major troughs are

consistent with one another with regards to their map patterns and degradation (Cheng and Klimczak, 2022). They are all superposed by impact craters with no pre-existing craters within the troughs (Cheng et al., 2021). These observations suggest that the series of troughs were formed at the same time. Taking together this timing relationship and the cross-cutting relationship between the Divalia Fossae and Rheasilvia basin, the entire Divalia Fossae structure has to be formed after the emplacement and modification of the Rheasilvia basin.

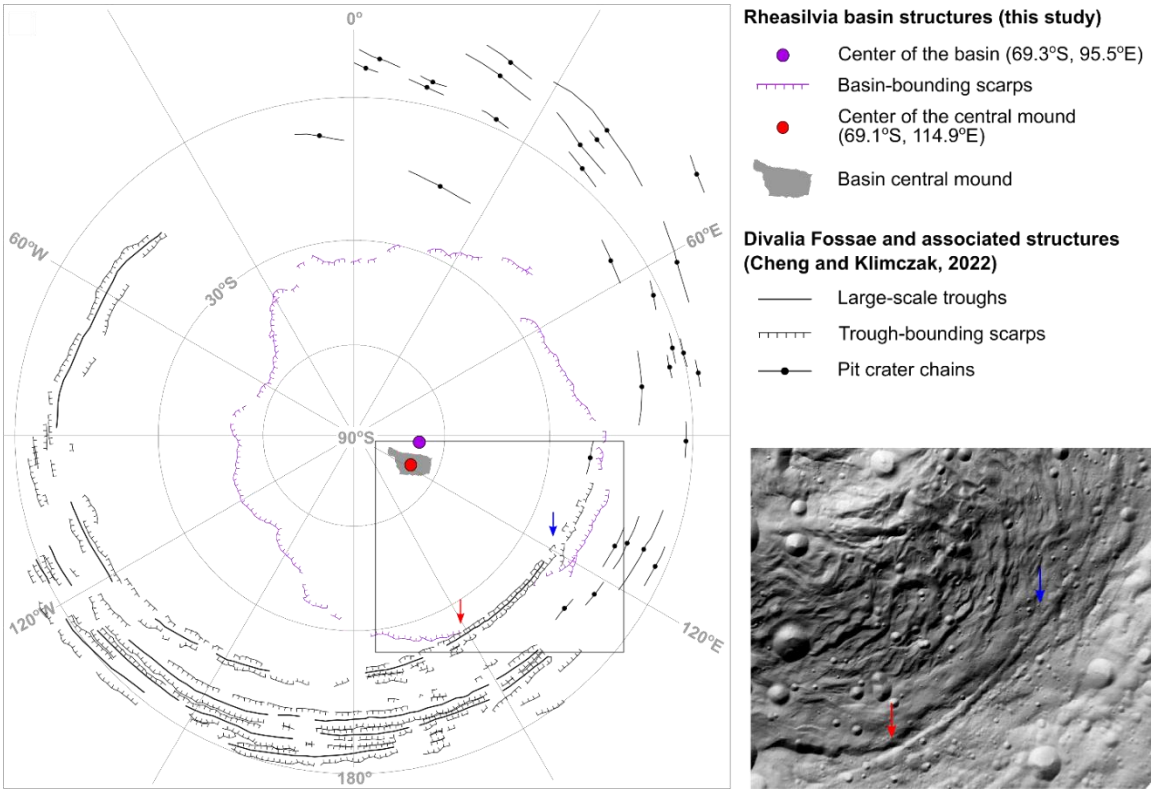

Figure 4.8. *Structural map (left) and hillshade (right) showing the basin-bounding scarps of the Rheasilvia basin with Divalia Fossae mapped by Cheng and Klimczak (2022). The southernmost trough is cutting the basin-bounding scarps (marked with a red arrow) and lying within the basin (marked with blue arrow). The geometric mean center of the basin is plotted on the map with a purple dot to show its configuration with Divalia*

Fossae. The outline of the central mound is shaded in grey with its geometric mean center plotted as a red dot. Pit-crater chains associated with the troughs on Vesta are also shown on the structural map. The hillshade image (with the azimuth of 146°E from Figure 4.2b and its extent outlined in black lines on the structural map on the left) captures the cross-cutting relationship of the southernmost trough of Divalia Fossa and the Rheasilvia basin-bounding scarps with the red and blue arrows. Refer to Figures 4.1 and 4.2 for the hillshade and elevation data.

The Divalia Fossae do not show an obvious concentric arrangement around the Rheasilvia basin center nor the central mound when viewed in stereographic projection centered on the south pole (Figure 4.8). To better evaluate their arrangement, I determined the planes defined by the Divalia Fossae using two methods and plotted their poles with respect to the basin centers on an equal-area stereonet (Figure 4.9). *Method 1* follows the procedure described in Jaumann et al. (2012), in which the planes defined by the troughs are assumed to be vertical, cutting through the center of the asteroid. The orientations of the planes located at the center positions of each of the trough segments are shown as great circles in an equal area stereonet (Figure 4.9a). The poles of the trough-defined planes are clustered around the center of the stereonet, consistent with the result from Jaumann et al. (2012).

I plot the confidence interval ellipses of the poles of the troughs in shades of gray. The confidence interval ellipse describes the uncertainty inherent in the estimate of the pole position, and it represents the set of acceptable hypotheses. For example, if a basin center lies outside of a 95% confidence interval, it can be rejected (i.e., the difference is statistically significant) with 95% confidence. The two basin centers determined by

Jaumann et al. (2012) and this study, as well as the center of the central mound, all lie outside of the 95% confidence interval of these poles, but the south pole of Vesta lies within it. Therefore, the south pole can be regarded as consistent with the poles to the trough, but the basin center and center of the central mound cannot. Even for highly conservative 99.7% confidence intervals (corresponding to ± 3 standard deviations), the centers of the basin and central mound can be rejected as being consistent with the locations of the poles of the troughs.

Since the planes defined by the Divalia Fossae troughs may not cut through the center of the asteroid, I also use *Method 2*, which determines the planes defined by the troughs without the assumption that they cut through the center of the asteroid. The trough segments of Divalia Fossae belong to four main trough structures (Figures 4.9; Cheng and Klimczak, 2022), and I use those four structures to redefine the planes. To determine the circular shape that best fits each structure, I used the three-point method in the *CraterTools plug-in* (Kneissl et al., 2011) that has a built-in projection correction by identifying the starting, middle, and ending points along the four structures. These circular planes are represented as small circles on an equal-area stereonet (Figure 4.9b), showing that these planes do not cut through the center of the asteroid. I calculated the center locations of these circular planes to plot their poles. The poles of the trough-defined planes cluster near the center of the stereonet, which coincides with Vesta's south pole. Like the results for *Method 1* (Figure 4.9a), the two basin centers and the center of the central mound all lie outside of the 95% confidence interval of the poles, but the south pole of Vesta lies within it. Even for highly conservative 99.7% confidence intervals, the centers of the basin and central mound can be rejected as being consistent

with the poles of the troughs. The basin center from Jaumann et al. (2012) lies just within the 99.7% confidence ellipse but close to the margin. As such, the observed poles to the troughs are inconsistent with the locations of the basin and central mound centers, but they are consistent with the south pole.

Troughs and basin-bounding scarps indicate that the Divalia Fossae are not concentrically arranged around the Rheasilvia basin center or around its central mound (Figure 4.8). Furthermore, the structural analysis indicates that the basin center does not fall within the 95% confidence limit of the poles of the troughs, irrespective of the method used to determine the poles of the troughs and what coordinates define the basin center. As such, the locations of the poles to the troughs are inconsistent with the Rheasilvia basin center. These lines of evidence indicate that the Rheasilvia basin and the Divalia Fossae do *not* show a clearly defined spatial relationship with one another.

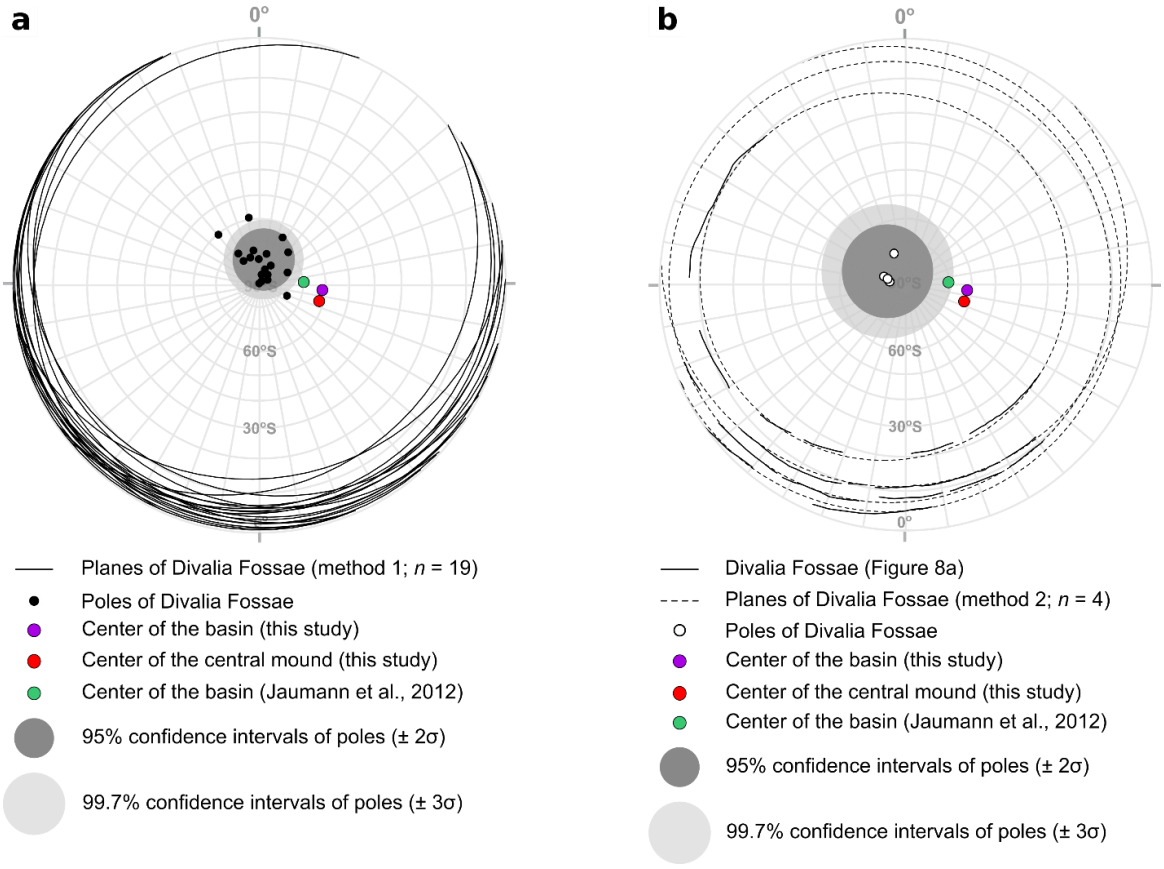

Figure 4.9. Equal area south pole projection stereonet showing the configuration of the Rheasilvia basin and Divalia Fossae. (a) The configuration of the Rheasilvia basin and Divalia Fossae is investigated using method 1 by Jaumann et al. (2012). Planes are defined by the center positions of the trough segments mapped by Cheng and Klimczak (2022), represented by great circles shown in black. The center of the Rheasilvia basin calculated in this study and from Jaumann et al. (2012) are plotted as purple and green dots, respectively. The center of the central mound calculated in this study is plotted as a red dot. The poles of the trough-defined planes are plotted in black. Confidence ellipses corresponding two standard deviations (95% confidence interval (CI)) and a very conservative three standard deviations (99.7% CI) of these poles are calculated and highlighted in dark grey and light grey, respectively. (b) The configuration of the

Rheasilvia basin and Divalia Fossae is investigated by defining small circles of the main trough structures (method 2). The 19 trough segments of Divalia Fossae (black lines) belong to four main structures (Cheng and Klimczak, 2022). The planes that best fit each of the four structures are presented as small circles in dashed lines with their poles shown as white dots. The two standard deviations (2σ; 95% CI) ellipse and three standard deviations (3σ; 99.7% CI) ellipse of these poles are calculated and highlighted in dark grey and light grey, respectively. The reader is advised that I applied the new coordinate system used for Vesta updated in 2014[6], which is different from the one used by Jaumann et al. (2012). <2-column, color>

Discussion

Basin structures and their formation processes

The structural map of the Rheasilvia basin presented in this study (Figure 4.4) allows us to conduct spatial analyses and assessments of the orientation of several types of structures in and around this large impact structure. These results of the analyses have implications for the geologic processes that took place within the basin. Basin-bounding scarps, such as Matronalia Rupes, are interpreted as the main scarp resulting from major mass-wasting events (Otto et al., 2013). Numerous scarps within the basin represent ruptures along which slumping took place, with ridges in the front of the slump representing the toes of the slumping masses (Otto et al., 2013). This interpretation is consistent with the observation that the scarps facing the basin center are clustered near the basin-bounding scarps at the perimeter of the Rheasilvia basin (Figure 4.6a), and the spatial density of ridges is higher closer toward the basin center on the basin floor around

[6] https://www.iau.org/news/announcements/detail/ann14003/

the central mound (Figure 4.6b), displaying an anti-correlation in their spatial distribution. This indicates the mass movement of basin material from the basin rim towards the floor, which is likely caused by the gravitational collapse and modification during the modification stage of basin formation. This interpretation is supported by the detailed observations of the nature and orientations of mass-wasting landforms within the basin (Otto et al., 2013).

The scarps and ridges are mutually cross-cutting across the basin (Figures 4.4 and 4.7), indicating that there were mass-wasting events across the basin without a sequence of events or specific temporal order of the mapped structure types. Since the scarps and ridges are all superposed by impact craters inside the basin (Figure 4.4), they must have formed prior to the superposition of the impact craters, likely soon after the emplacement of the Rheasilvia basin, with most mass wasting being complete shortly after basin formation. Otto et al. (2013) reported young slides and slumps at the Matronalia Rupes scarp and suggested they demonstrate the ongoing collapse of the basin. However, I find that this interpretation is not representative of the majority of mass-wasting that occurred in the basin.

Scarps display a well-preserved spiral pattern between 60°E and 150°E, coinciding with the area that does not superpose the Veneneia basin floor (Figure 4.5a, b). The spiral pattern is consistent with previous works in as far as it is clockwise extending from the central mound to basin rim. One possible explanation for this structural pattern is that the curved structures are remnants of the basin-collapse process when materials moving from the rim to the floor radially were deflected by the Coriolis effect (Jutzi et al., 2013; Otto et al., 2013; 2016). Otto et al. (2016) interpreted the spiral

patterns as ‘curved ridges’ of materials deposited along the predominant slope from the basin rim to the floor during the basin modification stage. The velocities of mass movement derived along these ‘curved ridges’ were calculated by assuming they were caused by the Coriolis effect (Otto et al., 2016), which generally agrees with the predicted mass motion velocity from numerical simulations (Jutzi et al., 2013). These “curved ridges” on a large-scale map consist of scarps and ridges based on the structural map (Figure 4.4). If the scarps represent rupture during slumping and the Coriolis effect is responsible for the spiral pattern, the Coriolis force may not just deflect the movement of slumping materials but also influence the preceding rupture during basin collapse.

However, the spiral pattern of the Rheasilvia basin should be expected to extend from the south pole of Vesta under the Coriolis effect, instead of the center of the impact basin. From the preserved structures mapped, it is impossible to distinguish if the spiral pattern is centered around the south pole or the Rheasilvia basin (Figure 4.4). Schenk et al. (2022) reported that spiral patterns are common to complex craters on Moon, Mars, Mercury, Ceres, and other icy bodies, which are not located near the poles. As such, the Coriolis effect does not need to be invoked to form the spiral pattern on the Rheasilvia basin. The crater examples given by Schenk et al. (2022) range in diameter from 9 to 66 km, which are much smaller than the 450-km-diameter Rheasilvia basin, and they thus have much lower size ratios relative to their parent bodies. Furthermore, the reported spiral patterns in these smaller craters were selected from visual inspection without structural analysis and they are mostly partially preserved, as the crater floors are buried by impact melt and debris. Therefore, these craters are likely not analogous to the

Rheasilvia basin and its pervasive spiral deformation pattern, leaving the Rheasilvia spiral pattern as uncommon among large impact structures in the solar system.

The spiral pattern is not present at the western extent of the Rheasilvia basin, where it is estimated to superpose the Veneneia basin (Figure 4.4). Any pre-existing Veneneia basin structures likely substantially influenced the orientations of structures in the Rheasilvia basin. In this case, the Veneneia basin floor and its structures would have been planes of weakness during the Rheasilvia impact. Thus, Vesta's lithosphere must have been highly fractured by the Veneneia impact, and it remained highly fractured until the Rheasilvia basin was emplaced. Any fracture healing and fracture annealing caused by shock residual or interior heat is therefore unlikely to have occurred on the Veneneia basin floor. This absence is possible if the Veneneia basin formed from a low-velocity impactor, similar to that proposed for the Rheasilvia impact (O'Brian and Sykers, 2011). This scenario is consistent with the lack of a melt sheet associated with the Veneneia impact on the preserved part of the basin.

Origin of the Divalia Fossae

The Divalia Fossae are widely accepted to have formed directly by the impact that formed the Rheasilvia basin (e.g, Buczkowski et al., 2012; Jaumann et al., 2012; Scully et al., 2014; Schäfer et al., 2014; Williams et al., 2014; Yingst et al., 2014). This scenario solely relied on the geographic relationship that the Divalia Fossae showed with respect to the center of the Rheasilvia basin (Jaumann et al., 2012; Scully et al., 2014; Schäfer et al., 2014). And although numerical modeling of the Rheasilvia impact suggests that extension is expected at the equatorial region when invoking the presence of a ductile core and other specific interior characteristics (Bowling et al., 2013), it is unknown if

Vesta's interior properties are consistent with the modeling parameters and/or if the predicted extension is consistent with the magnitude of strain and orientation of the observed troughs. Thus, the collocation of the troughs and basin center remains the only direct geological support of the hypothesis.

The reassessment of this geographic relationship indicates with upward of 95% confidence that the geometric mean centers of the basin and central mound both are not co-located with the poles of the Divalia Fossae (Figure 4.9) and that a collocation with the south pole is more probable. This result establishes that the Divalia Fossae do not display a clearly defined geographic relationship with the Rheasilvia basin. Due to the interior heterogeneities, geometry of the impact, and/or deformation mechanics, the Rheasilvia basin center would not necessarily have to coincide with the poles of troughs for them to be genetically linked. But the lack of a clear collocation of the basin center and troughs weakens the sole argument on which the hypothesis, by which the basin-forming impact triggered the formation of the troughs of Divalia Fossae, is based on.

The previously proposed origin of the troughs is further challenged by the newly identified cross-cutting relationship that the Divalia Fossae and Rheasilvia basin-bounding scarps display. The southernmost trough of the Divalia Fossae cuts the basin-bounding scarp and lies partly within the basin without being crosscut by the scarps and ridges in the basin interior (Figures 4.4 and 4.8), indicating that the troughs must be formed after the emplacement and modification of Rheasilvia. The emplacement and immediate modification of the Rheasilvia basin were estimated to take place over approximately 2 to 3 hours (Jutzi et al., 2013; Ivanov and Melosh, 2013; Otto et al., 2016), which is when near-surface downhill mass motion of highly shocked and fractured

material occurred radially from the crater walls toward the basin floor (Schenk et al., 2012; Otto et al., 2013; Jutzi et al., 2013), also marking by the formation of the basin-bounding scarps. In contrast, typical earthquake rupture propagation rates of approximately 3 km/s (Stein and Wysession, 2003) imply that fractures that formed deep within Vesta from the Rheasilvia impact propagated to the surface after ~100–150 s (Stickle et al., 2015), but with seismic shaking affecting the surface possibly for hours. Following the results of these studies, the formation of Divalia Fossae, if indeed caused by the Rheasilvia impact, would have to take place before or within the same timeframe of the modification stage of the Rheasilvia basin, which contradicts the observed cross-cutting relationship. As no impact crater, other than the Rheasilvia basin, are observed to be cut by the Divalia Fossae (Cheng et al., 2021), the structures are also unlikely to have first formed with the basin but experienced a later joint or fault reactivation to cause the present cross-cutting relationship with Rheasilvia. Hence, these geologic observations suggest that it is likely for the Divalia Fossae to be formed after the basin modification stage, questioning the previously proposed impact-induced origin of the Divalia Fossae.

It is widely accepted that large impacts can form major structures at the antipodes (e.g., Schultz and Gault, 1975; Murray et al., 1974; Melosh and McKinnon, 1988); however, no such structures on Vesta and Divalia Fossae occur at the antipode. Modeling of the Rheasilvia impact predicts significant deformation at and near the impact antipode, however no definite evidence of that amount of deformation at the Rheasilvia antipode are found from the Dawn dataset (Bowling et al., 2014). Blewett et al. (2014) found that the cratered highland near the north pole of Vesta is likely to be a remnant of ancient crust formed before the Rheasilvia impact, and no large-scale troughs were observed

there. While several reasons may explain the lack of major antipode structures, such as weakened antipodal constructive interference of seismic waves due to an oblique impact, the non-spherical shape of Vesta, or the physical properties of the interior (Blewett et al., 2014), it remains an open question of how structures as large scale as Divalia Fossae could have formed away from the antipode yet be directly caused by the impact.

The Divalia Fossae are concentric around the south pole of Vesta and the south pole falls well within the 95% confidence ellipse of the poles to planes through the troughs (Figures 4.8 and 4.9), establishing a geographic correlation with Vesta's spin axis. The asteroid is spinning rapidly with a well-determined rotational period of 5.342 hours, and it has a marked equatorial bulge and polar flattening. An origin of the Divalia Fossae related to Vesta's rotation has previously been proposed, including changes in the spin rate of the asteroid and reorientation of the spin axis by the Rheasilvia impact (Schmidt, 2011). These hypotheses suggest the Divalia Fossae were formed by long-term consequences of asteroid tectonics after the Rheasilvia impact, which are permissible with the cross-cutting relationships shown here and previously derived age relationships from crater statistics (Cheng et al., 2021).

In particular, the crater statistics were derived for the Divalia Fossae and compared with those of the Rheasilvia basin to determine their relative age (Cheng et al., 2021). Although the reported crater frequencies permit a simultaneous formation of the two landforms, large uncertainties allow for the Divalia Fossae to have formed well before or after the emplacement of the Rheasilvia basin (Cheng et al., 2021). Since the southernmost trough of the Divalia Fossae cuts the basin-bounding scarp and lies partly

within the basin (Figures 4.4 and 4.8), the age of formation of the Divalia Fossae can be constrained to after the Rheasilvia basin was formed.

Crater-counting studies interpreted that the Rheasilvia basin formed at ~0.8 Ga to 3.5 Ga. Crater counting of the entire basin floor (Marchi et al., 2012; Schenk et al., 2012) estimated the basin age to be ~1 Ga and ~1.8 Ga, based on the Main Belt crater production function (O'Brien et al., 2007) and lunar-derived crater production function (Schmedemann et al., 2014), respectively. A different crater counting study (Schmedemann et al., 2014) produced a basin age of ~3.5 Ga. A recently updated crater count and interpretation of Rheasilvia suggests a much younger basin age of ~0.8 to 0.9 Ga (Schenk et al., 2022). If the Rheasilvia basin is indeed very young, the trough that crosscuts it must be even younger. However, the Divalia Fossae are heavily degraded (Cheng and Klimczak, 2022), which points against the young age interpretation of the Rheasilvia basin.

Hypotheses that would tie the tectonics of Vesta to long-term consequences of the Rheasilvia impact include the possibility of asteroid reorientation (e.g., Karimi and Dombard, 2016). In particular, the study numerically modeled the potential for relaxation of large south polar basins and a rotational bulge after the asteroid reoriented. The models predict that Vesta's lithosphere was too cold to permit the relaxation of basin topography and the rotational bulge at a time after basin formation, and thus reorientation of Vesta by the Rheasilvia impact was found to be unlikely (Karimi and Dombard, 2016). Alternatively, Mao and McKinnon (2020) suggested an increase in spin rate based on the scale and location of the Rheasilvia impact, which was suggested in this study to have played a role in forming the Divalia and Saturnalia Fossae. The specifics of this scenario

for the formation of the Divalia Fossae have yet to be investigated. The findings challenge the previously proposed origin of the Divalia Fossae, that they were caused directly and immediately by the Rheasilvia impact. Future studies may need to consider alternative hypotheses that satisfy the geographic, cross-cutting, and age relationships I presented here.

Conclusions

I have produced a detailed structural map of the Rheasilvia basin to characterize the various structures using rigorous mapping criteria with the aim of quantitively analyzing the orientations, densities, and cross-cutting relationships of these structures. The basin surface is dominated by scarps near the basin rim and ridges on the basin floor near the central mound. Scarps display a well-preserved clockwise spiral pattern extending from the central mound to basin rim in the eastern part of the basin, with some ridges locally following the same structural trend. This pattern was previously interpreted as modification of the basin by mass-wasting, influenced by the Coriolis effect during the basin modification and collapse. The scarps and ridges lack a clear systematic pattern in the area coinciding with the superposed Veneneia basin, indicating that pre-existing Veneneia structures substantially influenced the orientation of Rheasilvia-associated structures. This indicates that the lithosphere must have been shattered by the Veneneia impact, and that no healing and annealing occurred before the impact that formed the Rheasilvia basin.

The Rheasilvia basin structural map shows that the Divalia Fossae crosscut the basin-bounding scarps, which has not been previously recognized. Likewise, the configuration of the Rheasilvia basin and Divalia Fossae, in contrast to conclusions of

previous studies, show no clear geographic correlation. The cross-cutting relationship and configuration of the Rheasilvia basin and Divalia Fossae greatly challenge the widely accepted hypothesis that the Divalia Fossae were formed directly and immediately by the Rheasilvia impact. Taken together with previously established age relationships and the collocation of the poles of troughs with the south pole, the Divalia Fossae are more likely to have formed as a long-term consequence of the Rheasilvia impact tied to changes in rotation of the asteroid, supporting alternative hypotheses of an impact-induced change in spin rate or reorientation of Vesta. The relationships between the Divalia Fossae and Rheasilvia basin established here serve as geologic constraints that must be accounted for when assessing hypotheses that seek to understand the tectonic evolution of Vesta.

Acknowledgments

I thank the editor Fabrizio Agosta and two anonymous reviewers very much for their feedback on the earlier version of this paper. I also thank Steven Holland for his discussions on the statistical aspects of this research. The supplemental shapefiles of this manuscript are available at https://data.mendeley.com/datasets/bxbykxrk7h/1. I acknowledge and thank the NASA Dawn Mission, instrument teams at the Max Planck Institute, and stereo analysis team at German Aerospace Center (DLR) for the acquisition and processing of Dawn data used in this work. All used Dawn data in this study are archived in the NASA Planetary Data System. The original data used in this study are available from https://pds-smallbodies.astro.umd.edu/data_sb/missions/dawn/index.shtml.

CHAPTER 5

LATITUDINAL VARIATIONS IN STRUCTURE DOMINATE THE TECTONICS OF VESTA AND CERES[7]

[7] Cheng, H. C. J. and Klimczak. C To be submitted to *Icarus*.

Abstract

Polygonal impact craters (PICs) form where pre-existing structure exists in the impact target rock. The straight rim segments of PICs and their preferred orientations reveal hidden tectonic patterns that otherwise are invisible in spacecraft data. Vesta and Ceres are heavily cratered bodies that also experienced tectonics. I map crater rims on Vesta and Ceres and identify their straight rim segments. Most mapped craters on Vesta and all craters on Ceres have at least one straight rim segment and thus are considered PICs. Analyses of straight rim segment orientations reveal multiple fracture sets that form complex but systematic regional and global patterns on both bodies. In particular, I detect an E–W trending fracture pattern in Vesta's north polar region. Ceres has predominantly NE–SW oriented fractures in the northern hemisphere and NW–SE oriented fractures in the southern hemisphere, which are most pronounced at the poles. None of the patterns revealed by PICs correlate with the orientations of tectonic structures (i.e., large-scale troughs on Vesta or pit chains on Ceres) or large impact basins (e.g., Rheasilvia basin on Vesta), indicating that their origins are not directly linked. While both bodies are fast-spinning, their different tectonic patterns indicate that other factors or planetary processes must have controlled the formation of the pre-existing fractures or the straight rim segments of the impact craters. I attempted to compare the tectonic maps of Vesta and Ceres with the predicted tectonic pattern caused by the change in spinning rate, volume change (specifically for icy bodies), and true polar wander. However, literature do not account for the low-gravity and the other rock properties specifically applicable to Vesta and Ceres when predicting the tectonic patterns formed by these processes, thus, these

patterns cannot be applied to this study. Future rock-mechanical reassessments are required to investigate the underlying processes that produced the fracture sets.

Introduction

Tectonics of polygonal impact craters

Polygonal impact craters (PICs) abound on various cratered planetary bodies in the solar system, including Earth (e.g., Meteor Crater in Arizona; Schoemaker, 1960), the Moon (e.g., Shoemaker, 1962; Baldwin, 1963; Öhman et al., 2010; Weber et al., 2022), Mercury (e.g., Wood et al., 1977; Melosh and McKinnon, 1988; Weihs et al, 2015), Venus (e.g., Aittola and Öhman, 2006; Aittola et al., 2010), Mars (e.g., Binder and McCarthy Jr., 1972; Öhman et al., 2006, 2010; Watters et al., 2011), icy moons (e.g., Beddingfield et al., 2016; Neidhart et al., 2017; Beddingfield and Cartwright, 2020), and asteroids (Prockter et al., 2002; Neidhart et al., 2017; Weber et al., 2022). PICs provide information about the structure of the target material of a planetary body. Numerous studies have characterized and cataloged PICs (e.g, Weihs et al., 2015; Neidhart et al., 2017; Zeilnhofer and Barlow, 2021), studied their global distribution (e.g., Weihs et al., 2015; Zeilnhofer and Barlow, 2021), invertiaged their cratering mechanics (e.g., Öhman et al., 2008), and examined their relationship with regional tectonics (e.g., Aittola et al., 2007; Beddingfield et al., 2016; Beddingfield and Cartwright, 2020; Zeilnhofer and Barlow, 2021).

Impact craters commonly exhibit straight rim segments creating polygonal geometries where pre-existing structures, such as faults, folds axes, joints, or lithologic boundaries, exist in the target rock (e.g., Fielder, 1961; Shoemaker, 1962, 1987; Öhman et al., 2005, 2008; Aittola et al., 2010; Weihs et al., 2015). These pre-existing structures

are reactivated or utilized during the cratering processes if they are suitably located/oriented, because it is mechanically simpler than making a new structure. PICs are commonly defined as having two or more straight rim segments intersecting at an angle, most commonly in the shape of a hexagon (e.g., Öhman et al., 2008; Zeilnhofer and Barlow, 2021). Different processes of interaction with pre-existing structures in the lithosphere during the impact are proposed to form PICs. Excavation flow preferentially moves along structures to form straight rim segments for simple craters, whereas slumping and terracing during the impact modification stage also preferentially occur along structures to form straight-rim segments for complex craters (Eppler et al., 1983). Öhman et al. (2008) proposed that thrusting along pre-existing structures could also form straight rim segments for small simple craters during the excavation stage. For example, the nearly square Meteor Crater is located almost on a monoclinal fold with straight rims controlled by the fold axis and two orthogonal regional joint sets present throughout the region where the crater was emplaced (e.g., Schoemaker, 1960). On Mars, the formation of specific PICs was controlled by radial fractures induced by the Argyre and Ladon impact basins (Öhman et al., 2008).

These pre-existing fractures may be hidden beneath the regolith layer or finer than the resolution of the camera, making them invisible in spacecraft imagery. Straight rim segments of the impact craters (including PICs) reactivate these hidden fractures, allowing the study of surface or subsurface structural patterns that would otherwise remain hidden in the geological record. Although the type of structures and the subsurface geometry (e.g., the dip angle of the fault plane) of pre-existing fractures cannot be determined from individual straight rim segments, their orientations (i.e., the

strike) can be analyzed as a regional or global tectonic pattern and compared to that of other planetary bodies as well as to predicted tectonic patterns formed by various planetary processes.

Polygonal impact craters on Ceres

NASA's Dawn mission (Russell and Raymond, 2011) revealed remarkable variety of tectonic landforms are observed on Ceres, including faults, ridges, scarps, facture, troughs/grooves, pit crater chains, lineaments, and PICs. Since the first descriptions of PICs on Ceres (e.g., Hiesinger et al., 2016), several studies examined such structures. Otto et al. (2016) reported 258 PICs on Ceres with diameters between 5 km and 280 km, the majority of which are 10 to 50 km in diameter with a mean of 21 km. Neidhart (2017) studied 90 craters on Ceres, and 63 of them (70%) are polygonal with diameters between 8 to 280 km, most of which have diameters of 10 to 40 km with a mean of 49.4 km. The number of straight rims ranges between two and seven.

Zeilnhofer and Barlow (2021) reported that among the 44,594 craters (~3.3%) in their near-global crater database of Ceres, 1,466 are PICs. They characterized these PICs according to their relationships with structures outside or inside the crater. Most of the characterized PICs are not related to any structures. Hexagonal crater shapes are the most common with an average angle between straight rim segments of ~122^{o}. Pit crater chains, i.e., Junina and Samhain Catenae, are with the highest number of PICs (Zeilnhofer and Barlow, 2021). PICs were identified throughout the different stages of crater degradation, indicating that pre-existing structures have influenced the formation of PICs on Ceres since its earliest preserved geologic record. The northern latitudes have a higher polygonal crater density than the southern latitudes (Otto et al., 2016; Zeilnhofer and

Barlow, 2021), which may indicate crustal heterogeneity across Ceres (e.g., Ammannito et al., 2016; Konopliv et al., 2018) or resurfacing of the southern hemisphere by younger and larger impact basin (i.e., Urvara and Yalode basins) that pre-date a proposed true polar wander (TPW) event at the early history of Ceres (Tricarico, 2018).

Polygonal impact craters on Vesta

Although the Dawn mission documented PICs as well as other structures on Vesta, PICs of Vesta have less attention than Ceres, and this underlying tectonics has not been studied. A few studies have cataloged the PICs since their first descriptions (e.g, Ruesch et al., 2014). Neidhart (2017) studied 90 craters, and 50 of them (56%) are polygonal with diameters between 3.1 to 53.2 km. Most of these craters fall between diameters of 10 to 30 km, with a mean of 20.6 km. The number of straight crater rims ranges from two to seven. Weber et al. (2022) conducted a regional study on Vesta with two regions close to fracture systems on Vesta, recorded as rilles, ridges, pit crater chains, troughs, and fractures. Of the 48 craters surveyed, only 8 are PICs. The most common number of straight rim segments is 4, with an average angle of 132^{o} between them. These PICs are not near any structures, and they are hypothesized to have formed from subsurface or buried structures.

Objectives of this study

Previous studies of PICs on Vesta and Ceres selected craters and their straight rim segments visually, and they investigated mainly the crater sizes, spatial distributions, number of straight rim segments, angle between straight rim segments, and length of the straight rim segments. The orientations of straight rim segments have yet to be analyzed,

and therefore any hidden tectonic patterns have not yet been explored. Most of the landforms identified from the Dawn mission have been recorded on the global geological maps of Vesta and Ceres (e.g., Williams et al., 2018; Yingst et al., 2014). While impact craters have been mapped globally, PICs and their straight rim segments, have not been specifically mapped and presented on a global map of Vesta. Furthermore, tectonic patterns in the lithosphere, if and where they occur, are largely hidden under the widespread and thick regolith cover on Vesta and Ceres (e.g., Prettyman et al., 2017; Parekh et al., 2021). Using PICs to uncover hidden tectonic patterns, especially where mapped and assessed using a well-defined mapping protocol to detect straight rim segments quantitatively, enables us to learn about the tectonics of Vesta and Ceres and to compare them.

This work aims to identify and analyze the orientations of straight rim segments on Vesta and Ceres to explore if they reveal previously hidden local, regional, or even global tectonic patterns. I quantify the number and orientation of straight rim segments. The orientations of all straight crater rim segments are visually and statistically analyzed to investigate whether they display preferred orientations regionally or globally. Preferred orientations are compared to orientations of nearby landforms on Ceres and Vesta to investigate if they could have utilized the same pre-existing structures. I compare regional and global tectonic patterns revealed by PICs to previous predictions of tectonic patterns for a series of planetary processes that could have influenced the tectonics on Vesta and Ceres.

Methodology

Datasets and mapping

This study makes use of the Dawn Framing Camera (FC; Sierks et al., 2011) image mosaics and digital elevation models (DEMs). For Vesta, the global mosaic has a resolution of 60 m/px, and the DEM has a resolution of 70 m/px (Preusker et al., 2016a). For Ceres, the global mosaic has a resolution of 140 m/px, and the DEM has a resolution of 137 m/px (Preusker et al, 2016b; Roatsch et al., 2016). All datasets are available in the NASA Planetary Data System[8].

I used the global crater catalogs of Vesta (Liu et al., 2018) and Ceres (Hiesinger et al., 2016). All impact structures with diameters ≥ 10 km on Vesta and ≥ 20 km on Ceres were mapped. These size ranges capture most of the previously reported PICs on Vesta and Ceres. Because the orientations of rims of large impact basins would dominate the length-weighted analysis (see below), I exclude the > 400 km diameter Veneneia and Rheasilvia basins on Vesta. I do, however, present their basin-bounding scarps as large-scale tectonic structures on the global maps. This crater mapping is inclusive of partially preserved craters, because some straight rim segments remain on such impact craters. As cratering is a stochastic process, I do not anticipate that mapping partially preserved craters would bias the tectonic patterns. In contrast, excluding partially preserved craters would bias the results toward the most recently emplaced craters.

For my mapping criteria, I define a crater rim as the most elevated region surrounding the topographic depression caused by the impact, often showing a raised edge. All mapping was carried out using ESRI ArcGIS software and followed a defined

[8] https://pds-smallbodies.astro.umd.edu/data_sb/missions/dawn/index.shtml

data collection protocol for consistency in data collection over the entire surfaces of Ceres and Vesta. Since the recognition and mapping of crater shapes are highly subjective and depend on the mapping scale, basemaps were reprojected to the cataloged centers for each crater using a stereographic projection at a fixed mapping scale of 1:200,000. This mapping scale allows for comfortable observation of crater rims and their geometries even for the smallest considered craters in the chosen dataset.

To detect straight segments of crater rims and thus identify PICs, I devised a method illustrated with an example of a crater displaying a planform shape on Vesta (Figure 5.1a). All rims were mapped as polylines with regularly spaced vertices of 1 km for both Vesta and Ceres (Figure 5.1b), using the streaming function of the ArcMap Editor to ensure consistent data sampling, followed by the line simplification function on the original polyline mapping (Figure 5.1c). The latter function simplifies polylines by connecting the endpoints of a line with a trend line and removing redundant vertices, which are closer to the trend line than the set tolerance. The applied tolerances for Vesta and Ceres are ~0.5 km and ~1 km, respectively. The lower applied tolerance on Vesta better captures straight rim segments from less obvious PICs (see Figure 5.1), whereas a higher value applied to craters on Ceres performs better for more obvious PICs (see Figure 5.2). A tolerance ranging from half to one vertex spacing (i.e., 0.5 and 1 km) returns a simplified crater shape that is in close agreement with the originally mapped polyline. I split all the simplified polylines at the remaining vertices. Following this simplification process, a curved crater rim segment should retain more vertices than a straight one, such that after splitting, the straight segments should be longer, and the curved segments should be shorter (Figure 5.1c). I find that segments with a length ≥ 5

km return geologically meaningful results of straight rim segments on either body (Figure 5.1d).

I test this method by applying it to multiple craters in a region, as shown in an example from Ceres (Figure 5.2a). The total preserved crater rim segments are captured in the mapping (Figure 5.2b) when streaming the crater rims with equally spaced vertices. The orientation distribution contains a wide spread of orientations resulting from curved rim segments, as well as degradation and minor orientation variations of the crater rim. After simplification and plotting only segments longer than 5 km, the orientation distributions contain only straight rim segments, with minor variations removed (Figure 5.2c). I visually verified that each simplified crater rim matched the planform shape of the crater in the photogeology. Craters with simplified polylines that mismatched the shape were excluded from any further analysis, removing them from the dataset.

I classified all remaining craters as circular craters (with no straight segment extracted) or PICs (with at least one straight segment extracted). In previous literature, PICs are defined as having two or more straight rim segments intersecting at a defined angle (e.g., Öhman et al., 2008), but for this study, any crater with at least one straight rim segment was classified as PIC. Each crater was recorded with a unique identification number and its center coordinates to produce the catalogs for Ceres and Vesta as shapefiles (available in the supplementary data).

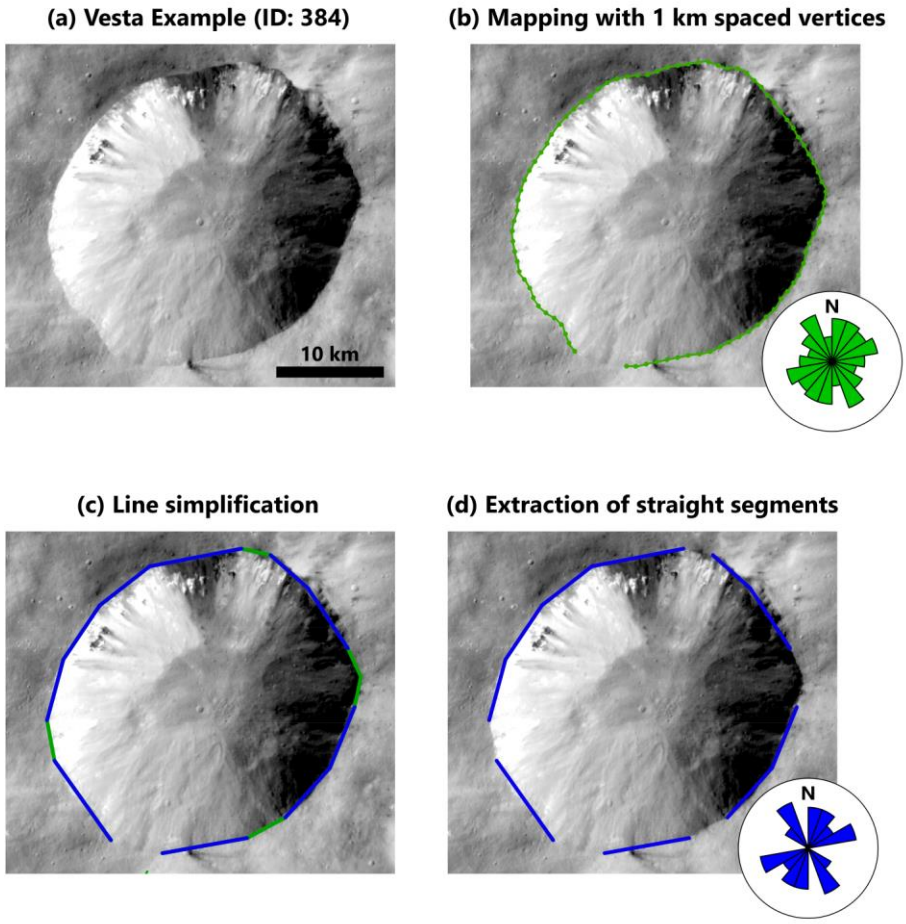

Figure 5.1. *An example of the plan view of impact crater geometry, showing how the mapping and straight segments extractions methods work on ArcMap. (a) A crater displaying a planform shape on Vesta (centered at 7.394°S and 37.486°E). (b) The rim is mapped as a polyline (green lines) with 1 km spaced vertices (green dot). (c) Straight rim segments are simplified to longer sections (blue lines with a length ≥ 5 km) between vertices while sections will be shorter along curved rim segments (green lines with a length < 5 km). (d) By deleting short segments, straight rim segments are extracted and rose diagrams can be plotted to visualize their orientations. The rose diagram in (d) illustrates only the three dominant orientations of the straight rim segment compared to (b).*

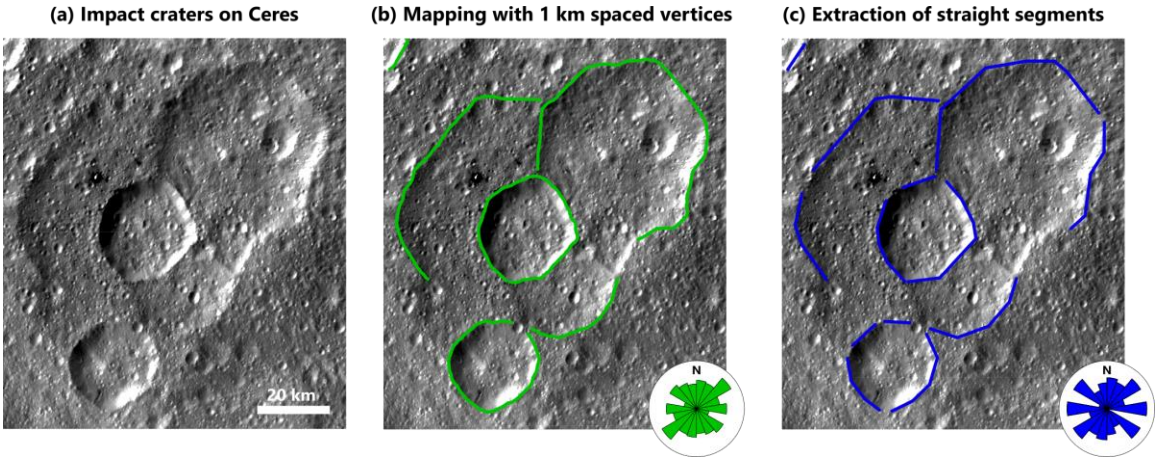

Figure 5.2. *Planform shapes of typical impact craters on Ceres showing stages of data collection. (a) View of typical PICs on Ceres in Dawn Ceres FC image mosaic centered at 23.657°N and 64.473°W. (b) The crater rims are mapped as polylines shown as green lines. (c) After performing line simplification on the mapped polylines, straight crater rim segments are extracted (blue lines) as those longer than 5 km. Length-weighted rose diagrams of (b) and (c) are plotted in green and blue, respectively, for comparison.*

Visual and statistical analyses

Length-weighed rose diagrams — circular histogram plots that display directional data — were produced to visualize the orientations of (1) all mapped crater rims and (2) the extracted straight rim segments across the surface of Ceres and Vesta. For analysis of the rose diagrams on the global scale, these bodies are binned into six 30° latitudinal bands and twelve 30° longitudinal strips. I assessed regional patterns on Ceres and Vesta by generating rose diagrams for 18 regions that have comparable surface areas to one another. Specifically, the regions consist of one polar, three mid-latitude, and five equatorial regions per hemisphere. Moreover, to test if the planetary-scale Rheasilvia

impact caused a global tectonic pattern on Vesta, 18 regions of equal areas were plotted with concentric and radial boundaries to the basin center.

I calculated the true lengths and true orientations (i.e., the strike), accounting for the shape model of Vesta and map projection, of all rim segments and its subsample containing only straight rim segments using the Tools for Graphics and Shapes plug-in (Jenness, 2011) for ArcMap to avoid errors caused by projection distortions that are unaccounted for in the ArcMap toolbox. To generate length-weighed rose diagrams, all mapped crater rims in polylines are split by the regularly spaced vertices of 1 km (according to the mapping criteria; see Figure 1b) and their orientations are plotted with the number of polylines segments (each 1 km long) as the counts. For length weighing the extracted straight rim segments, the calculated length of these segments were rounded down to the nearest whole number in km and plotted as the counts of the orientations, based on the binning described below.

The choice of bin size for the rose diagrams is based on the total length of the segments considered for each region. I calculated bin width (b) as a relationship of range (R) and sample size (N) where $b = R/(2\,N^{\frac{1}{3}})$ (Freedman and Diaconis, 1981; Sanderson and Peacock, 2020). I used the range of R = 360°, but for evaluating orientations of fracture planes where dip is unknown, only a scale of 0° to 180° is needed as strike values between 180° and 360° can be mirrored by those between 0° to 180°. Sample size is reported as the total length of all segments in kilometers, as I mapped with a vertex spacing of 1 km. I rounded the calculated values of bin width to the nearest whole number that allow us to split 180° evenly into bins. By doing so, rose diagrams in areas with a greater sample size will show more details in the overall orientations whereas

those with a smaller sample size will show a more general distribution without being unnecessarily complex for interpretation. The crater segments and rose diagrams for Ceres and Vesta were plotted on global tectonic maps for comparison.

I applied the Kuiper test for uniformity (Kuiper, 1960) to determine if the orientations of the mapped crater rims and straight rim segments have preferred orientation(s) using the open-access software environment for statistical computing and graphics, *R* (R Core Team, 2022). My null hypothesis is that the orientation distribution for crater rims in an area is uniform, assuming that planform crater shapes are completely circular and that superposition of impact crater happens randomly. If this Kuiper test returns *p*-values that are less than an alpha level of 0.05, I conclude that there are preferred orientations of crater rims with 95% confidence. I chose the Kuiper test of uniformity because it is based on plotting the cumulative frequency, which does not require binning of data. This allows preferred orientations to be identified and the departure from a uniform orientation distribution to be recognized without a binning bias. In particular, many visually assessed plots may have been interpreted as showing preferred orientations, whereas the null hypothesis of uniformity is accepted based on the data, especially when the sample size is small. Rose diagrams with uniform distributions and preferred orientations were labeled in the results accordingly to aid interpretations.

A different statistical approach for identifying PICs was developed and applied for Dione (Beddingfield et al., 2016) and Miranda (Beddingfield and Cartwright., 2020). However, the method used in these studies can test craters only with a complete rim preserved, which is rarely the case for craters on Vesta and Ceres. That approach skews the data toward the best preserved and generally youngest craters. Since the straight rim

segments from all PICs, including those that are partly preserved, are important to identify hidden fracture sets, I did not adopt the previous methodology.

Error assessment

The robustness of the mapping criteria and the efficacy of the mapping procedure was tested on craters of various sizes on Ceres and Vesta by both authors (Figure 5.3). Crater mapping was evaluated for consistency, accuracy, and potential sources of error; thus, their scientific use in detecting polygonal craters and/or orientations was assessed. Both authors mapped selected craters of various sizes and degradation stages on Ceres and Vesta separately but using the same criteria. This mapping results are presented for the tested craters in Figure 5.3, with green lines representing Cheng's mapping and blue lines representing Klimczak's mapping. Mappings of a select set of small to large craters on Vesta and Ceres are displayed in Figures 3a and 3b, respectively, with map traces before and after straight rim extraction shown in the left and right columns. Although the mapping style differed between the mappers, the overall geometries captured and their length-weighed rose diagrams are visually similar. These differences in approach include mapping clockwise vs. counterclockwise directions, placing map traces and therefore vertices on somewhat different paths, and choosing different line terminations at incompletely preserved craters.

Length-weighted rose diagrams were plotted for each of the craters separately for visual comparison. Rose diagrams for all crater rims show similar distributions, and their preferred orientations are displayed mostly in the same bin (Figure 5.3). Since straight rim segments are usually prominent, their mapped is less influenced by the differences in mapping styles. Therefore, rose diagrams for preferred orientations are more similar than

those of all crater rims, which result in more consistent interpretations of tectonic patterns among different mappers.

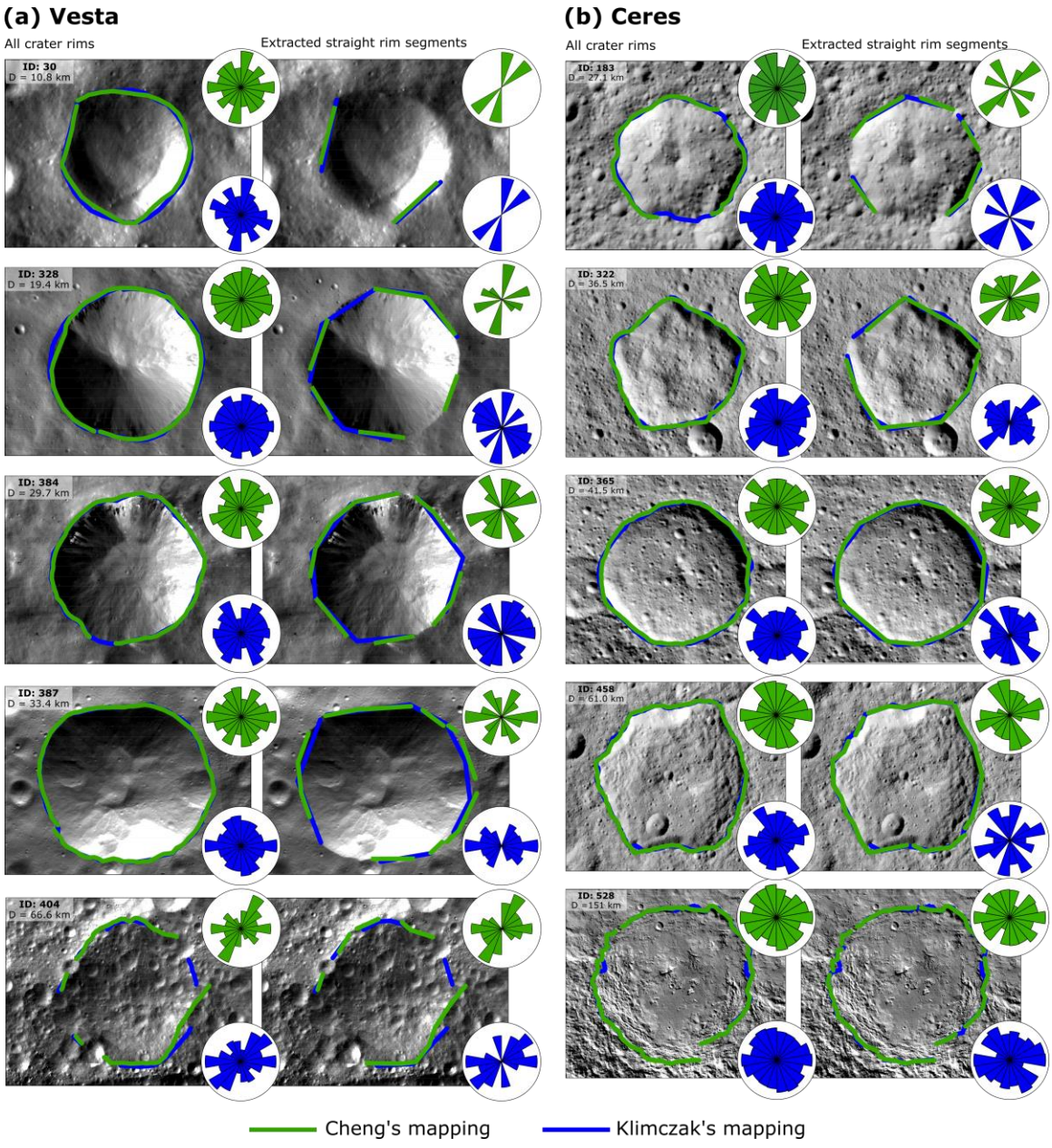

Figure 5.3. *Examples of craters of different sizes mapped by both authors individually following the same criteria. (a) Mapping of five different craters on Vesta. Green lines represent Cheng's mapping, and blue lines represent Klimczak's mapping. Mapping and length-weighed rose diagrams are plotted for each crater rim in the left column and the*

extracted straight crater rim segments are shown in the right column. Preferred orientations in the rose diagrams are represented by the longest wedges. (b) Mapping of five different craters on Ceres. Labels and figure organization follow the same format as in (a).

As discussed in section 5.2.1, craters were excluded from the analysis if the simplified polylines mismatched the crater shape. Since the rose diagrams in the analysis were calculated for all mapped craters per geographic region, with each region containing hundreds to thousands of kilometers of mapped rim segments, slight mismatches in orientations of a few crater rims, especially if smaller than the bin size within the rose diagrams, do not affect the overall tectonic interpretation of preferred orientations. I therefore conclude that the overall shape and orientations of impact crater rims were captured consistently in the analysis, and that straight rim segments were extracted consistently.

Polygonal Impact craters and structural relationships to tectonic landforms

Vesta

408 impact craters were mapped and analyzed on Vesta after omitting four craters that are too degraded to map any rim segments. 73.8% (301) have at least one straight rim segment extracted and are classified as PICs (Figure 5.4a; supplementary data). Eight craters, all with diameters less than 15 km, were excluded owing to a mismatch of simplified polylines with the crater shapes or false returns of straight segments.

I analyzed crater rim orientations by latitude and longitude. In the latitudinal binning, most regions have a non-uniform orientation distribution for all crater rims, except for the regions between 30^{o}S to 90^{o}S (Figure 5.4a; Appendix A: Table 5.1). All

latitudinal regions show preferred orientations of straight rim segments (Figure 5.4a; Appendix A: Table 5.2). The rose diagrams of all crater rims and extracted straight rim segments show a strongly E–W preferred orientation at the north polar region, indicating the presence of an E–W oriented fracture pattern influencing the shapes of impact craters. Multiple moderately preferred orientations are present between 60^{o}N to 30^{o}S for both all crater rims and straight rim segments (Figure 5.4a), indicating that the northern mid-latitudes and equatorial regions are fractured with several sets with preferred orientations including N–S, NE–SW, E–W, and SE–NW. While the orientations of all crater rims between 30^{o}S to 90^{o}S are uniformly distributed, the extracted straight rim segments show a strongly E–W preferred orientation. This indicates the presence of an E–W oriented fracture pattern near the south pole, mirroring the pattern of the north pole, but this pattern does not substantially influence the overall crater shape. Moderately preferred NE–SW and SE–NW orientations are also present in the southern mid-latitudes (Figure 5.4a), indicating this region is fractured by at least three major joint sets.

As for the longitudinal binning, most longitudes show a uniform orientation distribution of all crater rims, except for regions between 120^{o}W to 180^{o}W (Figure 5.4a; Appendix: A Table 5.3). However, all longitudes are dominated by an E–W preferred orientation and one or more other moderately preferred orientations in the straight rim segments (Figure 5.4a; Appendix A: Table 5.4). Overall, there is no obvious systematic change in pattern across longitudes, and the orientation distributions are primarily influenced by the latitudinal patterns of fracture systems.

I divided Vesta into 18 equal-area regions to investigate any regional preferred orientations of crater rims and compared them to mapped tectonic structures (Cheng and

Klimczak 2022a, 2022b). A total of 14 out of 18 regions show a uniform orientation distribution of all crater rims (Figure 5.4b; Appendix A: Table 5.5), but 17 regions show a non-uniform orientation distribution of the straight rim segments (Figure 5.4b; Appendix A: Table 5.6). This indicates that multiple fracture sets are present throughout Vesta, but they do not have a significant effect on crater shapes in 14 regions. The southern mid-latitudinal region between 60^{o}E to 180^{o}E shows a uniform orientation for all crater rims and straight rim segments (Figure 5.4b), even though the rose diagram of straight rim segments has preferred orientations of E–W and NW–SE in visual assessment. The lack of statistical significance of this pattern is likely a result of the small sample size.

Four regions have preferred orientations for all crater rims and straight rim segments, which are all in the northern hemisphere. The north polar region shows a strongly E–W preferred orientation, confirming the findings in the latitudinal analysis (Figure 5.4a). In the mid-latitudes, there are dominant NE–SW and NW–SE preferred orientations between 60^{o}E to 180^{o}E and E–W to ESE–WNW preferred orientations between 180^{o}W to 60^{o}W. In the equatorial regions, there are dominant preferred orientations of E–W and NE–SW between 180^{o}W to 108^{o}W and only NE–SW between 108^{o}W to 36^{o}W. These results indicate that impact crater shapes are controlled by fracture systems with preferred orientations in these regions.

Divalia and Saturnalia Fossae overlap only with regions that have a uniform orientation distribution of all crater rims (Figure 5.4b). Regions where the Divalia Fossae are present lack dominant E–W preferred orientations for all crater rims and straight rim segments, indicating PICs and the Divalia Fossae did not share the same pre-existing

fracture sets. The straight rim segments in the northern mid-latitudinal region between 60^{o}W to 60^{o}E have a preferred orientation that matches with the orientation of the Saturnalia Fossae (i.e., NW–SE), but the orientation of all crater rims in this region does not have a preferred orientation. In addition, the orientation distributions of crater rims and their straight segments in other regions overlapping with the Saturnalia Fossae do not have consistant orientations. I therefore find that PICs did also not share the same pre-existing fracture sets with the Saturnalia Fossae and that their geometries were influenced by other hidden structures.

To investigate if PICs utilized fracture systems introduced to Vesta's lithosphere by the impact that produced the Rheasilvia basin, I divided Vesta into equal-area regions with basin-concentric and basin-radial boundaries and re-calculated length-weighed rose diagrams for each of these regions (Figure 5.5; Appendix A: Tables 5.7 and 5.8). To aid the descriptions, I labeled the regions from RH1 at the center of the basin to RH18 at the antipode of the basin. Generally, it is common to find structures that formed radially or concentrically within or around impact craters and basins, as on Earth (e.g., Osinski and Spray, 2005; Kumar and Kring, 2008), Mercury (e.g., Byrne et al., 2018; Klimczak et al., 2023), Mars (e.g., Carr et al., 1977; Öhman et al., 2005), the Moon (e.g, Krishna and Kumar, 2016), and icy moons (e.g., Moore et al., 2004). On Vesta, some bins do show a basin-radial component (RH9 and RH16) or a basin-concentric component (RH3 and RH4). However, there is no consistent basin-related pattern observed in all other bins. Therefore, it is unclear how far the detected basin-radial and -concentric orientations used the pre-existing structures formed by the Rheasilvia impact. It is equally likely that PICs on Vesta instead were in largely influenced by other pre-existing structures or that basin-

radial and -concentric fractures from the Rheasilvia impact do not stand out in Vesta's heavily disturbed lithosphere, which contains fracture sets of multiple orientations.

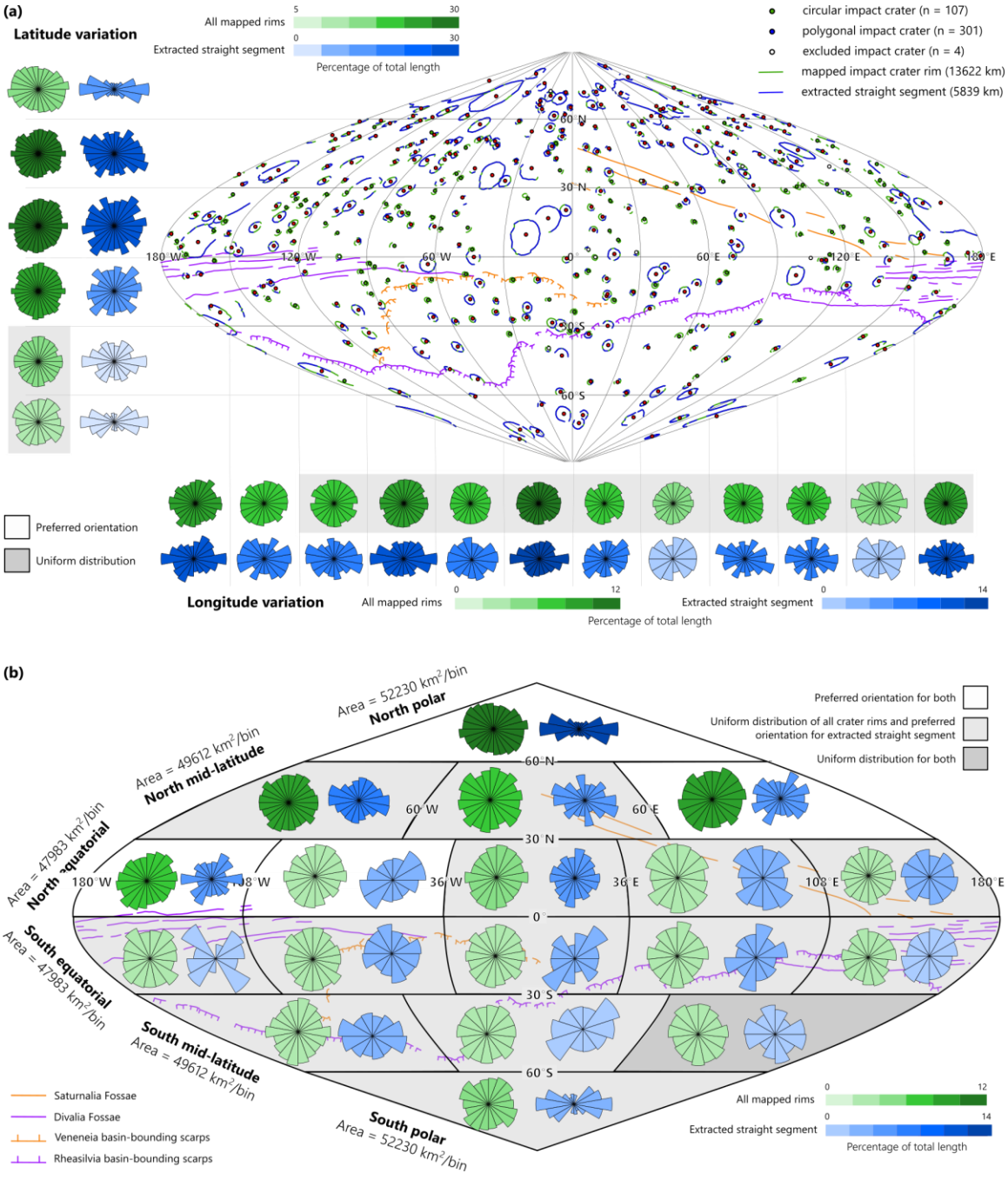

Figure 5.4. *Global map of Vesta in sinusoidal projection showing the mapping of crater rims and their orientations in different geographic bins. For comparison to crater data, the basin-bounding scarps of the Rheasilvia and Veneneia basins, Divalia Fossae, and*

Saturnalia Fossae are plotted. (a) All crater rims and straight rim segments and their orientations are displayed in rose diagrams shown in green and blue, respectively. The center coordinates for each crater, including circular, polygonal, or those that were excluded, are plotted with a point symbol. Length-weighted rose diagrams are plotted in 30^{o} latitudinal bands and longitudinal strips, with color intensity indicating the percentage they contribute toward the overall dataset. Rose diagrams statistically determined to show a uniform distribution are shaded in gray. (b) Orientations of all crater rims (green) and straight rim segments (blue) are shown as rose diagrams for each of 18 equal-area regions. Rose diagrams for all crater rims statistically determined to show a uniform distribution are shaded in light gray, those with uniform distribution for all crater rims and straight rim segments are displayed shaded in dark gray. All rose diagrams have the north direction pointing toward the top of the figure.

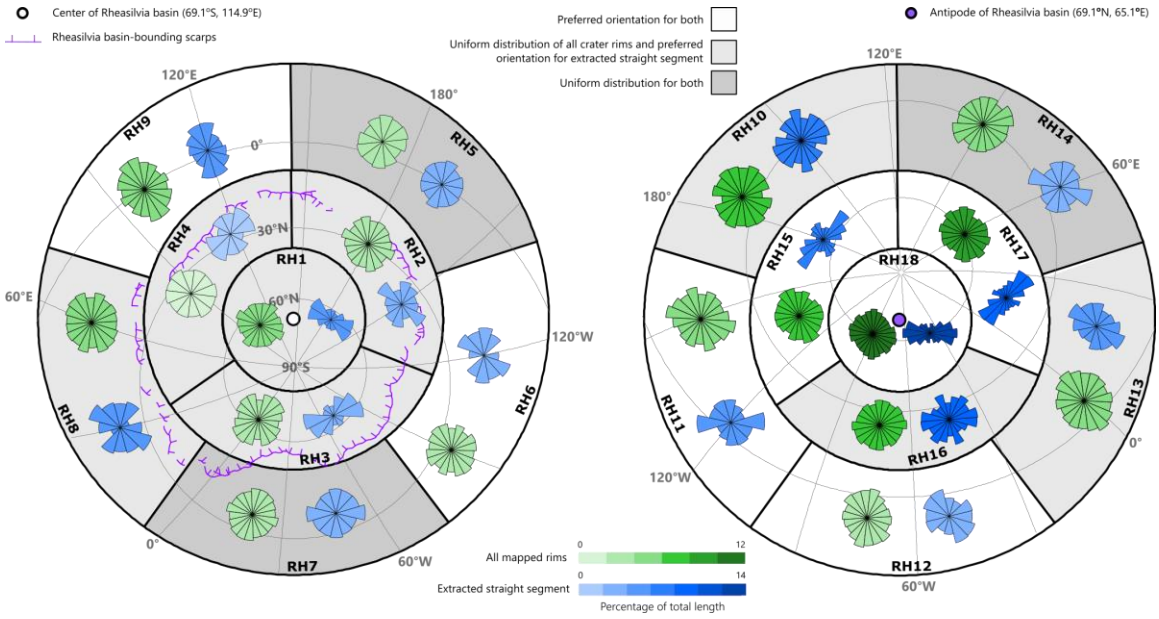

Figure 5.5. *Global map of Vesta shown as two stereographic projections centered on the Rheasilvia basin on the left and on the Rheasilvia antipode on the right. Orientations of all mapped crater rims (green) and straight segments (blue) are shown as length-*

weighted rose diagrams plotted within 18 basin-radial/concentric regions. Rose diagrams for all crater rims statistically determined to show a uniform distribution are shaded in light gray, those with uniform distributions for all crater rims and straight rim segments are displayed shaded in dark gray. All rose diagrams are rotated so that they align with the cardinal directions on the map.

Ceres

On Ceres, 525 impact craters were analyzed after omitting six craters that are too degraded to identify any rim segments. All of these have at least one straight rim segment and are classified as PICs (Figure 5.6a; supplementary data), with the vast majority of them forming clear hexagonal planform shapes, confirming previous findings (e.g., Otto et al., 2016; Zeilnhofer and Barlow., 2021). No mismatches of simplified polylines with the crater shapes or false returns of straight segments were detected, so all straight rim segments could be analyzed.

As with Vesta, I analyze crater rim orientations on Ceres by latitude and longitude. In the latitudinal bands, all craters show a non-uniform orientation distribution both for all crater rims and straight rim segments (Figure 5.6a; Appendix B: Tables 5.9 and 5.10), indicating the presence of one or more preferred orientations of fractures. The orientation distributions for all crater rims and straight rim segments are similar, because most crater rims were identified as straight rim segments. This shows that Ceres's lithosphere is fractured by several major joint sets which govern the planform shape of all craters. The northern hemisphere shows preferred NE–SW to E–W orientations at the polar and mid-latitudinal regions and NW–SE to N–S orientation at the equator. The

southern hemisphere shows preferred NW–SE to E–W orientations, which are most pronounced at the pole (Figure 5.6a).

Along the longitudinal strips, seven out of 12 regions have non-uniform orientation distributions of all crater rims (Figure 5.6a; Appendix B: Table 5.11). All regions but one show preferred orientations of straight rim segments (Figure 5.6a; Appendix B: Table 5.12) and all of the rose diagrams indicate one or more preferred orientations. This confirms the presence of several major fracture sets across Ceres. However, no distinctive systematic patterns are observed among the longitudinal bins.

I also divided the globe of Ceres into 18 equal-area regions to investigate any regional patterns of preferred orientations of crater rims that allow us to compare them with structures (Figure 5.6b; Appendix B: Tables 5.13 and 5.14). All regions but one show preferred orientations for all crater rims, but all regions show preferred orientations of straight rim segments. The orientation distributions for all crater rims and extracted straight rim segments are similar, confirming that the impact crater shapes are dominated by straight rim segments in all parts of Ceres.

A trend similar to that seen in the latitudinal variations of preferred orientations (Figure 5.6a) is confirmed throughout the regions (Figure 5.6b). All polar and mid-latitudinal regions in the northern hemisphere have a preferred NE–SW orientation component, and some also have other preferred orientations, and preferred NW–SE and N–S orientations at the equator. Most regions in the southern hemisphere show a pronounced preferred NW–SE orientation, except for the southern equatorial regions between 36^{o}E to 180^{o}E. These findings indicate that the latitudinal variation of preferred orientations is a global pattern on Ceres.

The orientations of previously mapped structures named Junina and Samhain Catenae (Scully et al., 2017) can be compared to the orientations of straight crater rims (Figure 5.6b) to test if their formation involves the same pre-existing fracture sets. Junina and Samhain Catenae are thought to be pit crater chains (Scully et al., 2017). The preferred orientations of crater rims in these regions are only partly consistent with the orientations of the Junina and Samhain Catenae. Preferred orientations of straight rim segments showing NW–SE trends in the equatorial regions between 180^{o}W to 36^{o}W are consistent with the mapped trends of the Samhain Catenae and also the southernmost parts of the Junina Catenae. The NW–SE tectonic pattern occurs not only near these catenae but also across the entire equatorial region and southern hemisphere (Figure 6b). Moreover, while a few straight rim segments in the region around the Junina Catenae match in orientations, the most pronounced preferred orientations of straight crater rim segments are nearly perpendicular to those of the Junina Catenae, indicating that the formation of the catenae and PICs did not necessarily utilize the same pre-existing structure.

The findings do not show a well defined relationship between the structures (Samhain and Junina Catenae) with PICs. The fracture systems revealed by PICs are not only localized around the structures, but they are present throughout a larger region or even most of the hemisphere (Figure 5.6). Zeilnhofer and Barlow (2021) have characterized PICs on Ceres and identified those related to eight sets of structures, including the Baltay Catena, Gerber Catena, Junina Catenae, Pongal Catena, Samhain Catenae, Uhola Catenae, Niman Rupes, Nabanna Fossa, based on their spatial relationship (maximum distance of 10 crater radii with relation to the structural system).

Among these structures, Junina and Samhain Catena have the most number of related PICs, but this likely reflects the larger area revealed by these two structures compared with other structures. The average angle measurement between the straight rim segments of the PICs to the Junina and Samhain Catena are around 27.61^{o} and 32.24^{o}, respectively (Zeilnhofer and Barlow, 2021) which is consistent with the findings that these structures do not align with the dominant preferred orientations of straight crater rim segment in the region (Figures 5.6). The PICs reveal more complex fracture systems, which may be due to the excavation of a more fractured or low-viscosity, deeper target on Ceres covered by low-density ice-rich material within the upper 1-10 km and/or ejecta blanket of larger impact craters, as proposed in previous studies (Bland et al., 2019; Zeilnhofer and Barlow, 2021).

Scully et al. (2017) suggested that the Junina Catenae are secondary crater chains that are non-radial to any specific source and that they could be associated with Urvara and Yalode impacts as a result of Ceres' fast rotation and low gravity. This non-tectonic origin of Junina Catenae fits with the observations that there is no clear relationship between PIC formation and these structures. Moreover, the Samhain Catenae was proposed to form by the upwelling caused by convection or diapirism associated with the Hanami Planum under an extensional tectonic regime (Scully et al., 2017). Zeilnhofer and Barlow (2021) assume that maximum tensile stresses are perpendicular to the structural orientation and may influence the smaller PICs, reaffirming that the PICs formed in a location adjacent to the system. However, the results show that the preferred orientations of PICs do not align with Samhain Catenae. In addition, the predicted structural orientation may not be perpendicular to the maximum tensile stresses. Rock

mechanical analyses are needed to predict the structural orientation related to principal stresses for comparison with the tectonic patterns revealed by PICs.

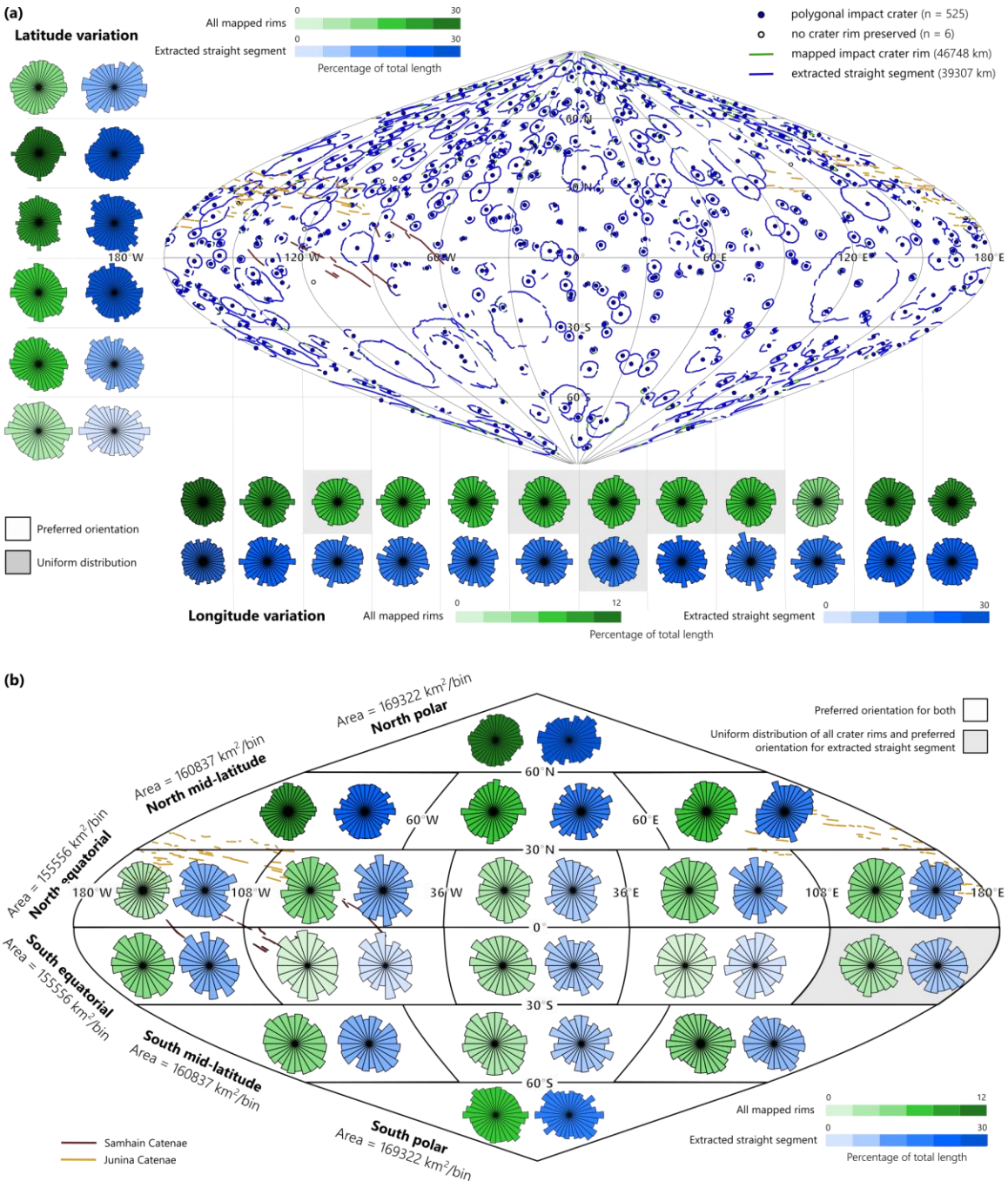

Figure 5.6. *Global map of Ceres in sinusoidal projection showing the mapping of crater rims and their orientations in different geographic bins. For comparison to crater data, the basin-bounding scarps of the Samhain and Junina Caternae are plotted. (a) All crater*

rims and straight rim segments and their orientations are displayed in rose diagrams shown in green and blue, respectively. The center coordinates for each crater, including circular, polygonal, or those that were excluded, are plotted with a point symbol. Length-weighted rose diagrams are plotted in 30° latitudinal bands and longitudinal strips, with color intensity indicating the percentage they contribute toward the overall dataset. Rose diagrams statistically determined to show a uniform distribution are shaded in gray. (b) Orientations of all crater rims (green) and straight rim segments (blue) are shown as rose diagrams for each of the 18 equal-area regions. Rose diagrams for all crater rims statistically determined to show a uniform distribution are shaded in light gray, those with uniform distribution for all crater rims and straight rim segments are displayed shaded in dark gray. All rose diagrams have the north direction pointing toward the top of the figure.

Comparison of Vesta's and Ceres' tectonic patterns

Processes that are hypothesized to have caused global tectonic patterns on minor bodies mainly include stresses from rotational bulging and large impacts (Thomas and Prockter, 2010). Stresses from rotational bulging could potentially cause global tectonic patterns, as Ceres and Vesta have fast rotation periods of ~9 and 5 hours, respectively. Moreover, large impacts (i.e., the impact forming the Rheasilvia basin) lack any relationship with the tectonic patterns on Vesta (Figure 5.5), and there is no large impact basin on Ceres comparable in size to Rheasilvia (Marchi et al., 2016). Therefore, if the fast spinning is the only cause of the tectonic patterns on Vesta and Ceres, any pattern from the PICs should be similar between these bodies.

PICs reveal hidden tectonic patterns on Vesta and Ceres. On Vesta, a systematic E–W trending fracture system is revealed at the north polar regions, and potentially mimicked at the south pole (Figure 5.7a), indicating that some tectonic processes produced preferred orientations that influenced the planform crater shapes. Less systematic fracture patterns are present in the equatorial region and mid-latitudes with no relationship with the Rheasilvia basin and Divalia Fossae (Figure 5.7a), indicating that Vesta contains fractures of all orientations, consistent with it being a highly fractured asteroid that likely got its fractures from billions of years of impact bombardment. Fractures on Vesta never healed or annealed, consistent with the previous findings (Cheng and Klimczak, 2022a); therefore, crater rims reflect those fractures. Moreover, strongly preferred fracture orientations vary latitudinally on Ceres (Figure 5.7b). The northern polar and mid-latitudinal region (30^{o}N to 90^{o}N) has a dominant fracture system with preferred orientations of NE–SW whereas the tectonic patterns become NW–SE trending in the southern hemisphere, especially towards the pole (Figure 5.7b), indicating that some tectonic processes produced preferred orientations that influenced the planform crater shapes. The tectonic patterns do not show a clear relationship with the structures (i.e., pit crater chains), indicating that the processes produced these preferred orientations are unlikely related to the formation of the pit crater chains.

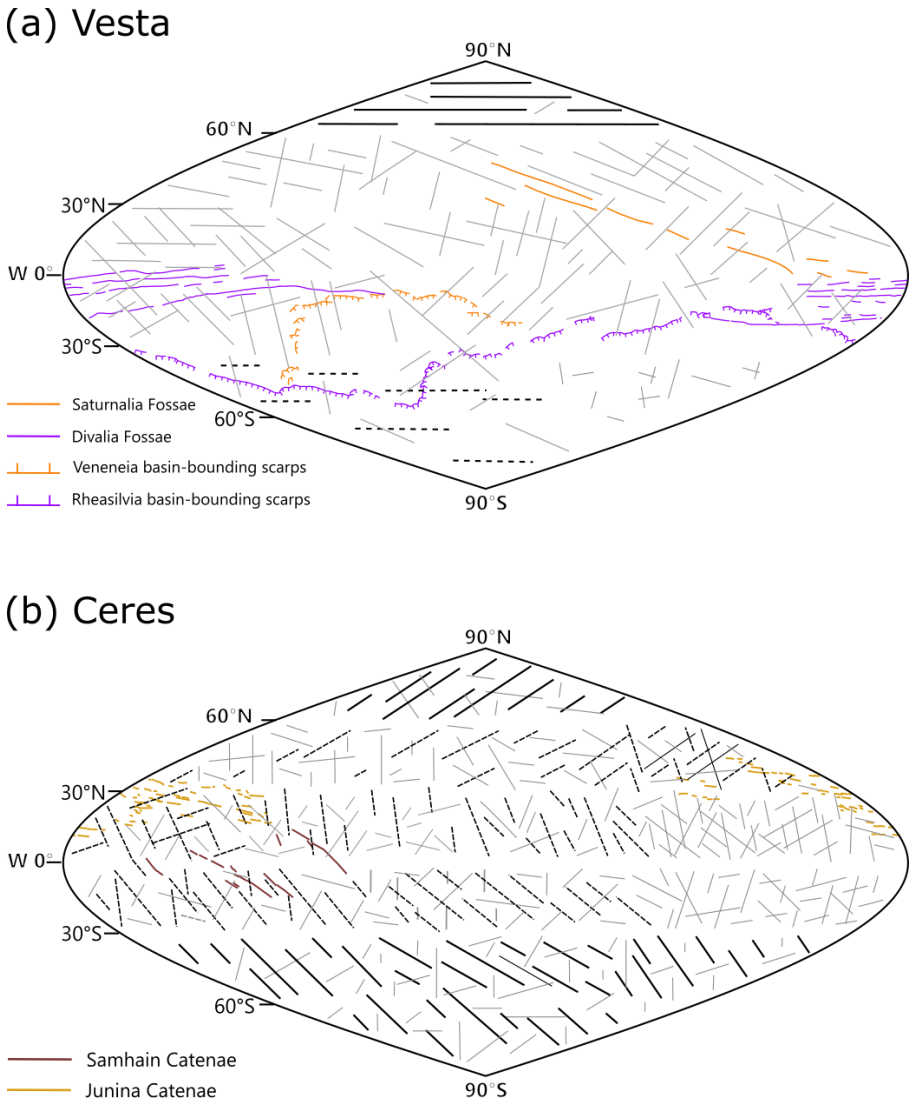

Figure 5.7. *Schematic global tectonic map of (a) Vesta and (b) Ceres based on the straight rim segments of impact craters. The bold solid black lines represent a pronounced fracture set dominating the region, and bold dashed black lines represent an inferred dominant fracture set. Gray lines represent where other fracture sets overlap with one another, forming a complex pattern.*

Both bodies display latitudinal variations across the globe with pronounced patterns towards the polar regions. No longitudinal variations are present on Vesta and Ceres. However, their patterns are entirely different in their orientations. Therefore, it is

unlikely that these fracture patterns are dominantly driven by the fast spinning of the bodies. While fast spinning may produce similar fractures on Vesta and Ceres, some factors may influence the process of impact cratering that results in the similar sets of pre-existing fractures did not get used in the same way, including the difference in crater sizes and types (i.e., simple vs. complex), surface gravity acceleration of the bodies, target materials (i.e., rock vs. ice). Other planetary processes beyond fast rotation may also cause the tectonic patterns on Vesta and Ceres.

Implications for hypothesized tectonic processes

Various planetary processes that could form distinct regional and global tectonic patterns have previously been hypothesized. On Ceres or Vesta, these include changes in the spin rate of both Ceres and Vesta (Mao and McKinnon, 2020), changes in volume on Ceres (McCord and Sotin, 2005), and true polar wander on Ceres (Tricarico, 2018) and Vesta (Matsuyama and Nimmo, 2011). Global stress distributions were derived for all of these processes, and tectonic patterns were predicted in some studies (e.g., Matsuyama and Nimmo, 2008; 2011; Tricarico, 2018).

To identify if these processes could be relevant to the tectonic histories of Vesta and Ceres, I compare the tectonic maps of Vesta and Ceres (Figure 5.7) to the predictions. However, since relative ages cannot be deduced from different fracture sets in the tectonic patterns revealed by PICs, I can compare only the preserved pattern as a whole. Furthermore, multiple processes could have overlapped, and some tectonic structures and their patterns may not be preserved, such that observations may not match the predicted patterns perfectly. Lastly, any predictions of global tectonic patterns rely on the methods and assumptions in the original studies. Therefore, I discuss the suitability of

previous predictions of fracture types and orientation to fracturing behavior and rock-mechanical properties of Ceres and Vesta.

Change in spin rate

Impacts have been proposed to cause a change in spin rate was proposed to have occurred on both Ceres and Vesta (Mao and McKinnon, 2020). Ceres likely spun up or down by one to two hours from its initial rate. Vesta may have spun up or down due to the Rheasilvia and Veneneia impacts, but up-spin is more likely based on the scale and location of these impacts. General studies of spin rate changes predict that a planetary up-spin produces a global tectonic pattern with normal fault trending N–S at the equatorial region, strike-slip faults trending NE–SW and NW–SE in the mid-latitudes, and thrust faults trending E–W in the pole regions (Matsuyama and Nimmo, 2008, Beuthe, 2010). In contrast, despinning is predicted to include thrust fault trending N–S at the equatorial region, strike-slip faults trending NE–SW and NW–SE in the mid-latitudes, and normal faults trending E–W in the pole regions (Melosh, 1977, Collins et al., 2010). However, Klimczak et al. (2015) determined that despinning produced a global set of mostly E-W-oriented joints on Mercury. These authors noted that the widely used Anderson's theory of faulting (Anderson, 1951) to predict the type of faults on planetary surfaces is not appropriate, as it does not apply to tensile stresses, but that N-S oriented stress components remain tensile across all latitudes during despinning. For Mercury's low surface gravitational acceleration, tensile stresses were found to not shift into a fully compressive stress state, in which Anderson's theory of faulting does apply until considerable depths are reached. Such conditions are equally applicable to bodies like

Vesta and Ceres that have even lower surface gravitational accelerations than Mercury (see Cheng and Klimczak, 2022b).

While the tectonic patterns on Ceres (Figure 5.7) do not fit with any of those generally predicted from changes in spin rates, some comparison is possible for Vesta. On Vesta, E–W preferred orientations at the poles, such as those predicted in general for changes in spin rates, are present in the orientations of straight crater rim segments (Figure 5.7). No distinctive N–S trending pattern occurs in the structural observations in the equatorial region (Figure 5.7). But the Divalia Fossae, which large joints (Cheng and Klimczak, 2022b) encircle the equator in E–W orientation, matching the type and orientation of the despinning scenario in Klimczak et al. (2015). Mao and McKinnon (2020) instead proposed that the extension driven by the up-spin has a role in the formation of the Divalia Fossae and perhaps even the Saturnalia Fossae. However, no studies predict the type and orientation of structures specifically for changes in spin rate on Vesta or Ceres, such that specific comparisons and evaluations of tectonic patterns are impossible at the time of this writing. Thus, a change in spin rate on either of these bodies cannot be confirmed or ruled out.

Volume change

Complex global contractions are thought to have occurred during Ceres's evolution, and tectonic structures formed during several stages are hypothesized to be present in the crust today (McCord and Sotin, 2005). Assuming a constant lithospheric thickness, an icy body like Ceres experiencing a global volume decrease is likely to have a global population of randomly oriented and uniformly distributed thrust faults. In contrast, a global volume increase, i.e., global expansion, is likely to produce randomly

oriented and uniformly distributed joints and perhaps normal faults (Melosh and McKinnon, 1988). The tectonic pattern on Ceres varies latitudinally with preferred orientations across the globe, which is inconsistent with the predicted effects of global expansion or contraction. This indicates that the process did not happen or that it overlapped with one or more other processes.

Furthermore, heterogeneities of lithospheric thickness greatly influence any predicted pattern induced by volume changes. For example, icy bodies with a thinner equatorial lithosphere but a thicker polar lithosphere are predicted to generate E–W trending normal faults from expansion or thrust faults from contraction in the equatorial region (Beuthe, 2010). As Ceres is proposed to have a thick lithosphere with heterogeneous crustal density, it is unclear what predicted tectonic patterns would produce unless it is specifically modeled.

True polar wander

Before the Dawn mission, Vesta was proposed to have TPW, caused by the emplacement of the Rheasilvia basin (Matsuyama and Nimmo, 2011). The TPW is predicted to have produced two regions of N–S trending normal faults covering ~90^{o} in latitude and ~70^{o} in longitude around the paleopoles, two regions of thrust faults covering ~90^{o} in latitude around the current poles, with the remaining regions near the equator having strike-slip faults. With additional despinning, the equator region is predicted to become covered with strike-slip faults with thrust faults covering the polar region. If contraction happens with TPW and with or without despinning, the entire surface is predicted to be covered by only thrust faulting, with the orientation controlled by the reorientation and despinning. However, the idea has not been further investigated since

the predicted tectonic pattern (Matsuyama and Nimmo, 2011) does not fit the observations of the Dawn data. However, no new reorientation calculations have been carried out that incorporate the new geologic constraints returned from the Dawn mission to investigate this process.

Numerical modeling of relaxation of the Rheasilvia basin and rotational bulge to investigate the possibility of TPW on Vesta suggests that the thickness and rigidity of Vesta's lithosphere following the impact likely inhabited any relaxation of Vesta's rotational bulge (Karimi and Dombard., 2016). However, the rigidity parameters used in this modeling (i.e., Young's modulus) pertained to intact rock samples and are not suitable for highly fractured rock masses such as those comprising Vesta's lithosphere. Therefore, the modeling results with these revised parameters (i.e., deformation modulus adjusted for the lithospheric properties) may reduce the rigidity and allow basin relaxation and polar flattening to occur; therefore, the possibility of TPW on Vesta cannot yet not be discounted.

Ceres is also proposed to have undergone true polar wander caused by heterogeneous crustal density (Tricarico, 2018), in which the associated changes in the figure of Ceres could fracture the lithosphere of Ceres and contribute to the formation of PICs. Tricarico (2018) proposed a reorientation of Ceres' pole by ~36^{o} with multiple stages of pole changes. In their work, true polar wander is predicted to form normal faults at regions migrating toward the equator and thrust faults at regions migrating toward the pole. Similar to the Vesta prediction by Matsuyama and Nimmo (2011) described above, the TPW is predicted to have produced two regions of N–S trending normal faults around the paleopoles, two regions of thrust faults around the current poles, and the remaining

regions near the equator with strike-slip faults (see Figure 5.4 in Tricarico, 2018). The Samhain Catenae and another pit crater chain, Uhola Catenae, were proposed to match the predicted pattern of TPW on Ceres (Tricarico, 2018). However, similar to the predicted tectonic pattern for change in spin rate (e.g., Melosh, 1977; Matsuyama and Nimmo, 2008; Beuthe, 2010; Collins et al., 2010), the tectonic pattern predicted by Tricarico (2018) considered faulting as the only fracturing type induced by TPW. Considering Ceres is a small and low-gravity body, faulting is unlikely to form near the surface of Ceres. Other fracturing types (i.e., jointing) need to be considered in rock-mechanical reassessment with appropriate lithospheric parameters to make a rigorous prediction of tectonic patterns and appropriate comparison with the observations.

The latitudinal variations in the tectonic pattern revealed by PICs on Ceres (Figure 5.7b) do not fit the predicted tectonic patterns of TPW by Tricarico (2018). The lithosphere of Ceres is complexly fractured (Figure 5.7b), and even though some fracture patterns may fit the predicted tectonic patterns, it does not confirm the TPW of Ceres. The finding agrees with the parameter space test conducted by Keane and Ermakov (2019) that reveals Ceres's tectonics are sufficiently ambiguous that a large fraction of random palaeo-poles can fit the tectonics observed; thus, there is no clear evidence that TPW occurred on Ceres based on the tectonic patterns or structures.

Conclusions and future work

The results reported here show that PICs are an important indicator of hidden fracture systems on Vesta and Ceres. I mapped and analyzed 412 craters with a diameter larger than 10 km on Vesta and 525 craters with a diameter larger than 20 km on Ceres. 301 out of 412 craters (73%) on Vesta and all mapped craters on Ceres have at least one

straight rim segment extracted and thus I identified those as PICs. By binning and plotting the orientations of crater rims, I identified the preferred orientations for different regions and revealed the hidden complex tectonic patterns on both bodies. Vesta has a pronounced E–W-oriented fracture pattern in the polar regions with several regional fracture sets intersecting one another across the globe. Ceres has many intersecting fractures showing a dominant NE–SW fracture set in the northern hemisphere and a NW–SE fracture set in the southern hemisphere, which are most pronounced near the poles.

None of the fracture patterns revealed by straight crater rim segments conclusively match the orientations of troughs on Vesta and pit chains on Ceres nor do they have a defined relationship with the Rheasilvia basin on Vesta, indicating that the tectonic patterns may be formed by different mechanisms. While Vesta and Ceres are fast-spinning bodies, their different tectonic patterns could be accounted for by their different crater sizes and types, surface gravity acceleration of the bodies, crustal materials (i.e., rock vs. ice), as well as other planetary processes that overlaps with the body spinning. I attempted to compare the tectonic maps of Vesta and Ceres with the predicted tectonic pattern caused by the change in spinning rate, volume change (specifically for icy bodies), and TPW. However, the prediction of tectonic patterns from the literature are not specific and applicable to Vesta and Ceres. Rock-mechanical reassessment applicable to Vesta and Ceres's lithosphere is needed to make a rigorous prediction of tectonic patterns and appropriate comparison with the observations in future studies.

Acknowledgments

This research is funded by the 2020 Eugene and Carolyn Shoemaker Impact Cratering Award. This work made use of NASA Dawn Mission data, which are archived in the NASA Planetary Data System.

Appendix

Appendix A: Statistics for mapped craters on Vesta

Table 5.1. Statistics of all crater rims binned by latitudes

Region #	**Lat**	**Length** [a]	**Total %** [b]	**# of bins** [c]	***V*** [d]	**P-value**
1	60N - 90N	1638	12%	24	3.0743	< 0.01
2	30N - 60 N	3611	26%	30	2.3484	< 0.01
3	0 - 30N	3478	25%	30	2.7523	< 0.01
4	30S - 0	2781	20%	30	1.8084	0.025 < P < 0.05
5	60S- 30S	1430	10%	24	1.1606	> 0.15
6	90S - 60S	760	6%	18	1.4002	> 0.15

[a] Total mapped crater rim length in km

[b] Percentage of mapped crater rim lengths in the region

[c] Number of bins in the rose diagram (see calculations in the main text)

[d] Test statistic for Kuiper's test

Table 5.2. Statistics of extracted straight-rim segments binned by latitudes

Region #	**Lat**	**Length** [a]	**Total %** [b]	**# of bins** [c]	***V*** [d]	**P-value**
1	60N - 90N	763	13%	18	11.3559	< 0.01
2	30N - 60 N	1454	25%	24	4.8351	< 0.01
3	0 - 30N	1589	27%	24	2.2847	< 0.01
4	30S - 0	1085	19%	20	2.2382	< 0.01
5	60S- 30S	544	9%	18	2.8471	< 0.01
6	90S - 60S	401	7%	18	6.7746	< 0.01

[a] Total mapped crater rim length in km

[b] Percentage of mapped crater rim lengths in the region

[c] Number of bins in the rose diagram (see calculations in the main text)

[d] Test statistic for Kuiper's test

Table 5.3. Statistics of all crater rims binned by longitudes

Region #	Lon	Length [a]	Total % [b]	# of bins [c]	*V* [d]	P-value
7	180W - 150W	1341	10%	24	1.8179	0.025 < P-value < 0.05
8	150W - 120W	1127	8%	20	1.8752	0.01 < P-value < 0.025
9	120W - 90W	1149	8%	20	0.986	> 0.15
10	90W - 60W	1426	10%	24	1.1603	> 0.15
11	60W - 30W	1038	8%	20	0.9924	> 0.15
12	30W - 0	1446	11%	24	1.1777	> 0.15
13	0 - 30E	1147	8%	20	1.4165	> 0.15
14	30E - 60E	748	5%	18	1.011	> 0.15
15	60E - 90E	1051	8%	20	1.1563	> 0.15
16	90E - 120E	1077	8%	20	1.0738	> 0.15
17	120E - 150E	785	6%	18	1.5638	0.10 < P-value < 0.15
18	150E - 180E	1363	10%	24	1.0411	> 0.15

[a] Total mapped crater rim length in km

[b] Percentage of mapped crater rim lengths in the region

[c] Number of bins in the rose diagram (see calculations in the main text)

[d] Test statistic for Kuiper's test

Table 5.4. Statistics of extracted straight rim segments binned by longitudes

Region #	Lon	Length [a]	Total % [b]	# of bins [c]	*V* [d]	P-value
7	180W - 150W	665	11%	18	4.6175	< 0.01
8	150W - 120W	403	7%	18	3.6928	< 0.01
9	120W - 90W	435	7%	18	3.1884	< 0.01
10	90W - 60W	624	11%	18	4.4393	< 0.01
11	60W - 30W	468	8%	18	2.539	< 0.01
12	30W - 0	737	13%	18	3.6182	< 0.01
13	0 - 30E	386	7%	18	2.8734	< 0.01
14	30E - 60E	281	5%	12	2.1053	< 0.01
15	60E - 90E	483	8%	18	3.8266	< 0.01
16	90E - 120E	466	8%	18	3.4086	< 0.01
17	120E - 150E	302	5%	12	2.7783	< 0.01
18	150E - 180E	583	10%	18	3.3627	< 0.01

[a] Total mapped crater rim length in km

[b] Percentage of mapped crater rim lengths in the region

[c] Number of bins in the rose diagram (see calculations in the main text)

[d] Test statistic for Kuiper's test

Table 5.5. Statistics of all crater rims binned by 18 global regions

Region #	Lat	Lon	Length [a]	Total % [b]	# of bins [c]	*V* [d]	P-value
19	60N - 90N	ALL	1638	12%	24	3.0743	< 0.01
20	30N - 60 N	180 - 60W	1330	10%	24	1.3339	> 0.15
21	30N - 60 N	60W - 60E	1069	8%	20	1.2447	> 0.15
22	30N - 60 N	60E - 180	1212	9%	20	2.033	< 0.01
23	0 - 30N	180 - 108W	1073	8%	20	2.6142	< 0.01
24	0 - 30N	108W - 36W	601	4%	18	1.9438	0.01 < P-value < 0.025
25	0 - 30N	36W - 36E	688	5%	18	1.6604	0.05 < P-value < 0.10
26	0 - 30N	36E - 108 E	442	3%	15	1.3787	> 0.15
27	0 - 30N	108E - 180	674	5%	18	1.069	> 0.15
28	30S - 0	180 - 108W	464	3%	15	1.2003	> 0.15
29	30S - 0	108W - 36W	743	5%	18	1.5789	0.10 < P-value < 0.15
30	30S - 0	36W - 36E	674	5%	18	1.031	> 0.15
31	30S - 0	36E - 108 E	485	4%	15	1.183	> 0.15
32	30S - 0	108E - 180	415	3%	15	1.1823	> 0.15
33	60S- 30S	180 - 60W	532	4%	18	1.1019	> 0.15
34	60S- 30S	60W - 60E	445	3%	15	0.7679	> 0.15
35	60S- 30S	60E - 180	453	3%	15	1.1146	> 0.15
36	90S - 60S	ALL	760	6%	18	1.4002	> 0.15

[a] Total mapped crater rim length in km

[b] Percentage of mapped crater rim lengths in the region

[c] Number of bins in the rose diagram (see calculations in the main text)

[d] Test statistic for Kuiper's test

Table 5.6. Statistics of extracted straight rim segments binned by 18 regions

Region #	Lat	Lon	Length [a]	Total % [b]	# of bins [c]	*V* [d]	P-value
19	60N - 90N	ALL	763	13%	18	11.3559	< 0.01
20	30N - 60 N	180 - 60W	556	10%	18	3.494	< 0.01
21	30N - 60 N	60W - 60E	461	8%	18	3.5749	< 0.01
22	30N - 60 N	60E - 180	436	7%	18	3.0269	< 0.01
23	0 - 30N	180 - 108W	436	7%	18	3.1152	< 0.01
24	0 - 30N	108W - 36W	211	4%	12	2.323	< 0.01
25	0 - 30N	36W - 36E	383	7%	18	1.7867	0.025 < P-value < 0.05
26	0 - 30N	36E - 108 E	246	4%	12	1.8818	0.01 < P-value < 0.025
27	0 - 30N	108E - 180	310	5%	12	1.9523	0.01 < P-value < 0.025
28	30S - 0	180 - 108W	149	3%	12	2.8751	< 0.01
29	30S - 0	108W - 36W	286	5%	12	1.7934	< P-value < 0.05
30	30S - 0	36W - 36E	243	4%	12	2.7693	< 0.01
31	30S - 0	36E - 108 E	232	4%	12	1.8405	0.025 < P-value < 0.05
32	30S - 0	108E - 180	172	3%	12	1.8191	0.025 < P-value < 0.05
33	60S- 30S	180 - 60W	237	4%	12	2.9545	< 0.01
34	60S- 30S	60W - 60E	139	2%	10	2.5533	< 0.01
35	60S- 30S	60E - 180	167	3%	12	1.5993	0.10 < P-value < 0.15
36	90S - 60S	ALL	401	7%	18	6.7746	< 0.01

[a] Total mapped crater rim length in km

[b] Percentage of mapped crater rim lengths in the region

[c] Number of bins in the rose diagram (see calculations in the main text)

[d] Test statistic for Kuiper's test

Table 5.7. Statistics of all crater rims binned by 18 regions from the center of Rheasilvia basin

Region #	Lat	Lon	Length [a]	Total % [b]	# of bins [c]	*V* [d]	P-value
1	60N - 90N	ALL	700	5%	18	1.11	> 0.15
2	30N - 60 N	180 - 60W	540	4%	18	1.346	> 0.15
3	30N - 60 N	60W - 60E	437	3%	18	1.0962	> 0.15
4	30N - 60 N	60E - 180	295	2%	12	0.8566	> 0.15
5	0 - 30N	180 - 108W	564	4%	18	1.3835	> 0.15
6	0 - 30N	108W -	536	4%	18	1.0411	> 0.15

		36W					
7	0 - 30N	36W - 36E	517	4%	18	0.7986	> 0.15
8	0 - 30N	36E - 108 E	793	6%	18	1.1981	> 0.15
9	0 - 30N	108E - 180	519	4%	18	1.9201	0.01 < P-value < 0.025
10	30S - 0	180 - 108W	946	7%	18	1.6369	0.05 < P-value < 0.10
11	30S - 0	108W - 36W	740	5%	18	1.9467	0.01 < P-value < 0.025
12	30S - 0	36W - 36E	609	4%	18	1.8158	0.025 < P-value < 0.05
13	30S - 0	36E - 108 E	710	5%	18	1.5728	0.10 < P-value < 0.15
14	30S - 0	108E - 180	626	5%	18	1.1363	> 0.15
15	60S- 30S	180 - 60W	1138	8%	20	2.1525	< 0.01
16	60S- 30S	60W - 60E	1132	8%	20	1.5358	> 0.15
17	60S- 30S	60E - 180	1194	9%	20	2.2914	< 0.01
18	90S - 60S	ALL	1702	12%	24	1.9831	0.01 < P-value < 0.025

[a] Total mapped crater rim length in km

[b] Percentage of mapped crater rim lengths in the region

[c] Number of bins in the rose diagram (see calculations in the main text)

[d] Test statistic for Kuiper's test

Table 5.8. Statistics of extracted straight rim segments binned by 18 regions from the center of Rheasilvia basin

Region #	**Lat**	**Lon**	**Length** [a]	**Total %** [b]	**# of bins** [d]	***V*** [c]	**P-value**
1	60N - 90N	ALL	317	5%	12	4.8625	< 0.01
2	30N - 60 N	180 - 60W	230	4%	12	2.5043	< 0.01
3	30N - 60 N	60W - 60E	211	4%	12	4.487	< 0.01
4	30N - 60 N	60E - 180	85	1%	10	2.1615	< 0.01
5	0 - 30N	180 - 108W	207	4%	12	1.6992	0.05 < P-value < 0.10
6	0 - 30N	108W - 36W	173	3%	12	2.7792	< 0.01
7	0 - 30N	36W - 36E	233	4%	12	1.5365	> 0.15
8	0 - 30N	36E - 108 E	339	6%	12	2.3731	< 0.01
9	0 - 30N	108E - 180	277	5%	12	2.8181	< 0.01
10	30S - 0	180 - 108W	465	8%	18	2.2696	< 0.01

11	30S - 0	108W - 36W	326	6%	12	2.7512	< 0.01
12	30S - 0	36W - 36E	210	4%	12	1.7954	0.01 < P-value < 0.025
13	30S - 0	36E - 108 E	328	6%	12	2.1478	< 0.01
14	30S - 0	108E - 180	250	4%	12	1.6663	0.10 < P-value < 0.15
15	60S- 30S	180 - 60W	380	7%	18	4.7307	< 0.01
16	60S- 30S	60W - 60E	498	9%	18	2.5235	< 0.01
17	60S- 30S	60E - 180	529	9%	18	6.0582	< 0.01
18	90S - 60S	ALL	774.1785517	13%	18	7.5653	< 0.01

[a] Total mapped crater rim length in km

[b] Percentage of mapped crater rim lengths in the region

[c] Number of bins in the rose diagram (see calculations in the main text)

[d] Test statistic for Kuiper's test

Appendix B: Statistics for mapped craters on Ceres

Table 5.9. Statistics of all crater rims binned by latitudes

Region #	**Lat**	**Length** [a]	**Total %** [b]	**# of bins** [c]	***V*** [d]	**P-value**
1	60N - 90N	4058	10%	30	5.57	< 0.01
2	30N - 60 N	9923	25%	36	4.7947	< 0.01
3	0 - 30N	9678	25%	36	6.0365	< 0.01
4	30S - 0	7067	18%	36	4.3931	< 0.01
5	60S- 30S	5908	15%	36	5.8524	< 0.01
6	90S - 60S	2669	7%	30	4.6199	< 0.01

[a] Total mapped crater rim length in km

[b] Percentage of mapped crater rim lengths in the region

[c] Number of bins in the rose diagram (see calculations in the main text)

[d] Test statistic for Kuiper's test

Table 5.10. Statistics of extracted straight rim segments binned by latitudes

Region #	**Lat**	**Length** [a]	**Total %** [b]	**# of bins** [d]	***V*** [c]	**P-value**
1	60N - 90N	1638	12%	24	3.0743	< 0.01
2	30N - 60 N	3611	26%	30	2.3484	< 0.01
3	0 - 30N	3478	25%	30	2.7523	< 0.01

4	30S - 0	2781	20%	30	1.8084	0.025 < P-value < 0.05
5	60S- 30S	1430	10%	24	1.1606	> 0.15
6	90S - 60S	760	6%	18	1.4002	> 0.15

[a] Total mapped crater rim length in km

[b] Percentage of mapped crater rim lengths in the region

[c] Number of bins in the rose diagram (see calculations in the main text)

[d] Test statistic for Kuiper's test

Table 5.11. Statistics of all crater rims binned by longitudes

Region #	**Lon**	**Length** [a]	**Total %** [b]	**# of bins** [c]	***V*** [d]	**P-value**
7	180W - 150W	4855	12%	36	2.699	< 0.01
8	150W - 120W	3599	9%	30	2.2982	< 0.01
9	120W - 90W	2904	7%	30	3.0117	< 0.01
10	90W - 60W	3134	8%	30	2.1374	< 0.01
11	60W - 30W	2897	7%	30	2.5721	< 0.01
12	30W - 0	2988	8%	30	1.9001	0.01 < P-value < 0.025
13	0 - 30E	2938	7%	30	1.7071	0.05 < P-value < 0.10
14	30E - 60E	3397	9%	30	2.2768	< 0.01
15	60E - 90E	2694	7%	30	2.1445	< 0.01
16	90E - 120E	2586	7%	30	2.6747	< 0.01
17	120E - 150E	3510	9%	30	4.0474	< 0.01
18	150E - 180E	3798	10%	30	2.2552	< 0.01

[a] Total mapped crater rim length in km

[b] Percentage of mapped crater rim lengths in the region

[c] Number of bins in the rose diagram (see calculations in the main text)

[d] Test statistic for Kuiper's test

Table 5.12. Statistics of extracted straight rim segments binned by longitudes

Region #	**Lon**	**Length** [a]	**Total %** [b]	**# of bins** [c]	***V*** [d]	**P-value**
7	180W - 150W	1341	10%	24	1.8179	0.025 < P-value < 0.05
8	150W - 120W	1127	8%	20	1.8752	0.01 < P-value < 0.025
9	120W - 90W	1149	8%	20	0.986	> 0.15
10	90W - 60W	1426	10%	24	1.1603	> 0.15
11	60W - 30W	1038	8%	20	0.9924	> 0.15

12	30W - 0	1446	11%	24	1.1777	> 0.15
13	0 - 30E	1147	8%	20	1.4165	> 0.15
14	30E - 60E	748	5%	18	1.011	> 0.15
15	60E - 90E	1051	8%	20	1.1563	> 0.15
16	90E - 120E	1077	8%	20	1.0738	> 0.15
17	120E - 150E	785	6%	18	1.5638	0.10 < P-value < 0.15
18	150E - 180E	1363	10%	24	1.0411	> 0.15

[a] Total mapped crater rim length in km

[b] Percentage of mapped crater rim lengths in the region

[c] Number of bins in the rose diagram (see calculations in the main text)

[d] Test statistic for Kuiper's test

Table 5.13. Statistics of all crater rims binned by 18 global regions

Region #	**Lat**	**Lon**	**Length** [a]	**Total %** [b]	**# of bins** [c]	***V*** [d]	**P-value**
19	60N - 90N	ALL	4058	10%	30	5.57	< 0.01
20	30N - 60 N	180 - 60W	3981	10%	30	2.7884	< 0.01
21	30N - 60 N	60W - 60E	3200	8%	30	3.4891	< 0.01
22	30N - 60 N	60E - 180	2742	7%	30	4.5204	< 0.01
23	0 - 30N	180 - 108W	2393	6%	24	3.4898	< 0.01
24	0 - 30N	108W - 36W	1856	5%	24	3.4614	< 0.01
25	0 - 30N	36W - 36E	1617	4%	24	3.1868	< 0.01
26	0 - 30N	36E - 108 E	1923	5%	24	3.1826	< 0.01
27	0 - 30N	108E - 180	1887	5%	24	2.7744	< 0.01
28	30S - 0	180 - 108W	2103	5%	24	3.7472	< 0.01
29	30S - 0	108W - 36W	950	2%	20	2.7969	< 0.01
30	30S - 0	36W - 36E	1596	4%	24	3.0847	< 0.01
31	30S - 0	36E - 108 E	951	2%	20	2.4685	< 0.01
32	30S - 0	108E - 180	1465	4%	24	2.341	< 0.01
33	60S- 30S	180 - 60W	2023	5%	24	3.391	< 0.01
34	60S- 30S	60W - 60E	1501	4%	24	3.3147	< 0.01
35	60S- 30S	60E - 180	2382	6%	24	4.3499	< 0.01
36	90S - 60S	ALL	2669	7%	30	4.6199	< 0.01

[a] Total mapped crater rim length in km

[b] Percentage of mapped crater rim lengths in the region

[c] Number of bins in the rose diagram (see calculations in the main text)

[d] Test statistic for Kuiper's test

Table 5.14. Statistics of extracted straight rim segments binned by 18 global regions

Region #	Lat	Lon	Length [a]	Total % [b]	# of bins [c]	*V* [d]	P-value
19	60N - 90N	ALL	1638	12%	24	3.0743	< 0.01
20	30N - 60 N	180 - 60W	1330	10%	24	1.3339	> 0.15
21	30N - 60 N	60W - 60E	1069	8%	20	1.2447	> 0.15
22	30N - 60 N	60E - 180	1212	9%	20	2.033	< 0.01
23	0 - 30N	180 - 108W	1073	8%	20	2.6142	< 0.01
24	0 - 30N	108W - 36W	601	4%	18	1.9438	0.01 < P-value < 0.025
25	0 - 30N	36W - 36E	688	5%	18	1.6604	0.05 < P-value < 0.10
26	0 - 30N	36E - 108 E	442	3%	15	1.3787	> 0.15
27	0 - 30N	108E - 180	674	5%	18	1.069	> 0.15
28	30S - 0	180 - 108W	464	3%	15	1.2003	> 0.15
29	30S - 0	108W - 36W	743	5%	18	1.5789	0.10 < P-value < 0.15
30	30S - 0	36W - 36E	674	5%	18	1.031	> 0.15
31	30S - 0	36E - 108 E	485	4%	15	1.183	> 0.15
32	30S - 0	108E - 180	415	3%	15	1.1823	> 0.15
33	60S- 30S	180 - 60W	532	4%	18	1.1019	> 0.15
34	60S- 30S	60W - 60E	445	3%	15	0.7679	> 0.15
35	60S- 30S	60E - 180	453	3%	15	1.1146	> 0.15
36	90S - 60S	ALL	760	6%	18	1.4002	> 0.15

[a] Total mapped crater rim length in km

[b] Percentage of mapped crater rim lengths in the region

[c] Number of bins in the rose diagram (see calculations in the main text)

[d] Test statistic for Kuiper's test

Supplementary Data

All mapping shapefiles can be previewed at https://data.mendeley.com/datasets/tr7wwdz68c/draft?a=c9dbff41-a2ae-47ea-96ad-fbe8dd25d53f.

CHAPTER 6

THE TRANSITION FROM JOINTING TO FAULTING OBSERVED AT THE KOE'A FAULT SYSTEM, HAWAII VOLCANOES NATIONAL PARK, HAWAII [9]

[9] Cheng, H. C. J., Mrazek. J and Klimczak. C To be submitted to *GSA Bulletin*.

Abstract

The active Koa'e Fault Zone in the Hawaii Volcanoes National Park, Hawaii shows prominent fault scarps with opening displacement components of up to several meters. These are locally accompanied by monoclines, numerous subparallel minor faults, and joints. The opening displacement components of the structures include apertures from jointing and dilation from normal faulting, making them mixed-mode structures. To investigate the transition from opening-mode to sliding-mode fracturing, I conducted structural mapping along the Koa'e Fault Zone and collected measurements of orientations, structural relief, opening displacements, lengths, and depths of openings along faults and joints of various sizes. From the field observations, I developed a conceptual model with the different stages and spatial connections of the growth of the Koa'e Fault Zone. Growth of the largest faults started by jointing but transitioned to faulting, displaying similar profiles of opening and relief along the fault length. Monoclines were interpreted to form when the upward propagating subsurface fault or blind fault interacts with the surface faults in previous studies. I establish a sub-linear displacement-to-length scaling relationship of the fault zone that captures the transition of jointing to faulting and accounts for the complex structure associated with the monoclines. The scaling indicates that monoclines form shortly after the fracturing mode transition from jointing to faulting, but before faulting entirely dominates the accumulation of displacement. The growth and displacement of this type of mixed-mode fracturing may be applicable elsewhere on Earth and other planetary bodies.

Introduction

Mixed-mode Fracturing

In an extensional tectonic regime, tensile stresses at and near the surface allow for the formation of joints that may propagate downward until they reach a depth where the overburden counteracts any tensile stresses causing the lithosphere to shift to a fully compressive stress state. At and below that depth, conditions are met for joints to transition to normal faults (Figure 6.1a) and normal faulting becomes the dominant fracturing type. The resulting fractures in such a tectonic regime possess both opening-mode and sliding-mode displacement components, and joints and normal faults form as part of the same fracture population. Such rock fracturing behavior is a form of mixed-mode fracturing. Mixed-mode structures are commonly associated with large rift systems on Earth, such as the Almannagjá normal fault at the Reykjaneshryggur-Langjökull rift system of southwest Iceland (e.g., Gudmundsson, 1992, 2011), Koa'e Fault Zone associated with the Kīlauea volcano rift zone in Hawaii (Figure 6.1b; Denlinger and Okubo, 1995; Holland et al., 2006; Martel and Langley, 2006; Ge et al., 2019), and the Wonji Fault Belt associated with the Ethiopian Rift in East Africa (e.g., Acocella et al., 2003). Structures on other planetary bodies, such as pit crater chains associated with normal faulting on Mars (Ferrill et al., 2004) and troughs on asteroid Vesta (Cheng and Klimczak, 2022) are also interpreted as mixed-mode structures.

A widely used method to characterize fracture growth and fracture populations are maximum displacement-to-length (D_{max}/L) scaling. This sacling has been applied to Earth (e.g., Dawers et al., 1993; Poulimenos, 2000; Wilkins and Gross, 2002) but also other rocky planetary bodies (e.g., Schultz, 1997; Schultz et al., 2006; Polit et al., 2009).

The method is applied widely in structural geology and tectonics, such as inferring tectonic strains (e.g., Nahm and Schultz, 2011), studying fault growth, segmentation, and linkage (e.g., Cowie et al., 1993; Hughes and Shaw, 2014), inferring geometric or mechanical properties of the rock volume (e.g., Dawers et al., 1993; Soliva et al., 2005), as well as fluid flow through jointed rock (Klimczak et al., 2010).

Numerous studies have demonstrated that maximum displacements along faults and opening-mode fractures scale with their lengths (e.g., Delaney and Pollard, 1981; Muraoka and Kamata, 1983; Cowie and Scholz, 1992; Vermilye and Scholz, 1995; Olson, 2003; Schultz et al., 2006; 2008; 2013). Faults display a power-law scaling relationship (Scholz et al, 1993; Schultz et al., 2013), where the exponent is 1, indicating a linear relationship between *Dmax* and *L*. Such fault growth is self-similar, with smaller and larger faults in the same population sharing the same overall geometries. It is consistent with the elastic-plastic fracture mechanism by which faults propagate when the shear yield strength is exceeded at their tips and singular stress magnitudes may not be produced during the structural growth.

In contrast, opening-mode fractures have a power-law exponent of 0.5 (Olson, 2003). Their growth is not self-similar, with the aperture being proportional to the square root of fracture length for the fracture geometries. This scaling is predicted by linear elastic fracture-mechanics model with the structure propagation governed by mode-I (opening) dynamic fracture toughness and attendant dilatant cracking under small near-tip stress within a zone of small-scale yielding at the structural tip where the effects of plastic zone are negligible.

The D_{max}/L scaling behavior of mixed-mode fractures has not yet been established, including the evolution from opening- to shear displacements, and any associated fault dilation (Figure 6.1). In this scenario, pure joints, sheared joints, and dilational normal faults may occur within the same fracture population. The total observed displacement of fractures in this population (Figure 6.1, black vector) consists of different displacement components. Pure joints show only opening displacement, i.e., the joint aperture (Figure 6.1a, red vector). Sheared joints show the largest component along the horizontal contributed by the joint aperture and the fault dilation (heave), with a smaller vertical component with the fault throw (Figure 6.1a, red and blue vectors). Dilational normal faults may or may not have an aperture from a pre-existing joint preserved. If a blind normal fault started slipping, all opening is dilation with no aperture. Otherwise, if a joint transitioned to become a major fault, the opening will have joint aperture and fault dilation. For such structures, the dilational component dominates the opening whereas the relief is substantial and is the largest of the displacement components.

I hypothesize the scaling of the mixed-mode fractures should follow the scaling of joints and subsequently that of faults. To estimate the jointing-faulting transition in the scaling, I calculated the expected behavior using the scaling behaviors for a set of typical joint and fault parameters (Figure 6.1b). Following the idealized geometry of mixed-mode fracture development from Figure 6.1a, I assume values for γ and α to be 0.1, typical values for faulting and jointing on Earth. Normal faulting is assumed to take place with fault dips (θ) of 60º. Considering the depth of the jointing-faulting transition for basalt (Gudmundsson et al., 2003) and assuming a penny-shaped fracture shape, the joint

could reach a length of ~1600 m it they reactivates as a fault. For the scaling, it follows that joint displacement is equal to the aperture (*A*; Figure 6.1a), and it follows the scaling of pure jointing at short fracture lengths (Figure 6.1b). At lengths where joints are expected to transition to faults, faulting is expected to have much higher displacements and show a larger slope of the scaling relationship than jointing. The opening of the fracture is expected to increase for non-vertical fault planes, adding the dilational component (S_h) to the aperture. The total fracture displacement should include *A* and the fault slip (*S*), and its scaling should change to follow that normal faulting. However, it is unclear what happens at the jointing/faulting transition.

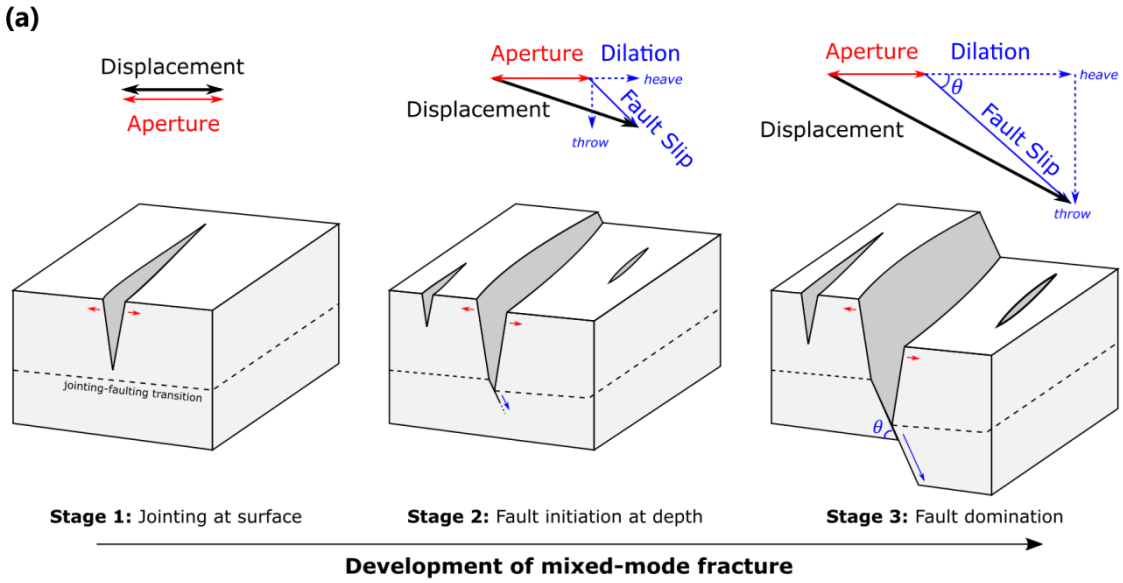
(a)
Displacement
Aperture
Aperture
Dilation
heave
Displacement
Fault Slip
throw
Aperture
Dilation
θ
heave
Displacement
Fault Slip
throw
jointing-faulting transition
θ
Stage 1: Jointing at surface
Stage 2: Fault initiation at depth
Stage 3: Fault domination
Development of mixed-mode fracture

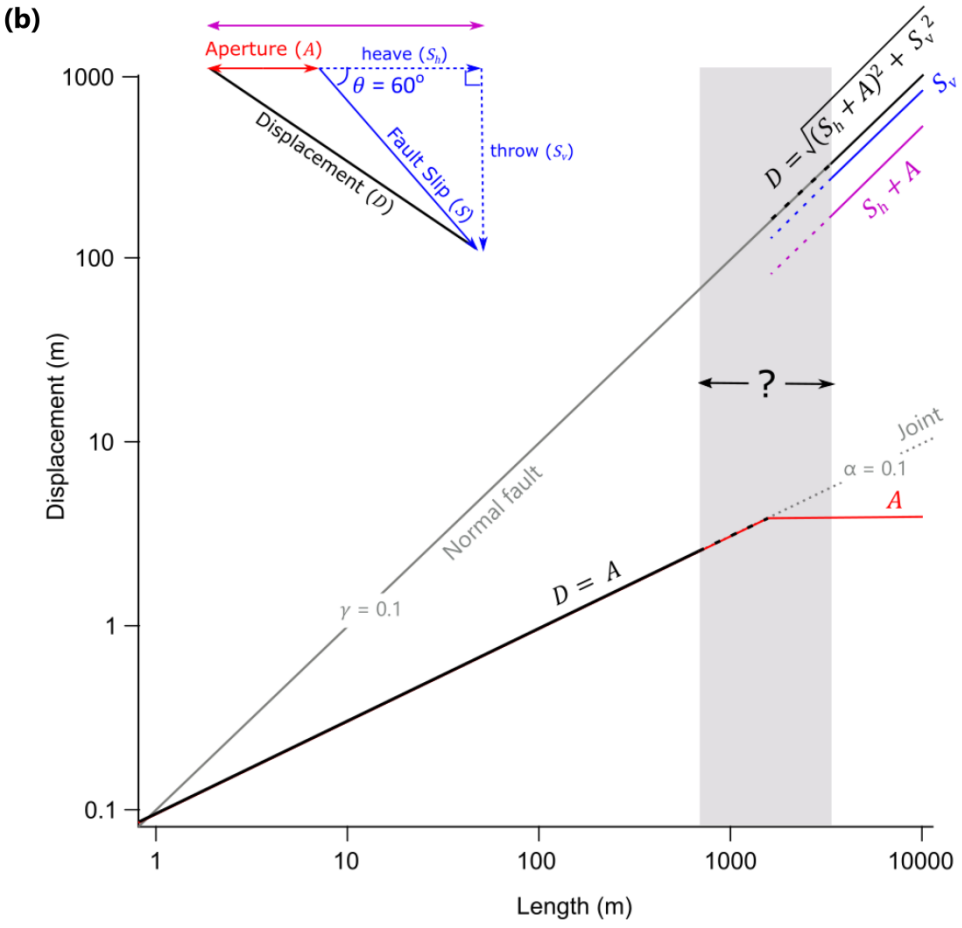
(b)
Aperture (A)
heave (Sh)
θ = 60°
Displacement (D)
Fault Slip (S)
throw (Sv)
D = √((Sh + A)² + Sv²)
Sv
Sh + A
?
Joint
α = 0.1
A
Normal fault
γ = 0.1
D = A
Displacement (m)
1000
100
10
1
0.1
1
10
100
1000
10000
Length (m)

Figure 6.1. *Growth and scaling of mixed-mode fractures. (a) Block diagrams of a pure joint (left), sheared joint (middle), and dilational normal fault (right) that may be found within the same mixed-mode fracture population representing different stages of fracture growth. Pure jointing occurs at the surface, in which the displacement (black arrows) is equal to the joint aperture (red arrows). When the joints reach a critical depth, they transit to become sheared joints. At this stage, the displacement is a combination of the aperture of the joint (red arrows) and the fault slip (blue arrows). The horizontal displacement is the sum of the joint aperture and horizontal displacement component of the fault slip vector. The horizontal displacement widens the original aperture, thus adding a dilational component to the faulting. When the sheared joint is penetrating deep into the lithosphere, it becomes a dilational normal fault with the total displacement dominated by its slip. (b) Predicted D_{max}/L scaling of mixed-mode fracturing. The D_{max}/L scaling behaviors of jointing and faulting are plotted in grey solid and dotted lines, respectively, as reference. The scaling for mixed-mode fracturing is plotted as a black solid line. It starts by following the joint scaling. After it reaches the jointing-faulting transition, it follows the normal fault scaling, with an unknown transition (grey area). For comparison, the individual displacement components are also plotted as presented in (a), including the aperture of jointing (A) in red, the total opening of the fault (sum of A and heave, S_h) in purple, and the fault throw, S_v, in blue.*

Geologic Setting

To investigate the evolution of fracture growth from jointing to faulting and its scaling, I conducted field work at the Koa'e Fault Zone at Hawaii Volcanoes National Park, Hawai‘i. The Koa'e Fault Zone is an active ~12-km long, ~3-km wide, SW-trending

normal fault zone (e.g., Denlinger and Okubo, 1995; Peacock and Parfitt, 2002; Ge et al., 2019) located between the Southwestern and East Rift Zones that join at the Kīlauea edifice (Figure 6.2a). There are three major faults in the system: the Kulanaokuaiki Fault, Ohale Fault, and an unnamed fault (Figure 6.2b). All show a dilational component, and all are associated with numerous subparallel minor faults and joints (Holland et al., 2006; Martel and Langley, 2006). The normal faults have scarps mostly facing toward Kilauea with reliefs of as much as 25 m and a dilational component of up to several meters wide (Holland et al., 2006). The Koa'e Fault Zone is an ideal site to investigate the transitional structure from opening to sliding-mode fracturing by D_{max}/L scaling analyses because the structures are well-preserved and their length scales range over a few orders of magnitude.

Field studies have previously been conducted to understand the propagation of faults and the fault internal structure within basaltic sequences (e.g., Macdonald, 1957; Duffield, 1975; Holland et al., 2006; Martel and Langley, 2006; Kaven and Martel, 2007; Podolsky and Roberts, 2008; Figure 6.2b). Geologic observations and lava flow records indicate that the current scarp must have formed after the cooling of surface lava flow, with the most recent resurfacing event at this fault zone occurring ~400–750 years ago (Duffield, 1975; Wolfe and Morris, 1996). The subvertical fault scarps have a fractured slab-like ramp structure, connecting the footwall and hanging wall with a joint between the fault scarp and a monocline (Figure 6.2c). This ramp structure is often referred to as a monocline or monoclinal bridge. Some monoclines have a cavity underneath their surface slab, or they have debris accumulated at the base of their hanging wall.

Several conceptual models of fault geometry and interpretation of the monocline have been proposed. Duffield (1975) suggested that faults are formed by en echelon cracks at the surface, which propagate down with the down-dropped northern block, and warping into a monoclinal flexure. Echelon cracks subsequently join to form a single master fault, with the tilted slabs of the monocline collapsing at an advanced stage of the faulting. Based on two- and three-dimensional mechanical modeling, Martel and Langley (2006) and Kevan and Martel (2007) argue that the monocline is a remnant of flexure formed by a blind, upward-propagating, subvertical fault with a cavity forming at the upper tip of the blind fault. Based on scaled analog modeling, Holland et al. (2006) inferred that the early stage of normal faulting involves prominent subvertical surface joints propagating downwards, where some joints are connected with blind faults at depths. The monocline has also been interpreted as the result of antithetic fracturing after initial surface flexure and resurfacing events influencing the fault morphology (e.g., Holland et al., 2006; Martel and Langley, 2006; Kevan and Martel, 2007). Podolsky and Roberts (2008) suggested that the width of monoclines represents the heave of blind faults beneath the most recent lava flow that resurfaced the active fault, and that it records the reemergence of the fault that had previously propagated to the surface before recent lava deposition rather than upward propagation of a new fault.

The Koa’e Fault Zone develops at the southern flank of the Kilauea volcano (Figure 6.2a) and it has an overall southward displacement, breaking off from the volcanic structure. The fault slip is caused mostly by the gravitational forces from the weight of the Kilauea volcano, as well as historical earthquakes and magmatic activity (e.g., two earthquakes with magnitude > 7 in 1975 and 2018; Chen et al., 2019). The age

of the Koa'e Fault Zone has been suggested to be ~1000 years old owing to its subdued topographic expression (e.g., Duffield., 1975), but recent studies suggested an even older age of the fault zone owing to the lava coverage (e.g., Day et al., 2005). In addition, the topography of the seafloor on the south coast of the Big Island of Hawaii has massive landslides that parallel the Koa'e Fault Zone, with the same direction of displacements (Figure 6.2a). These landslides potentially occurred as a result of the past rifting and catastrophic collapse of the southern flank of the Kilauea volcano, and that may recor in the future.

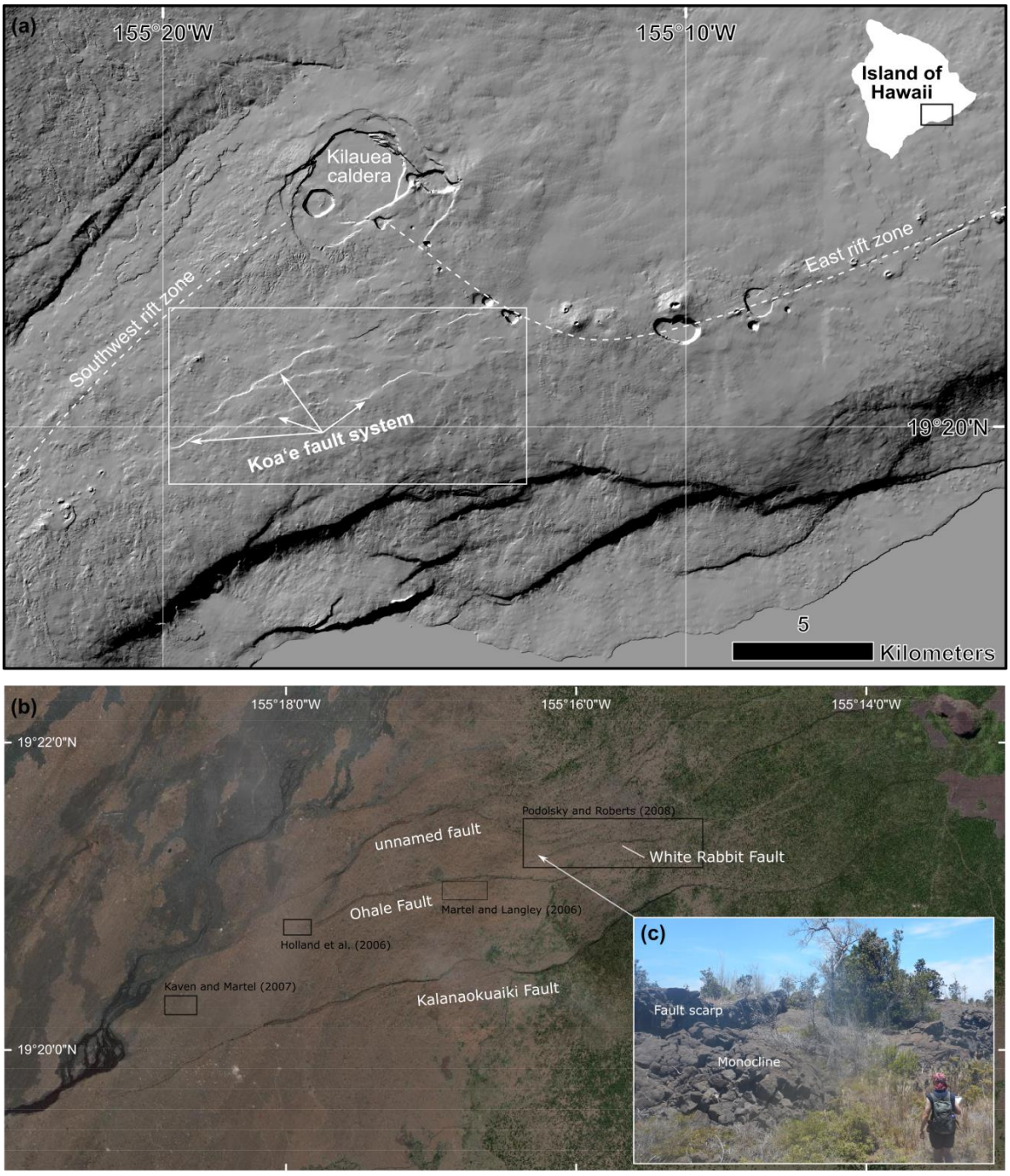

Figure 6.2. *Geographic overview of the Koa'e Fault Zone located in Hawaii Volcanoes National Park, Hawaii. (a) Shaded-relief location map of the east and southwest rift zone merging at the Kilauea caldera at the Hawaii Volcanoes National Park, Hawai'i. The Koa'e Fault Zone is located at the south of the caldera inbetween the two rift zones. The upper right insert shows the location on the Island of Hawaii. (b) Satellite image of the*

field area of the Koa'e Fault Zone. The field field localities of previous studies (Holland et al., 2006; Martel and Langley, 2006; Kaven and Martel, 2007; Podolsky and Roberts, 2008) are outlined with a black box on the map. The Kulanaokuaiki Fault, Ohale Fault, White Rabbit Fault, and an unnamed fault are labeled in white. (c) Photograph of the White Rabbit Fault showing the fault scarp and monocline separated by an opening. The view is to the south, and the fault scarp is facing the north.

Goal and Significance of the Study

I aim to investigate the transition from jointing to faulting by developing a conceptual model of Koa'e Fault Zone evolution and establishing the D_{max}/L scaling of this mixed-mode fracture system. Importantly, this D_{max}/L scaling of this type of fracture population has not been investigated before. While previous studies mapped the fault exposures of single segments (see Figure 6.2b), the mapping and their measurements are not continuously conducted and collected as one large fracture system. Expanding upon these previous studies, I focus on geologic and structural observations and displacement and length measurements of joints, normal faults, and monoclines to capture the development of the fault system. I combine the field observations with previous studies to develop a conceptual model of the structures of various lengths along the fault zone that represent stages in the formation of the overall fault system. The conceptual model, particularly the role of the monoclines and what aspect of the overall fault geometry they represent, is essential to interpret the meaning of displacement and length measurements. I analyze the fault relief, joint aperture, fault dilation, structural length, and the width and height of the monoclines to establish the D_{max}/L scaling relationship of this mixed-mode fracture system.

Field methods

I conducted structural field mapping in the Koa'e Fault Zone, focusing on the Kulanaokuaiki Fault, Ohale Fault, White Rabbit Fault, and their associated joints and sheared joints. The mapping was made on satellite photographs printed at a scale of 1:10,000. I measured fracture orientations, structural reliefs, opening displacements, lengths, and, where possible, joint depths at 234 field localities recorded with a Garmin handheld GPS. Measurements were taken using handheld tapes on smaller exposures and a *TruPulse 200X* laser rangefinder on larger exposures. The accuracy of the tape is ±0.05 cm and, the accurany of the laser rangefinder is ±4 cm in distance. The attitudes of faults and joints were measured with a Brunton compass.

In the field, I recorded the geologic observations as structural descriptions on maps, field sketches, and photographs. The various types of displacement components, including the reliefs of fault scarps, dilational components of faults, and heights and widths of monoclines, were collected with approximately equal spacing of field localities along the faults and monoclines all named above. I also measured displacement profiles of five unnamed faults without monoclines, as well as the maximum apertures and corresponding lengths of 26 sheared joints and 50 pure joints. Measurements were taken mostly from the hanging wall of the fault where offset geological markers (such as the shape of the fracture sides, lava flows, and rock pieces) indicated the original connection of the two fracture sides.

Koa'e Fault Zone

The structural map (Figure 6.3) includes all accessible exposures along the main faults of the Koa’e Fault Zone with part of the measurements presented. The main fault

structures include the Kalanaokuaki Fault, Ohale Fault, and White Rabbit Fault. All of these have fault scarps with an opening, as well as a monocline throughout the entire or part of the structure (see measurements in Figure 6.3). Two minor faults have a monocline; one is associated with the Ohale Fault, and the other is associated with the White Rabbit Fault. Numerous small joints and faults are associated with the fault zone (Figure 6.3).

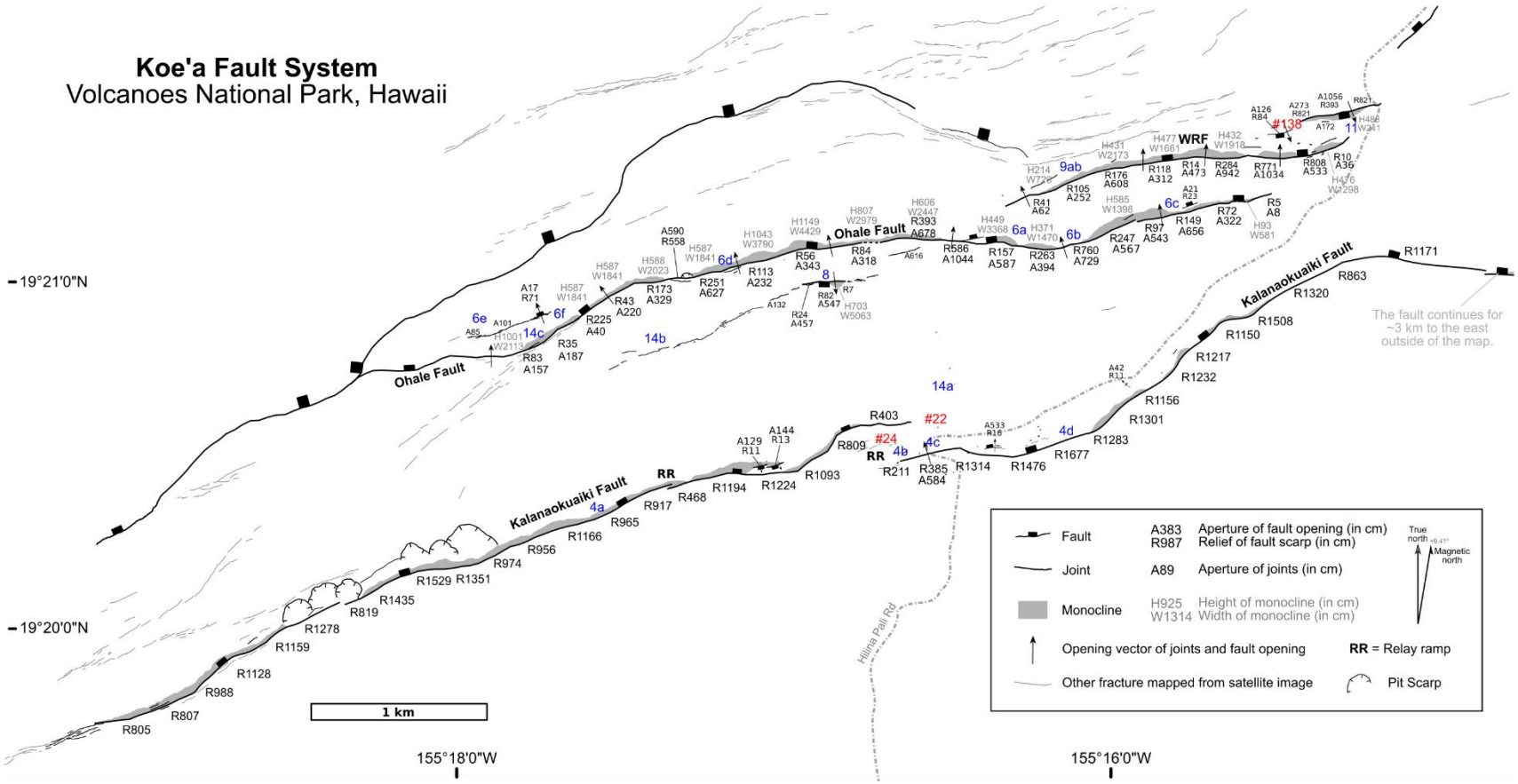

Figure 6.3. *Structural map of the Koa'e Fault Zone. Some field measurements are not shown on the map owing to the scale. Blue labels indicate the locations of subsequent figures, and red labels indicate the field locality of Figures 6.10–6.12. WRF = White Rabbit Fault.*

Kalanaokuaiki Fault

The Kalanaokuaiki Fault is approximately 12 km long, and I mapped 8.6 km of this from the western tip. Beyond this for ~3 km to this east, the fault is impossible to discern due to the dense vegetation. Three mapped fault segments are separated by relay ramps. The western tip of the fault ends in a zone of en echelon jointing that extends for another ~1 km, possibly representing part of the fault damage zone. Associated subparallel joints and minor faults are mapped along the Kalanaokuaiki Fault with some minor faults being synthetic and others being antithetic to the Kalanaokuaiki Fault (Figure 6.3). Pit craters with widths that exceed 10 m are located near the center of the westernmost section of the Kalanaokuaiki Fault.

The Kalanaokuaiki Fault has monoclines directly adjacent to the fault scarps, especially in the western section (Figure 6.3). The exposed subvertical fault scarp utilizes preexisting columnar joints as indicated by the jagged edges of the scarp (Figure 6.4a). The monocline is highly fractured and covered with a fine-grained weathered layer of sand. A fresher brecciated edge has rock debris in hexagonal shapes from columnar joints. No dilational component of the fault was seen, but that may be because the monocline is collapsed in many places, which may have filled the void. In some areas, only the interior of the monocline collapsed into any dilational void, with the monoclinal flexure of the uppermost basaltic layer forming a monocline bridge (Figure 6.4b). A side view of the internal structure of the fault is exposed where the Hilian Pali Road cuts the fault, which coincides with one of the relay ramps of the fault (Figures 6.3, 6.4c). The monocline collapsed into the 5.8-meter-wide void directly beneath the fault scarp, and the remaining parts of the monocline show the surface flexure of the structure (Figure 6.4c).

A large portion of the eastern parts of the fault lacks a monocline and has only a predominantly subvertical fault scarp (Figures 6.3 and 6.4d). The fault scarp is highly irregular owing to vertical columnar joints and horizontal basaltic layers, and debris obscures the lower part of the scarp (Figure 6.4d). The hanging wall shows hexagonal columnar joints. Distinctly larger joints that are not part of the columnar jointing are subparallel to the major fault scarp, utilize the preexisting basaltic joints, and result in a zigzag pattern of the opening displacement (Figure 6.4d). While some joints are isolated and subparallel to one another, other joints interact with other joints, creating en echelon patterns.

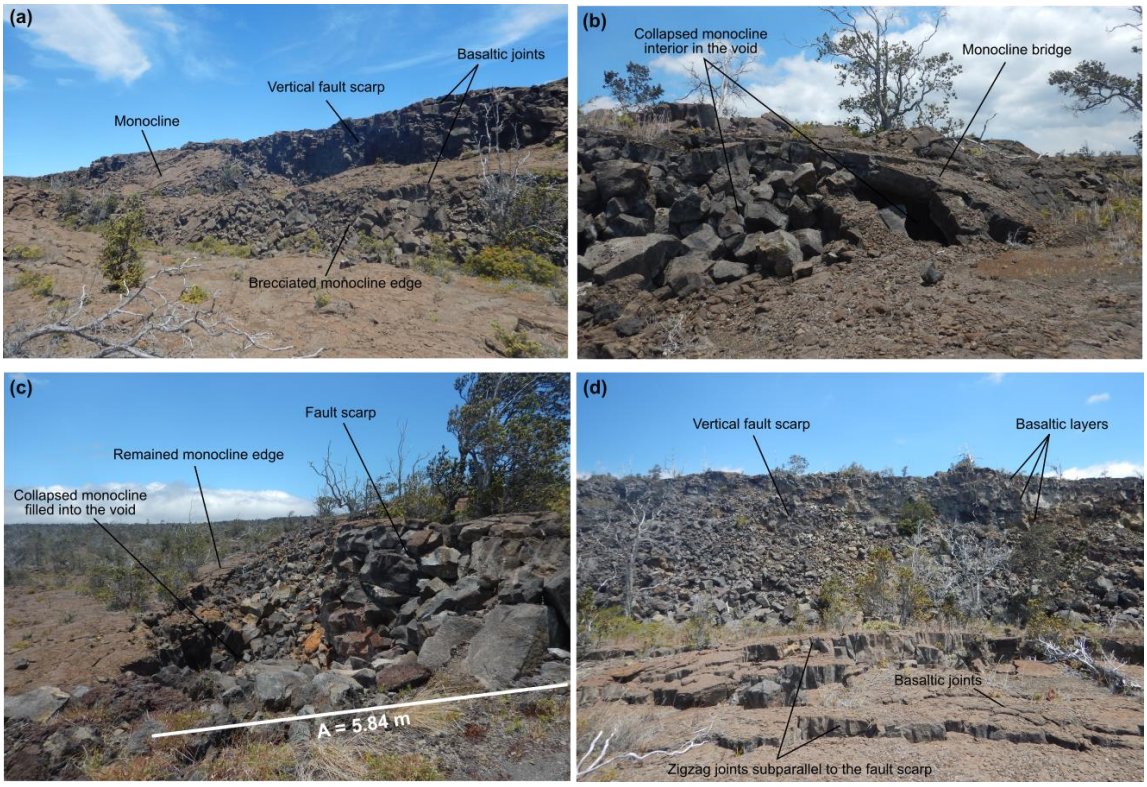

Figure 6.4. *Photographs of the fault scarp at the Kalanaokuaiki Fault. (a) Subvertical fault scarps with monocline. The view is toward the southeast. (b) The interior of the monocline collapse leaving the monocline bridge. The view is toward the southwest. (c)*

Side view of the Kalanaokuaiki Fault cut by Hilian Pali Road. The view is toward the east. (d) Vertical fault scarps with subparallel joints. The view is toward the south. Photo locations are indicated in Figure 6.3.

Since the monocline is mostly collapsed and opening displacements cannot be systematically observed, I recorded only the total relief as measured from the top of the footwall to the hanging wall. I plotted the relief along the length of the fault to analyze the relief profile (Figure 6.5), consisting of 45 measurements taken at a spacing of ~200 m. The middle segment of the relief profile has a maximum relief of 12.2 m near its center. Relay ramps are presented in the profiles with overlapping reliefs, indicating fault linkage where the fault segments are not yet coalesced into one fault plane but have interacted with one another. The general plateaued shape of the relief profile can also be attributed to these fault interactions, which is consistent with the field observations.

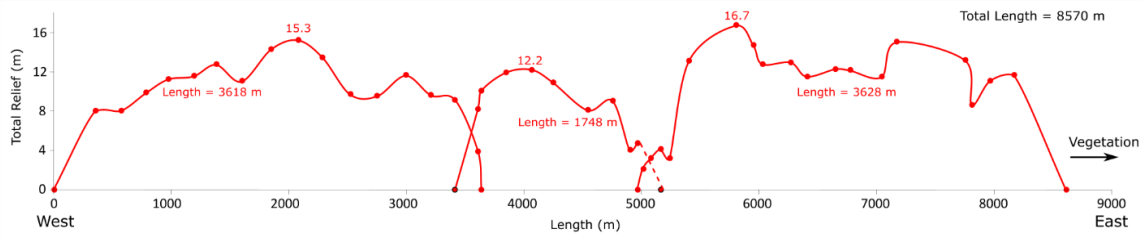

Figure 6.5. *Relief profile of the Kalanaokuaiki Fault.*

Ohale Fault

The Ohale Fault was mapped along its 5.4 km length to its western tip, where it merges with the unnamed fault (Figure 6.3). A monocline is present along almost the entire fault scarp (Figure 6.6a), except for a few locations (Figure 6.3, such as in Figure 6.6b). The fault scarp is highly fragmented by preexisting columnar joints and

subhorizontal basaltic layer contacts. No relay ramps were noted; however, the fault scarp and monocline are absent in two locations near the center of the Ohale fault with only jointing connecting the fault (dashed line in Figure 6.3). These may be locations of fault segmentation and linkage occur. The minor faults have scarps that face northwest (such as in Figure 6.6c), thus being synthetic faults. Subparallel joints, minor faults, and small pits are associated with the Ohale Fault, with some large joints on the footwall (Figure 6.6d).

No fault scarp occurs within ~ 1 km of the western tip of the Ohale Fault, leaving the monocline as the main observable structure (Figure 6.3). The fault scarp of an unnamed fault merges with the monocline at the western tip of the Ohale Fault, and a prominent fault scarp extends to the west of this intersection (Figures 6.3 and Figure 6.6e). A zone of en echelon joints is present between the Ohale Fault and the unnamed fault (Figures 6.3 and 6.6e) on the hanging wall of the Ohale Fault, which is also the footwall of the unnamed fault. The joints have a zigzag map pattern created the preexisting hexagonal columnar joints. The base of the unnamed fault is filled with a thick layer of black sand. As a result, the relief and structures on the hanging wall cannot be accurately measured. The western part of the Ohale Fault has well-preserved pahoehoe lava, compared with the eastern part where the surface is more degraded (such as in Figure 6.6a). Along the monoclines, pahoehoe lava flows commonly have an upslope paleo-flow direction (Figure 6.6f), indicating that the terrain was flat or sloped in the opposite direction at the time of flow emplacement, and that the relief of the monocline and fault scarp formed later.

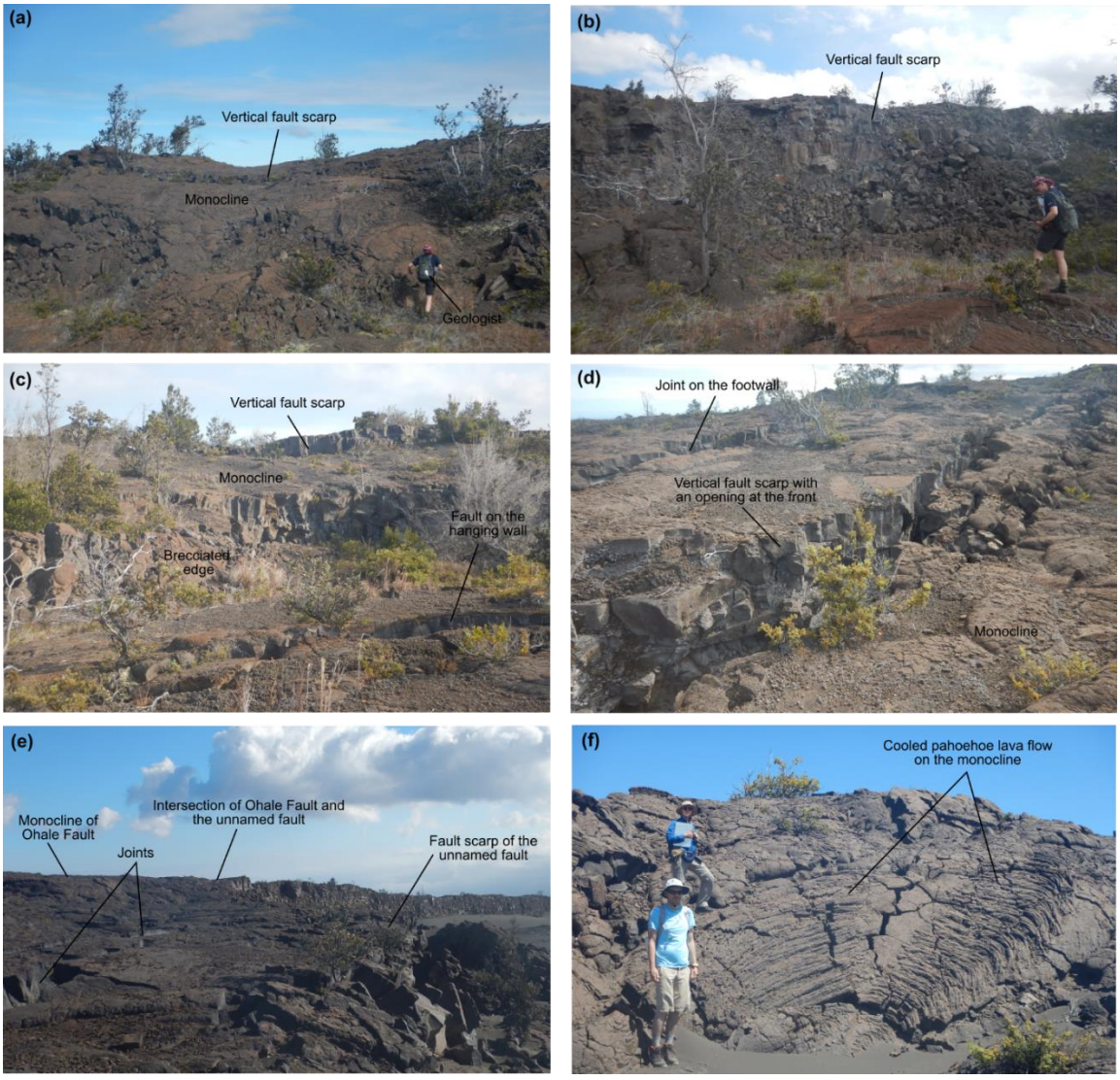

Figure 6.6. *Photographs of structural relationships of the Ohale Fault. (a) Subvertical fault scarps with monocline. The view is toward the south. (b) Vertical fault scarps with no monocline. The view is toward the south. (c) A subparallel small fault at the hanging wall. The view is toward the south. (d) Opening in front of the fault scarp with a large subparallel on the footwall, viewing from the top of the monocline. The view is toward the southeast. (e) The intersection of the western tip of Ohale Fault and the unnamed fault, with the view direction to the west. (f) Pahoehoe lava flow with the flow direction*

upslope of the monocline. The view is toward the southeast. Figure locations are shown on Figure 6.3.

The morphology of the Ohale Fault is dominated by the widths and heights of the monocline (Figure 6.7). The relief of the fault and the opening displacement are the only morphologically most pronounced fault geometric structures in the displacement profile where there are no monoclines (Figure 6.7a). The relief and opening measured along the fault scarp mostly mimic one another. The relief profile has several maxima and minima, which may be the result of fault segmentation, with segments having coalesced during fault growth. That preexisting columnar joints were utilized during fault growth may also contribute to the non-systemic relief and opening profiles. The width and height of the monocline vary along the profile, but their maxima are both located near the center, and relief decreases towards the tips (Figure 6.7b). The monocline is typically taller than it is wide along the fault. Local minima of displacements on the fault (Figure 6.7a) and on the monocline (Figure 6.7b) occur at a large joint is on the footwall.

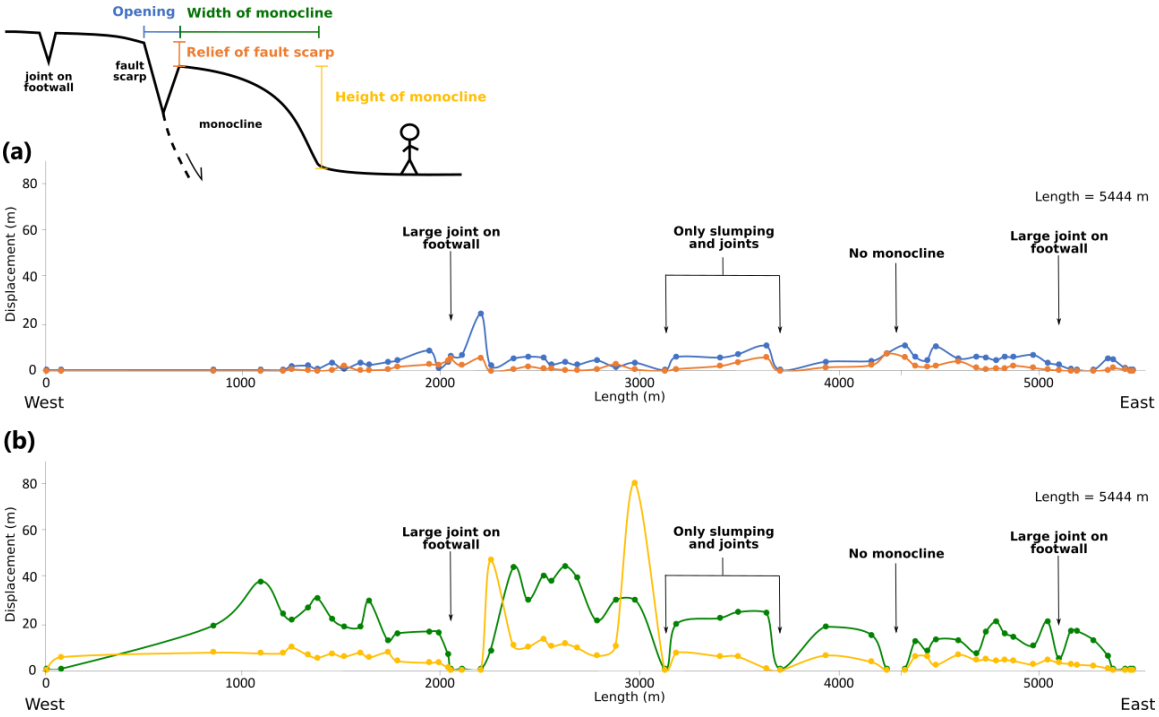

Figure 6.7. *Displacement profile of the Ohale Fault. (a) Displacement profile of the fault, including opening in blue and relief in orange. (b) Measurements profile of the monocline, including the height in yellow and width in green. Note the fault morphologic measurements in the cross-sectional diagram match the colors in the profile.*

A minor fault is associated with monoclines at the south of the Ohale Fault where it connects to a large set of echelon joints. The fault scarp faces south to southeast, antithetical to the major faults and most of the smaller faults in the area. Its displacement and monocline profiles are dominated by the opening at the western portion and the width of the monocline at the eastern portion (Figure 6.8). Maximum relief of the fault scarp coincides with maximum aperture of the opening. The height profile of the monocline has a plateau shape.

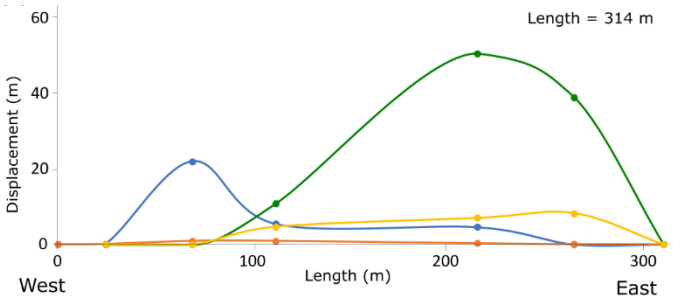

Figure 6.8. *Displacement profile of the fault with monoclines associated with the Ohale Fault. See the cross-sectional diagram in Figure 6.7 for the color code of the displacement profile.*

White Rabbit Fault

The White Rabbit Fault is 2.1 km long, and a monocline is present along nearly the entire length of the fault (Figures 6.3 and 6.9). The fault is located north of the eastern portion of the Ohale Fault (Figure 6.3), with which it overlaps for 1.5 km and shares similar observations (Figures 6.6a and 6.8a). The fault scarp is highly fragmented by preexisting columnar joints and subhorizontal lava flow contacts. No relay ramps could be seen. The structures interpreted as “breached relay ramp” by Podolsky and Roberts (2008) along the White Rabbit Faults do not show any differences to the monocline and I do not observe two interacting fault tips bounding a relay ramp, such as at the Kalanaokuaiki Fault (Figure 6.3). Therefore, I consider the structure as part of the monocline. Only the monocline is present at the two tips of the structure, with no fault scarps and opening (Figure 6.3; also see Figure 6.9). The White Rabbit Fault is associated with several subparallel joints and minor faults.

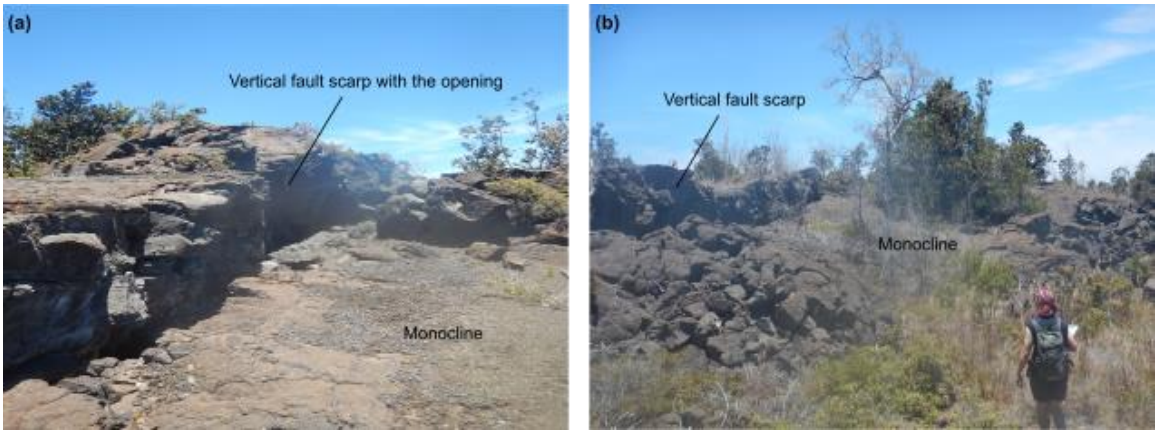

Figure 6.9. *Photographs of the White Rabbit Fault. (a) View of the total opening and relief of the fault scarp. The view is toward the southwest. (b) View of the fault scarp and monocline as seen from the hanging wall. The view is toward the south.*

Based on the field measurements, the geomorphology of the White Rabbit Fault is mostly dominated by the width of its monocline (Figure 6.10). Similar to the Ohale Fault, the reliefs of the fault and the opening are more pronounced where the monocline is not present, which is only in one location toward the eastern tip of the White Rabbit Fault (Figure 6.10, between 1500 and 1750 m). The overall displacement is skewed towards the western tip of the fault (Figure 6.3), since either the monocline or fault scarp is missing near the eastern tip (from 1500 m to 2126 m in Figure 6.9), which may be due to interaction with another smaller fault north of that portion (Figure 6.3) onto some of the displacements may have been transferred. The relief of the fault scarp and the opening are generally similar, especially along the western portion of the fault (Figure 6.10). Variations in opening and relief profiles may indicate that the White Rabbit Fault was formed because different fault segments coalesced during their growth. Similar to the findings for the Ohale Fault, the height of the monocline is much smaller than the width

along the entire fault. Like with the displacements, the maximum width of the monocline is skewed toward the western tip. The height of the monocline shows a plateau shape.

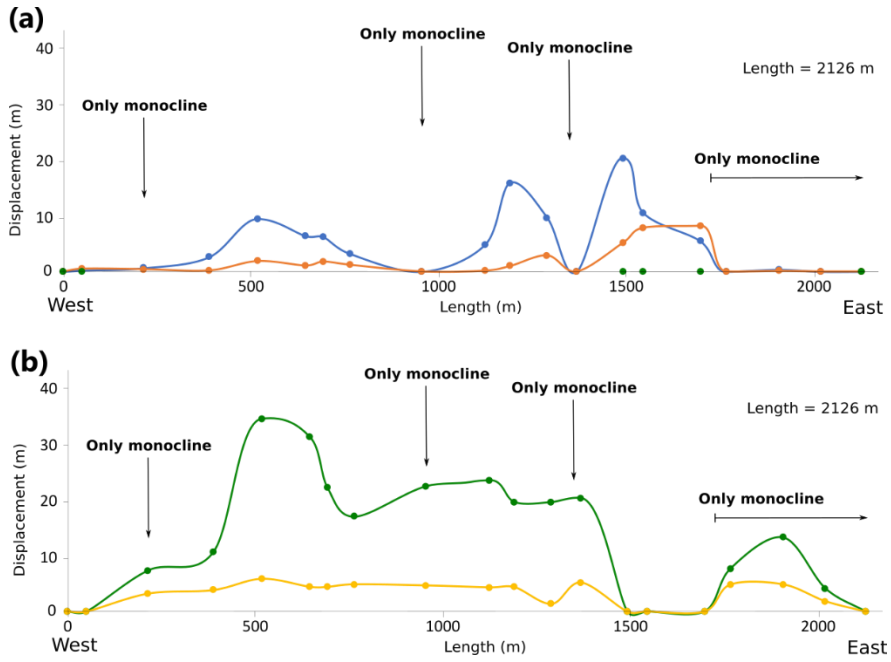

Figure 6.10. *Displacement profile of the White Rabbit Fault. (a) Displacement profile of the fault, including opening in blue and relief in orange. (b) Measurements profile of the monocline, including the height in yellow and width in green. See the cross-sectional diagram in Figure 6.7 for the color code of the profiles.*

A minor fault is associated with monoclines at the northeast of the White Rabbit Fault (Figure 6.3). This scarp of this fault faces south to southeast, antithetical to the major faults and most of the smaller faults in the area. The profile of displacements and monocline geometry of this minor fault is dominated by the relief of the fault scarp and aperture of the opening with a small monocline (Figure 6.11) compared with the monoclines of all other faults. The maximum aperture occurs closer to the eastern tip, and the maximum relief is skewed to the western tip as a transferred towards the White

Rabbit Fault. The width of the monocline has two peaks with one co-located with the point of maximum relief at the west and the other co-located with the point of maximum aperture toward the east. The height of the monocline is relatively constant along the structure. The western tip shows only a monocline, and the actual termination of the structure is unclear in the field.

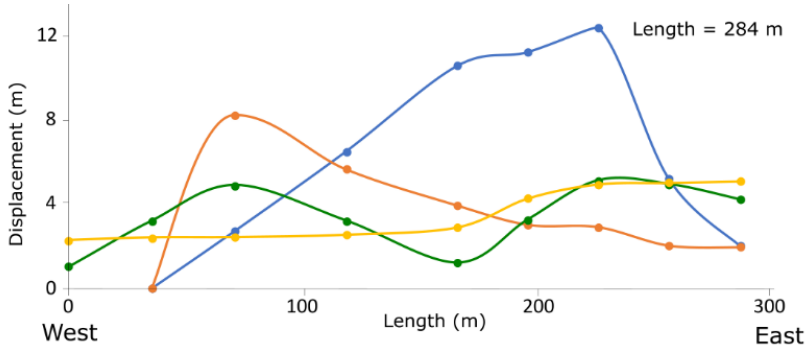

Figure 6.11. *Displacement profile of the minor faults with monoclines associated with the White Rabbit Fault. See the cross-sectional diagram in Figure 6.7 for the color code of the displacement profile.*

Sheared Joints

Sheared joints mapped in the field (such as the examples in Figures 6.12 and 6.13) show minor vertical relief and have an opening, and they strike subparallel to the main faults. Their shape in map view is heavily influenced by preexisting columnar joints, resulting in zigzag patterns (Figures 6.12a,b; 13a). The sheared joint example at GPS #22 (see location in Figure 6.3) has a length of 4.6 m. The aperture dominates the total structural displacement (Figure 6.12c) reaches its maximum at 0.26 m. The relief and aperture profiles mimic one another, with the points of maximum relief and aperture

being located near the center of the structure. Two local maxima occur on either side of the center of the fault, which may indicate a previous linkage of three joint segments.

Another example of a sheared joint is at GPS #138 (Figure 6.13a,b; see location in Figure 6.3). It has a length of 10.6 m, and the predominant displacement component throughout the displacement profile is the relief. The point of maximum displacement (approx. 0.28 m) is located near the center of the fault, and it is mostly contributed by the opening (Figure 6.13c).

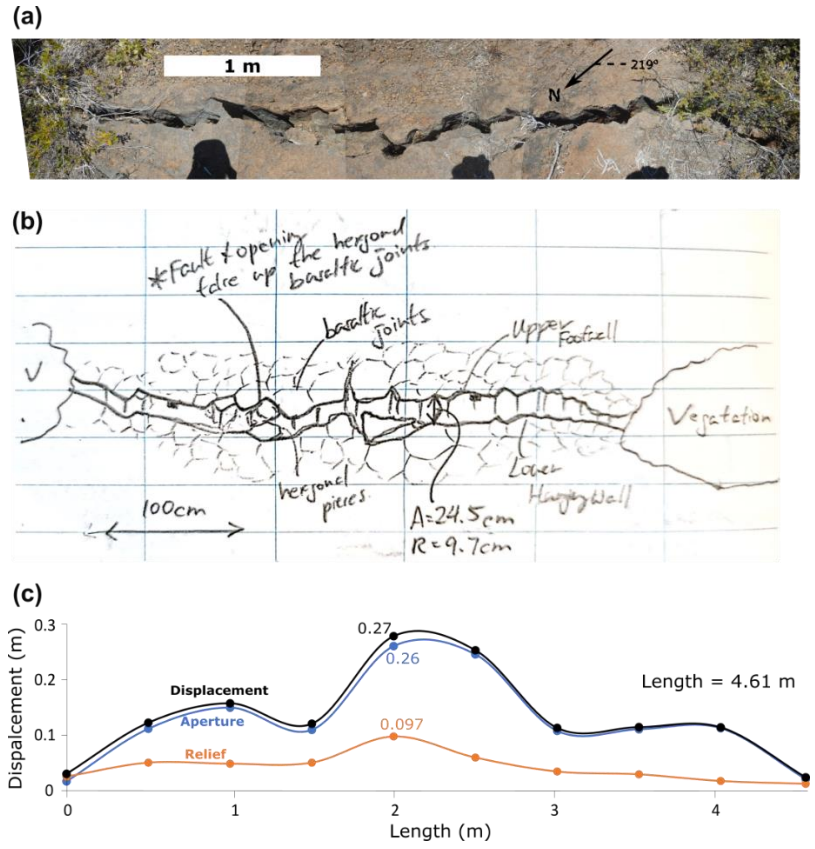

Figure 6.12. *Fault example at GPS #22. (a) Field pictures from the top view, (b) an associated field sketch, and (c) the displacement profile are shown.*

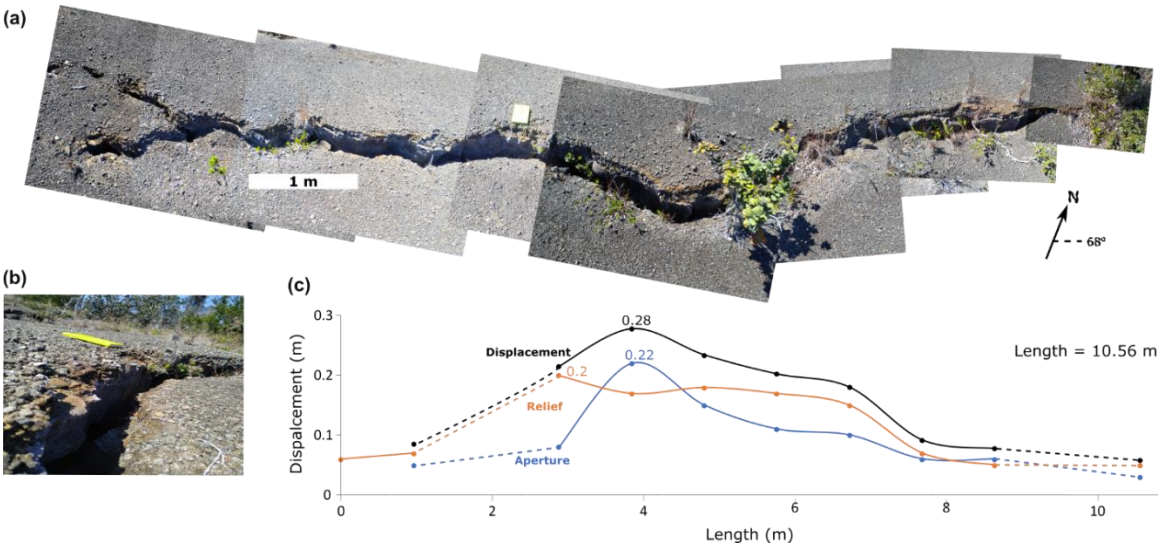

Figure 6.13. *Fault examples at GPS #138. (a) Field pictures from the top view, (b) a side-viewed picture of the fault, and (c) the displacement profile are shown. The field notebook is at the same location as in (a) and is used as a scale.*

Pure Joints

Pure joints include those with simple joint geometries where the maximum aperture is located in the center of the fracture that tapers to the two tips (Figure 6.14a) and those with en echelon patterns with curving tips and overlapping steps (Figure 6.14a and b; also see Figure 6.3 for map patterns). The individual lengths of joints range from less than a meter (Figure 6.14a) to up to ~200 meters, with maximum apertures ranging from 0.005 to 3.08 m. En echelon patterns and overlapping joints are common (Figures 6.14a,b), and their total lengths commonly exceed 1 km (Figure 6.3). Preexisting columnar joints heavily influence the geometry of joints, resulting in zigzag patterns, especially for larger joints (Figures 6.14b,c; see also Figures 6.4d and 6.6d).

Most of the joints strike northeast to southwest, subparallel to the main faults (Figure 6.3). Some of them occur at the tip of the faults, and in places they represent a

continuation of the fault opening, such as the small-scale example in Figure 6.13a and the large-scale western tip of the Kalanaokuaiki Fault (Figure 6.3). The large joints have a similar appearance as the opening displacement component of the main faults (such as Figures 6.6d and 6.8a), including highly fractured subvertical walls influenced by preexisting columnar joints and basaltic flow contacts (Figure 6.14c). All large joints crosscut lava flows (Figure 6.14c), and no lava is observed to have flowed into the opening. This is consistent with the observations at the faults (Figure 6.6f), where deformation post-dating the emplacement of lava flows.

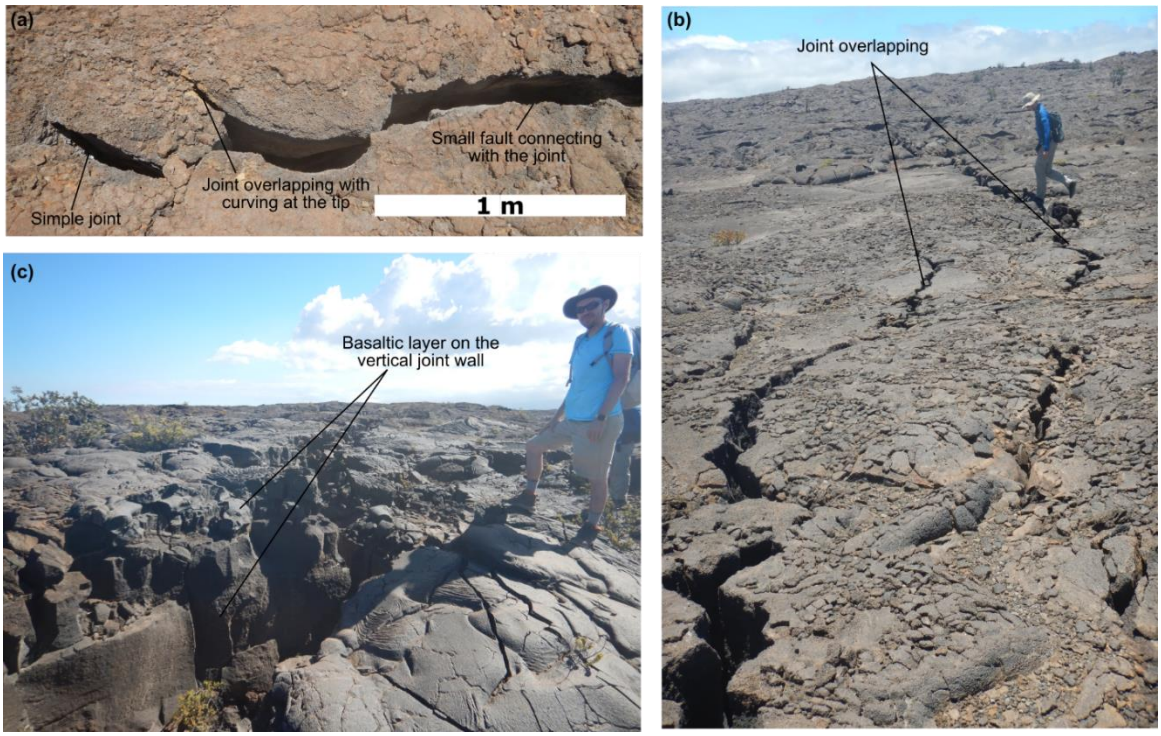

Figure 6.14. *Examples of joints observed in the field. (a) En echelon joints located at GPS #24 observed at the tip of a fault. (b) Two large overlapping of joints as part of an en echelon joint array south of the Ohale Fault (Figure 6.3). (c) Large joints separating lava flow and exposing the basaltic joints on the walls.*

Conceptual model

I incorporate the mapping results and observations into a conceptual model consisting of a series of block diagrams representing different stages of fault development in a morphological continuum along the faults (Figure 6.15). The model is based on the field observations that all structures formed after the emplacement of the uppermost lava flows, and it does not show the effect of any previous volcanic resurfacing that may have occurred. At the earliest stage of deformation, jointing initiates subvertically at the surface along pre-existing basaltic joints and propagates downwards (Figure 6.15a). Some joints may be sheared where the stress at depth reaches a fully compressive regime, and frictional sliding is activated. Where the structure further propagates, it develops into a fault. If the faulting continues non-vertically, the aperture from the jointing and dilation from the fault sliding will contribute to the opening of the fracture (refer to Figure 6.1a; also see Figure 1.1a). Some sheared joints become inactive and stay isolated (Figure 6.15a), such the structures in Figures 6.12 and 6.13.

As sliding continues for active sheared joints, they become small faults with flexure in the hanging wall that forms a small monocline (Figure 6.15b). The topographic expression of the monocline in this stage is subtle, and it remains largely intact as a titled block. As the fault grows larger, the opening grows, and the monocline becomes unstable, partially collapsing into the opening created by the fault, frequently leaving a slab of the most recent basaltic layer as the monoclinal bridge (Figure 6.15c). With continuing fault growth, the monoclinal bridge collapses starting from the hanging wall and forming a rubble pile (described here as a brecciated edge; Figures 6.4a and 6.15c). Eventually, the monocline collapses, in places leaving remnants of the monocline behind (Figure 6.15c).

At this stage, large subparallel joints are commonly seen on the footwall of the fault (Figure 6.15c). Where the fault grows even larger, such as seen in Figures 6.4d and 6.6b, no evidence of a monocline remains, and its rubble entirely fills the opening, leaving only a pronounced fault scarp with rubble piles at its base (Figure 6.15d). This stage is represented at the Kalanaokuaiki Fault and some areas along the Ohale Fault.

These stages form a morphological continuum that is observed along individual structures or at separate structures of different sizes at the Koa'e Fault Zone. The smallest structures may display only characteristics shown in the initial stages (e.g., Figure 6.15a), whereas the full continuum may be developed in part or fully along the largest structures. Its characteristics are displayed in Figure 6.15a, starting at the fault tips and extending toward the fault center, with all characteristics in progression displayed in Figures 6.15b to d. This interpretation is generally consistent with previous ideas in that it involves the initial development of surface joints and interaction with the active normal fault at the subsurface forming the monocline (e.g., Duffield, 1975; Holland et al., 2006; Martel and Langley, 2006; Kevan and Martel, 2007; Podolsky and Roberts, 2008). Previous conceptual models capture mainly the structures and morphology of the monocline (see Figure 6.8 in Holland et al, 2008 and Figure 6.15 in Martel and Langley, 2006), which are represented in Figure 6.15b in the model. Based on that, the upward propagation of the active subsurface fault is proposed to interact with the surface structures, forming the monoclines. The findings agree with the interpretation that the monocline is likely a result of surface flexure with a shallow antithetic fracture associated with the subsurface normal fault causing the buckling at its base (Figure 6.15b). However, the model captures the morphological continuum, and it proposes that the structure develops with the surface

joint propagating downwards and interacting with the subsurface blind fault. Importantly, faulting does not occur at or near the surface as the overburden pressure is not enough for a fully compressive stress regime (refer to Figure 1.1). Hence, the growth of fault initiated only at some depth and does not propagate upward.

The growth process of the fault shown in Figure 6.15 differs from that proposed by Martel and Langley (2006) in the study of the Ohale Fault. They proposed that cavities open within the hanging wall near the proposed upward propagating fault tip, and their growth causes the monoclinal bridges to form and later collapse. Their model illustrates that the hanging wall is connected continuously to the footwall wall, with the monocline bridge and a subsurface cavity underneath at the early stage of fault development. After that, the monocline bridge collapsed and entirely filled the cavity, leaving the base of the fault scarp with rubble piles. This formation process ignores the observed opening displacements between the fault scarp and the monocline at the Ohale Faults (Figure 6.6d) and other fault structures (e.g., Figures 6.8, 6.9, and 6.11). I propose that surface opening represents the aperture of jointing and the dilational component of faulting in the process of fracture growth from Figure 6.15a to Figure 6.15c (also refers to Figure 6.1a), which is consistent with the morphology of the faults, indicating that the opening initiates near the fault tips and develops along the lengths (Figure 6.3), with the relief and aperture profiles mimicking one another (see Figure 6.7). Although the dilation of a blind fault (Figure 6.1a) could cause subsurface cavities that may later contribute to the surface opening and the collapse of the monocline, they do not solely account for the morphology of the Ohale Fault.

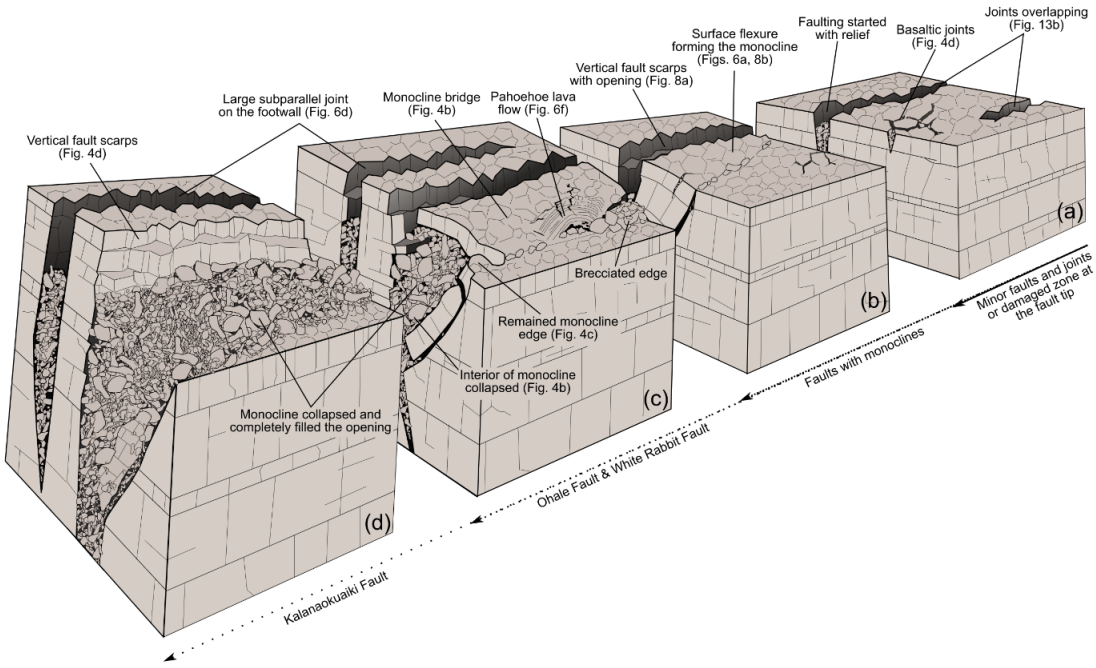

Figure 6.15. *Conceptual model incorporating all geologic observations associated with the mixed-mode fractures at the Koa'e Fault Zone. The figures of field pictures showing the geological observations are labeled in the block diagrams. The model is drawn based on the field observations that all structures formed after the emplacement of the uppermost lava flows without any effect of previous volcanic resurfacing that may have occurred.*

Displacement-to-length scaling

I evaluated the maximum displacements and lengths of a total of 76 fractures, of which 53 are joints, 18 are sheared joints, and 5 are normal faults. The 53 joints range in length from 0.25 to 191.7 m, with maximum apertures of 0.005 to 3.08 m. I plotted their maximum apertures as a function of joint length, following the methods described for statistical evaluations of fracture scaling in Clark and Cox (1996) to assess any

correlation of the data for all of the following regressions. The plot shows a correlation of D_{max} to L with a scaling exponent of 0.858 and R^2 = 0.47 (Figure 6.16a).

The openings of the faults are contributed by the apertures from jointing and the dilations from faulting (Figure 6.1). The opening of 18 sheared joints (without monoclines, including those in Figures 6.12 and 6.13) are plotted for comparison to investigate the displacement transition from jointing to faulting (Figure 6.16a). The faults range in length from 1.53 to 2720 m, with maximum openings of 0.03 to 5.33 m. Their scaling relationship has a slope of 0.0668 with R^2 = 0.06, which indicates that there is no clear relationship between the fault lengths and openings. The scaling of the opening of the fault does not follow the scaling of the aperture of joints. This is expected since the openings contain the apertures from the inactive jointing and the dilation of faulting (Figure 6.1a). However, the weak correlation between the fault lengths and openings does not allow for more interpretations. The accumulation of the dilation in addition to the joint aperture is also less pronounced with the growth of fault length compared to the increase in maximum aperture with growing joint lengths (Figure 6.16a). The fault displacement is likely accommodated mostly by the relief (throw), especially if faults here have high dip angles, which at the surface is observed to be consistent with the observations of steep fault scarps that are influenced by the pre-existing basaltic joints. The scaling of the aperture of joints has a similar slope to previous studies (Figure 6.16b; Vermilye and Scholz, 1995a; 1995b; Schultz et al., 2008; Delaney and Pollard, 1981; Moros, 1999; Babiker and Gudmundsson, 2004; Klimczak et al., 2010).

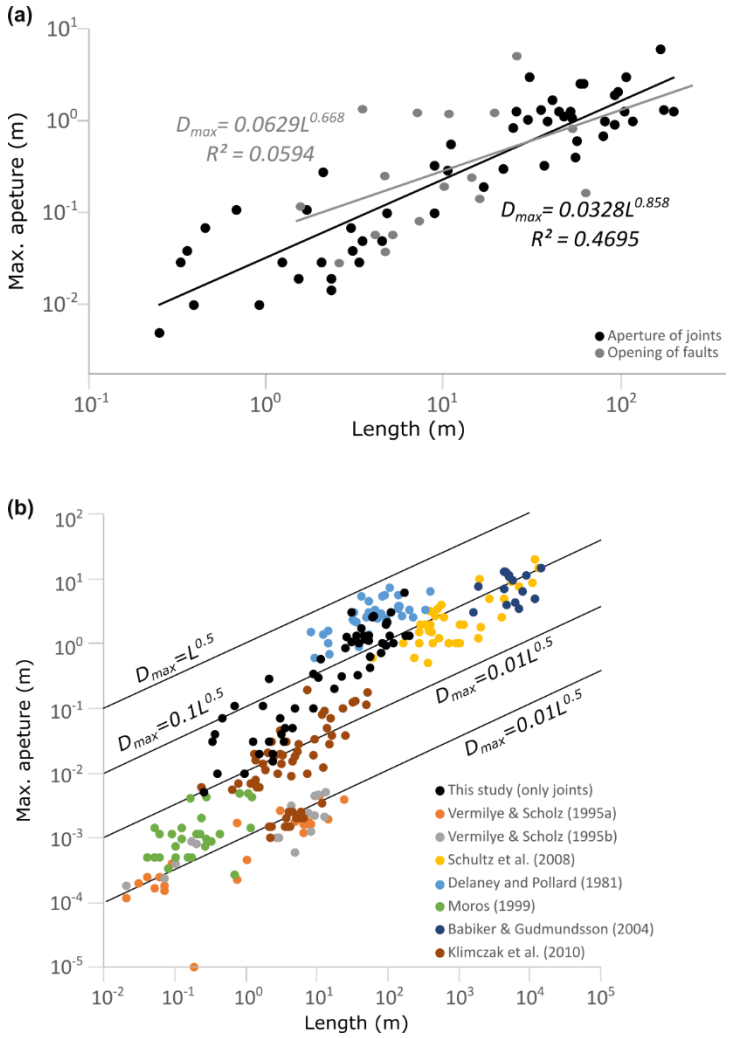

Figure 6.16. *Displacement-to-length scaling of opening displacements. (a) Maximum aperture-length scaling of joints (black dots) at the Koa'e Fault Zone with the opening of faults (without monoclines) plotted as gray dots for comparison. (b) Compilation of* D_{max}/L *scaling for joints from Vermilye and Scholz (1995a; 1995b), Schultz et al. (2008), Delaney and Pollard (1981), Moros (1999), Babiker and Gudmundsson (2004), and Klimczak et al. (2010) showing the data in comparison.*

I measured 18 sheared joints and minor faults without monocline (such as those in Figures 6.12 and 6.13) ranging in length between 0.004 to 2.7 km, with maximum relief between 0.01 and 7.34 m (Figure 6.17a). I consider only the relief of the scarps, (i.e., the

throw) for the fault scaling because it is the only measurable displacement component that is solely formed by the shear along the faults. The measurements exhibit a clear D_{max}/L scaling relationship with a slope of 0.754 and R^2 = 0.98 (Figure 6.17a). I compared the data with published results (Figure 6.16b). The scaling of the relief of sheared joints and faults with no monoclines is consistent with the published scaling of normal fault with a slightly gentler slope of 0.75 than the expected slope of ~1. Since all sheared joints and faults are associated with an opening component, the measurements contain an unknown amount of aperture from the jointing at the early fracturing stage, in addition to the heave from the faulting (Figure 6.1a). However, since the fault dip is unknown, I am unable to estimate the individual opening components.

To investigate how major faults and their monoclines accommodate the displacements for larger structures, I compare the relief of the fault scarps and the total relief, including that of fault scarps to the heights of the monoclines, in the scaling. The measurements of the total relief exhibit a weak D_{max}/L scaling relationship with a slope of 0.455 and R^2 = 0.42 (Figure 6.17a). The measurements of the total relief exhibit an unclear D_{max}/L scaling relationship with a slope of 0.486 and R^2 = 0.24 (Figure 6.17a). The slopes of both scaling is similar, smaller than that of the faults without monoclines (Figure 6.17a), indicating that the relief of the fault scarps and the total relief do not increase as much for the longer and more complex structures. This could be explained by the development of fault linkages that are consistent with the field observations of the relay ramps (Figure 6.3) and the plateau shapes of displacement profiles (Figures 6.5, 6.8, and 6.10). When compared to other published datasets (Walsh and Watterson, 1987; Muraoka and Kamata, 1983; Opheim and Gudmundsson, 1989; Dawer et al., 1993;

Schlische et al., 1996; Cartwright et al., 1995; Wilkins and Gross, 2002; Morley and Wonganan, 2000; Soliva et al., 2008), the field data populate a data gap in the normal fault scaling between the lengths of 1 to 100 m (Figure 6.17b).

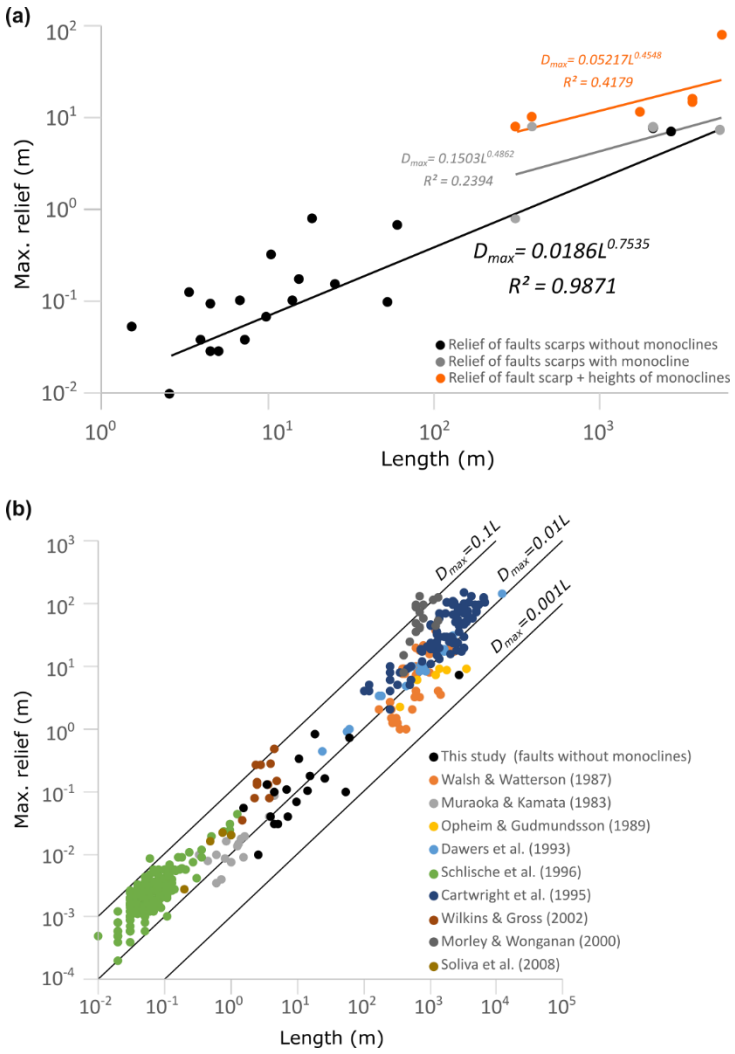

Figure 6.17. *Displacement-to-length scaling of the displacement component related to the shear along normal faults. (a) Maximum relief-length scaling of normal faults at the Koa'e Fault Zone. The black dots represent the reliefs of fault scarps for faults without monoclines. The orange dots represent the sums of the reliefs of the fault scarps and the heights of the monoclines for faults with monoclines. The grey dots represent only the*

reliefs of the fault scarps for faults with monoclines. (b) Compilation of D/L scaling for normal faults from Walsh and Watterson (1987), Muraoka and Kamata (1983), Opheim and Gudmundsson (1989), Dawer et al. (1993), Schlische et al. (1996), Cartwright et al. (1995), Wilkins and Gross (2002), Morley and Wonganan (2000), and Soliva et al. (2008) with a power-law scaling relation having a slope of 1.

I scale the total displacements of the structures including joints, sheared joints, faults lacking monoclines, and faults displaying monoclines with their lengths (Figure 6.18). While joints have only apertures (same as in Figure 6.16), the total displacements of the faults contain the aperture of any jointing that occurred prior to the faulting and the shear displacement from faulting. I infer the displacement of the faults with monoclines as the distance between the top of the fault scarp to the base of the monocline on the hanging wall, which has the components of the relief of the fault scarp, the opening of the faults, and the widths and heights of the monocline (refer to Figure 6.7). Despite the different types of displacement plotted, the scaling shows a relationship with a single slope of 0.866 (R^2 = 0.632), between the expected slope of 0.5 for joint scaling (Figure 6.16b) and 1 for faulting scaling (Figure 6.17b) established by the literature.

All data of faults with monoclines have substantially longer lengths and are located at the upper end of the scaling (Figure 6.18). The data points of joints, sheared joints, and faults cluster together in the plot and share similar scaling statistics (Figure 6.17), which indicate the displacement of these faults is still heavily controlled by jointing develop before the jointing-faulting transition (Figure 6.1a). None of the data show a transition from joint scaling to fault scaling, instead they are all scattered around one another along the same scaling. Therefore, these shear joints or faults without

monoclines are likely deactivated before they can propagate downwards and interact with the subsurface faults. The transition from joint and faults to a fault with monocline is closely connected along the same scaling without a gap in structural length or sudden change in slope. This indicates that the monoclines are likely formed and accommodate displacements shortly after the jointing to faulting transition.

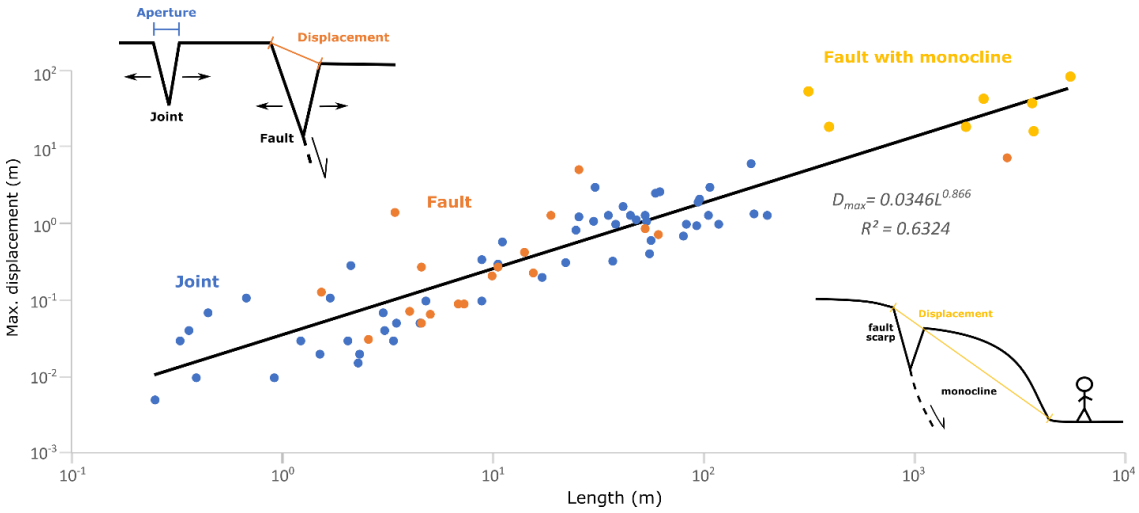

Figure 6.18. *Displacement-to-length scaling of all fractures in the mixed-mode fracture population of the Koa'e Fault Zone. The apertures (which is the total displacements) of pure joints are plotted in blue. The displacements of shear joints and faults, contributed by the joint aperture and fault slip (Figure 6.1a), are plotted in orange. The inferred displacement of faults with monoclines, which is the distance between the top of the fault scarp to the base of the monocline on the hanging wall, are plotted in yellow. The fault morphologic measurements in the cross-sectional diagram match the colors in the profile.*

Conclusion

To investigate the transitional structure from jointing to faulting in an extensional tectonic regime, I conducted structural mapping along the Koa'e Fault Zone and collected measurements of orientations, structural relief, opening displacements, lengths, and depths of openings along faults and joints of various sizes. I incorporated a series of geological observations along the Koa'e Fault Zone at the Hawaii Volcanoes National Park into a conceptual model representing different stages of structure growth and the morphological continuum. I infer that the monocline associated with the normal fault is formed by upward propagating faults, and interpretation that is broadly consistent with previous studies (e.g., Duffield, 1975; Holland et al., 2006; Martel and Langley, 2006; Kevan and Martel, 2007; Podolsky and Roberts, 2008). The model allows us to not identify only the structures and geometry of the faults and monoclines but also to identify the spatial connections of the fault structures at different stages. The observations and displacement profiles indicate the aperture from jointing and dilation from faulting contribute to the surface opening of the fault scarps until a monocline is formed, a process not indicated in previous studies. These results may be applied to investigate the growth and displacement of this type of mixed-mode fractures as a morphological continuum on Earth (such as Iceland or other rift zones) (e.g., Gudmundsson, 1992; Acocella et al., 2003), as well as on other planetary bodies, such as normal fault systems on Mars (e.g., Schultz and Lin, 2001; Polit et al., 2009; Wyrick et al., 2011) in future research.

I also established the displacement-to-length scaling of the Koa'e Fault Zone, which captures the transition from jointing to faulting and to more complex structures

associated with monoclines. The scaling implies that monoclines are formed and accommodate displacements shortly after the jointing to faulting transition. How far this scaling is applicable to other mixed-mode fractures is unknown, as the faults show more complex structures (i.e., monoclines) with the structural development still under debate (i.e., downward of joints vs. upward propagation of faults). Nevertheless, the work demonstrates that detailed field observations and measurements help conceptualize fracture growth and thus can establish the displacement-to-length scaling of mixed-mode fracture populations showing the transition from jointing to faulting.

Acknowledgments

The field research was funded by the Frank E. Kottlowski Memorial Grant that is part of the AAPG Foundation Grants-in-Aid program. H.C.J.C. is also thankful for receiving the Miriam Watts-Wheeler Scholarship Fund from the Department of Geology at the University of Georgia. I thank Sierra McDaniel for her assistance with obtaining the Hawaii Volcanoes National Park research permit.

CHAPTER 7

CONCLUSIONS

The growth and origin of fractures in an extensional tectonic regime (Figure 1.1a) on small bodies were studied on a broad array of topics. First, I have investigated the tectonics of Asteroid 4 Vesta, which has remarkably large troughs (Divalia Fossae; Figure 1.1c) that are visible on high-resolution spacecraft imagery. The fracturing type and origin of Divalia Fossae were assessed, and the findings were tied to the overall tectonic evolution of the small body. Second, the hidden tectonic patterns on Vesta and Ceres were revealed by planform impact crater shapes and their origins were discussed by means of comparative planetology. Third, an analog field study was conducted along the Koa'e Fault Zone (Figure 1.1b) to investigate the transition of jointing to faulting for a population of mixed-mode fractures formed in an extensional tectonic regime on Earth for further comparative planetology. Here, the contributions of these three topics of this dissertation to the field of structural geology are summarized, and future directions originating from this research are discussed.

Structural Geology and Tectonics of Vesta

Before this dissertation, the structure and origin of the Divalia Fossae and Saturnalia Fossae were widely believed to be grabens that were directly and simultaneously formed by the impacts that led to the emplacements of the Rheasilvia and

Veneneia basins, respectively (e.g., Buczkowsk et al., 2012; Jaumann et al, 2012; Yingst et al., 2015). These troughs were interpreted as formed by normal faulting based on the trough geomorphology (Buczkowsk et al., 2012). The analysis by Jaumann et al. (2012) proposed that the poles of vertical planes defined along the Divalia Fossae and Saturnalia Fossae cluster near the center of Rheasilvia and Veneneia impact basins, respectively, and this was taken as evidence for an impact-induced origin of these troughs. Ever since the publication of these studies, these hypotheses have been accepted by numerous studies of the geological history and tectonics of Vesta (e.g., Schäfer et al., 2014; Scully et al., 2014; Yingst et al., 2015) without any further testing. In Chapters 2 to 4 of this dissertation, the geographic relationship between the troughs and the basin was reanalyzed using the Dawn mission data (Roatsch et al., 2015; Preusker et al., 2016). The structure and origin of the troughs were tested by structural mapping, crater counting, and rock-mechanical calculations.

Chapter 2 distinguishes the faulting-, versus opening-mode origin of the Divalia Fossae using structural mapping, morphological analysis, and rock-mechanical calculation. Results of chapter 2 show that the trough morphology of the Divalia Fossae is not flat-floored as typical for grabens, that maximum reliefs are not at the center of the troughs, and that the two scarps bounding each trough have their relief maxima at different locations (Cheng and Klimczak, 2022a). These observations are inconsistent with the previously proposed faulting origin (Buczkowski et al., 2012). Instead, the troughs have their maximum widths near the center, pointing to an opening-mode fracture origin. Rock-mechanical calculations that account for Vesta's low gravitational acceleration and degree of lithospheric fracturing reveal that fault initiation is favored

only at depths deeper than at least ~3 km but likely much deeper to as much as below 55 km. Therefore, opening-mode displacements are more plausible explanations for the morphology of the Divalia Fossae. This type of fracturing predicts that the Divalia Fossae were formed by north-south oriented tensile stresses.

In *Chapter 3*, the temporal relationship of troughs and basins as derived from crater statistics permit Divalia Fossae formation well after or even before the emplacement of the Rheasilvia basin (Cheng et al., 2021). Although the crater statistics restrict the age of the Divalia Fossae, there is no consensus on the age of the Rheasilvia basin, owing to the large uncertainty in cater statistics and disagreement among meaningful count areas. Crater counting by itself did not yield tight constraints of the relative ages of the troughs and the basin.

In *Chapter 4*, the structures within the Rheasilvia basin were mapped in detail and compared with the mapping of Divalia Fossae from *Chapter 2* to investigate their relationship. The Divalia Fossae crosscut the Rheasilvia basin, suggesting that the troughs formed after basin emplacement and modification (Cheng and Klimczak, 2022b). Even though seismic shaking could still have affected the surface for a substantial time after the impact, the formation of Divalia Fossae would have to have taken place before or within the same timeframe of the modification stage of the Rheasilvia basin, contradicting the cross-cutting relationship shown in this dissertation. A reassessment of the geographic relationship between the Divalia Fossae and the Rheasilvia basin further indicated that the troughs are not concentric around the basin center. Instead, the Divalia Fossae are concentric around the south pole—Vesta's spin axis— suggesting a spinning-related origin. This result establishes that the Divalia Fossae do not display a clearly

defined geographic relationship with the Rheasilvia basin as previously thought; thus, the lack of a clear collocation of the basin and troughs refutes the sole argument on which the hypothesis is based on, namely that the basin forming impact directly triggered the formation of the troughs of Divalia Fossae.

In short, a series of geologic constraints are inconsistent with the leading hypothesis that the large-scale troughs on Vesta are grabens formed by large impacts via normal faulting. Instead, they point to a spinning-related origin as a long-term consequence of the large impact, accommodating entirely or mostly opening-mode displacements. Together these chapters provide a comprehensive account of the fracturing behavior of Vesta as a low-gravity, small body and the origin of the large-scale fractures that tie with the evolution of the asteroid. These chapters also highlight the different approaches for investigating the fracture behavior and tectonics of small bodies.

Hidden Tectonic Pattern on Small Bodies

Tectonic patterns that contain information about important parts of the geological history of the small bodies can be hidden by the limitation of spacecraft imagery or a thick layer of regolith. Although studies have been conducted on polygonal impact craters on small bodies (e.g., Beddingfield et al., 2016; Neidhart, 2018), the orientations of straight rim segments have yet to be analyzed on global scales, and therefore any hidden tectonic patterns on the small bodies have not yet been explored. Results in *Chapter 5* reveal regional to global tectonic patterns on Vesta and Ceres by the planform shape of impact craters, including an E–W trending fracture system around the polar regions on Vesta and a global pattern with strongly preferred fracture orientations varying latitudinally on Ceres. Although these bodies are likely too small to have had internally

driven tectonic processes in the recent geologic past, large impacts and stresses from rotational bulging are hypothesized to generate regional and global tectonic structures on minor bodies (Thomas and Prockter, 2010). The patterns revealed in *Chapter 5* do not match structural trends of visible tectonic- or large-impact structures on either body, and other planetary processes are therefore needed to account for these patterns.

While other planetary processes have been suggested for Vesta and Ceres (e.g., McCord and Sotin, 2005; Tricarico, 2018; Mao and McKinnon, 2020), either the predicted tectonic patterns are not specifically tied to the specific planetary body, or the predictions show shortcomings, or both. Therefore, a comparison between the predicted and actual patterns is not currently possible. Future modeling must be specifically tied to these bodies and account for the low gravity and rock properties to investigate how these fractures are formed and what planetary processes are involved in small bodies.

Terrestrial Analog of Mixed-mode Fractures and Implications to Vesta

Field investigations at planetary analog sites on Earth are essential for understanding fracture processes on other bodies in the Solar System. The Koa'e Fault Zone is one of the best analog sites to study the opening- and sliding mode of fracturing in an extensional tectonic regime with well-exposed joints and faults with an opening dilation (Figure 1.1a and b). This site allows the investigation of the transition from jointing to faulting, as well as the displacement-length (D_{max}/L) scaling relationship. *Chapter 6* presents a conceptual model of the mixed-mode fracture system, highlighting the different growth stages and a morphological continuum, and showing the spatial connection between these stages. These field observations and measurements provide new insight into the development of fractures from jointing to faulting and to more

complex structures, such as monoclines. The D_{max}/L scaling derived in *Chapter 6* shows a clear relationship in the development of the displacements, including the opening, sliding, and any associated dilation, for this type of mixed-mode fracture.

Using the conceptual model of the Koa'e Fault Zone in *Chapter 6*, as a comparison to the Divalia Fossae on Vesta (Figure 1.1c) in *Chapter 2*, the fracturing type and evolution of the Divalia Fossae are analogous to the earlier stages of mixed-mode fracturing, including pure jointing, sheared jointing, to minor faulting. The Divalia Fossae are entirely or mostly accommodating opening-mode displacements, because the low gravity prohibits fault initiation within the uppermost ~3 to 55 km of the lithosphere. The pure and sheared joints on the D_{max}/L scaling of the Koa'e Fault Zone also entirely or mostly accommodate opening-mode displacements or, at the very least, exhibit a similar scaling of jointing, likely because the monoclines developed after the initiation of major faulting to accommodate the displacements. These results provide insight for future researchers on the growth and displacement of this type of mixed-mode fracturing on large terrestrial bodies like Earth, such as on Iceland or in other rift zones (e.g., Gudmundsson, 1992; Acocella et al., 2003), on Mars (e.g., Schultz and Lin, 2001; Polit et al., 2009; Wyrick et al., 2011), as well as other small bodies with large-scale troughs, such as Phobos.

Open Questions and Future Work

This dissertation research exemplifies a series of approaches for investigating the growth and origin of fractures on low-gravity small bodies, which is a field that has not been widely studied in structural geology and planetary geology. However, it is a critical interdisciplinary field to understand the interplay of fundamental concepts in rock

deformation and the early evolution of the solar system. It has great potential application to current and future NASA missions to low-gravity, small rocky planetary bodies, such as the Lucy mission to the Trojan Asteroids, the Psyche mission to unique metal-rich asteroid, and Europa Clipper to the icy moon. A continued study of fracture growth and origin on small and large bodies will shed light on planetary evolution and what role gravity plays in the tectonic evolution on various bodies.

Throughout the research conducted for this dissertation, more open questions and thoughts have been raised for future research. One major question is *what is the origin of Divalia Fossae* and even *how does that relate to the tectonic evolution of Vesta? Chapters 2 to 4* propose a spinning-related origin that could be a long-term consequence of the large impacts that produced tensile stresses in north-south orientation at the equator of Vesta. The geographic relationship between the basins, troughs, and spin axis of Vesta suggest that the combination of the Veneneia and Rheasilvia basins created a single hemisphere-scale depression at the south pole (Figure 7.1a). Despite the effect of the Rheasilvia central mound, the irregularity of the depression, and some large impact craters on the basin floor, the geometric mean center defined by the basin-bounding scarps of both basins (83.6^{o}S, 34.4^{o}E) almost coincides with the south pole and the center of the polar topographic low, forming a large negative geoid anomaly on the small body. A planetary object is predicted to reorient with a large positive geoid anomaly toward the equator and a large negative geoid anomaly toward the poles. Under this scenario, the polar depression created by both impacts supports true polar wander.

To explore the possibility of a spinning-related trough origin, the orientations of the planes of Divalia Fossae are plotted as poles as done in *Chapter 4* and compared to

the geometric mean center of the Rheasilvia and Veneneia basins combined (see Figure 7.1a). The 95% confidence interval ellipses of the poles of the troughs in shades of a grey ellipse describe the uncertainty inherent in the estimate of the pole position, representing the set of acceptable hypotheses. The calculated geometric mean center of both basins and the south pole (spin axis) are both within the 95% confidence interval ellipse of the poles of the planes defined by Divalia Fossae (Figure 7.1b and c), and so coincide with the center of the topographic low of the polar depression (Figure 7.1a). This well-defined geographic relationship indicates that the locations of the troughs are correlated with the spinning axis of Vesta.

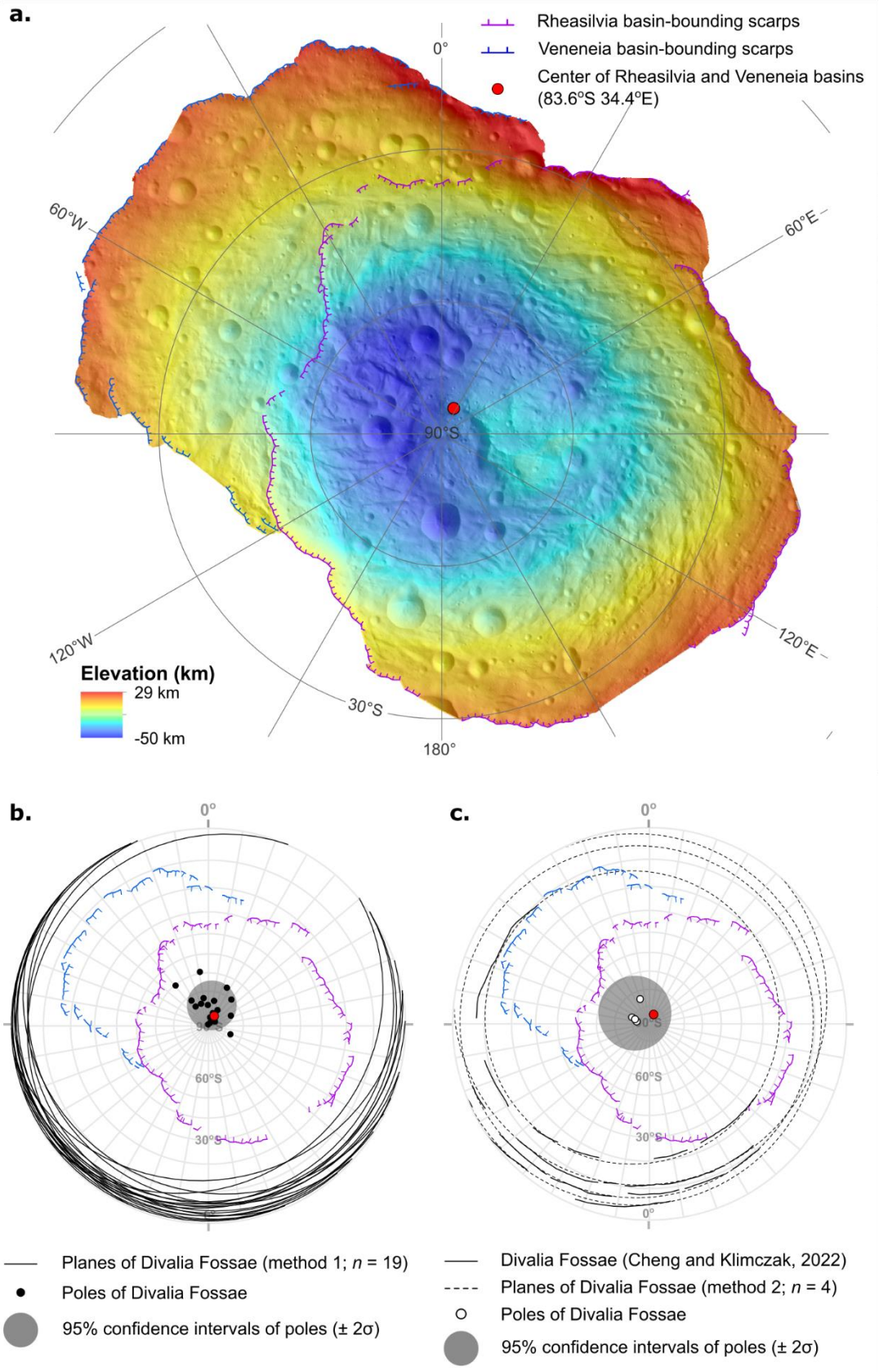
a.
Rheasilvia basin-bounding scarps
Veneneia basin-bounding scarps
Center of Rheasilvia and Veneneia basins
(83.6°S 34.4°E)
0°
60°W
60°E
120°W
120°E
90°S
30°S
180°
Elevation (km)
29 km
-50 km
b.
0°
60°S
30°S
Planes of Divalia Fossae (method 1; n = 19)
Poles of Divalia Fossae
95% confidence intervals of poles (± 2σ)
c.
0°
60°S
30°S
Divalia Fossae (Cheng and Klimczak, 2022)
Planes of Divalia Fossae (method 2; n = 4)
Poles of Divalia Fossae
95% confidence intervals of poles (± 2σ)

Figure 7.1 *The geographic relationship between the basins, troughs, and spin axis of Vesta. (a) Elevation map within the basin-bounding scarps of Rheasilvia (purple) and Veneneia (blue) in south polar stereographic projection. The reference elevation is defined to be the mean planetary radius of 262 km. The geometric mean center defined by the basin-bounding scarps of both basins is plotted as a red dot. (b) Equal area south pole projection stereonet showing the configuration of the center of Rheasilvia and Veneneia basins with the Divalia Fossae using method 1 by Jaumann et al. (2012), in which planes are defined by the center positions of the trough segments mapped by Cheng and Klimczak (2022), represented by great circles shown in black. Confidence ellipses corresponding to two standard deviations (95% confidence interval (CI)) of these poles are calculated and highlighted in grey. (b) Equal area south pole projection stereonet showing the configuration of the center of Rheasilvia and Veneneia basins with the Divalia Fossae, investigated by defining small circles of the main trough structures (method 2). The 19 trough segments of Divalia Fossae (black lines) belong to four main structures (Cheng and Klimczak, 2022a). The planes that best fit each of the four structures are presented as small circles in dashed lines with their poles shown as white dots. Confidence ellipses corresponding to two standard deviations (2σ; 95% CI) of these poles are calculated and highlighted in grey.*

I propose a new scenario of the origin of the large-scale troughs caused by impact-induced true polar wander that modifies the orientation of the surface relative to the spin axis and causes deformation along the new equator by a change in tidal bulging. (Figure 7.2). First, the Veneneia impact hit Vesta from an unknown orientation and angle, forming a large depression and negative geoid anomaly, causing the asteroid to reorient

with the impact basin toward the south pole (Figure 7.2a). Under the fast-spinning rate of Vesta, equatorial bulging occurred and flattened the asteroid perpendicular to the spin axis (Figure 7.2b). The process caused the formation of Saturnalia Fossae via jointing at the equator (Figure 7.2c). After that, the Rheasilvia impact hit Vesta at ~30^{o} of the south pole, and the newly formed impact basin superposed on the Veneneia basin (Figure 7.2d). The preexisting Veneneia basin and the newly formed Rheasilvia basin co-created a large negative geoid, which reoriented towards the south pole (Figure 7.2d). The changes in geoid and reorientation may also have caused a change in spin rate. Again, tidal bulging occurred (Figure 7.2e) and caused the formation of Divalia Fossae at the new equator whereas the Saturnalia Fossae are no longer along the equator but differ in orientation by approximately 30° and are cross cut by the Divalia Fossae (Figure 7.2f).

This new hypothesis explains all geologic constraints presented. The Veneneia basin, Rheasilvia basin, Divalia Fossae, and Saturnalia Fossae are in the right configuration and stratigraphic relationships as observed (Figure 7.2f). In this scenario, the formation of the Rheasilvia basin did not directly cause any noticeable antipodal or immediate equatorial deformation. Tensile stresses induced by tidal bulging formed the troughs, as a long-term consequence of the large impacts, which provides enough time for the modification of the Rheasilvia basin before being crosscut by the Divalia Fossae. This scenario also accounts for the well-defined geographic relationship between the troughs, south pole (spin axis), and center of the polar depression co-created by the two basins, as well as the causal geographic linkage between the Rheasilvia impact with the Divalia Fossae and Veneneia basin with the Saturnalia Fossae. While an increase in spin rate caused by the Rheasilvia impact may have formed the Divalia Fossae (Mao and

McKinnon, 2020) and explain some of the constraints, it is difficult to account without true polar wander for the formation of Saturnalia Fossae related to the Veneneia impact, which is neither located at the equator nor south pole.

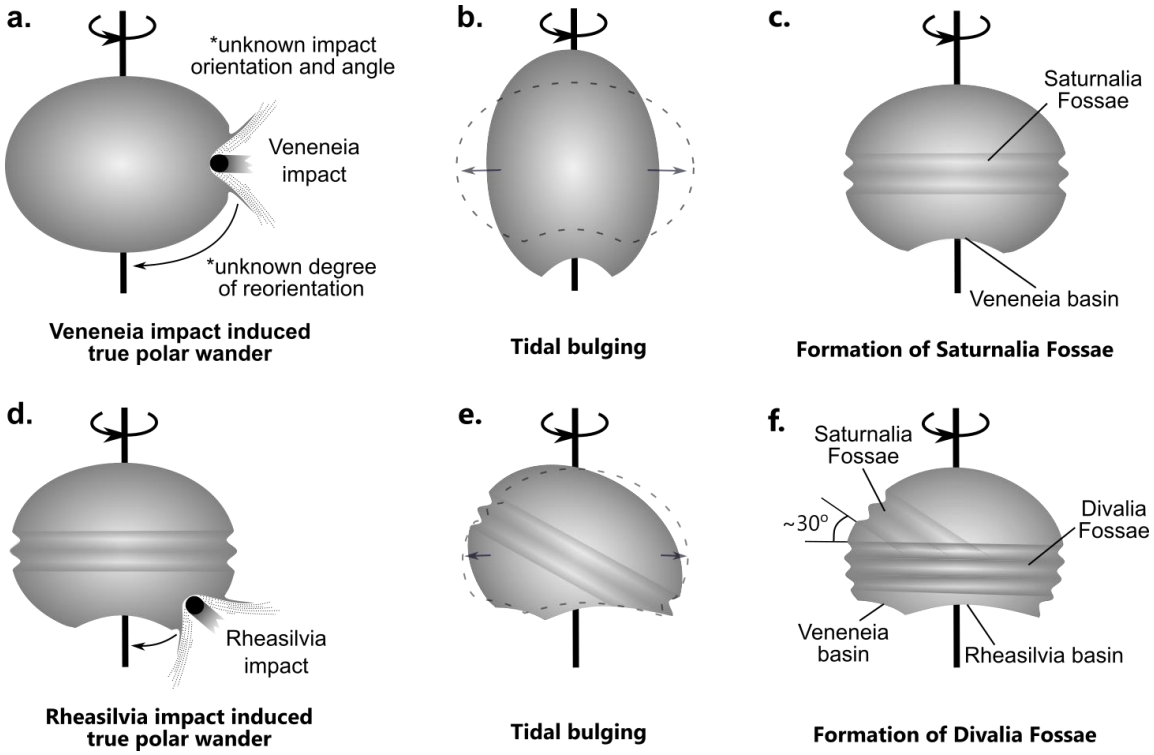

Figure 7.2 *Conceptual diagrams showing the new hypothesis of the Divalia Fossae as a long-term consequence of large impacting events and reorientation. (a) Veneneia impact induced true polar wander with the Veneneia basin rotated towards the south pole. (b) Tidal bulging occurred and flattened the asteroid perpendicular to the spin axis. (c) Formation of Saturnalia Fossae via jointing. (d) Rheasilvia impact emplaced a basin superposing the Veneneia basin and induced true polar wander. (e) Tidal bulging occurred again and flattened the asteroid in a new orientation. (f) The Divalia Fossae form via jointing at the equator, and they crosscut the Saturnalia Fossae, which now differ in the orientation of ~30° trending northwest–southeast.*

Two major questions that need to be answered for this new tectonic model of Vesta are: *did tidal bulging induce tensile stresses that triggered jointing in the predicted orientation on Vesta?* And *is it possible for true polar wander to have occurred on Vesta?* The second question has been explored if Veneneia and Rheasilvia impacts created a permanent mass deficit, they may have driven the true polar wander of Vesta (Matsuyuma and Nimmo, 2011; Jutzi et al., 2013). Numerical modeling suggests that the thickness and rigidity of Vesta's lithosphere following these impacts likely severely limited any relaxation of Vesta's rotational bulge (Karimi and Dombard., 2016). However, Young's modulus, the parameter used to define Vesta's lithospheric rigidity, is strictly speaking only valid for intact rock samples. For larger scales, especially highly fractured lithospheres, the deformation modulus is a better approximation of this elastic rock property (Schultz, 1996). The orientations of structures within the Rheasilvia basin in the area coinciding with the superposed Veneneia basin are substantially influenced by the pre-existing Veneneia structures. This indicates that the lithosphere must have been shattered by the Veneneia impact, and that no healing and annealing occurred before and during the impact that formed the Rheasilvia basin. The deformation modulus adjusted for the lithospheric properties of a highly fractured Vesta is likely up to an order of magnitude lower than Young's modulus of 52 GPa used in the simulation by Karimi and Dombard. (2016), warranting a reassessment of basin relaxation and polar flattening with lower rigidities.

Overall, it is undeniable that fracture growth and origin on small bodies are heavily influenced by the low gravity and are different than what I generally observe on Earth at grabens. To answer these questions, future work will require reassessing the

possibility of true polar wander with more appropriate rock mechanical parameters. In particular, my conceptual model requires a specific degree of reorientation by the Rheasilvia impact, which allows it to be tested by numerical modeling of Vesta reoriented by 30^{o} to predict the structure type and orientation and compare them with the trough observations. Related to that, modeling is also needed and must be specifically tied to the low gravity and the associated rock properties of Vesta to investigate how fractures indicated by the planform impact crater shape in *Chapter 5* are formed, and what planetary processes are involved that fit the proposed evolution (Figure 7.2) from *Chapters 2 to 4*. Similar research is needed for Ceres to investigate the origin of the fracture patterns revealed in *Chapter 5* with modeling that accounts for not just the low gravity but also the properties of its icy crust. In addition, terrestrial analog studies of mixed-mode fractures on Earth, such as those found in rift zones exposed on Iceland (e.g., Gudmundsson, 1992; Acocella et al., 2003), will be needed to further explore fracture growth with D_{max}/L scaling and the factors controlling the processes, which has implications for small bodies. Answering these questions will not only shed light on the tectonics of Vesta, Ceres, and Earth, but also reveal underlying mechanisms of rock deformation and planetary evolution in recent and past lithospheres of large and small, rocky and non-rocky planetary bodies in the Solar System.

REFERENCES

Acocella, V., Korme, T. and Salvini, F., 2003, Formation of normal faults along the axial zone of the Ethiopian Rift. *Journal of structural Geology*, *25*(4), pp. 503–513.

Aittola, M., & Ohman, T. 2006. Polygonal impact craters on Venus. In *European Planetary Science Congress*, pp. 430.

Aittola, M., Öhman, T., Leitner, J. J., Kostama, V. P., & Raitala, J. 2010. The structural control of Venusian polygonal impact craters. *Icarus*, *205*(2), pp. 356–363. https://doi.org/10.1016/j.icarus.2009.08.004

Allmendinger, R.W., Cardozo, N.C., and Fisher, D., 2013. Structural geology algorithms: Vectors & tensors. Cambridge, England, *Cambridge University Press*.

Ammannito, E., DeSanctis, M. C., Ciarniello, M., Frigeri, A., Carrozzo, F. G., Combe, J. P., Ehlmann, B. L., Marchi, S., McSween, H. Y., Raponi, A., & Toplis, M.J. 2016. Distribution of phyllosilicates on the surface of Ceres. *Science*, *353*(6303), aaf4279. https://doi.org/10.1126/science.aaf4279

Anderson, E. M. 1951. *The Dynamics of Faulting, Etc.(Revised.)*. Edinburgh, London.

Asphaug, E., 1997. Impact origin of the Vesta family. *Meteoritics & Planetary Science*, *32*(6), pp.965-980. https://doi.org/10.1111/j.1945-5100.1997.tb01584.x

Asphaug, E., Moore, J. M., Morrison, D., Benz, W., Nolan, M. C. and Sullivan, R. J., 1996. Mechanical and geological effects of impact cratering on Ida. *Icarus*, *120*(1), pp.158-184. https://doi.org/10.1006/icar.1996.0043

Babiker, M., & Gudmundsson, A., 2004. Geometry, structure and emplacement of mafic dykes in the Red Sea Hills, Sudan. *Journal of African Earth Sciences*, *38*(3), pp.279–292.

Baldwin, R. B. 1963. The Measure of the Moon. *University Chicago Press, Chicago*, pp. 128.

Barker, M. K., Mazarico, E., Neumann, G. A., Zuber, M. T., Haruyama, J., & Smith, D. E. 2016. A new lunar digital elevation model from the Lunar Orbiter Laser Altimeter and SELENE Terrain Camera. *Icarus*, *273*, pp. 346–355.

Beddingfield, C. B., & Cartwright, R. J. 2020. Hidden tectonism on Miranda's Elsinore Corona revealed by polygonal impact craters. *Icarus*, *343*, pp. 113687. https://doi.org/10.1016/j.icarus.2020.113687

Beddingfield, C. B., Burr, D. M., & Tran, L. T. 2016. Polygonal impact craters on Dione: Evidence for tectonic structures outside the wispy terrain. *Icarus*, *274*, pp. 163–194. https://doi.org/10.1016/j.icarus.2016.03.020

Benz, W. and Asphaug, E., 1994. Impact simulations with fracture. I. Method and tests. *Icarus*, *107*(1), pp. 98-116. https://doi.org/10.1006/icar.1994.1009

Beuthe, M. 2010. East–west faults due to planetary contraction. *Icarus*, *209*(2), pp. 795–817. https://doi.org/10.1016/j.icarus.2010.04.019

Bieniawski, Z. T. 1989. Engineering rock mass classifications: a complete manual for engineers and geologists in mining, civil, and petroleum engineering. *John Wiley & Sons*.

Bierhaus, E.B., McEwen, A.S., Robbins, S.J., Singer, K.N., Dones, L., Kirchoff, M.R., Williams, J.P., 2018. Secondary craters and ejecta across the solar system: Populations and effects on impact-crater–based chronologies. *Meteoritics & Planetary Science 53*(4), pp. 638–671.

Binder, A. B., & McCarthy Jr, D. W. 1972. Mars: The lineament systems. *Science*, *176*(4032), pp. 279–281. https://doi.org/10.1126/science.176.4032.279

Bland, M. T., Buczkowski, D. L., Sizemore, H. G., Ermakov, A. I., King, S. D., Sori, M. M., Raymond, C.A., Castillo-Rogez, J.C., & Russell, C. T. 2019. Dome formation on Ceres by solid-state flow analogous to terrestrial salt tectonics. *Nature Geoscience*, *12*(10), pp. 797–801.

Blewett, D.T., Buczkowski, D.L., Ruesch, O., Scully, J.E., O'Brien, D.P., Gaskell, R., Roatsch, T., Bowling, T.J., Ermakov, A., Hiesinger, H. and Williams, D.A., 2014. Vesta's north pole quadrangle Av-1 (Albana): Geologic map and the nature of the south polar basin antipodes. *Icarus, 244*, pp. 13-22. https://doi.org/10.1016/j.icarus.2014.03.007

Bottke Jr, W. F., Morbidelli, A., Jedicke, R., Petit, J. M., Levison, H. F., Michel, P., & Metcalfe, T. S. 2002. Debiased orbital and absolute magnitude distribution of the near-Earth objects. *Icarus*, *156*(2), 399–433.

Bowling, T.J., Johnson, B.C. and Melosh, H.J., 2014. Formation of equatorial graben on 4 Vesta following the Rheasilvia basin forming impact. *Vesta in the Light of Dawn: First Exploration of a Protoplanet in the Asteroid Belt, 1773*, 2018.

Bowling, T.J., Johnson, B.C., Melosh, H.J., Ivanov, B.A., O'Brien, D.P., Gaskell, R. and Marchi, S., 2013. Antipodal terrains created by the Rheasilvia basin forming impact on asteroid 4 Vesta. *Journal of Geophysical Research: Planets, 118*(9), 1821-1834. https://doi.org/10.1002/jgre.20123

Brace, W. F., & Kohlstedt, D. L. 1980. Limits on lithospheric stress imposed by laboratory experiments. *Journal of Geophysical Research: Solid Earth*, *85*(B11), pp. 6248–6252.

Buczkowski, D.L., Wyrick, D.Y., Iyer, K.A., Kahn, E.G., Scully, J.E.C., Nathues, A., Gaskell, R.W., Roatsch, T., Preusker, F., Schenk, P.M. and Le Corre, L., 2012. Large-scale troughs on Vesta: A signature of planetary tectonics. *Geophysical Research Letters*, *39*(18). https://doi.org/10.1029/2012GL052959

Burov, E. B., & Diament, M. 1992. Flexure of the continental lithosphere with multilayered rheology. *Geophysical Journal International*, *109*(2), pp. 449–468.

Byerlee, J. D. 1978. Friction of rocks. *Pure and Applied Geophysics*, *116*, 615–626.

Cardozo, N. and Allmendinger, R.W., 2013. Spherical projections with OSXStereonet. *Computers & Geosciences*, *51*, pp. 193-205. https://doi.org/10.1016/j.cageo.2012.07.021

Caristan, Y. 1982. The transition from high temperature creep to fracture in Maryland diabase. *Journal of Geophysical Research: Solid Earth*, *87*(B8), pp. 6781–6790.

Cartwright, J. A., Mansfield, C., & Trudgill, B. 1996. The growth of normal faults by segment linkage. *Geological Society of London Special Publication*, *99*(1), pp. 163–177.

Chapman, C.R., Haefner, R.R., 1967. A critique of methods for analysis of the diameter-frequency relation for craters with special application to the Moon. *Journal of Geophysical Research 72*(2), pp. 549–557.

Chapman, C.R., Merline, W.J., Ostrach, L.R., Xiao, Z., Solomon, S.C., Head, J.W., 2011. Small craters (secondaries) on Mercury's northern plains. *EPSC-DPS Joint Meeting 2011*, 1497 (abstract).

Cheng, H. 2021. The large-scale troughs on Asteroid 4 Vesta accommodate opening-mode displacement. *Open Science Framework.* https://doi.org/10.17605/OSF.IO/GH5R9

Cheng, H. C. J., & Klimczak, C. 2022a. Structural relationships in and around the Rheasilvia basin on Vesta. *Journal of Structural Geology*, *161*, pp. 104677. https://doi.org/10.1016/j.jsg.2022.104677

Cheng, H. C. J., & Klimczak, C. 2022b. Large-Scale Troughs on Asteroid 4 Vesta Accommodate Opening-Mode Displacement. *Journal of Geophysical Research: Planets*, *127*(6), e2021JE007130. https://doi.org/10.1029/2021JE007130

Cheng, H.C.J., Klimczak, C. and Fassett, C.I., 2021. Age relationships of large-scale troughs and impact basins on Vesta. *Icarus*, *366*, pp. 114512. https://doi.org/10.1016/j.icarus.2021.114512

Cloos, E. and Hershey, H.G., 1936. Structural age determination of Piedmont intrusives in Maryland. *Proceedings of the National Academy of Sciences*, *22*(1), pp. 71–80.

Collins, G.C., McKinnon, W.B., Moore, J.M., Nimmo, F., Pappalardo, R.T., Prockter, L.M., & Schenk, P.M. 2010. Tectonics of the outer planet satellites, in Watters, T.R., and Schultz, R.A., eds., *Planetary Tectonics: New York, Cambridge University Press*, p. 264–350.

Collins, G.S., Morgan, J., Barton, P., Christeson, G.L., Gulick, S., Urrutia, J., Warner, M. and Wünnemann, K., 2008. Dynamic modeling suggests terrace zone asymmetry in the Chicxulub crater is caused by target heterogeneity. *Earth and Planetary Science Letters*, *270*(3-4), pp. 221-230. https://doi.org/10.1016/j.epsl.2008.03.032

Cowie, P.A. and Scholz, C.H., 1992. Displacement-length scaling relationship for faults: data synthesis and discussion. *Journal of Structural Geology*, *14*(10), pp. 1149–1156.

Cowie, P.A., Gupta, S. and Dawers, N.H., 2000. Implications of fault array evolution for synrift depocentre development: insights from a numerical fault growth model. *Basin Research*, *12*(3–4), pp. 241–261.

Crane, K. T., & Klimczak, C. 2017. Timing and rate of global contraction on Mercury. *Geophysical Research Letters*, *44*(7), pp. 3082–3089.

Crater Analysis Techniques Working Group, 1979. Standard techniques for presentation and analysis of crater size-frequency data. *Icarus 37*, pp. 467–474.

Crider, J. G., & Pollard, D. D., 1998. Fault linkage: Three-dimensional mechanical interaction between echelon normal faults. *Journal of Geophysical Research: Solid Earth*, *103*(B10), pp. 24373–24391.

Cunje, A. B., & Ghent, R. R. 2016. Caloris basin, Mercury: History of deformation from an analysis of tectonic landforms. *Icarus*, *268*, pp. 131–144.

Davison, T. M., Ciesla, F. J., Collins, G. S., & Elbeshausen, D., 2014. The effect of impact obliquity on shock heating in planetesimal collisions. *Meteoritics & Planetary Science*, *49*(12), pp. 2252–-2265. https://doi.org/10.1111/maps.12394

Davison, T. M., O'Brien, D. P., Ciesla, F. J., & Collins, G. S., 2013. The early impact histories of meteorite parent bodies. *Meteoritics & Planetary Science*, *48*(10), pp. 1894–1918.

Dawers, N. H., Anders, M. H., & Scholz, C. H., 1993. Growth of normal faults: Displacement-length scaling. *Geology*, *21*(12), pp. 1107–1110.

Delaney, P. T., & Pollard, D. D., 1981. Deformation of host rocks and flow of magma during growth of minette dikes and breccia-bearing intrusions near Ship Rock, New Mexico. *U.S. Government Publishing Office*.

Denevi, B. W., Beck, A. W., Coman, E. I., Thomson, B. J., Ammannito, E., Blewett, D. T., Sunshine, J. M., De Sanctis, M.C., Li, J.Y., Marchi, S., Mittlefehldt, D.W, Petro, N. E., Raymond, C. A., & Russell, C. T., 2016. Global variations in regolith properties on asteroid Vesta from Dawn's low-altitude mapping orbit. *Meteoritics & Planetary Science*, *51*(12), pp. 2366–2386.

Denlinger, R.P. and Okubo, P., 1995, Structure of the mobile south flank of Kilauea Volcano, Hawaii. *Journal of Geophysical Research: Solid Earth*, *100*(B12), pp. 24499–24507.

Drake, M.J. and Consolmagno, G.J., 1977. Asteroid 4 Vesta: Possible bulk composition deduced from geochemistry of eucrites. *Lunar and Planetary Science Conference* (Vol. 8).

Duffield, W.A., 1975. *Structure and origin of the Koae fault system, Kilauea volcano, Hawaii* (No. 856). US Govt. Print. Off.

Dula Jr, W. F., 1991. Geometric models of listric normal faults and rollover folds. *AAPG Bulletin, 75*(10), 1609–1625.

Eppler, D. T., Ehrlich, R., Nummedal, D. & Schultz, P. H., 1983. Sources of shape variation in lunar impact craters: Fourier shape analysis. *Geological Society of America Bulletin, 94*, pp. 274–291.

Ermakov, A. I., Zuber, M. T., Smith, D. E., Raymond, C. A., Balmino, G., Fu, R. R., & Ivanov, B. A., 2014. Constraints on Vesta's interior structure using gravity and shape models from the Dawn mission. *Icarus*, *240*, pp. 146–160.

Fassett, C.I., Head, J.W., 2008. The timing of Martian valley network activity: Constraints from buffered crater counting. *Icarus 195*(1), pp. 61–89.

Fassett, C.I., Hirabayashi, M., Ostrach, L.R., Watters, W.A., Whitten, J.L., 2018. The Nature and Mobility of Regolith on Mercury's Smooth Plains from Observations of Crater Degradation and Equilibrium Size-Frequency Distributions. *Mercury: Current and Future Science of the Innermost Planet 2047*, pp. 6129.

Ferrill, D.A., Wyrick, D.Y. and Smart, K.J., 2011, Coseismic, dilational-fault and extension-fracture related pit chain formation in Iceland: Analog for pit chains on Mars. *Lithosphere*, *3*(2), pp. 133–142.

Fielder G., 1961. *Structure of the Moon's surface*. London: Pergamon Press, pp. 246.

Fossen, H. 2016. Faults. *Structural Geology*. Cambridge University Press. pp. 151–188

Freedman, D., & Diaconis, P., 1981. On the histogram as a density estimator: L 2 theory. *Zeitschrift für Wahrscheinlichkeitstheorie und verwandte Gebiete*, *57*(4), pp. 453–476.

Fu, R. R., Hager, B. H., Ermakov, A. I., & Zuber, M. T., 2014. Efficient early global relaxation of asteroid Vesta. *Icarus*, *240*, pp. 133–145.

Gaskell, R.W., 2012. SPC shape and topography of Vesta from DAWN imaging data. *AAS/Division for Planetary Sciences Meeting*, *44* (abstracts), pp. 209–03.

Gaskell, R.W., 2012. SPC shape and topography of Vesta from DAWN imaging data. *AAS/Division for Planetary Sciences Meeting*, 44 (abstracts), pp. 209–03.

Gault, D.E., 1970. Saturation and equilibrium conditions for impact cratering on the lunar surface: Criteria and implications. *Radio Science 5*, pp. 273–291.

Ge, S., Lin, G., Amelung, F., Okubo, P.G., Swanson, D.A. and Yunjun, Z., 2019, The Accommodation of the South Flank's Motion by the Koa ‘e Fault System, Kīlauea, Hawai ‘i: Insights From the June 2012 Earthquake Sequence. *Journal of Geophysical Research: Solid Earth*, *124*(11), pp. 11116–11129.

Goetze, C., & Evans, B., 1979. Stress and temperature in the bending lithosphere as constrained by experimental rock mechanics. *Geophysical Journal International*, *59*(3), pp. 463–478.

Gordon, R.G., 1998. The plate tectonic approximation: Plate nonrigidity, diffuse plate boundaries, and global plate reconstructions. *Annual Review of Earth and Planetary Sciences*, *26*(1), pp. 615–642.

Grasemann, B., Martel, S., & Passchier, C., 2005. Reverse and normal drag along a fault. *Journal of Structural Geology, 27*(6), pp. 999–1010.

Gudmundsson, A., 2011. *Rock fractures in geological processes*. Cambridge University Press.

Gudmundsson, A., 1992, Formation and growth of normal faults at the divergent plate boundary in Iceland. Terra Nova, 4(4), pp. 464–471.

Gwinner, K., Scholten, F., Spiegel, M., Schmidt, R., Giese, B., Oberst, J., Heipke, C., Jaumann, R., & Neukum, G., 2009. Derivation and validation of high-resolution digital terrain models from Mars Express HRSC data. *Photogrammetric Engineering & Remote Sensing, 75*(9), pp. 1127–1142.

Haight, F.A., 1967. Handbook of the Poisson Distribution.

Handin, J., 1969. On the Coulomb-Mohr failure criterion. *Journal of Geophysical Research, 74*(22), pp. 5343–5348.

Hartmann, W.K., 1984. Does crater "saturation equilibrium" occur in the Solar System? *Icarus 60*(1), pp. 56–74.

Hauber, E., & Kronberg, P., 2005. The large Thaumasia graben on Mars: Is it a rift? *Journal of Geophysical Research: Planets, 110*(E7), pp. E07003.

Hiesinger, H., Marchi, S., Schmedemann, N., Schenk, P., Pasckert, J. H., Neesemann, A., O'Brien, D. P., Kneissl, T., Ermakov, A. I., Fu, R. R. & Bland, M. T., 2016. Cratering on Ceres: Implications for its crust and evolution. *Science, 353*(6303), pp. aaf4759. https://doi.org/10.1126/science.aaf4759

Hoek, E., 1994. Strength of rock and rock masse.

Hoek, E., 2007. Practical rock engineering: RocScience.

Hoek, E., & Brown, E. T., 1997. Practical estimates of rock mass strength. *International Journal of Rock Mechanics and Mining Sciences*, *34*(8), pp. 1165–1186.

Hoek, E., Carranza-Torres, C., & Corkum, B., 2002. Hoek–Brown failure criterion—2002 edition. *Proceedings of NARMS-Tac*, *1*(1), pp. 267–273.

Holland, M., Urai, J.L. and Martel, S., 2006, The internal structure of fault zones in basaltic sequences. *Earth and Planetary Science Letters*, *248*(1-2), pp. 301–315.

Hughes, A.N. and Shaw, J.H., 2015, Insights into the mechanics of fault-propagation folding styles. *Bulletin*, *127*(11-12), pp. 1752–1765.

Ivanov, B.A. and Melosh, H.J., 2013. Two-dimensional numerical modeling of the Rheasilvia impact formation. *Journal of Geophysical Research: Planets*, *118*(7), pp. 1545-1557. https://doi.org/10.1002/jgre.20108

Jaumann, R., Williams, D.A., Buczkowski, D.L., Yingst, R.A., Preusker, F., Hiesinger, H., Schmedemann, N., Kneissl, T., Vincent, J.B., Blewett, D.T. and Buratti, B.J., 2012. Vesta's shape and morphology. *Science*, *336*(6082), pp. 687-690. https://doi.org/10.1126/science.1219122

Jenness, J., 2011. Tools for Graphics and Shapes. *Jenness Enterprises*.

Jutzi, M., Asphaug, E., Gillet, P., Barrat, J.A. and Benz, W., 2013. The structure of the asteroid 4 Vesta as revealed by models of planet-scale collisions. *Nature*, *494*(7436), pp. 207-210. https://doi.org/10.1038/nature11892

Karimi, S. and Dombard, A.J., 2016. On the possibility of viscoelastic deformation of the large south polar craters and true polar wander on the asteroid Vesta. *Journal of Geophysical Research: Planets*, *121*(9), pp. 1786-1797. https://doi.org/10.1002/2016JE005064

Kaven, J.O. and Martel, S.J., 2007, Growth of surface-breaching normal faults as a three-dimensional fracturing process. *Journal of Structural Geology*, *29*(9), pp. 1463–1476.

Keane, J. T., & Ermakov, A. I., 2019. No evidence for true polar wander of Ceres. *Nature Geoscience*, *12*(12), pp. 972–974. https://doi.org/10.1038/s41561-018-0232-3

Kinczyk, M. J., Prockter, L. M., Byrne, P. K., Susorney, H. C., & Chapman, C. R., 2020. A morphological evaluation of crater degradation on Mercury: Revisiting crater classification with MESSENGER data. *Icarus*, *341*, pp. 113637. https://doi.org/10.1016/j.icarus.2020.113637

Klimczak, C., 2015. Limits on the brittle strength of planetary lithospheres undergoing global contraction. *Journal of Geophysical Research: Planets*, *120*(12), pp. 2135–2151.

Klimczak, C., Byrne, P.K., Şengör, A.C. and Solomon, S.C., 2019, Principles of structural geology on rocky planets. *Canadian Journal of Earth Sciences*, *56*(12), pp. 1437–1457.

Klimczak, C., Ernst, C. M., Byrne, P. K., Solomon, S. C., Watters, T. R., Murchie, S. L., Preusker, F., & Balcerski, J. A., 2013. Insights into the subsurface structure of the Caloris basin, Mercury, from assessments of mechanical layering and changes in long-wavelength topography. *Journal of Geophysical Research: Planets*, *118*(10), pp. 2030–2044.

Kneissl, T., Gasselt, S.v., Neukum, G., 2011. Map-projection-independent crater size-frequency determination in GIS environments—New software tool for ArcGIS. *Planetary and Space Science 59*(11-12), pp. 1243–1254.

Kneissl, T., Michael, G.G., Platz, T., Walter, S.H.G., 2015. Age determination of linear surface features using the Buffered Crater Counting approach–Case studies of the Sirenum and Fortuna Fossae graben systems on Mars. *Icarus 250*, pp. 384–394.

Kneissl, T., Schmedemann, N., Reddy, V., Williams, D.A., Walter, S.H.G., Neesemann, A., Michael, G.G., Jaumann, R., Krohn, K., Preusker, F., Roatsch, T., Le Corre, L., Nathues, A., Ho¬mann, M., Schäfer, M., Buczkowski, D., Garry, W.B., Yingst, R.A., Mest, S.C., Russell, C.T., Raymond, C.A., 2014. Morphology and Formation Ages of Mid-Sized Post-Rheasilvia Craters - Geology of quadrangle Tuccia, Vesta. *Icarus 244*, pp. 133–157.

Kneissl, T., van Gasselt, S. and Neukum, G., 2011. Map-projection-independent crater size-frequency determination in GIS environments—New software tool for ArcGIS. *Planetary and Space Science*, *59*(11-12), pp. 1243-1254. https://doi.org/10.1016/j.pss.2010.03.015

Kohlstedt, D. L., & Mackwell, S. J. (2010). Strength and deformation of planetary lithospheres. *Planetary Tectonics*, pp. 397–456.

Konopliv, A. S., Park, R. S., Vaughan, A. T., Bills, B. G., Asmar, S. W., Ermakov, A. I., Rambaux, N., Raymond, C. A., Castillo-Rogez, J. C., Russell, C. T. & Smith, D. E., 2018. The Ceres gravity field, spin pole, rotation period and orbit from the Dawn radiometric tracking and optical data. *Icarus*, *299*, pp. 411–429. https://doi.org/10.1016/j.icarus.2017.08.005

Kreslavsky, M.A., Ivanov, M.A., Head, J.W., 2015. The resurfacing history of Venus: Constraints from buffered crater densities. *Icarus 250*, pp. 438–450.

Krishna, N., & Kumar, P. S., 2016. Impact spallation processes on the Moon: A case study from the size and shape analysis of ejecta boulders and secondary craters of Censorinus crater. *Icarus*, *264*, pp. 274–299. https://doi.org/10.1016/j.icarus.2015.09.033

Krohn, K., Jaumann, R., Otto, K., Hoogenboom, T., Wagner, R., Buczkowski, D.L., Garry, B., Williams, D.A., Yingst, R.A., Scully, J. and De Sanctis, M.C., 2014. Mass movement on Vesta at steep scarps and crater rims. *Icarus*, *244*, pp. 120-132. https://doi.org/10.1016/j.icarus.2014.03.013

Krohn, K., Jaumann, R., Otto, K., Hoogenboom, T., Wagner, R., Buczkowski, D.L., Garry, B., Williams, D.A., Yingst, R.A., Scully, J., De Sanctis, M.C., Kneissl, T., Schmedemann, N., Kersten, E., Stephan, K., Matz, K.-D., Pieters, C.M., Preusker, F., Roatsch, T., Schenk, P., Russell, C.T., Raymond, C.A., 2014. Mass Movements on Vesta at Steep Scarps and Crater Rims. *Icarus 244*, pp. 120–132.

Kuiper, N. H., 1960. On the random cumulative frequency function. *Indag. Math*, *22*, pp. 32–37.

Langford, J. C., & Diederichs, M. S. 2015. Quantifying uncertainty in Hoek–Brown intact strength envelopes. *International Journal of Rock Mechanics and Mining Sciences, 74*, pp. 91–102.

Li, J.Y., Mafi, J.N., 2012. Body-fixed coordinate systems for Asteroid (4) Vesta. *Planetary Data System.*

Liu, Z., Yue, Z., Michael, G., Gou, S., Di, K., Sun, S. and Liu, J., 2018. A global database and statistical analyses of (4) Vesta craters. *Icarus*, *311*, pp. 242-257. https://doi.org/10.1016/j.icarus.2018.04.006

Lucchitta, B. K., & Watkins, J. A., 1978. Age of graben systems on the Moon. In *Lunar and Planetary Science Conference Proceedings, 9*, pp. 3459–3472.

Macdonald, G., 1957, The epidemiology and control of malaria. *The Epidemiology and Control of Malaria.*

Mackwell, S. J., Bai, Q., & Kohlstedt, D. L., 1990. Rheology of olivine and the strength of the lithosphere. *Geophysical Research Letters*, *17*(1), pp. 9–12.

Malin, M. C., Bell, J. F., Cantor, B. A., Caplinger, M. A., Calvin, W. M., Clancy, R. T., Edgett, K. S., Edwards, L., Haberle, R. M., James, P. B., & Lee, S. W., 2007. Context camera investigation on board the Mars Reconnaissance Orbiter. *Journal of Geophysical Research: Planets*, *112*(E5), pp. E05S04.

Mao, X. and McKinnon, W.B., 2020. Spin evolution of Ceres and Vesta due to impacts. *Meteoritics & Planetary Science*, *55*(11), pp. 2493-2518. https://doi.org/10.1111/maps.13594

Marchi, S., McSween, H.Y., O'Brien, D.P., Schenk, P., De Sanctis, M.C., Gaskell, R., Jaumann, R., Mottola, S., Preusker, F., Raymond, C.A. and Roatsch, T., 2012. The violent collisional history of asteroid 4 Vesta. *Science*, *336*(6082), pp. 690-694. https://doi.org/10.1126/science.1218757

Martel, S.J. and Langley, J.S., 2006, Propagation of normal faults to the surface in basalt, Koae fault system, Hawaii. *Journal of Structural Geology*, *28*(12), pp. 2123–2143.

Marzari, F., Cellino, A., Davis, D.R., Farinella, P., Zappala, V. and Vanzani, V., 1996. Origin and evolution of the Vesta asteroid family. *Astronomy and Astrophysics*, *316*, pp. 248-262.

Matsuyama, I., & Nimmo, F., 2008. Tectonic patterns on reoriented and despun planetary bodies. *Icarus*, *195*(1), pp. 459–473. https://doi.org/10.1016/j.icarus.2007.12.003

Matsuyama, I., & Nimmo, F., 2011. Reorientation of Vesta: Gravity and tectonic predictions. *Geophysical research letters*, *38*(14). https://doi.org/10.1029/2011GL047967

McCord, T. B., & Sotin, C., 2005. Ceres: Evolution and current state. *Journal of Geophysical Research: Planets*, *110*(E5). https://doi.org/10.1029/2004JE002244

McCord, T.B., Adams, J.B. and Johnson, T.V., 1970. Asteroid Vesta: Spectral reflectivity and compositional implications. *Science*, *168*(3938), pp. 1445-1447. https://doi.org/10.1126/science.168.3938.1445

Medwedeff, D. A., & Krantz, R. W., 2002. Kinematic and analog modeling of 3-D extensional ramps: Observations and a new 3-D deformation model. *Journal of Structural Geology*, *24*(4), pp. 763–772.

Melosh, H. J., 1977. Global tectonics of a despun planet. *Icarus*, *31*(2), pp. 221–243. https://doi.org/10.1016/0019-1035(77)90035-5

Melosh, H. J., & McKinnon, W. B., 1988. The tectonics of Mercury. *Mercury*, *University of Arizona Press*, pp. 374–400.

Melosh, H. J., & Williams Jr, C. A., 1989. Mechanics of graben formation in crustal rocks: A finite element analysis. *Journal of Geophysical Research: Solid Earth*, *94*(B10), pp. 13961–13973.

Melosh, H.J., 1989. *Impact cratering: A geologic process*. New York: Oxford University Press; Oxford: Clarendon Press.

Meschede, M.A., Myhrvold, C.L. and Tromp, J., 2011. Antipodal focusing of seismic waves due to large meteorite impacts on Earth. *Geophysical Journal International, 187*(1), pp. 529-537. https://doi.org/10.1111/j.1365-246X.2011.05170.x

Michael, G.G., 2013. Planetary surface dating from crater size–frequency distribution measurements: Multiple resurfacing episodes and differential isochron fitting. *Icarus 226*(1), pp. 885–890.

Michael, G.G., Kneissl, T., Neesemann, A., 2016. Planetary Surface Dating from Crater Size-Frequency Distribution Measurements: Poisson Timing Analysis. *Icarus 277*, pp. 279–285.

Michael, G.G., Neukum, G., 2010. Planetary surface dating from crater size-frequency distribution measurements: Partial resurfacing events and statistical age uncertainty. *Earth and Planetary Science Letters 294*, pp. 223–229.

Michael, G.G., Platz, T., Kneissl, T., Schmedemann, N., 2012. Planetary surface dating from crater size–frequency distribution measurements: Spatial randomness and clustering. *Icarus 218*(1), pp. 169–177.

Minton, D.A., Fassett, C.I., Hirabayashi, M., Howl, B.A., Richardson, J.E., 2019. The equilibrium size-frequency distribution of small craters reveals the effects of distal ejecta on lunar landscape morphology. *Icarus 326*, pp. 63–87.

Montési, L. G., 2001. Concentric dikes on the flanks of Pavonis Mons: Implications for the evolution of Martian shield volcanoes and mantle plumes. *Special Papers-Geological Society of America*, pp. 165–182.

Moore, J. M., Schenk, P. M., Bruesch, L. S., Asphaug, E., & McKinnon, W. B., 2004. Large impact features on middle-sized icy satellites. *Icarus, 171*(2), pp. 421–443. https://doi.org/10.1016/j.icarus.2004.05.009

Morley, C. K., & Wonganan, N., 2000. Normal fault displacement characteristics, with particular reference to synthetic transfer zones, Mae Moh mine, northern Thailand. *Basin Research, 12*(3-4), pp. 307–327. https://doi.org/10.1111/j.1365-2117.2000.00127.x

Muraoka, H. and Kamata, H., 1983, Displacement distribution along minor fault traces. *Journal of Structural Geology*, *5*(5), pp. 483–495.

Murray, B.C., Belton, M.J., Danielson, G.E., Davies, M.E., Gault, D.E., Hapke, B., O'Leary, B., Strom, R.G., Suomi, V. and Trask, N., 1974. Mercury's surface: Preliminary description and interpretation from Mariner 10 pictures. *Science, 185*(4146), pp. 169-179.

Nahm, A. L., & Schultz, R. A., 2007. Outcrop-scale physical properties of Burns Formation at Meridiani Planum, Mars. *Geophysical research letters, 34*(20).

Nahm, A.L. and Schultz, R.A., 2011, Magnitude of global contraction on Mars from analysis of surface faults: Implications for martian thermal history. *Icarus*, *211*(1), pp. 389–400.

Neidhart, T., Leitner, J., & Firneis, M., 2017. Polygonal Impact Craters on selected Minor Bodies: Rhea, Dione, Tethys, Ceres, and Vesta. In *EGU General Assembly Conference Abstracts*. pp. 10081

Neukum, G., 1984. Meteorite bombardment and dating of planetary surfaces. National Aeronautics and Space Administration, Thesis, February 1983, Washington,

DC. Translated into English of "Meteoritenbombardement und Datierung Planetarer Oberflaechen" Munich, February 1983, pp. 1–186.

Neukum, G., Ivanov, B.A. and Hartmann, W.K., 2001. Cratering records in the inner solar system in relation to the lunar reference system. *Chronology and evolution of Mars*, pp. 55–86.

O'Brien, D.P. and Sykes, M.V., 2011. The origin and evolution of the asteroid belt—Implications for Vesta and Ceres. *Space science reviews*, *163*(1-4), pp. 41-61. https://doi.org/10.1007/s11214-011-9808-6

O'Brien, D.P., Morbidelli, A., Bottke, W.F., 2007. The primordial excitation and clearing of the asteroid belt—revisited. *Icarus 191*, pp. 434–452.

O'Brien, D.P., Marchi, S., Morbidelli, A., Bottke, W.F., Schenk, P.M., Russell, C.T., Raymond, C.A., 2014. Constraining the cratering chronology of Vesta. *Planetary and Space Science 103*, pp. 131–142.

Öhman, T., Aittola, M., Kostama, V. P., Hyvärinen, M., & Raitala, J., 2006. Polygonal impact craters in the Argyre region, Mars: Evidence for influence of target structure on the final crater morphology. *Meteoritics & Planetary Science*, *41*(8), pp. 1163–1173.

Öhman, T., Aittola, M., Kostama, V. P., Raitala, J., & Korteniemi, J., 2008. Polygonal impact craters in Argyre region, Mars: Implications for geology and cratering mechanics. *Meteoritics & Planetary Science*, *43*(10), pp. 1605–1628.

Öhman, T., Aittola, M., Korteniemi, J., Kostama, V. P., & Raitala, J., 2010. Polygonal impact craters in the solar system: Observations and implications. *Special Papers*

- *Geological Society of America*, *465*, pp. 51–65. https://doi.org/10.1130/2010.2465(04)

Okubo, C. H., 2010. Structural geology of Amazonian-aged layered sedimentary deposits in southwest Candor Chasma, Mars. *Icarus*, *207*(1), pp. 210–225.

Okubo, C. H., & Martel, S. J., 1998. Pit crater formation on Kilauea volcano, Hawaii. *Journal of Volcanology and Geothermal Research*, *86*(1–4), pp. 1–18.

Olson, J. E., 2003. Sublinear scaling of fracture aperture versus length: An exception or the rule? *Journal of Geophysical Research*, *108*(B9), pp. 2413.

Opheim, J. A., & Gudmundsson, A., 1989. Formation and geometry of fractures, and related volcanism, of the Krafla fissure swarm, northeast Iceland. *Geological Society of America Bulletin*, *101*(12), pp. 1608–1622.

Osinski, G. R., & Spray, J. G., 2005. Tectonics of complex crater formation as revealed by the Haughton impact structure, Devon Island, Canadian High Arctic. *Meteoritics & Planetary Science*, *40*(12), pp. 1813–1834. https://doi.org/10.1111/j.1945-5100.2005.tb00148.x

Otto, K. A., Jaumann, R., Krohn, K., Buczkowski, D., Von der Gathen, I., Kersten, E., Mest, S., Naß, A., Neesemann, A., Schulzeck, F. & Preusker, F., 2016. Origin and distribution of polygonal craters on (1) Ceres. In *Lunar and Planetary Science Conference Proceedings*, *47*. Abstract 1493.

Otto, K.A., Jaumann, R., Krohn, K., Matz, K.D., Preusker, F., Roatsch, T., Schenk, P., Scholten, F., Stephan, K., Raymond, C.A. and Russell, C.T., 2013. Mass-wasting features and processes in Vesta's south polar basin Rheasilvia. *Journal of*

Geophysical Research: Planets, *118*(11), pp. 2279-2294. https://doi.org/10.1002/2013JE004333

Otto, K.A., Jaumann, R., Krohn, K., Spahn, F., Raymond, C.A. and Russell, C.T., 2016. The Coriolis effect on mass wasting during the Rheasilvia impact on asteroid Vesta. *Geophysical Research Letters*, *43*(24), pp. 12-340. https://doi.org/10.1002/2016GL071539

Parekh, R., Otto, K. A., Jaumann, R., Matz, K. D., Roatsch, T., Kersten, E. & Raymond, C., 2021. Influence of volatiles on mass wasting processes on Vesta and Ceres. *Journal of Geophysical Research: Planets*, *126*(3), e2020JE006573. https://doi.org/10.1029/2020JE006573

Peacock, D. C. P., & Sanderson, D. J., 1994. Geometry and development of relay ramps in normal fault systems. *AAPG Bulletin*, *78*(2), pp. 147–165.

Peacock, D.C.P. and Parfitt, E.A., 2002, Active relay ramps and normal fault propagation on Kilauea Volcano, Hawaii. *Journal of structural geology*, *24*(4), pp. 729–742.

Pfiffner, O. A., & Ramsay, J. G., 1982. Constraints on geological strain rates: arguments from finite strain states of naturally deformed rocks. *Journal of Geophysical Research: Solid Earth*, *87*(B1), pp. 311–321.

Pieters, C.M., Ammannito, E., Blewett, D.T., Denevi, B.W., De Sanctis, M.C., Gaffey, M.J., Le Corre, L., Li, J.Y., Marchi, S., McCord, T.B. and McFadden, L.A., 2012. Distinctive space weathering on Vesta from regolith mixing processes. *Nature*, *491*(7422), pp. 79-82. https://doi.org/10.1038/nature11534

Podolsky, D.M. and Roberts, G.P., 2008, Growth of the volcano-flank Koa'e fault system, Hawaii. *Journal of Structural Geology*, *30*(10), pp. 1254–1263.

Poelchau, M.H. and Kenkmann, T., 2008. Asymmetric signatures in simple craters as an indicator for an oblique impact direction. *Meteoritics & Planetary Science*, *43*(12), pp. 2059-2072. https://doi.org/10.1111/j.1945-5100.2008.tb00661.x

Polit, A.T., Schultz, R.A. and Soliva, R., 2009, Geometry, displacement–length scaling, and extensional strain of normal faults on Mars with inferences on mechanical stratigraphy of the Martian crust. *Journal of Structural Geology*, *31*(7), pp. 662–673.

Pollard, D. D., & Aydin, A., 1988. Progress in understanding jointing over the past century. *Geological Society of America Bulletin*, *100*(8), pp. 1181–1204.

Poulimenos, G., 2000, Scaling properties of normal fault populations in the western Corinth Graben, Greece: implications for fault growth in large strain settings. *Journal of Structural Geology*, *22*(3), pp. 307–322.

Povilaitis, R.Z., Robinson, M.S., Bogert, C.H.V.d., Hiesinger, H., Meyer, H.M., Ostrach, L.R., 2018. Crater density differences: Exploring regional resurfacing, secondary crater populations, and crater saturation equilibrium on the Moon. *Planetary and Space Science 162*, pp. 41–51.

Prettyman, T.H., Yamashita, N., Toplis, M.J., McSween, H.Y., Schörghofer, N., Marchi, S., Feldman, W.C., Castillo-Rogez, J., Forni, O., Lawrence, D.J., Ammannito, E., Ehlmannm, B. L., Sizemore, H. G., Joy, S. P., Polanskey, C. A., Rayman, M. D., Raymond, C. A. & Russell, C. T., 2017. Extensive water ice within Ceres' aqueously altered regolith: Evidence from nuclear spectroscopy. *Science*, *355*(6320), pp. 55–59.

Preusker, F., Scholten, F., Matz, K. D., Elgner, S., Jaumann, R., Roatsch, T., Joy, S. P., Polanskey, C. A., Raymond, C. A., & Russell, C. T., 2016b. *Dawn at Ceres - Shape model and rotational state*. Paper presented at the 47th Lunar and Planetary Science Conference, Lunar and Planetary Institute, Houston, TX.

Preusker, F., Scholten, F., Matz, K. D., Roatsch, T., Jaumann, R., Raymond, C. A., & Russell, C. T.,2014. Global shape of (4) Vesta from Dawn FC Stereo images. *Vesta in the light of Dawn: First exploration of a protoplanet in the asteroid belt, 1773*, 2027.

Preusker, F., Scholten, F., Matz, K. D., Roatsch, T., Jaumann, R., Raymond, C. A., & Russell, C. T., 2016a. Dawn FC2 Derived Vesta DTM SPG V1. 0. *NASA Planetary Data System*, DAWN-A.

Prockter, L., Thomas, P., Robinson, M., Joseph, J., Milne, A., Bussey, B., Veverka, J. & Cheng, A., 2002. Surface expressions of structural features on Eros. *Icarus*, *155*(1), pp. 75–93. https://doi.org/10.1006/icar.2001.6770

R Core Team (2022). *R: A language and environment for statistical computing. R Foundation for Statistical Computing*, Vienna, Austria. URL https://www.R-project.org/

Ranalli, G., & Murphy, D. C., 1987. Rheological stratification of the lithosphere. *Tectonophysics*, *132*(4), pp. 281–295.

Reches, Z. E., & Eidelman, A. 1995. Drag along faults. *Tectonophysics*, *247*(1–4), pp. 145–156.

Resor, P. G., 2008. Deformation associated with a continental normal fault system, western Grand Canyon, Arizona. *Geological Society of America Bulletin, 120*(3–4), pp. 414–430.

Roatsch, T., Kersten, E., Matz, K. D., Preusker, F., Scholten, F., Jaumann, R., Raymond, C. A. & Russell, C. T., 2016. High-resolution Ceres high altitude mapping orbit atlas derived from Dawn framing camera images. *Planetary and Space Science, 129*, pp. 103–107.

Roatsch, T., Kersten, E., Matz, K.D., Preusker, F., Scholten, F., Elgner, S., Schroeder, S.E., Jaumann, R., Raymond, C.A. and Russell, C.T., 2015. Dawn FC2 derived vesta global mosaics V1. 0. *NASA Planetary Data System*, DAWN-A.

Robbins, S.J., Antonenko, I., Kirchoff, M.R., Chapman, C.R., Fassett, C.I., Herrick, R.R., Singer, K., Zanetti, M., Lehan, C., Huang, D., Gay, P.L., 2014. The variability of crater identification among expert and community crater analysts. *Icarus, 234*, pp. 109–131.

Robinson, M. S., Brylow, S. M., Tschimmel, M., Humm, D., Lawrence, S. J., Thomas, P. C., Denevi, B. W., Bowman-Cisneros, E., Zerr, J., Ravine, M. A., & Caplinger, M. A. (2010). Lunar reconnaissance orbiter camera (LROC) instrument overview. *Space Science Reviews, 150*(1–4), pp. 81–124.

Ruesch, O., Hiesinger, H., Blewett, D. T., Williams, D.A., Buczkowski, D., Scully, J., Yingst, R. A., Roatsch, T., Preusker, F., Jaumann, R. & Russell, C. T., 2014. Geologic map of the northern hemisphere of Vesta based on Dawn Framing Camera (FC) images. *Icarus, 244*, pp. 41–59. https://doi.org/10.1016/j.icarus.2014.01.035

Ruj, T., Komatsu, G., Pasckert, J. H., & Dohm, J. M., 2019. Timings of early crustal activity in southern highlands of Mars: Periods of crustal stretching and shortening. *Geoscience Frontiers*, *10*(3), pp. 1029–1037.

Russell, C. T., & Raymond, C. A., 2011. The dawn mission to Vesta and Ceres. In *The dawn mission to minor planets 4 Vesta and 1 Ceres*. Springer, New York, NY. pp. 3–23.

Russell, C. T., Raymond, C. A., Coradini, A., McSween, H. Y., Zuber, M. T., Nathues, A., Sanctis, M. C. D., Jaumann, R., Konopliv, A. S., Preusker, F., & Asmar, S. W., 2012. Dawn at Vesta: Testing the protoplanetary paradigm. *Science*, *336*(6082), pp. 684–686.

Russell, C.T., Raymond, C.A., 2011. The Dawn Mission to Vesta and Ceres. In: *Russell, C., Raymond, C. (eds) The Dawn Mission to Minor Planets 4 Vesta and 1 Ceres*. Springer, New York, NY. pp. 3-23. https://doi.org/10.1007/978-1-4614-4903-4_2

Russell, C.T., Raymond, C.A., Coradini, A., McSween, H.Y., Zuber, M.T., Nathues, A., De Sanctis, M.C., Jaumann, R., Konopliv, A.S., Preusker, F. and Asmar, S.W., 2012. Dawn at Vesta: Testing the protoplanetary paradigm. *Science*, *336*(6082), pp. 684-686. https://doi.org/10.1126/science.1219381

Ruzicka, A., Snyder, G. A., & Taylor, L. A., 1997. Vesta as the howardite, eucrite and diogenite parent body: Implications for the size of a core and for large-scale differentiation. *Meteoritics & Planetary Science*, *32*(6), pp. 825–840.

Sanderson, D. J., & Peacock, D. C., 2020. Making rose diagrams fit-for-purpose. *Earth-Science Reviews*, *201*, pp. 103055. https://doi.org/10.1016/j.earscirev.2019.103055

Schäfer, M., Nathues, A., Williams, D. A., Mittlefehldt, D. W., Corre, L. L., Buczkowski, D. L., Kneissl, T., Thangjam, G. S., Hoffmann, M., Schmedemann, N., & Schäfer, T., 2014. Imprint of the Rheasilvia impact on Vesta–Geologic mapping of quadrangles Gegania and Lucaria. *Icarus*, *244*, pp. 60–73.

Schäfer, M., Nathues, A., Williams, D.A., Mittlefehldt, D.W., Le Corre, L., Buczkowski, D.L., Kneissl, T., Thangjam, G.S., Ho¬mann, M., Schmedemann, N., Schäfer, T., Scully, J.E.C., Li, J.Y., Reddy, V., Garry, W.B., Krohn, K., Yingst, R.A., Gaskell, R.W., Russell, C.T., 2014. Imprint of the Rheasilvia impact on Vesta - Geologic mapping of quadrangles Gegania and Lucaria. *Icarus 244*, pp. 60–73. https://doi.org/10.1016/j.icarus.2014.06.026

Schenk, P., O'Brien, D.P., Marchi, S., Gaskell, R., Preusker, F., Roatsch, T., Jaumann, R., Buczkowski, D., McCord, T., McSween, H.Y., Williams, D., 2012. The geologically recent giant impact basins at Vesta's south pole. *Science 336*, pp. 694–697.

Schenk, P., Vincent, J.B., O'Brien, D.P., Jaumann, R. and Williams, D., 2012, September. Impact crater morphologies on Vesta. In *European Planetary Science Congress* (Vol. 7, pp. 700).

Schenk, P.M., Neesemann, A., Marchi, S., Otto, K., Hoogenboom, T., O'Brien, D.P., Castillo-Rogez, J., Raymond, C.A. and Russell, C.T., 2022. A young age of formation of Rheasilvia basin on Vesta from floor deformation patterns and crater counts. *Meteoritics & Planetary Science, 57*(1), pp. 22–47. https://doi.org/10.1111/maps.13772

Schlische, R. W., Young, S. S., Ackermann, R. V., & Gupta, A., 1996. Geometry and scaling relations of a population of very small rift-related normal faults. *Geology, 24*(8), pp. 683–686. https://doi.org/10.1130/0091-7613(1996)024<0683:GASROA>2.3.CO;2

Schmedemann, N., Kneissl, T., Ivanov, B.A., Michael, G.G., Wagner, R.J., Neukum, G., Ruesch, O., Hiesinger, H., Krohn, K., Roatsch, T., Preusker, F., 2014. The cratering record, chronology and surface ages of (4) Vesta in comparison to smaller asteroids and the ages of HED meteorites. *Planetary and Space Science 103*, pp. 104–130.

Schmidt, B.E., 2011, December. Tectonics of Vesta: Indication of Spin-up and Reorientation?. In *AGU Fall Meeting Abstracts* (Vol. 2011, pp. U21B-06).

Schofield, A. N., 2005. *Disturbed soil properties and geotechnical design*. Thomas Telford.

Schultz, P.H. and Crawford, D.A., 2011. Origin of nearside structural and geochemical anomalies on the Moon. *Geological Society of America Special Papers, 477*, pp. 141–159.

Schultz, P.H. and Gault, D.E., 1975. Seismic effects from major basin formations on the Moon and Mercury. *The Moon, 12*(2), pp. 159–177. https://doi.org/10.1007/BF00577875

Schultz, R. A., 1992. Limitations on the applicability of Byerlee's law and the Griffith criterion to shallow crustal conditions. *Lunar and Planetary Science Conference, 23* (abstracts),

Schultz, R. A., 1996. Relative scale and the strength and deformability of rock masses. *Journal of Structural Geology, 18*(9), 1139–1149.

Schultz, R. A., 1995. Limits on strength and deformation properties of jointed basaltic rock masses. *Rock Mechanics and Rock Engineering, 28*(1), 1–15.

Schultz, R. A., 2019. *Geologic fracture mechanics*. Cambridge University Press.

Schultz, R. A., & Lin, J., 2001. Three-dimensional normal faulting models of the Valles Marineris, Mars, and geodynamic implications. *Journal of Geophysical Research: Solid Earth, 106*(B8), pp. 16549–16566.

Schultz, R. A., Moore, J. M., Grosfils, E. B., Tanaka, K. L., & Mege, D., 2007. The Canyonlands model for planetary grabens: Revised physical basis and implications. In M. Chapman (Ed.), *The Geology of Mars: Evidence from Earth-Based Analogs* (pp. 371–399). Cambridge University Press.

Schultz, R. A., Okubo, C. H., & Wilkins, S. J., 2006. Displacement-length scaling relations for faults on the terrestrial planets. *Journal of Structural Geology, 28*(12), pp. 2182–2193.

Schultz, R.A. and Lin, J., 2001, Three-dimensional normal faulting models of the Valles Marineris, Mars, and geodynamic implications. *Journal of Geophysical Research: Solid Earth, 106*(B8), pp. 16549–16566.

Schultz, R.A., 1997, Displacement-length scaling for terrestrial and Martian faults: Implications for Valles Marineris and shallow planetary grabens. *Journal of Geophysical Research: Solid Earth, 102*(B6), pp. 12009–12015.

Schultz, R.A., Klimczak, C., Fossen, H., Olson, J.E., Exner, U., Reeves, D.M. and Soliva, R., 2013, Statistical tests of scaling relationships for geologic structures. *Journal of Structural Geology*, *48*, pp. 85–94.

Schultz, R.A., Okubo, C.H. and Wilkins, S.J., 2006, Displacement-length scaling relations for faults on the terrestrial planets. *Journal of Structural Geology*, *28*(12), pp. 2182–2193.

Schultz, R.A., Soliva, R., Fossen, H., Okubo, C.H. and Reeves, D.M., 2008, Dependence of displacement–length scaling relations for fractures and deformation bands on the volumetric changes across them. *Journal of Structural Geology*, *30*(11), pp. 1405–1411.

Scully, J. E., Buczkowski, D. L., Schmedemann, N., Raymond, C. A., Castillo-Rogez, J. C., King, S. D., Bland, M. T., Ermakov, A. I., O'Brien, D. P., Marchi, S., Longobardo, A. N., Russell, C. T., Fu, R. R. & Neveu, M., 2017. Evidence for the interior evolution of Ceres from geologic analysis of fractures. *Geophysical Research Letters*, *44*(19), pp. 9564–9572. https://doi.org/10.1002/2017GL075086

Scully, J.E., Yin, A., Russell, C.T., Buczkowski, D.L., Williams, D.A., Blewett, D.T., Ruesch, O., Hiesinger, H., Le Corre, L., Mercer, C. and Yingst, R.A., 2014. Geomorphology and structural geology of Saturnalia Fossae and adjacent structures in the northern hemisphere of Vesta. *Icarus*, *244*, pp. 23-40. https://doi.org/10.1016/j.icarus.2014.01.013

Shoemaker, E. M., 1960. *Impact mechanics at Meteor Crater, Arizona*. Princeton University.

Shoemaker, E. M., 1962. Interpretation of lunar craters. *Physics and Astronomy of the Moon*, pp. 283–359.

Shoemaker, E. M., & Wolfe, R. F., 1987. Crater production on Venus and Earth by asteroid and comet impact. *NASA, Washington, Reports of Planetary Geology and Geophysics Program, 1986*.

Sierks, H., Keller, H. U., Jaumann, R., Michalik, H., Behnke, T., Bubenhagen, F., Büttner, I., Carsenty, U., Christensen, U., Enge, R., Fiethe, B., Gutiérrez Marqués, P., Hartwig, H., Krüger, H., Kühne, W., Maue, T., Mottola, S., Nathues, A., Reiche, K. U., Richards, M. L., Roatsch, T., Schröder, S. E., Szemerey, I. & Tschentscher, M., 2011. The Dawn framing camera. *Space science reviews*, *163*(1), pp. 263–327. https://doi.org/10.1007/s11214-011-9745-4

Smith, D. E., Zuber, M. T., Frey, H. V., Garvin, J. B., Head, J. W., Muhleman, D. O., Pettengill, G. H., Phillips, R. J., Solomon, S. C., Zwally, H. J., & Banerdt, W. B., 2001. Mars Orbiter Laser Altimeter: Experiment summary after the first year of global mapping of Mars. *Journal of Geophysical Research: Planets*, *106*(E10), pp. 23689–23722.

Soliva, R., Benedicto, A., Schultz, R. A., Maerten, L., & Micarelli, L., 2008. Displacement and interaction of normal fault segments branched at depth: Implications for fault growth and potential earthquake rupture size. *Journal of Structural Geology*, *30*(10), pp. 1288–1299. https://doi.org/10.1016/j.jsg.2008.07.005

Soliva, R., Schultz, R.A. and Benedicto, A., 2005, Three-dimensional displacement-length scaling and maximum dimension of normal faults in layered rocks. *Geophysical Research Letters*, *32*(16).

Spudis, P. D., & Guest, J. E., 1988. Stratigraphy and geologic history of Mercury. *Mercury*, pp. 118–164.

Stein, S. and Wysession, M., 2009. *An introduction to seismology, earthquakes, and earth structure*. John Wiley & Sons.

Sterenborg, M. G., & Crowley, J. W., 2013. Thermal evolution of early solar system planetesimals and the possibility of sustained dynamos. *Physics of the Earth and Planetary Interiors*, *214*, 53–73.

Stickle, A.M., Schultz, P.H. and Crawford, D.A., 2015. Subsurface failure in spherical bodies: A formation scenario for linear troughs on Vesta's surface. *Icarus*, *247*, pp. 18-34. https://doi.org/10.1016/j.icarus.2014.10.002

Tanaka, K. L., & Golombek, M. P., 1989. Martian tension fractures and the formation of grabens and collapse features at Valles Marineris. *Lunar and Planetary Science Conference Proceedings*, *19*, pp. 383–396.

Tanaka, K.L., 1982. A new time-saving crater-count technique, with application to narrow features. *NASA Technical Memo, NASA TM-85127*, pp. 123–125.

The IAU WG Cartographic Coordinates & Rotational Elements (WGCCRE), 2014.. New Coordinate System for (4) Vesta.

Thomas, P.C., Binzel, R.P., Gaffey, M.J., Zellner, B.H., Storrs, A.D. and Wells, E., 1997. Vesta: Spin pole, size, and shape from HST images. *Icarus*, *128*(1), pp. 88-94. https://doi.org/10.1006/icar.1997.5736

Thomas, P. C., and Prockter, L. M.., 2010. Tectonics of small bodies. *Planetary Tectonics*, 11, 233.

Torabi, A., Alaei, B. and Libak, A., 2019, September. Fault Architecture, an Integrated Study. In *Fifth International Conference on Fault and Top Seals* (Vol. 2019, No. 1, pp. 1–5). EAGE Publications BV.

Tricarico, P., 2018. True polar wander of Ceres due to heterogeneous crustal density. *Nature Geoscience*, *11*(11), pp. 819–824. https://doi.org/10.1038/s41561-018-0232-3

Vermilye, J. M., & Scholz, C. H., 1995. Relation between vein length and aperture. *Journal of Structural Geology*, *17*(3), pp. 423–434.

Walsh, J. J., & Watterson, J., 1987. Distributions of cumulative displacement and seismic slip on a single normal fault surface. *Journal of Structural Geology*, *9*(8), pp.1039–1046.

Watters, W. A., Grotzinger, J. P., Bell III, J., Grant, J., Hayes, A. G., Li, R., Squyres, S. W. & Zuber, M. T., 2011. Origin of the structure and planform of small impact craters in fractured targets: Endurance Crater at Meridiani Planum, Mars. *Icarus*, *211*(1), pp. 472–497. https://doi.org/10.1016/j.icarus.2010.08.030

Weber, P., Zeilnhofer, M. F., Martorana, M., & Nocera, K., 2022. Regional Investigations of Polygonal Impact Craters on the Moon and Vesta. *Research Notes of the AAS*, *6*(4), pp. 87. https://doi.org/10.3847/2515-5172/ac69f3

Weihs, G. T., Leitner, J. J., & Firneis, M. G., 2015. Polygonal impact craters on mercury. *Planetary and Space Science*, *111*, pp. 77–82.

Wichman, R.W., Schultz, P.H., 1989. Sequence and mechanisms of deformation around the Hellas and Isidis impact basins on Mars. *Journal of Geophysical Research: Solid Earth 94*, pp. 17333–17357.

Wilkins, S.J. and Gross, M.R., 2002, Normal fault growth in layered rocks at Split Mountain, Utah: influence of mechanical stratigraphy on dip linkage, fault restriction and fault scaling. *Journal of Structural Geology*, *24*(9), pp. 1413–1429.

Williams, D. A., Buczkowski, D. L., Mest, S. C., Scully, J. E., Platz, T., & Kneissl, T., 2018. Introduction: the geologic mapping of Ceres. *Icarus*, *316*, pp. 1–13. https://doi.org/10.1016/j.icarus.2017.05.004

Williams, D.A. and Greeley, R., 1994. Assessment of antipodal-impact terrains on Mars. *Icarus, 110*(2), pp. 196-202. https://doi.org/10.1006/icar.1994.1116

Williams, D.A., Jaumann, R., McSween Jr, H.Y., Marchi, S., Schmedemann, N., Raymond, C.A. and Russell, C.T., 2014. The chronostratigraphy of protoplanet Vesta. *Icarus, 244*, pp. 158-165. https://doi.org/10.1016/j.icarus.2014.06.027

Williams, D.A., Yingst, R.A., Garry, W.B., 2014. Introduction: The geologic map of Vesta. *Icarus 244*, pp. 1–12.

Wilson, L. and Head, J.W., 2015. Groove formation on Phobos: Testing the Stickney ejecta emplacement model for a subset of the groove population. *Planetary and Space Science, 105*, pp. 26-42. https://doi.org/10.1016/j.pss.2014.11.001

Wolfe, E.W. and Morris, J., 1996, *Geologic map of the island of Hawaii* (No. 2524-A). US Geological Survey.

Wood, C. A., Head, J. W., & Cintala, M. J., 1977. Crater degradation on Mercury and the Moon-Clues to surface evolution. In *Lunar and Planetary Science Conference Proceedings*, *8*. pp. 3503–3520

Wyrick, D., Ferrill, D. A., Morris, A. P., Colton, S. L., & Sims., D. W., 2004. Distribution, morphology, and origins of Martian pit crater chains. *Journal of Geophysical Research: Planets*, *109*(E6), pp. E06005.

Wyrick, D.Y., Morris, A.P. and Ferrill, D.A., 2011, Normal fault growth in analog models and on Mars. *Icarus*, *212*(2), pp. 559–567.

Xiao, H., & Suppe, J., 1992. Origin of rollover (1). *AAPG Bulletin, 76*(4), pp. 509–529.

Yingst, R. A., Mest, S. C., Berman, D. C., Garry, W. B., Williams, D. A., Buczkowski, D., Jaumann, R., Pieters, C. M., Sanctis, M. C. D., Frigeri, A., & Corre, L. L., 2014. Geologic mapping of Vesta. *Planetary and Space Science*, *103*, pp. 2–23.

Yingst, R. A., Mest, S. C., Berman, D. C., Garry, W. B., Williams, D. A., Buczkowski, D., Jaumann, R., Pieters, C. M., De Sanctis, M. C., Frigeri, A. L., Le Corre, L., Preusker, F., Raymond, C. A., Reddy, V., Russell, C. T., Roatsch, T. & Schenk, P. M., 2014. Geologic mapping of Vesta. *Planetary and Space Science*, *103*, pp. 2–23. https://doi.org/10.1016/j.pss.2013.12.014

Zeilnhofer, M. F., & Barlow, N. G., 2021. The characterization and distribution of polygonal impact craters on Ceres and their implications for the cerean crust. *Icarus*, *368*, pp. 114586. https://doi.org/10.1016/j.icarus.2021.114586

Zuber, M. T., McSween, H. Y., Binzel, R. P., Elkins-Tanton, L. T., Konopliv, A. S., Pieters, C. M., & Smith, D. E., 2011. Origin, internal structure and evolution of 4 Vesta. *Space Science Reviews*, *63*, pp. 77–93.